Institute of Engineering, Surveying and Space Geodesy

Integration of ARAIM Technique for Integrity Performance Prediction, Procedures Development and Pre-Flight Operations

By

Simone Paternostro

Project Supervisors

Prof Terry Moore

Dr Chris Hill

Dr Jason Atkin

Prof Herve P. Morvan

Thesis submitted to the University of Nottingham for the degree of

Doctor of Philosophy

September 2017

ABSTRACT

Advanced Receiver Autonomous Integrity Monitoring (ARAIM) is a new Aircraft Based Augmentation System (ABAS) technique, firstly presented in the two reports of the GNSS Evolutionary Architecture Study (GEAS). The ARAIM technique offers the opportunity to enable GNSS receivers to serve as a primary means of navigation, worldwide, for precision approach down to LPV-200 operation, while at the same time potentially reducing the support which has to be provided by Ground and Satellite Based Augmented Systems (GBAS and SBAS).

Previous work analysed ARAIM performance, clearly showing the potential of this new architectures to provide the Required Navigation Performance down to LPV 200 approach procedures. However, almost all of the studies have been performed with respect to fixed points on a grid on the Earth's surface, with full view of the sky, evaluating ARAIM performance from a geometrical point of view and using nominal performance in simulated scenarios which last several days. Though, the operational configuration was not examined; attitude changes from manoeuvres, obscuration by the aircraft body and shadowing from the surrounding environment could all affect the incoming signal from the GNSS constellations, leading to configurations that could adversely affect the real performance.

In this research, ARAIM performances in simulated operational configurations are presented. Four different algorithms were developed that integrate the ARAIM technique for performance prediction analysis. These algorithms could usefully be implemented:

- In the design of instrument approach procedures. The algorithms could be used to improve the procedure of the development of new instrument approaches, reducing time, effort and costs.
- In the aircraft Flight Management Systems. The algorithms could support the pilots in the pre-flight briefing, highlighting possible integrity outage in advance and allowing them to select a different approach or making them aware of the need to utilise additional positioning systems.

Increased awareness and better pre-flight planning could ultimately improve the safety of flights and contribute to the safe introduction of GNSS as a viable positioning method for instrument approach.

The results showed that the aircraft attitude and the surrounding environment affect the performance of the ARAIM algorithm; each satellite lost generates a peak in the performance parameters that depends on the total number of satellites in view, their relative geometry and on the number of satellites lost at the same time. The main outcome of this research is the identification that the ideal scenario would be to have a tri-constellation system that provides at the same time high redundancy, reliability and increased safety margin.

ACKNOWLEDGEMENT

This research was conducted at the Institute for Aerospace Technology in collaboration with the Nottingham Geospatial Institute.

I would like to thank my academic supervisors Professor Terry Moore, Dr Chris Hill, Dr Jason Atkin and Prof Hervé Morvan for their support, guidance throughout this research and for giving me the opportunity to be part of the INNOVATE project.

During the project, I had the opportunity to attend a wide variety of courses and events that helped me to develop the set of skills and the network that allowed me to get a position in one of the fields I am really passionate about and it wouldn't have been possible without their support.

I would like to thank Mr John Wilde and Mr Kieran Conlon of the DW International Ltd, Chris Teubert from NASA and Juan Blanch from Stanford University for supporting this work and for their helpful technical comments.

For their continuous collaboration and mutual backing and encouragement, I would like to thank all the other INNOVATE researchers.

And finally, and most importantly, I would like to thank my partner and my family for all their support through all of my years of study. Without their support, this work would not have been possible.

ACRONYMS

3-DOF	Three Degrees of Freedom
ABAS	Aircraft Based Augmentation System
AIRAC	Aeronautical Information Regulation and Control
AL	Alert Level
APPATT	ARAIM Performance on Predicted Aircraft Trajectory Tool
APV	Approach Procedures with Vertical guidance
ARAIM	Advanced Receiver Autonomous Integrity Monitoring
ATC	Air Traffic Controller
ATM	Air Traffic Management
ATMRPP	Air Traffic Management Requirements and Performance Panel
C/A	Coarse/Acquisition
CAA	Civil Aviation Authority
CAS	Calibrated Airspeed
CDA	Continuous Descent Approach
CDO	Continuous Descent Operations
CoG	Center of Gravity
CONOPS	Concept of Operations
DA/H	Decision Altitude/Height
DFMC	Dual-Frequency-Multi-Constellation
DLR	Deutschen Zentrums für Luft- und Raumfahrt
DME	Distance Measuring Equipment
DoD	Department of Defence
DTA	Distance of Turn Anticipation
ECEF	Earth-Centered-Earth-Fixed
EGM	Earth Geopotential Model
EGNOS	European GNSS Navigation Overlay System
EMT	Effective Monitoring Threshold
ENU	East North UP

ESR	Early Stage Researcher
ETA	Estimated Arrival Time
FA	False Alert
FAA	Federal Aviation Administration
FANS	Future Air Navigation Service
FD	Fault Detection
FDE	Fault Detection and Exclusion
FDI	Fault Detection and Isolation
FDR	Fault Detection and Recovery
FMEA	Failure Mode Effect Analysis
FMS	Flight Management System
FOC	Flight Operation Centre
FPG	Flight Path Generator
FPM	Flight Path Modifier
GAGAN	GPS Aided Geo Augmented Navigation
GBAS	Ground Based Augmented Systems
GEAS	GNSS Evolutionary Architecture Study
GEO	Geostationary Earth Orbit
GIC	GNSS Integrity Channel
GNSS	Global Navigation Satellite System
GPS	Global Positioning System
GUI	Graphical User Interface
HAL	Horizontal Alert Level
HMI	Hazardous Misleading Information
HPE	Horizontal Position Error
HPL	Horizontal Protection Level
IAS	Indicated Airspeed
IAT	Institute for Aerospace Technology
IBPL	Isotropy-Based Protection Level
ICAO	International Civil Aviation Organization

ICC	Inter-Constellation Comparison
IDP	Innovative Doctoral Programme
IERS	International Earth Rotation and Reference Systems Service
IFR	Instrument Flight Rules
IGS	International GNSS Service
ILS	Instrumental Landing System
INNOVATE	INtegration of NOVel Aerospace TEchnologies
ION	Institute of Navigation
ISA	International Standard Atmosphere
ISM	Integrity Support Message
LNAV	Lateral Navigation
LOC	Localizer
LoS	Line of Sight
LP	Localizer Performance
LPV-200	Localizer Performance with Vertical guidance
LSR	Least-Squares Residual
LT	Long Term
MAAST	MATLAB Algorithm Availability Simulation tool
MCS	Master Control Station
MDA	Minimum Descent Altitudes
MEO	Medium Earth Orbit
MHSS	Multi-Hypothesis Solution Separation
MLS	Microwave Landing System
MR	Maximum Residual
MSAS	Multi-Functional Satellite Augmentation System
NASA	National Aeronautics and Space Administration
NAVAID	Navigational Aid
NDB	Non-Directional Beacon
NED	North East Down
NextGen	Next Generation Air Transportation System

NIORAIM	Novel Integrity-Optimized RAIM
NPA	Non-Precision Approach
NRT APPT	Near Real Time ARAIM Performance Prediction Tool
OPD	Optimized Profile Descent
OWAS	Optimally Weighted Average Solution
PA	Precision Approach
PAR	Precision Approach Radar
PBN	Performance Based Navigation
PE	Position Error
PL	Protection Level
PRN	Pseudo Random Noise
QPPTW	Quickest path problem with Time Windows
RAIM	Receiver Autonomous Integrity Monitoring
RF	Radio Frequency
RNAV	Area Navigation
RNP	Required Navigation Performance
RNP AR	Required Navigation Performance Authorization Required
RRAIM	Relative Receiver Autonomous Integrity Monitoring
RVR	Runway Visual Range
RVT	RNAV Validation Tool
SARPS	Standards and Recommended Practices
SBAS	Satellite Based Augmented Systems
SDCM	System for Differential Corrections and Monitoring
SESAR	Single European Sky ATM Research
SID	Standard Instrument Departures
SISA	Signal-in-Space-Accuracy
SISE	Signal-in-Space-Error
SoR	Specification of Requirements
SS	Solution Separation
SSE	Error Sum of Squares

ST	Short Term
STAR	Standard Terminal Arrival Routes
STRM	Space Shuttle Radar Topography Mission
SV	Space Vehicle
TAS	True Airspeed
TBO	Trajectory Based Operations
TOA	Time of Almanac
TRL	Technology Readiness Level
TTA	Time to Alert
TWD	Tailwind
UAV	Unmanned Aerial Vehicle
UDP	User Datagram Protocol
URA	User Range Accuracy
URE	User Range Error
VAL	Vertical Alert Level
VHF	Very High Frequency
VNAV	Vertical Navigation
VOR	VHF Omni-directional Radio Range
VPE	Vertical Position Error
VPL	Vertical Protection Level
VS	Vertical Speed
WAAS	Wide Area Augmentation System
WG	Working Group
WGS	World Geodetic System
WP	Waypoint
WP	Work package
WSSE	Weighted Sum of the Squared Errors
XPC	X-Plane Connect

(this page is left intentionally blank)

TABLE OF CONTENTS

1. INTRODUCTION

The stringent requirements imposed by the Civil aviation community on the levels of precision, integrity, continuity of service and availability, pushed the GNSS community to develop new solutions that could guarantee the required level of performances. In particular, the integrity and its impact on safety are one of the major drivers in the civil aviation domain, due to its capability of providing timely warnings to the user when the GNSS service is not available.

The development of new constellations and the modernization of existing ones have increased the availability and the number of satellite-in-view, paving the way to new navigation algorithms and techniques and giving the chance to improve the navigation performances. At the same time, the increased number of satellites could reduce the support provided by the Ground Based Augmented System (GBAS) and Satellite Based Augmented Systems (SBAS). On the other hand, this means becoming GNSS dependant, since it seems to be the most reliable system for Positioning, Navigation and Timing (PNT) purpose.

These enhanced future capabilities can enable GNSS receivers to serve as a primary means of navigation, worldwide, and have provided the motivation for the Federal Aviation Administration (FAA) to form the GNSS Evolution Architecture Study (GEAS). This panel, formed in 2008, investigates the new GNSS-based architectures, with a focus on precision approach down to LPV-200 operations (Localizer performance with vertical guidance down to 200 feet). GEAS identified and defined a new technique as the most promising system, named ARAIM, Advanced Receiver

Autonomous Integrity Monitoring, an improved version of the current RAIM. The literature, produced through a series of studies, has analysed the performance of this new technique and has clearly shown the potential of ARAIM architectures to provide the Required Navigation Performance for LPV 200.

1.1. INNOVATE PROJECT BACKGROUND INTRODUCTION

The current doctoral project has been developed within the INNOVATE research project and a brief presentation is provided in the following section.

INNOVATE acronym stands for "the systematic INtegration of NOVel Aerospace TEchnologies" and it is European Union-funded Marie Curie Innovative Doctoral Programme (IDP) arose from the need for an integrated approach to the development and exploitation of technology within the aerospace engineering sector that aims to promote fundamental research, Technology Readiness Level (TRL) 1-3, but also to implement and support development and demonstration activities at TRL 4-6, hereby addressing a significant gap identified both by government and industry. The INNOVATE team is formed by 13 Early Stage Researchers (ESRs) and each of us had the opportunity to undertake some fundamental research activities inside and as part of a world-leading research group, but also to bring these technologies and methods into a systems context, thus to think about development and, ultimately, demonstration. In other words, we had the opportunity to explore elements of base science, as individuals (as PhD students), in the group, and then to accelerate its use as part of a team project towards a paper demonstrator for an integrated air transport system (as research engineers, members of the INNOVATE Research Team).

The following section is an extract of the description of the INNOVATE programme, that briefly and fully summarises the objectives of the project.

The design and operation of an aircraft as one integrated system is becoming an ever-stronger requirement due to increased complexity, demands in performance and market pressures forcing the industry to better integrate its design, processes and operations to meet their targets. It is not sufficient to develop the vehicle in isolation. An overall strategy for developing integrated systems requirements to meet these demands is required and suitable training needs to be provided which allows in-depth technical studies combined with a global vision, inclusive of exploitation and operations, for air transportation. An overall, performing air transport solution needs to see the integration of aircraft and their operation and be looked at as a super-system in its own right.

INNOVATE's aim is to train the next generation of highly skilled engineers and scientists able to understand, undertake and support state-of-the-art technological activities and challenges for the aero-sector in a multi-disciplinary environment (Figure 1.1).

Individual research projects have delivered individual system concepts connected to innovations in propulsion, airframe, ground operations, navigation and communication technologies.

The outcomes of the projects are a series of specific technological advances which links up to underpin a demonstrator integrating the benefits of the various research strands and embodying the system vision developed by the Early Stage Researchers (ESRs) engaged in the programme.

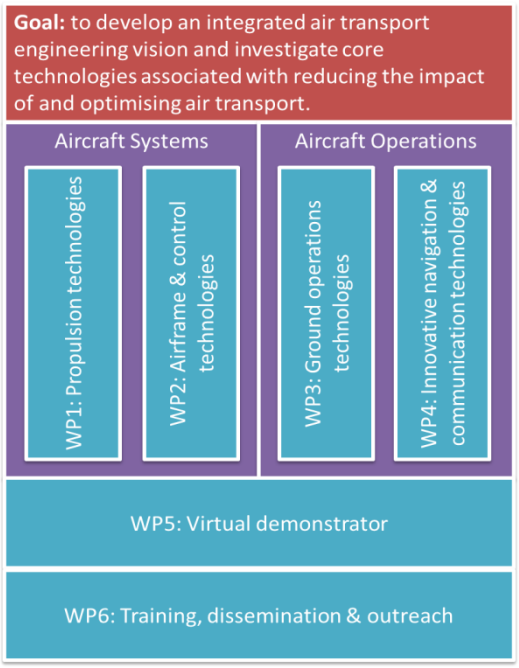

Figure 1-1 - Innovate Project Statement and Structure.

The objectives are to achieve the next stage technology demonstrator by:

- Investigating technologies toward higher pressure-temperature cycles & the more electric engine (WP1);
- Investigating drag reducing, electrical actuation & structural technologies (WP2);
- Investigating technologies aimed at green ground and take-off operations (WP3);
- Enhancing the reliability of GNSS & communication (WP4);
- Integration and virtual demonstrator (WP5);

The IDP has therefore seen each research project interact with others and, to incorporate the progress of each activity and stress the integrated nature of the IDP vision, a demonstration work package, WP5, is programmed to which all ESRs has

contributed. This work package integrates the various technologies developed by the group into physical demonstrators.

WP6 included the dissemination and review of the work done but also the presentation of the prototypes defined in WP5. Dissemination involved workshops and attendance to professional shows and conferences.

The ESRs were based at the University of Nottingham Institute for Aerospace Technology (IAT) and worked in close proximity with one another.

Uniquely this project brought together students, academics and industrial partners from across academic disciplines and areas of the air transport domain to take on the challenge of the integrated air transport system.

1.2. Research Project Aim and Objectives

GEAS Preliminary analysis clearly shows the potential of Advanced RAIM architectures to provide the Required Navigation Performance and achieve a global coverage of LPV-200 using, at least, two constellations.

Almost all the previous analysis was performed by simply studying a constellation's configuration with respect to fixed points on a grid on the Earth's surface, with a full view of the sky, evaluating ARAIM performance from a geometrical point of view and using nominal performance in simulated scenarios lasting several days.

However, aircraft flights can last for hours and on-board receivers don't always have a full view of the sky. Attitude changes from manoeuvres, obscuration by the aircraft body and shadowing from the surrounding environment could all affect the incoming

signal from the GNSS constellations, leading to configurations that could adversely affect the real performance.

For the above reason, the first main objective of this research project is to analyse the above-mentioned shadowing effects on the performance of the ARAIM technique when implemented and integrated with a predicted flight path using different combinations of three constellations (GPS, GLONASS and Galileo), considered as fully operational.

The aim is to assess the capabilities of this new technique in operational configurations, how the use of multiple sources of position information benefits both the accuracy and integrity of the navigation system, in particular in situation in which the presence of obstacles could limit the access to a subset of these sources, and to provide an overview of the performances using different combinations of the constellations, highlighting the level of improvement and their limits, together with a recommendation of the minimum set to be used.

The second main objective is to develop new and innovative algorithms that integrate the ARAIM technique for performance prediction analysis in operational configurations.

The aim is to provide alternative concepts that could support other functions and processes, for example these algorithms may be implemented:

- In the design and testing of instrument approach procedures. The algorithms could be used to improve the process of the development of new instrument approaches, reducing time, effort and costs.
- In the flight planning and scheduling process. The algorithms could support airline planners and ATCs in the analysis of the integrity of a flight procedure,

and its related trajectory, and use the information as additional parameter for the definition of the optimal departure time.

- In the aircraft Flight Management System. The algorithms could support the pilots in the pre-flight briefing, highlighting in advance possible integrity outage in nominal conditions and allowing them to select a different approach or making them aware of the need to utilise additional positioning systems, or in real-time as additional avionics system.

Increased awareness and better pre-flight planning could ultimately improve the safety of flights and contribute to the safe introduction of GNSS as a viable positioning method for instrument approach. Additionally, Global Navigation Satellite Systems could reduce the amount of airspace needed by each airport, consequently reducing the amount of fuel used, the environmental footprint, dependence on ground navaids and potentially increasing the capacity of airports and coping with the increased demand for air travel.

1.3. RESEARCH METHODOLOGY

The following research methodology is carried out in this thesis to meet the aims and objectives outlined in the previous section:

- Review existing ARAIM algorithms
- Define and simulate ARAIM operational configuration, using different airports and approach procedures.

- Define the integration of terrain database in the algorithm and the strategy to analyse its shadowing effect.
- Analyse algorithm performances for the selected scenarios, comparing different combinations of the Global Navigation Satellite Systems in nominal conditions (single, dual and tri-constellation configurations with GPS, Galileo and GLONASS).
- Using specifically developed tools, the ARAIM Performance on Predicted Aircraft Trajectory Tool (APPATT), analysis has been performed both on the short-term (ST), considering the effective duration of the trajectory for a set date and time, and on the long-term (LT), considering a range of days/weeks.
- Based on the analysis of the performances, two new and innovative types of system that integrates ARAIM have been defined and use its prediction capability.
- Test of the two new algorithms:
  - Flight path generator and modifier (FPG and FPM). This tool generates the aircraft path using the basic model described in the ICAO manual of design criteria in the implementation of RNP operational procedures (ICAO, 2009).

    The trajectory is then analysed by APPATT with the objective of evaluating its integrity performance considering the attitude. if it doesn't satisfy the required navigation performance and it presents one or more integrity outages, the Flight Path Modifier (FPM) function tries to modify the trajectory in order to remove the integrity outages and satisfy the required navigation performance.

- The Near Real Time ARAIM Performance Prediction Tool (NRT APPT) provides a near real-time prediction computation of the parameters. The objective of this process is to develop a system that can be integrated into the Avionics of an aircraft/UAV and can provide timely warning to the user/pilot whenever the current aircraft configuration could lead to a dangerous situation.

1.4. THESIS OUTLINE

Chapter 2 starts with an overview of GNSS use in civil aviation together with a simple and brief explanation of the navigation problem, how a position solution is computed and which factors affect its accuracy. Then it describes the general principle of integrity monitoring, its history and provides a wide overview of the different algorithms and techniques used in the field and presented in the literature, like RAIM and ARAIM.

Chapter 3 describes in detail the ARAIM algorithm, how it works, the inputs and outputs (the integrity parameters defined by the protection levels) and the new tool developed and used in this research, the ARAIM Performance on Predicted Aircraft Trajectory Tool (APPATT). In this chapter, the functions used and integrated into the algorithm are presented, starting from the original MAAST, the MATLAB ARAIM Availability Simulation Tool (MAAST) a tool developed by Stanford University that is the basis of the APPATT, to the new functions and models that evaluate the shadowing effect of the aircraft attitude and terrain, highlighting how these functions have been modelled and implemented.

Chapter 4 provides an extensive analysis of approach procedures in the selected airports, using different configurations (single, dual and tri-constellations) and combinations of the GNSS constellations (GPS, Galileo and GLONASS). The chapter is divided into three main parts: a first one that gives a detailed introduction to the civil aviation procedures, their categorization and definition, the second one introduces one of the two versions of the APPATT algorithm, the Short-Term, that analyses the integrity of a single trajectory during its expected duration, trying to identify "weak spot" along the path and flagging them to the user. The third section introduces the second version of the APPATT, the Long-Term, that analyses the integrity of a trajectory within a predefined period of time (from hours to days), in order to identify possible integrity outages and to help the user in selecting the appropriate starting time to perform the flight.

The Flight Path Generator and Modifier tools are introduced in Chapter 5; the concept behind these new functions is to introduce the integrity as new parameter in the design and optimisation of flight path.

These two functions are designed to generate a trajectory based on the inputs provided by the user (a list of waypoints that defines the expected flight path), to analyse the integrity parameters using the APPATT ST and to attempt to modify the trajectory in order to satisfy the integrity requirements for the selected procedure. These two functions can be used as an intermediate step between the current procedures development and testing process, in which trajectories design is based on fixed waypoints where terrestrial navigational aids (NAVAIDs) may be located, and the introduction of GNSS based procedures, in which the trajectories will not be any longer based on static procedures but a more dynamic and flexible process might be

introduced that could further optimise them on a multi-aspects base (such as costs, environmental impact, safety and integrity).

Chapter 6 presents and summarise the challenges of the integration of different technologies and explaining the final objectives of the WP4 Physical Demonstrator, developed in collaboration with other two INNOVATE researchers, and its research contribution to the INNOVATE WP5. The physical demonstrator integrates three technology/system demonstrators covering different areas of the operations related to the civil aviation field, such as:

- Integration of ARAIM as new avionics system that supports pilots in safety-critical phase of flight by providing near real-time integrity performance prediction (the Near-Real-Time ARAIM Performance Prediction Tool or (NRT APPT).
- Optimisation of the ground movement operations before take-off and after landing that could reduce delays and related costs that could affect airports with high level of flight traffic.
- Analysis of human performances and psychophysical status of subjects ((e.g. pilots and ATCs) using physiology parameters (e.g. temperature and heart rate) to identify their level of tiredness and stress.

Chapter 7 summarises the achieved results and proposes ideas to further develop the concepts and tools exploited in this research.

2. INTEGRITY MONITORING, RAIM AND ARAIM ALGORITHM, PERFORMANCE BASED NAVIGATION AND LOCALIZER PERFORMANCE WITH VERTICAL GUIDANCE

2.1. INTRODUCTION TO GNSS

The Global Satellite Navigation Satellite Systems (GNSS) are radio-navigation systems that allow users equipped with receivers to worldwide locate themselves in a predefined reference system through its set of coordinates (longitude, latitude and altitude), and to define the local time to high precision, using radio-signals transmitted from orbiting satellites. A GNSS system usually consists of a ground control segment, which tracks and monitors the health of each satellite in the constellation, and a network of 24-30 satellites homogeneously distributed in Medium Earth Orbits (MEO) or Geostationary orbits (GEO).

Originally, the U.S. Department of Defence (DoD) developed the Global Positioning System (GPS) for military applications, but, nowadays, GNSS systems have a wide range of applications from the basic navigation purpose to transport and agriculture, search and rescue, energy, telecommunications and world finance.

The increased interest in GNSS applications has pushed other countries to develop their own system, like the European Galileo system and the Chinese COMPASS that aim to be ready by the end of this decade, or to improve and modernize the existing

ones, such as the Russian GLONASS and the American GPS itself. At the time of writing, the status of the different constellation is the following:

- GPS has 31 operational satellites (more than a nominal constellation) and the U.S. are already planning the future of the constellation, developing the new generation of satellites that will include new features, such as new civilian and military signals.
- The European Galileo satellite system has 18 satellites in orbit, with four more on their way by the end of 2017.
- GLONASS is back to the operational status, with 25 satellites in orbit.
- The Chinses BeiDou system has 14 operational satellites in orbit.

In the near future, more than 100 satellites will be available, together with an increase in diversity in the radio frequency spectrum due to the introduction of new signals that will mitigate the risks of interference.

In this chapter, a quick overview of the fundamentals of GNSS and its use in civil aviation is presented, together with a simple and brief explanation of the positioning problem, how a position solution is computed and which factors affect its accuracy. The reader can refer to Hofmann-Wellenhof et al. (2008), Groves (2013b) and Paternostro (2008) for a detailed description of Global Navigation Satellite Systems.

Then it describes the general principle of integrity monitoring, a bit of its history and it provides a wide overview of the different algorithms and techniques used in the field and presented in the literature, like RAIM and ARAIM.

2.1.1. FUNDAMENTAL OF GNSS

GNSS is based on the emission of complex electromagnetic waves by a network of artificial satellites that are received by an appropriate instrumentation which tracks and interprets these signals and therefore it becomes possible to determine, in real time or in subsequent times, the distance between the satellites and the point where the instrumentation is located.

The position of the points occurs with respect to a spatial reference system X, Y, Z with origin in the centre of the terrestrial mass (geocentric); these coordinates can be transformed into geographic coordinates and Cartesian coordinates of a local reference system.

The level of accuracy achieved depends on several factors such as:

- Measurement mode;
- Point-to-satellite distance;
- Characteristics of the receiver;
- Relevant techniques;
- Number and configuration of the satellites used.

It is possible to obtain rough position estimates with an accuracy of meters in real time up to a millimetric accuracy but with a post-acquisition data processing.

The GNSS have three segments:

1) Space segment:

These are the satellites that send electromagnetic signals towards the earth; as mentioned before, each constellation consists of a certain number satellites, depending on its operational status, most of which are operative and others are back-up ready to be activated in case one fails.

For example, GPS currently counts 32 satellites in orbit placed on 6 circular orbits with a radius of about 26000 km, inclined 55 ° on the equatorial plane and spaced 60

The main tasks of the satellites are:

• Transmit and receive information from control stations;

• Measure time with atomic clocks;

• Perform orbital corrections according to the parameters assigned by the control stations.

• Transmit information to users via electromagnetic signals; currently, there are several signals generated by the different constellation and the generation of the satellites. For example, for GPS, a total of four different signals are expected to become operational for civil use in the next years: L1 Coarse/Acquisition (C/A), L2C, L5 and L1C. The reader can find further information on the official GPS governmental website (GPS.GOV, 2017).

The transmitted signals carry the navigation message that includes some of the information the receivers need to determine positions:

- location of the GNSS satellites, called the ephemerides, that provides a GNSS receiver with ephemeris information to calculate the coordinates of all the satellites in the constellation with an approximate accuracy of a couple of kilometres.

- time of satellite transmission;

- clock corrections, the ways the satellite can tell the receiver what time it is on-board.

- health of the satellites on orbit

- information about the ionosphere. The ionosphere is a layer of the atmosphere through which the GPS signals must travel to get to the user; hat atmospheric information will allow the receiver to make some corrections on the signal it receives from a specific satellite.

2) Control segment:

The control segment consists of:

- A main control station (master control station, MCS) and an alternative main control station (alternate master control station);

- Dedicated terrestrial antennas;

- Dedicated control stations;

These stations perform the function of monitoring the satellites, in order to determine their position, the synchronization error of the clocks and their operating status. Satellites tracking data obtained from monitor stations are used by MCS to compute the ephemeris, the parameters that allow determining the orbital position of the satellites, and the analytical models for the correction of the satellite clocks which are transmitted back to the satellites.

These ephemerides are actually predicted satellite positions broadcast within the navigation message that are transmitted from the satellites in real time.

Upload is performed daily with new predicted orbital elements and transmitted every hour by the navigation message allowing the receivers to predict their position in the short-term time. They are therefore called "broadcast" (transmitted) or predicted.

3) User segment:

The user segment consists of all civil and military users equipped with at least one antenna and a receiver, capable of acquiring the signals emitted by the satellites.

There are several types of receivers that differ in their technical characteristics, the strategy adopted in decoding the received signal and the precision they provide in positioning.

All receivers are equipped with an oscillator (receiver clock) that produces a continuous electromagnetic signal similar to that received by the space segment, called precisely the replica. In order to carry out this operation simultaneously for each signal coming from different satellites, the receiver dedicates to each of them a different reception channel.

2.1.1.1. GNSS MEASUREMENTS

The signal sent by the satellites is picked up by the antennas of the receivers, which generate a replica within them, engaging the receiver for a few minutes after it is

switched on. The signal reproduced by the receiver oscillator is similar to the received one, aside for a phase shift in time (Figure 2-1).

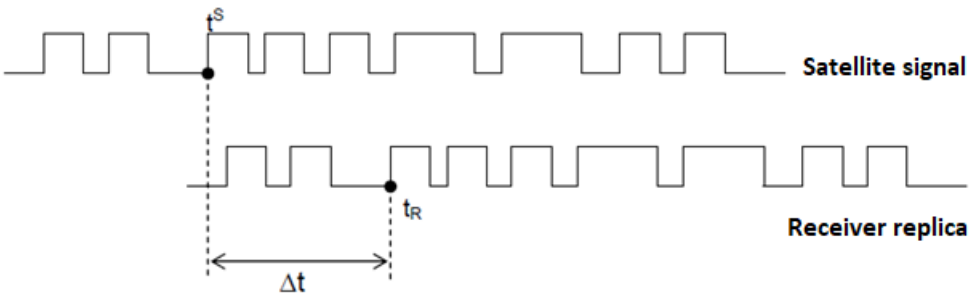

Figure 2-1 Example of transmitted signal, generated and phases shift.

Using GPS signals, it is possible to perform two different types of measurements:

- Pseudo-range
- Carrier phase

which have the same geometric content (satellite-receiver distance) but with different precision.

The principle of pseudo-range observations is the measurement of the flight time Δt necessary for the satellite signal to reach the receiving station. Knowing the signal propagation speed c and measuring Δt, the satellite-receiver distance is given by the following relation:

$$d = c\,\Delta t \tag{2.1}$$

The phase observations are based on the measurement of the number of cycles (phases ϕ) of the GPS signal necessary for transmission from the satellite to the receiver. Known the number of cycles it is possible to calculate the satellite-receiver distance:

$$\mathrm{d} = \frac{\phi\lambda}{2\pi} \tag{2.2}$$

where λ is the signal wavelength.

2.1.1.2. PSEUDO RANGE MEASUREMENTS

The pseudo-range measurements are carried out on the carriers modulated by the codes and are based on the measurement of the flight time, i.e. the time interval between the transmission of the electromagnetic wave sent by the satellite and its arrival at the receiver. This measurement is obtained through the correlation of two signals:

- the satellite signal arrived at the receiver
- the identical signal generated by the receiver

Once a GPS receiver is turned on, it picks up the signal from the satellites and generates the replica, knowing in advance the code that modulates it. These two signals are identical but out of phase over time, as the wave transmitted by the satellite has already travelled the satellite-receiver distance.

The receiver is able to move the generated replica over time in order to obtain the maximum correlation with the signal transmitted by the satellite.

The flight time will be nothing more than the displacement to be given to the replica to align it with the signal coming from the satellite.

$$\Delta t = t_R - t^S \tag{2.3}$$

In the previous equation we must consider the asynchronism of clocks, in fact in the GPS measurements there are three time scales:

- GPS time, that is the atomic time taken as a fundamental reference;
- the time scale of the satellite (in advance with respect to GPS time), determined by the oscillators on board;
- the time scale of the receiver (in advance of the GPS time), determined by the receiver's clock.

The non-synchronism between the clocks causes the measured flight time (Δt) to be given by the following expression:

$$\Delta t = \left(t_{R(GPS)} - t_{GPS}^{S}\right) - \delta t_R - \delta t^S \tag{2.4}$$

Where:

- subscript R stands for Receiver
- subscript S stands for Satellite
- δt_R is the receiver clock offset
- δt^S is the satellite clock offset

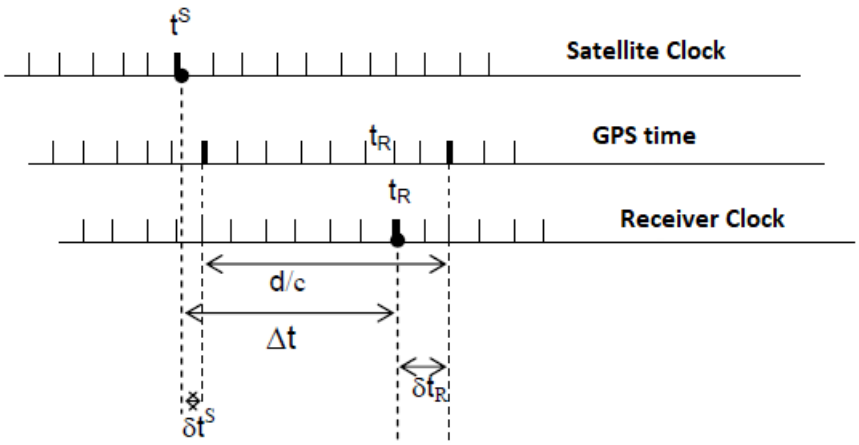

Figure 2-2 GPS time and satellite and receiver clock offsets

Given the quality of the satellite clocks, all the atomic oscillators of the satellites can be considered synchronized with each other.

The clocks of the receiver, normally quartz, are of inferior quality to those of the satellites, so the synchronization error is higher (around 1 ms, i.e. 10-3 s) and consequently also the error on the satellite distance- receiver is more than 300 km.

This value is not acceptable, so it is necessary to estimate it at each epoch, introducing, as an additional unknown, the synchronization error of the clocks in the observation equation.

Taking into account synchronization errors, for each observation period the equation of the pseudo-range measurements is:

$$P_R^S = c * \Delta t_R^S = \sqrt{(X^S - X_R) + (Y^S - Y_R) + (Z^S - Z_R)} + c * (\delta t^S - \delta t_R) = d_R^S + c * (\delta t^S - \delta t_R) \quad (2.5)$$

Where:

- P_R^S is the pseudo-range between the satellite S and receiver R
- c is the speed of light
- $\Delta\ t_R^S$ is the shift in time between the incoming satellite signal at the receiver and its replica.
- (X_S, Y_S, Z_S) and (X_R, Y_R, Z_R) = satellite and receiver coordinates in the WGS84 reference frame
- d_R^S is the direct distance between satellite and receiver
- δt^S is the clock offset between the GPS time and the satellite time
- $\delta\ t_R$ is the clock offset between GPS time and receiver

Eq. (2.5) there are four unknowns, the receiver coordinates $(X, Y, Z)_R$ and the total clock offset $(\delta t^S - \delta t_R)$, therefore, at least four different measurements (or pseudo-ranges) are required in order to compute a position fix.

The system of equations that solves the mathematical problem can be generally expressed as:

$$\underline{y} = F(\underline{x}) + \underline{e} \quad (2.6)$$

Where:

- y is the vector of the measurements

- F() is the generic term to define the function that related the measurements with the unknowns
- $\underline{x}$ is the vector of the unknowns
- $\underline{e}$ is the vector of measurement errors

The last element, the vector of measurement errors, considers other factors, other sources of random errors and biases aside from the clock offsets, such as:

- biases in the orbital parameters
- atmospheric biases (tropospheric and ionospheric)
- antenna offset
- other nominal bias used to include non-Gaussian factors, usually introduced as a conservative Gaussian distribution displaced from the zero that can over-bound the real distribution.

A different measurement model, often used in algorithms, that includes some of the previous errors can be represented as:

$$P_R^S = c \cdot \Delta t = d_R^S + c \cdot (\delta t^S - \delta t_R) + \delta d_{atm} + \delta d_{nom} \quad (2.6)$$

In which only the atmospheric effects ($\delta \mathrm{d}_{\mathrm{atm}}$) and the nominal bias ($\delta \mathrm{d}_{\mathrm{nom}}$) are considered since are the types of error sources always affecting the measurements. Additional information about errors can be found in the following sections.

Eqs. (2.5) are non-linear and need to be inverted in order to find the unknown. The system is then linearized through the approximation of the function F(x) as:

$$F(x) \approx F(x_0) + \partial_{x^T} F(x_0)(x - x_0) \quad (2.7)$$

and Eqs (2.5) become:

$$\underline{\hat{y}} = G\underline{\hat{x}} + \underline{e} \quad (2.8)$$

Where:

- G is the geometry matrix given by $\partial_{x_T} F(x_0)$
- $\underline{\hat{y}}$ is the vector of incremental observation $\Delta \underline{y} = \underline{y} - y_o = \underline{y} - F(x_0)$
- $\underline{\hat{x}}$ is the vector of the unknown incremental parameters
- e is the error vector modelled to have a normal distribution N(0,C), where C is a diagonal matrix which elements are the standard deviation of the observation expressed as:

$$\sigma_i^j = \sqrt{\sigma_{URA/URE}^2 + \sigma_{tropo}^2 + \sigma_{user}^2} \quad (2.9)$$

Where i is the satellite of the constellation *j* (GPS, Galileo, GLONASS) and the final value of the standard deviation will depend on the final utilization of the matrix C, since, as it will be presented in the section related to the ARAIM algorithm, two different matrices are computed, one for the integrity requirement and one for the accuracy and continuity, that will respectively make use of the User Range Error (URE) and User Range Accuracy (URA).

2.1.1.3. CARRIER PHASE MEASUREMENTS

The satellite-receiver distance can also be determined with phase measurements on the demodulated L1 and L2 carriers. The observation consists of the difference between the received carrier wave phase and the phase of a reference wave generated by the receiver at the instant of reception.

By turning on a receiver at a certain time t_0, a fraction of the phase ϕ is measured, indicated as Fr(ϕ, t_0), given by the difference between the carrier transmitted by the satellite and the replica generated by the receiver, and a counter of whole cycles of phase, indicated as Int (ϕ, t_0), which is incremented each time the fraction of the

phase changes from 2π to 0. This counter takes into account the relative motion between satellite and receiver.

At a given epoch, the observation of phase ϕ consists therefore in the sum of the fractional phase and the count of the whole cycles:

$$\phi_{mis}(t) = Fr(\phi, t_0) + Int(\phi, t_0, t) \tag{2.10}$$

However, the number of integer cycles $N_R^S(t_0)$ covering the satellite-receiver distance is not known.

This unknown factor is called phase ambiguity. The total phase at a generic instant of time t is therefore:

$$\phi_{tot}(t) = \phi_{mis}(t) + N_R^S(t_0) = Fr(\phi, t_0) + Int(\phi, t_0, t) + N_R^S(t_0) \tag{2.11}$$

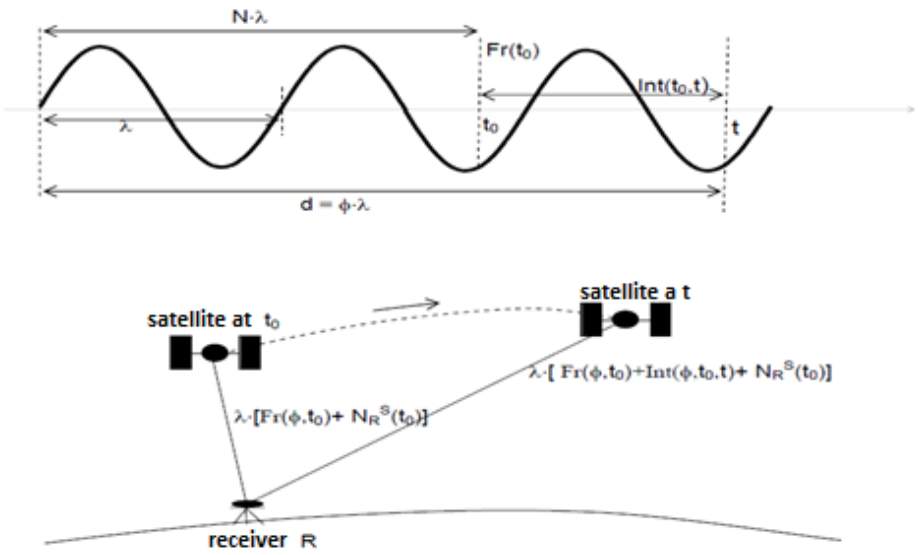

Figure 2-3 Variation of the initial ambiguity

The phase is then measured less than integer multiples of the cycle, like reading a clock in which only the second hand is working (the time read is without the minutes and hours).

The satellite-receiver distance is given by the product of the number of carrier cycles for its wavelength:

$$d_R^S = \lambda\phi_{tot}(t) = \lambda\, Fr(\phi, t_0) + \lambda\, Int(\phi, t_0, t) + \lambda\, N_R^S(t_0) \quad (2.12)$$

Taking into account the offsets of the receiver and satellite clocks, it is possible to write the observation equation for phase measurements at the time t as:

$$\phi_R^S(t) = -\frac{f}{c}\, d_R^S - f(\delta t_R - \delta t^S) + N_R^S(t_0) \quad (2.13)$$

Where:

- $\phi_R^S(t)$ is the phase at the time t
- $\frac{f}{c}$ is the ratio between the frequency f and the propagation speed of the wave
- d_R^S is the satellite-receiver distance
- δt^S is the clock offset between the GPS time and the satellite time
- $\delta\, t_R$ is the clock offset between GPS time and receiver
- $N_R^S(t_0)$ is the integer part of the phase ambiguity that is equal to the number of cycles incurred from the signal departure from satellite S to reception in receiver R at time t_0.

In the calculation of the unknowns of phase measurements, in addition to the geocentric Cartesian coordinates of the receiver, it is necessary to introduce also the initial ambiguity $N_R^S(t_0)$ for each satellite which signal has been received. Because of these additional unknowns, phase measurements cannot be used alone for absolute positioning in real time.

As long as the phase is received without interruption, for each observation session there is only one unknown ambiguity for each satellite-receiver pair. Having available observations related to different periods, it is possible to determine the value of $N_R^S(t_0)$.

Whenever the receiver loses signal reception, the count of the number of whole cycles is renamed and a new unknown must be introduced, which takes into account the number of whole cycles covering the signal reception gap. This cycle jump is called cycle slip and is given by the difference:

$$N_R^S(t_{i+1}) - N_R^S(t_i) \neq 0 \tag{2.14}$$

Cycle slips are mainly determined by the following causes:

- signal obstructions due to trees, buildings, low elevation of the satellites etc ...
- low signal-to-noise ratio due to "bad atmospheric conditions" (ionosphere), multiple reflections of the signal
- Oscillator malfunctions

The phase measurements are therefore more precise than those of the pseudo-range, but given a single receiver, they cannot be used for real-time positioning. If we compare the pseudo-range observation equations and the phase expressed in units of distance, we can make the following observations:

A. they contain the same geometric content, i.e. the satellite-receiver distance (in the expression d_R^S the coordinates $(X, Y, Z)_R$ of the receiver are contained, i.e. the unknowns of the problem);
B. the phase measurements contain an extra unknown, i.e. the phase ambiguity N_R^S.

To summarise, the mathematical model of the two different measurements can be expressed as

C. Pseudorange:

$$P_R^S = d_R^S + c * (\delta t^S - \delta t_R) \tag{2.15}$$

D. Carrier Phase:

$$\lambda\phi_R^S(t) = d_R^S - c * (\delta t_R - \delta t^S) + \lambda \mathrm{N}_\mathrm{R}^\mathrm{S}(\mathrm{t}_0) \quad (2.16)$$

2.1.1.4. MEASUREMENT ERRORS

As mentioned in the previous section, measurements are or might be affected by several error sources:

- Pure instrumental biases. There is an empirical method to evaluate this type of error, depending on the technique used for the transmitted signal, that the error is 1-2% of the wavelength:
  - C/A code: $\sigma \cong 3 - 6m$
  - P (precision) code: $\sigma \cong 30 - 60cm$
  - Carrier: $\sigma \cong 2 - 4mm$
- Systematic or model errors (biases)
- Observation errors
- Elaboration errors

The following model errors are common to pseudo-range and phase measurements:

• orbit biases

• atmospheric biases (signal curvature, ionospheric biases, and tropospheric biases)

•biases of clocks, due to the asynchronousness between atomic clocks, as discussed in the paragraph on pseudo-range measurements

Characteristic only of phase measurements are:

• biases of the ambiguity of the carriers

• modelling of the antenna phase centre

A. Orbit Errors

The GPS positioning is based on the knowledge of the ephemeris of the satellites, from which their positions are derived.

The ephemerides of the satellites are contained in the GNSS signal through the message. These ephemerides are called transmitted or broadcast and have been calculated by the master station based on observations collected previously, they are therefore predicted. The aforementioned ephemerides have a precision of the order of a few tens of meters.

Since 1992, the Precise ephemerides, calculated by the IGS (International GNSS Service), are available on the basis of the observations 24/7 coming from a network of GNSS stations, distributed over the entire surface of the land. Given a generic day X, at least a week is required before the exact ephemerides are available for free via the Internet, as they derive from GPS observations made on the same day X. For this reason, the exact ephemerides cannot be used for real-time positioning. Their precision is of the order of some tens of centimetres; there are however less precise solutions (called Ultra-rapid and Rapid), but available in shorter times (even after a day).

B. Atmospheric Biases

Atmospheric biases are due to the propagation of the signal through the atmosphere. The distance between satellite and receiver, measured with electromagnetic signals, differs from the straight geometric distance due to three atmospheric phenomena:

1) curvature of the signal

2) ionospheric bias

3) tropospheric bias

In the observation equations, both of pseudo-range and carrier phase, the distance is considered rectilinear, while in reality it is not, so it is necessary to make appropriate corrections to the measured distance.

1) Refraction errors

Fermat's principle states that an electromagnetic wave in going from one point to another follows a curve that minimizes flight time. The path followed by the signal is defined by the integral:

$$s = \int n \cdot ds \tag{2.17}$$

where it integrates along the entire signal path.

If the signal propagates in the vacuum (n = 1), s would be equal to the geometric distance s_0 measured along the straight line that connects the satellite to the receiver.

$$s_0 = \int ds_0 \tag{2.18}$$

The difference between s_0 and s, calculated along the real path of the electromagnetic wave, gives the error due to the curvature of the electromagnetic signal.

The effect of the curvature depends on the angle of elevation of the satellite, as shown in Table 2-1, and as it is very small for angles of above elevation of 15 ° -20 and for this reason it can be neglected.

Table 2-1 Effect of the curvature when the elevation angle changes

Elevation angle (°)	$(s-s_0)$ (m)
0	3.200
2	0.415
5	0.075
10	0.019
15	0.009
20	0.005
30	0.002
40	0.001
70	0.000

2) Ionospheric biases

The ionosphere is the part of the atmosphere that extends approximately between 50 and 100 km of altitude, in which the ultraviolet solar radiation from the Sun causes the dissociation and ionization of the gaseous molecules present, determining a layer of free electrons.

At the frequencies of the GNSS signal, the ionosphere is a dispersive medium, so that the electromagnetic waves of the GNSS signal that propagate in it have the speed that depends on their frequency. The dispersivity of a medium is determined by the interaction between the external field of the wave and the field of the electrically charged medium (in this case the ionosphere), due to the presence of dipole moments induced in the molecules and free electrons. When the atomic frequency of the medium and the frequency of the penetrating wave are close, we are witnessing the phenomenon of resonance, which generates the dependence of the propagation velocity from the wave frequency.

The ionospheric bias is defined, respectively, for the pseudo-range and phase measurements, as follows:

$$\delta d_P^{ion} = s - s_0 = \frac{C}{f^2} \int n_e ds \tag{2.19}$$

$$\delta d_\varphi^{ion} = s - s_0 = -\frac{C}{f^2} \int n_e ds \tag{2.20}$$

where:

- C = 40.3 is a coefficient that contains all the constant parameters.
- f is the frequency;
- n_e is the density of the electrons in the ionosphere expressed in [electrons / m³];

Eqs. (2.19) and (2.20) can be expressed as follow, for further details please refer to the material provided by IERS (2010):

$$\delta d_P^{ion} = \frac{s_1}{f^2} + \frac{s_2}{f^3} + \frac{s_3}{f^4} \tag{2.21}$$

$$\delta d_\varphi^{ion} = -\frac{s_1}{f^2} - \frac{s_2}{f^3} - \frac{s_3}{f^4} \tag{2.22}$$

Where

- s_1, s_2 and s_3 are the coefficients of the Ionospheric delay up to the third order that depend on n_e, the magnetic field B and θ, the angle between the magnetic field B and the electromagnetic (EM) propagation

Eqs. 2.21 and 2.22 show that the magnitude of the ionospheric disturbance is the same for both phase and code observations, but the effect is different:

- the ionospheric delay on the code pseudorange is positive, associated to a decrease of the EM signal group velocity in the transionospheric propagation.

- the ionospheric delay on the carrier phase is negative, indicating an increase of the phase velocity of the EM transionospheric signal propagation

The delay, or the anticipation, suffered by the signal depends on the electronic density, for which it is difficult to find a satisfactory model able to take into account its variations over time. The concentration of free electrons in the ionosphere is strongly correlated to the altitude and, above all, to the activity of sunspots, therefore it presents seasonal and daily variations.

The most effective method for reducing ionospheric influence is the use of signals with different frequencies. Combining simultaneous measurements with different frequencies allows to cancel the ionospheric effects up to order k − 1, where k is the number of different frequencies.

An example is the combination of the L1 and L2 frequencies of the GPS system, which allows removing the first order term of the ionospheric delay, which accounts for more than 99.9% of the total delay, through a technique called ionospheric-free combination of observables:

$$LC_P = \frac{f_1^2}{f_1^2 - f_2^2} d_{P1} - \frac{f_2^2}{f_1^2 - f_2^2} d_{P2} \quad (2.23)$$

$$LC_\varphi = \frac{f_1^2}{f_1^2 - f_2^2} d_{\varphi 1} - \frac{f_2^2}{f_1^2 - f_2^2} d_{\varphi 2} \quad (2.24)$$

Where:

- d_{Pi} and $d_{\varphi i}$ are the Pseudo-range and carrier phase observables from the two frequencies.

This technique is implemented in the ARAIM technique that is going to be presented in the next chapter and that is used in this research.

And in the future, with Galileo and modernized GPS systems (broadcasting at three frequencies), the full correction can be extended to second order ionospheric terms too.

3) Tropospheric biases

The troposphere is the band of the atmosphere closest to the earth's surface. It contains 90% of the atmospheric mass and 75% of water vapour, which involves a pronounced refractivity and diffusion of the electromagnetic waves that propagate there. Above 30 km of altitude, the density of neutral atmospheric components is considerably reduced, so much so that the aforementioned phenomena can be neglected. In atmospheric gases, the refractivity is due to a displacement in the distribution of the constituents of the gases and therefore to the alignment of the polar molecules with the magnetic and electric field that propagates there. The major constituents of the atmosphere are electrically polar molecules, while the only important molecule presenting a magnetic moment is CO_2.

The effect of the neutral atmosphere on wave propagation is less than that introduced by the ionosphere, however, it creates more problems for two main reasons.

First, the troposphere is not a dispersive means of radio waves up to frequencies of 15 GHz, so there is no advantage in using two frequencies because the propagation of waves is independent of frequency. Secondly, there can be identified two components, a "dry", given by the molecules in which there is not a moment of permanent dipole, and a "wet", given by the water vapour. The water vapour has a polar nature, due to the great electronic affinity of the oxygen atom, which attracts the electrons to complete the orbital p at the second level of energy, thus inducing

an asymmetry in the electronic cloud, then a dipole that will oscillate under the effect of electromagnetic waves.

The effect of the dry component can be modelled knowing the pressure on the surface, while the effect of the wet component depends on the atmospheric conditions along the entire path travelled by the signal, and these are not necessarily related to the conditions on the Earth's surface, but time and in space. In stable weather conditions, the water vapour content shows a regional correlation over horizontal distances of up to 30 km.

In the case of longer baselines or less favourable weather conditions, the disturbance can be minimized by using standard models of the vertical refractive profile (e.g. Saastamoinen or Hopfield), using a standard atmosphere, or using meteorological data taken on the surface, or even by restoring the parameters.

There is also a stochastic method, in which the contribution of the troposphere is estimated indirectly by looking at the difference between the experimental and theoretical data, and then minimizing it through the parameters that have been introduced. It is also possible to use strategies other than modelling, for example using water vapour radiometers, which observe the sky, allowing the determination of the water vapour content, thus giving a direct measure.

It has been observed that signals from satellites that are low on the horizon are more delayed than those coming from higher satellites, so a stratagem commonly used to minimize atmospheric problems is to fix a cutting angle is to use only observations from satellites at an elevation angle greater than 10 - 15 degrees.

C. ANTENNA PHASE CENTRE

The satellite-receiver distance measured with the GNSS has as its initial and final point the phase centres of the antennas, which are not precise geometric or mechanical points, but electromagnetic points, which vary both in function of the elevation and the azimuth of the satellites (point B in the figure below), that of the signal frequency, whereby the phase centre of the carrier L1 is different from that of the carrier L2.

For each antenna the middle position of the phase centre is provided with respect to an established antenna point (point A in the figure), generally the point where the antenna is screwed to the antenna holder (ARP).

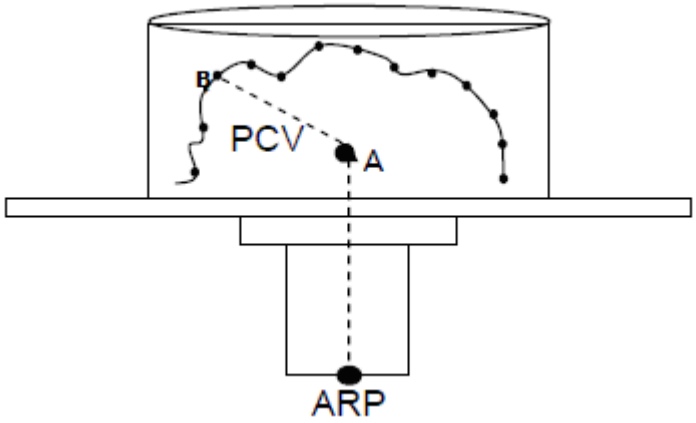

Figure 2-4 Section of a receiver antenna and phase centres

D. OBSERVATION ERRORS

The observation errors common to the pseudo-phase and phase observations are as follows:

1) Multipath

2) Cycle slips

1) Multipath

The GNSS signal does not always follow the direct satellite-receiver path, as during its journey it can undergo the phenomenon of multiple reflections by surfaces surrounding the antenna (metallic, water surfaces, buildings). In this case, the signal travels a distance longer than a few centimetres or becomes unrecognizable, thus increasing the signal/noise ratio of the observations.

If the GNSS antenna is not moved, this effect repeats with the same characteristics until the satellite configuration changes, so by repeating the observation on consecutive days it is possible to determine its effects.

To minimize the multipath effect, especially in precision positioning, appropriate antennas, such as choke-ring antennas, should be used, namely circular antennas formed by concentric rings spaced apart to reduce multipath, or antennas covered with appropriate materials.

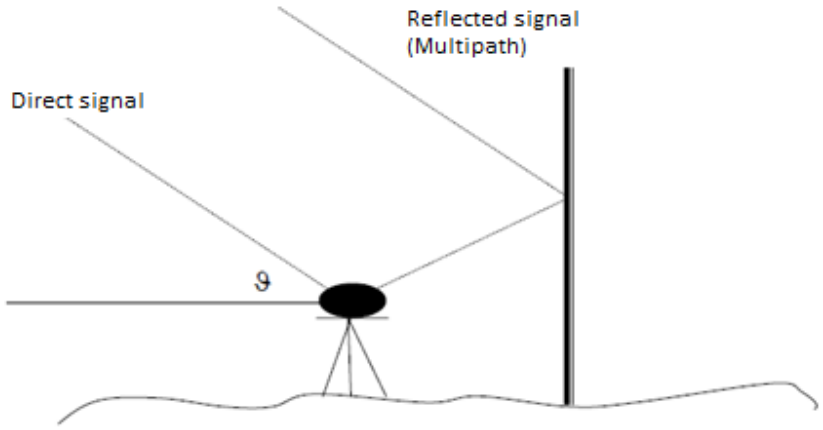

Figure 2-5 Example of Multipath

2) Cycle slips

The interruption in the acquisition of data due, for example, to the presence of obstacles along the path of the signal generates a jump in the count of the number of whole cycles, called cycle slip.

During data processing, there are various techniques, such as the differentiation of observations, the use of combinations of carriers, which allow to "repair" the cycle jumps. In cases where these jumps are too large, a new unknown is introduced, analogous to the initial phase ambiguity.

E. SATELLITE GEOMETRY

The position and the number of satellites vary continuously due to the orbital trajectories, generating various configurations more or less favourable.

To measure the quality of the geometric configuration of the satellites, specific parameters have been defined, called DOP parameters that constitute an index of decrease in precision (the smaller the better).

The DOP value is inversely proportional to the volume of the figure that is created by joining the centre of the antenna to the satellites being registered.

When the satellites are 4, the figure is like an inverted pyramid (the more the satellites are distant from each other, the larger the volume of the figure will be and the lower the DOP value).

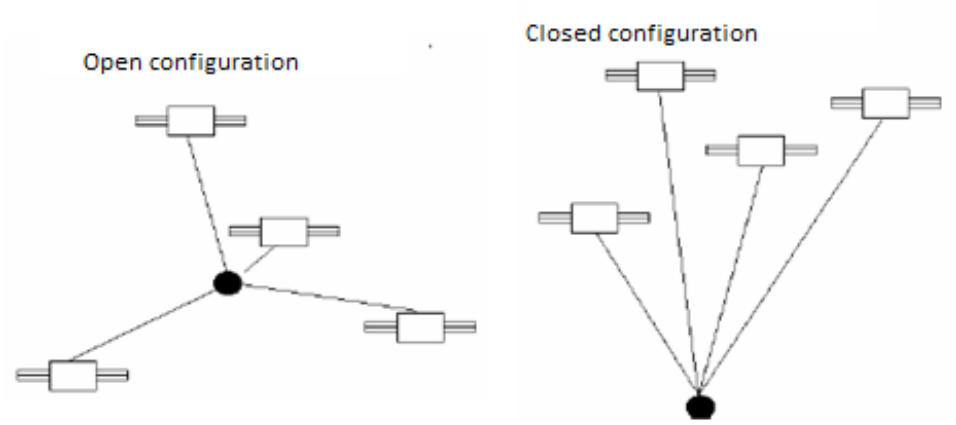

Figure 2-6 Example of optimal (left) and not optimal (right) satellite geometry

There are several DOPs in relation to the type of coordinates:

• PDOP: index of precision decrease in the three-dimensional determination of the point (X; Y; Z);

• HDOP: index of precision decrease in the planimetric determination of the point (X, Y);

• VDOP: index of precision decrease in the altimetric determination of the point (Z);

• TDOP: index of precision decrease in the determination of the time.

The PDOP and TDOP value combination are called GDOP (precision decrease in volumetric determination and time):

$$GDOP = \sqrt{PDOP^2 + TDOP^2} \tag{2.25}$$

The precision with which the points are defined with the GNSS depends on:

1) Geometric configuration and number of satellites;

2) Accuracy with which the receiver-satellite distance was measured.

The level of precision that can be achieved in the positioning of points is linked to the number of satellites participating in the measurement session and their dislocation in the sky.

As already mentioned, the smaller the value of the PDOP index the more accurate the observations will be; in any case it must not exceed the value of 7.

Based on the error sources presented in the previous sections, the equation for the Pseudo-range and Carrier Phase observables can be written in a more complete form:

- Pseudo-range:

$$P_R^S = c \cdot \Delta t = d_R^S + c \cdot (\delta t^S - \delta t_R) + \delta d_{ion} + \delta d_{trop} + \delta d_{orb} + \delta d_{PCV} + \delta d_{mul} \tag{2.26}$$

- Carrier Phase:

$$\Phi_R^S = \lambda \cdot \phi_{\text{mis}} = d_R^S + c \cdot (\delta t^S - \delta t_R) + N_R^S + \delta d_{ion} + \delta d_{trop} + \delta d_{orb} + \delta d_{PCV} + \delta d_{mul} \quad (2.27)$$

2.1.2. GNSS FOR CIVIL AVIATION USE

In 2003 the Imperial College Consultant Limited performed a study for the Civil Aviation Authority (CAA) related to the level of safety that GPS could provide as main navigation system for civil aviation, since the interest for air travel worldwide was growing at a fast rate, exceeding the predictions, but this increment wasn't matched by availability of capacity (CAA-Paper, 2003). An issue that the International Civil Aviation Organization (ICAO) already observed in the 80's, highlighting that the air traffic control (ATC) systems wouldn't have had the capability of managing this sudden growth in demand, instituting the Special Committee on Future Air Navigation Service (FANS) to analyse and design advanced navigation systems for civil aviation.

For decades, inertial systems or radio navigation has been used as main navigation systems; in particular, radio navigation aids are used in commercial aviation, using visual cues or RF-based guidance systems for final approach and landing, such as VHF Omni-directional Radio Range (VOR), Distance Measuring Equipment (DME) or Instrumental Landing System (ILS). However, the maintenance and calibration needed to ensure continuous availability are the main drawbacks of these systems.

The implementation of GNSS-based air navigation could reduce some of these disadvantages, allowing the introduction of curved or steep approaches for optimal

noise abatement as described by Lüken et al. (2008), remarkably diminishing costs of ground systems and additionally improving airspace capacity, favouring smaller airports that could increase their traffic.

In 2008, European organizations already started to address these challenges resulting in the definition of a collaborative project, named SESAR, to modernize the European airspace and air traffic management (ATM) (EC, 2004). The project aims to develop a new generation of technological system and components that will guarantee high-performance air transport activities in the European skies. Satellite navigation is going to play an important role in overhaul and the operational, technical, economic and legal objectives of the use of multi-constellation and multi-frequency GNSS for Navigation applications in civil aviation are presented by EUROCONTROL (2008). A similar concept is getting implemented in the U.S., called Next Generation Air Transportation System (NextGen) (FAA, 2012). Both projects will enhance civil aviation capabilities and bring significant operational benefits, supporting the stringent requirements that will be needed by the new applications and operation expected in the near future.

However, in the so-called Required Navigation Performance (RNP, see following sections for further details), a concept for civil aviation approved and explained in ICAO (1999) and (2000), poses stringent requirements that GNSS requires to meet if meant to be used as the main navigation system for aviation. Accuracy, integrity, continuity of service and availability are the four parameters that are defined in the RNP for each phase of flight, described in the regulation as:

a) ***Accuracy:*** this is the basic requirement for a navigation system and it is defined as the degree of conformance between an estimated or measured

value and its reference value, a true value or some agreed-upon standard value. More specifically, the accuracy is measured as the size of the bias or systematic error given by the difference between the mean value and the reference value. In GNSS the requirement is defined as the value α_{ac} for which 95% of the positions calculated have an error equal or lower to that value:

b) ***Integrity:*** it relates to the trustworthiness of the information provided by the navigation system and includes the ability of the navigation system to detect and warn in time the user (within a given period defined as time-to-alert, TTA) when some system anomaly results in unacceptable navigation accuracy. Integrity risk, or probability of hazardous misleading information P(HMI), is the probability that the navigation position error exceeds the alert limit and that event is not detected. There are two types of loss of integrity, when a fault is not detected or when the detection occurs, but the system fails to alert the user within the required TTA.

c) ***Continuity:*** it is defined as the capability of the system to perform its function of providing a navigation output with the specified level of accuracy and integrity without non-scheduled interruptions during the intended period of operation, assuming that navigation accuracy and integrity are provided at the start of the operation.

d) ***Availability:*** it is the percentage of time during which the navigation system is available for use, considering all the outages, and provides to the user reliable information (a reliable information must meet the accuracy, integrity and continuity specifications).

In Table 2-2, the RNP for the different flight phases are summarised:

Table 2-2 GNSS Aviation Operational Performance Requirements (CAA-Paper, 2003).

Operation	Accuracy 95%	Integrity			Continuity (1-risk)	Availability
		Integrity (1-risk)	Alert Limit	Time-to-Alert		
Oceanic	12.4 nmi	$1\text{-}10^{-7}$/hr	12.4 nmi	2 min	$1\text{-}10^{-5}$/hr	0.99 to 0.99999
En-route	2.0 nmi	$1\text{-}10^{-7}$/hr	2.0 nmi	1 min	$1\text{-}10^{-5}$/hr	0.99 to 0.99999
Terminal	0.4 nmi	$1\text{-}10^{-7}$/hr	1.0 nmi	30 secs	$1\text{-}10^{-5}$/hr	0.99 to 0.99999
NPA	220 m	$1\text{-}10^{-7}$/hr	0.3 nmi	10 secs	$1\text{-}10^{-5}$/hr	0.99 to 0.99999
APV I	220 m (H) 20 m (V)	$1\text{-}2x10^{-7}$/ approach	0.3 nmi (H) 50m (V)	10 secs	$1\text{-}8x10^{-6}$/ 15 secs	0.99 to 0.99999
APV II	16 m (H) 8 m (V)	$1\text{-}2x10^{-7}$/ approach	40 m (H) 20 m (V)	6 sec	$1\text{-}8x10^{-6}$/ 15 secs	0.99 to 0.99999
CAT I	16 m (H) 4.0 to 6.0 m (V)	$1\text{-}2x10^{-7}$/ approach	40 m (H) 10-15 m (V)	6 sec	$1\text{-}8x10^{-6}$/ 15 secs	0.99 to 0.99999
CAT II	6.9 m (H) 2.0 m (V)	$1\text{-}10^{-9}$/15 sec.	17.3 m (H) 5.3 m (V)	1 sec	$1\text{-}4x10^{-6}$/ 15 secs	0.99 to 0.99999
CAT III	6.2 m (H) 2.0 m (V)	$1\text{-}10^{-9}$/15 sec.	15.5 m (H) 5.3 m (V)	1 sec	$1\text{-}2x10^{-6}$/ 30 sec (H) $1\text{-}2x10^{-6}$/ 15 sec (V)	0.99 to 0.99999

The addition of sources of position information, in forms of new or betters signal, better geometry or removal of failure modes, benefits both the accuracy and integrity of the system. In section 2.2, few examples of sources are presented of which design and quality determine the level of improvement in the integrity performance necessary to satisfy the requirement, however defining their costs as well. Kovach (1998) considers continuity as the most difficult parameter to satisfy and so the major driver of the costs, determined by the failure rate of the satellite hardware. He states that two options are possible:

1) Use much more reliable components.
2) Increase the number of satellites, that helps to improve at the user level the capability of detecting and excluding the erroneous data.

Each parameter represents and covers the risk of events that could lead to unreasonable error in the estimated position:

a) Accuracy: risk of a system error that could generate a position failure
b) Integrity: risk of a latent system failure
c) Continuity: risk of an unexpected loss of the capability of providing a position fix determined by a failure detection
d) Availability: risk that the requirements of the other three parameters are expected to not be satisfied during a specific operation

However, the four parameters are tightly correlated and a navigation algorithm cannot be simply optimised with respect to a specific parameter.

2.2. INTEGRITY MONITORING AND PREDICTION

The overall objective of the integrity monitoring is to evaluate the state of the system and its safe use through the quantification of the possibility of using data affected by errors. Ober (2003) provides a detailed explanation and description of the integrity monitoring concept and this section tries to provide a basic understanding of some of the described notions. In his thesis, he states that a system is safe to use when:

1) It is physically in good shape
2) It operates correctly within its specifications
3) It is trustworthy

The first condition is not sufficient to guarantee the safe use of the collected data, while it is a required condition for the second and third ones. The correct operation of the system within its specifications is a sufficient condition for its trustworthiness, however, is not a necessary condition since the system can still be trustworthy outside the area of specification but it must not be used by definition (subsystems usually monitor and alert the users in this case). For the previous reasons, trustworthiness is considered the best choice as "loose" definition of integrity for navigation systems (Ober, 2003).

Integrity has been recognised as key safety parameter within the RNP and its definition can be associated with the following parameters:

- *Alert Limit*: it is the maximum error tolerance, above which an alert needs to be raised
- *Time to Alert* (TTA): maximum allowed time between the detection of an integrity event and the warning to the user.

- *Integrity Risk*: Probability of exceeding the alert limit.
- *Protection level*: Statistical bound derived from the Integrity Risk. In navigation, it is usually divided in Vertical and Horizontal Protection Levels (VPL and HPL) that together define the region within which the true position is expected to be contained (Figure 2-7).

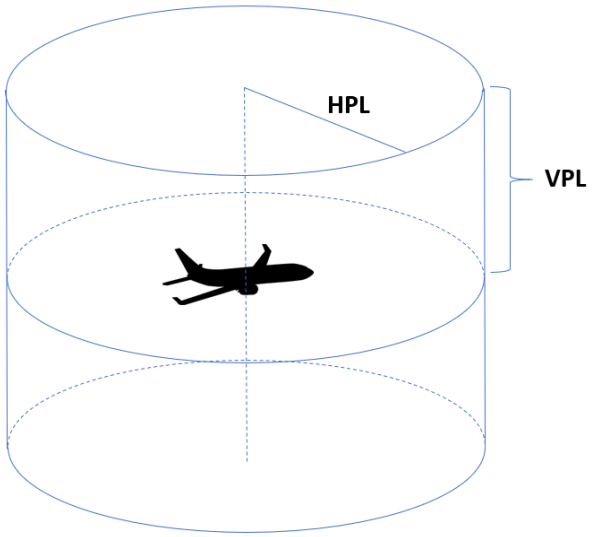

Figure 2-7 Integrity Protection Levels.

Integrity events can be divided into different categories depending on the values assumed by the position error (PE), protection level (PL) and alert limit (AL), described in the Stanford Diagram in Figure 2-8:

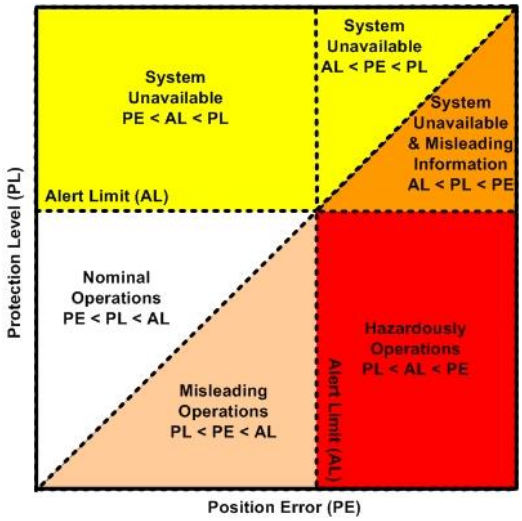

Figure 2-8 Integrity events as defined in the Stanford Diagram (Ober, 2003).

The diagram characterises two different regions, above the diagonal line, in which the PL succeeds in covering the PE, and below the line, in which the PL fails in covering the PE, for a total of four main events:

- the system is in nominal operation when the PE is smaller than the PL that is in turn smaller than the AL
- the system is unavailable when the PL is higher than AL, in this case the system raises an alert to the user that must not use it.
- Misleading operations when PE is higher than PL. In this case, since the position error cannot be measured, the system does not generate an alert and the information provided might not correspond to the real status, therefore possibly providing misleading information on the true position. In this situation, the system shouldn't be used but no alert is provided to the user.

- Hazardously Misleading Information when the PE exceeds not only the PL, but also the AL, leading to a possibly dangerous situation. Also in this case, the system does not provide any alert and it is considered available.

The last two events are defined Integrity Failures, when an event lasts longer than the TTA without providing an alert and they are the most critical situation due to the fact that the system is considered available while the position errors exceed the requirements, possibly leading to a hazardous situation.

For the above reasons, the real-time monitoring of the integrity performance parameters is an important but, at the same time, very challenging task.

However, real-time monitoring is often supported and complemented by performance prediction, a different task based on models and conservative assumptions that could bring two advantages:

- Prediction of the expected performances of the system.
- Prediction of the expected performances during a future operation.

Both the outcomes rely on the models used for the measurements and position-estimation algorithm.

This research focuses on the second advantage, demonstrating how the prediction capability of ARAIM algorithm can be implemented and used in the future of the aviation, integrating effects in the models that could consistently affect the performances of the system.

2.3. REVIEW OF CURRENT INTEGRITY MONITORING TECHNIQUES

As mentioned in the previous sections, integrity is a safety-critical parameter in GNSS applications, usually expressed in terms of 'maximum deviation from the true position, given a certain amount of probability, that indicates the level of trustworthiness of the position solution provided by the system' (InsideGNSS, 2013), an information that must be timely delivered to users to avoid hazardous situations. There are three different methods that provide integrity, for further details the reader can refer to the text by Hofmann-Wellenhof et al. (2008). One method is the ***Space-Based Augmentation System (SBAS)***, a network of monitoring stations, which positions are well-defined, that covers the area of interest and is connected to a master control station that elaborates the errors that affect the position estimate to compute the corrections that uplinks to a geostationary satellite from where they are distributed to users. Examples of implemented SBASs are the U.S. Wide Area Augmentation System (WAAS) the covers most of the countries in North America, the European GNSS Navigation Overlay System (EGNOS) for the European continent, the Multi-Functional Satellite Augmentation System (MSAS) in Japan and the GPS Aided Geo Augmented Navigation (GAGAN) in India, while Russia is realising a WAAS-compatible SBAS called System for Differential Corrections and Monitoring (SDCM). SBAS integrity message improves the accuracy of the position estimation from five to less than one meter and additionally the updated rate of the message is sufficiently small to satisfy the time-to-alert (TTA) requirement (e.g. it is six seconds for LPV-200 approach). SBAS supports a wide range of operations, from en-route to terminal area

navigation, non-precision approach and vertically aided approaches down to LPV-200.

A second method is the ***Ground-Based Augmentation System (GBAS)***, in which ground monitoring stations are placed near the airports and transmit correction message directly to the users through RF links. The corrections are computed as the difference between the accurate and well-known position of the station against the position provided GNSS receivers placed in proximity to the station. GBAS accuracy level reaches values lower that one meter, with an update rate of the message of 0.5 seconds, allowing it to satisfy the TTA for every type of precision approach.

SBAS and GBAS are very powerful systems, their capabilities include a high computational power that allows them to satisfy the stringent requirements of the most demanding approach procedure, in particular, the TTA. At the same time, the TTA requirement of providing timely warning to the users (down to few seconds) and the related computational power drive the architecture of these system making them very complex and expensive facilities.

A third way is to integrate the integrity function at the user's equipment level, called ***Receiver Autonomous Integrity Monitoring (RAIM)***. This method is based on a self-consistency check of the received measurements and its efficiency is totally dependent on the redundancy of information. The history, development and evolution of RAIM algorithms will be further analysed in the next section since they are the basis of this research project.

These three systems, SBAS, GBAS, and RAIM, have all the capability of monitoring the integrity of the information provided by the GNSS, however, their level of performances differ considerably.

Nowadays, GBAS is the only system that meets the requirements for the most demanding approach categories (down to CAT-III), but this system is rarely enforced in airports, due to the higher level of complexity of the ground infrastructure that the other systems do not have (e.g. an SBAS station might cover more than one airport). Additionally, SBAS systems are developing new capabilities that will bring them to support the integrity function for a new type of approach, named LPV-200 that provides vertical guidance down to a decision height of 200 feet.

Instead, RAIM algorithms are only certified as auxiliary navigation in some phases of the flight (such as en-route and terminal area) and for lateral guidance during approach (LNAV), as stated in FAA (2007a), satisfying the minimum operational performance standards for global positioning system/satellite-based augmentation system for airborne equipment (RTCA/DO-229D, 2006).

However, the development and renewal of GNSS constellations being deployed and the implementation of dual-frequency signals will increase the quantity and type of signals used in positioning systems, opening the way to new capabilities, such as upgraded versions of SBAS as well as improved RAIM algorithms (Speidel et al., 2013).

2.4. RAIM AND ARAIM LITERATURE REVIEW AND DESCRIPTION

2.4.1. RECEIVER AUTONOMOUS INTEGRITY MONITORING (RAIM) LITERATURE REVIEW

RAIM techniques are based on a statistical detection theory that allows answering to two fundamental hypothesis-testing questions:

a) Has a failure occurred?

b) Which satellite is affected? (one of the main hypothesis of RAIM is that there can be only one affected measurement per epoch)

If the GNSS integrity monitoring system is used as an auxiliary navigation system, it is sufficient to answer to only the first question, since it is supposed that it possible to switch to the complementary system in case of a detected failure. Instead, if GNSS is the main and only system, the second question is required to be addressed and answered, because the faulty measurement and the related satellite must be identified and excluded from the computation, in this way the aircraft can proceed safely with an uncontaminated GNSS solution. However, the identification of the faulty satellite is far more trivial than simply determine that a fault is occurred and a good number of redundant measurements might be necessary.

To estimate the aircraft position, four satellites are necessary in order to compute the unknowns of the system, three for the user location and one for the user clock offset; However, to implement the fault detection, at least five measurements are needed and six or more to identify the satellite and to isolate/exclude it. Groves, (2013a) lists four techniques for faults detection and correction:

- ***Fault Detection (FD)*** simply detects a fault and warns the user.
- ***Fault Detection and Recovery (FDR)*** detects when the fault has occurred and attempts to recover the navigation solution.
- ***Fault Detection and Isolation (FDI)*** detects and identify the faulty measurement and removes it from the navigation solution.
- ***Fault Detection and Exclusion (FDE)*** detects and identify the faulty satellite and removes it from the computation of the navigation solution until the

ground segment clear it or if the following satellite measurements, after a predefined time, pass a consistency check test.

Generally, modern RAIM algorithms include the following functions:

1. Detection of faulty satellites (and exclusion/isolation/ recovery depending on the technique implemented, as described in the previous paragraph):
   - Using a discriminator called test statistics and knowing enough about the likely noises in the system and their interaction with the test statistic, the relationship between the test statistic and the faulty measurement can be statistically described.
   - Establishing the fault-free limit, called detection threshold, typically based on the false alert probability specified for that particular application. The fault-free limit is rarely exceeded by the observed test statistic if no faults are present.
   - Comparing the test statistic with the detection threshold and declare that the fault is present if the test statistic exceeds the limit.
   - If a fault is detected, attempt exclusion
2. Compute the Horizontal and Vertical Protection Levels (HPL and VPL) defined as the minimum position errors (HPE and VPE) that have to be detected with the required probabilities of false alert and missed detection. This function is also called RAIM availability and this research focuses on this specific function, demonstrating how the prediction capability of ARAIM algorithm can be implemented and used in the future of the aviation, integrating effects in the models that could consistently affect the performances of the system.

The development of RAIM techniques started in the latter half of the 1980s, with the term of "self-contained" methods and the acronym RAIM appeared for the first time in 1987 in an article published by Kalafus (1987) and then officially recognised from the aviation community.

Two different approaches to RAIM were presented at the ION meeting 1986:

a) ***Recursive Scheme****:* typically a Kalman filter, in which both past and present measurements are used to compute the solution and the fault detection function is performed by monitoring the innovations. Additional information can be found in the article published by Brown and Hwang (1986).

b) ***Snapshot Scheme****:* it only uses redundant measurements for the self-consistency check. Please refer to Lee (1986) for further details.

The former gives more accurate position estimation and is used to detect rapidly growing measurement errors, but it fails to catch slowly growing errors (soft failures or ramp type). Conversely, the snapshot scheme has the advantages of detecting soft failures and not making hypotheses on how the system reached its current state.

Perepetchai (2000) combines the two schemes using the output of the recursive scheme in the snapshot in order to improve the fault detection.

Afterwards, the snapshot scheme has gained more acceptance that the other and several methods have been developed:

1) ***Range Comparison Method****.* Described by Lee (1986)*, t*his method estimates the solution using *n* of the *m* available measurements (e.g. for the navigation solution n=4) and uses it to predict the remaining *m-n* measurements and then it computes their residuals (the difference between real and predicted measurements). If the residuals are small, the consistency check is passed and

"no failure" is declared. The main issue is to define the decision rule, a common way is to consider an equal probability density contour and if the noise has a Gaussian distribution, then the contour will be a closed hypersurface with *m-n* dimensions. This makes the rule conceptually simple, but awkward computationally: if the test statistic falls within the hypersurface, there is no fault, otherwise, the algorithm declares a failure.

2) ***Least-squares Residual (LSR) Method***. This method uses all the measurements to compute a least-squares estimate of the navigation solution and then calculate all the measurement residuals between the real and predicted measurements computed using the all-in-view solution. The sum of the squares of the residuals (SSE) represents the test statistic and it is compared against a detection threshold. If a fault is detected, the test statistic is computed for the *m* subsets of *(m-1)* satellites, the subset with the minimum value is the position solution with the faulty satellite excluded, A full description of the LSR method can be found in the articles published by Parkinson and Axelrad (1988), Parkinson et al. (1996), Perepetchai (2000) and in the book by Groves (2013a).

3) ***Parity Method.*** There are two main parity methods described by Sturza (1988), Brenner (1990) and Graas and Farrell (1993). The base of the two methods is to compute the parity vector *p* through a linear transformation on the measurement vector *y.*

   Sturza (1988) uses as test statistic for simple detection, the squared magnitude of the *p* vector, which has been demonstrated to be equal to the SSE of the LSR methods, so the detection method turns out to be the same.

Brenner (1990) forms an identification test statistic through the Householder transformation that optimizes the error visibility for each satellite, in order to improve the identification of the faulty satellite.

4) ***Maximum Residual (MR) Method***. Kelly (1996b, 1997) applies the Maximum Residual Method, a technique used in statistics community for data outlier detection and identification, to RAIM. This method calculates the residuals through a likelihood ratio test and compares the maximum with a detection threshold. The main advantage of the MR method is that is able to perform detection and identification in one step. Kelly (1996a) demonstrated the mathematical equivalence of the MR method with the Parkinson's LSR method, the Sturza's and Brenner's Parity methods.

5) ***Solution Separation (SS) Method***. Brown and McBurney (1987) present a different and more heuristic method from the previous ones developed. The main assumption of the method is that no more than one satellite has failed (in the next session will be presented an evolution of this technique that allows to detect and exclude more than one failure at a time). If *n* satellites in view, *n* different calculation of the position solution can be made, each excluding a different satellite. The differences between each subset are then formed and either the largest difference or the scalar average of the all the differences is compared against a threshold. If the considered quantity doesn't pass the test, a failure is declared.

2.4.2. RAIM CONCEPT DESCRIPTION

In Section 2.1 a brief description of the positioning problem has been presented and summarised in Eqs. (2.4), in this section, the integrity side of that equations is quickly introduced, a highly detailed description can be found in the work done by Imparato (2016). The navigation solution is essentially an estimation problem of finding the unknown x given a set of measurement y within predefined bounds and a certain probability:

$$\underline{\hat{x}} = f(\underline{y}) \tag{2.28}$$

Where:

- $\underline{\hat{x}}$ is the position estimation
- f() is the estimation function
- $\underline{y}$ is the statistical distribution of the measurements that belongs to the admitted region $\Omega \epsilon \mathrm{R}^{\mathrm{m}}$

that satisfy:

$$P(\underline{x} - x \notin \Omega_{AL}) \leq P_{req} \tag{2.29}$$

Where Ω_{AL} is the region that bounds the true position, which borders are the Alert Levels. In the RAIM concept, the probability in (2.29) is the probability of Hazardous Misleading Information, or integrity risk, and P_{req} is the integrity risk requirement for a specific application (P_{HMI}). The estimator needs to satisfy not only the condition on the integrity risk, but also the following one related to the continuity:

$$P(y \notin \Omega) = P_{FA} \leq P_{FA}^{req} \tag{2.30}$$

Where P_{FA} is the probability of False Alert; a False Alert is defined when the system discontinues the operation generating a warning to the user but without a real cause. The requirement on the probability is computed from the requirement on the continuity as:

$$P_{FA}^{req} = 1 - cont_{req} \tag{2.31}$$

Figure 2-9 summarises the basic process of RAIM:

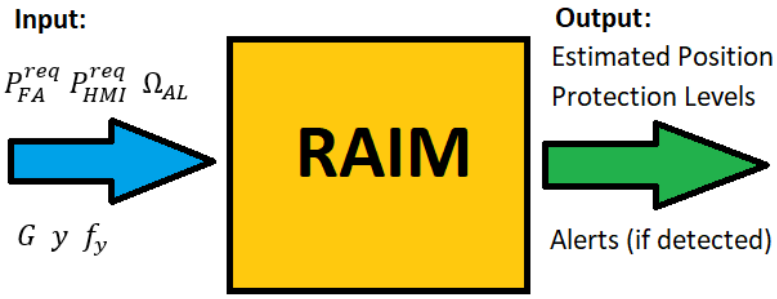

Figure 2-9 RAIM Main Process.

The RAIM technique takes as input the parameters introduced in the previous sections with the main objective of evaluating the reliability and availability of the GNSS service, expressed in terms of three outputs:

- Estimated Position (x)
- Protection Levels (PL)
- Alerts, if any occurred, to warn the user to not use the system

The alerts are not only triggered by faults or errors in the incoming measurement, there is another factor that affects the integrity performances of the system that it is the satellite geometry; if it is too weak, the computed PLs could be larger than the Alert Levels. The integrity performances prediction capability of RAIM (ARAIM as well) algorithm and its geometry dependency are the features exploited in this

research that has the main goal of evaluating the effectiveness of these techniques in supporting the deployment of GNSS as primary system in the future of aviation.

2.4.3. ADVANCED RAIM (ARAIM) HISTORY AND LITERATURE REVIEW

As mentioned in the previous sections, an increased number of Global Navigation Satellite System (GNSS) satellites are expected to become operational over the next decade, paving the way to improved navigation capabilities and techniques as a result of the availability of multi-frequency civil signals, the deployment of new constellations (Galileo and COMPASS) and the modernization of the existing ones (GPS and GLONASS). These enhanced future capabilities can enable GNSS receivers to serve as a primary means of navigation worldwide and provided the motivation for Federal Aviation Administration (FAA) to form the GNSS Evolution Architecture Study (GEAS) panel to investigate new GNSS-based architectures with a focus on precision approach down to LPV-200 operations.

In the first report, the GEAS panel (2008) identified and made a first analysis of three different integrity architectures:

1) *The GNSS Integrity Channel (GIC).* This system combines the GNSS Space System (the satellites) with a global Space Based Augmentation System (SBAS) that exploit the dual-frequency technology and associated to a regional ground-based monitoring network, that has the task of supplying the users with the integrity message and corrections. The main advantage of GIC it is that requires the lowest computational workload for the avionics with respect to the other concepts is that it. The main drawback is that the Ground system

has the burden of satisfying the TTA and providing timely alerts to users in case of hazards.

2) *The Relative RAIM (RRAIM).* The on-board avionics autonomously monitors the integrity and compute the aircraft position, using the real-time measurements and a set of measurements validated by the Ground Systems that will be used for a predefined time (coasting period between two validated sets). The main advantage of RRAIM is that TTA requirements are less demanding relative to the GIC concepts because the data set can be used for minutes. The main drawbacks of this concept are that this system completely relays on the Ground system for the provision of the sets of measurement and the constellation geometry requirements are more stringent compared to GIC, but relatively relaxed respect to the last concept developed by the GEAS panel.

3) *The Absolute RAIM (ARAIM)*. The GEAS panel defined this integrity architecture as an enhanced version of the RAIM algorithm. The dual-frequency measurement diversity would improve RAIM architecture by removing the large ionospheric errors affecting range measurements. ARAIM is almost autonomous, however, it still requires external support, with a key difference compared to the previous architectures, a higher level of independency. The Ground system provides the failure probabilities for the individual satellites and constellation together with a set of parameters (e.g. the user range accuracy, URA). ARAIM has the advantage of being less demanding concepts with respect to Ground support (integrity message rate and size), but it requires good constellations geometry, not only for the all-in-

view solution, but also for the subsets that the algorithm generates to perform the fault detection and exclusion function.

In the second report, GEAS (2010) identified the ARAIM (renamed Advanced RAIM) as the most promising system because it could reduce the cost of ground infrastructure and eliminate single points failure (e.g. interference at the monitoring station). In the document, GEAS has also defined the possible architecture, made assumptions and suggestions related to the Ground Monitoring, the data link and the information that should be provided through the integrity message, called Integrity Support Message (ISM). Moreover, it clearly stated the necessary performance requirements that ARAIM systems must satisfy to support LPV-200 capabilities; the following list resumes the most demanding requirements for GNSS systems:

- 4m 95% accuracy requirement: the probability of a vertical error exceeding 4 m must be below 5%.
- The Probability of Hazardously Misleading Information (PHMI) is the probability that the position error (horizontal and vertical) exceeds the protection level (PL) for longer than the Time-to-Alert (TTA) and its value should be less than $2\text{x}10^{-7}$ per approach:

$$PHMI = \sum_{threats} p_{threat_i} P(VPE > VPL \; or \; \mathrm{HPE} > \mathrm{HPL} | threat_i) \leq 2 * 10^{-7} \tag{2.32}$$

- 15m Effective Monitoring Threshold (EMT) requirement: the probability of an undetected fault resulting in a vertical position error exceeding 15 m must be less than 10^{-5}:

$$P(VPE \geq 15m | fault) P(fault) \leq 10^{-5} \tag{2.33}$$

- $8x10^{-6}$ continuity requirement: an approach at a given location and future time can only be declared available if there is a probability below $8x10^{-6}$ of not being able to complete it (under normal condition).

However, ARAIM performances depends on the assumption made on faults that could occur, their frequency and the process implemented for their mitigation, if at user or ground level (e.g. using a long latency Integrity Support Message); GEAS's report includes a list of possible threats that could affect the system, dividing them into three different categories (a more detailed scheme can be found in (Appendix A):

- *Nominal faults:* errors that are always present and whose magnitude is not expected to change
- *Narrow faults:* faults that can affect each satellite independently and cause the pseudo-range error to grow well beyond the nominal behaviour
- *Wide Faults:* faults that could cause a whole constellation to be faulted

For these reasons, the EU/US Working Group C (WG-C) established a technical sub-group, which main objective was to design a multi-constellation ARAIM concept that allows vertical guidance worldwide. The outcome of the WG-C (2012) subgroup is the report that fully describes a preliminary multi-constellation ARAIM algorithm based on the Multiple Hypothesis Solution Separation method, one of the first algorithms to implement multi-constellation RAIM with the possibility of multiple simultaneous failures across the constellation, presented by Pervan et al. (1998) and also used by Ene (2007, 2009) and by Ene et al. (2008), in which the authors developed an ARAIM algorithm with real-time dual frequency L1-L2 GPS flight data.

Most of the literature produced afterwards is based either on the algorithms developed by Ene (2009), GEAS (2010), WG-C (2012) or Blanch et al. (2010).

These preliminary analyses clearly show the potentialities of Advanced RAIM architectures of providing the Required Navigation Performance and achieving global coverage of LPV-200 using at least two constellations, confirmed by other related research performed by Choi et al. (2011a , 2012), El-Mowafy (2013) and Pham et al. (2013).

Blanch et al. (2013d, 2011) analysed the algorithm performance in different constellation configurations (single, dual and tri-constellation), highlighted the critical elements and proposed new approaches or possible improvements that they applied in a further developed algorithm fully described in another paper (Blanch et al., 2012).

More in general, the developed algorithms can be split into two groups, depending on which domain the consistency check is executed:

- ***Range domain***, that uses the Chi-square method presented by Brown and Chin (1998). Choi et al (2011b) use a modified Chi-square test, named Weighted Sum of the Squared Errors (WSSE) to perform the fault detection; Young and Surathu (2012) and Lee (2012) test the performance of a new Chi-square test statistics for detecting four different type of Constellation-wide faults using two constellations.
- ***Position Domain,*** that uses the Solution Separation Method developed by Brenner (1995), or the improved version Multiple Hypothesis Solution Separation that allows multiple fault detection (Pervan et al., 1998).

Other research groups focused on the development, improvement or optimization of some aspects of the ARAIM algorithm:

a) ***Ground segment****:*

- Walter et al. (2012) state that airborne ARAIM algorithms are comparatively mature and it is time to start investigating the architecture that should support the operations. They examine important components for different architectural choices, such as monitoring network size and density, how to provide the integrity information to the aircrafts and its latency, how to handle consistent faults and the methodology for demonstrating the integrity performance.
- Milner et al. (2013) define a possible solution for the allocation of responsibility and risk between the ground segment and airborne segment. The authors proposed three different ISMs configuration with increasing amount of data transmitted and latency time.
- While Blanch et al. (2013a) describe an architecture that minimizes the ground requirements by using a Long Latency ISM and outline a possible path to transition from current horizontal RAIM to ARAIM.
- Martini et al. in (2013b), from the Institute of Communication and Navigation of German Aerospace Center (DLR), propose an architecture that provides the two different type of ISMs, a long-term one addressing nominal conditions and a short one to detect anomaly conditions, that aims to maximise the reuse of existing infrastructure and to provide the necessary robustness required. At the same time the DLR research group of Martini et al. (2013a) tested the proposed architecture with real data collected from

three different constellation (GPS, GLONASS and Galileo), in the presence of a source of interference, a GNSS repeater, and then tested the algorithm with data collected in flight together with ground reference data (Rippl et al., 2014).

b) ***Improved Fault Detection and Exclusion Function****:*

- Young and Surathu (2012) present an FDE algorithm based on the parity space more computationally efficient than Solution-Separation methods.
- Blanch et al. (2014) modify and complete the approach presented by Blanch et al. (2012), presenting an FDE algorithm that in the presence of an unambiguous fault, the protection level is the same as if the excluded had not been included in the first place.
- Spletter and Rippl (2011) describe a procedure to reintroduce the satellites removed from the computation, using an integrated self-health check or using a validated information provided by external systems.
- ***Failure mode analysis:*** Validation of GNSS based applications, such as flight operations, needs a deep analysis of all the possible failure modes and how they affect the performances of the system and this process is called Failure Mode Effect Analysis (FMEA)
- Walsh et al. (2004) provide a good summary of the complexity of the FMEA process, the issues in the evaluation of the impact of the failures on the performances and the current gaps in the process.
- Ioannides et al. (2005) present a new complete FMEA process for the validation of GNSS based flight operations that has the objective of assess

the performances in the presence of geometry, biases and nominal range errors using two new parameters: the ratio of the position error over the bias applied to the faulty satellite and the ratio of the bias applied to the faulty satellite over the test statistics contribution due to the bias. The authors generate a model that correlates geometry to the Probability of Missed Detection, Probability of False Alarm and Accuracy. The model proved to reduce the complexity of the validation process for GNSS based flight operations.

c) ***Optimization of the performance****:*

- Milner and Ochieng (2010) present an algorithm based on the MHSS technique that allows computing the Protection Levels 10-20% lower than standard algorithms.
- Blanch et al. (2013b) provide an algorithm that optimises the allocation of the integrity and continuity over the fault modes with the objective of minimizing the Protection Levels.
- Jiang and Wang (2014) define a new procedure to compute the VPL; the authors show that the new method is more reliable and efficient, in terms of computational effort, increasing ARAIM availability from 32-38% to 74% with GPS and from 43%-44% to 85% with Galileo.
- Walter et al. (2014) describe methods for reducing the total number of subsets to be evaluated, neglecting many of the less likely scenarios and simplifying the overall user airborne algorithm.
- Lee (2013) provides a different approach to detect a consistent constellation-wide fault, the Earth Orientation Parameter fault.

- Another problem addressed in the work by Feng et al. (2006a, 2006b) and Feng and Ochieng (2005) is how to reduce the computational burden of the FMEA process. RAIM performance analyses are based on simulations that use large spatial and temporal sampling intervals in order to reduce the number of computations to be performed for a single area or trajectory but with the disadvantage of reducing the accuracy of the results and increasing the risk of missing critical points or moments. The authors present three different ways to reduce the computational workload and at the same time to improve the accuracy of the results. The first algorithm by Feng et al. (2006a) presents a different approach in the definition of the data sample points; instead of being defined by a set grid, the authors propose to generate the sample points from the intersection of the satellite coverage boundaries and the Earth surface. The algorithm is capable of defining the different areas and identifying the number of satellites in view within them, along the boundaries and the intersection points, highlighting what the authors call RAIM-holes. RAIM holes are areas, boundaries or points that do not have sufficient satellite coverage in order to satisfy the minimum requirement for consistency checks (minimum 5 satellites) or FDE function (minimum 6 satellites). The second algorithm by Feng et al. (2006b) addresses the problem of sampling intervals in a dynamic scenario (e.g. an aircraft trajectory) by analysing the spatial-temporal correlation characteristic of both the satellite geometry and the measurement errors to optimally reduce the number of samples to analyse. The algorithm proved to reduce the computational workload and demonstrated the ability of capture areas of

potential risk to integrity that could have been missed by standard grid-based schemes. The third one by Feng and Ochieng (2005) uses the resolved orbital errors to estimate an approximate worst user location at the first step on a spherical model of the Earth and then uses an iterative transformation process to estimate the location on a selected ellipsoid model. In this work, the worst user location depends on the satellite orbit errors and it is considered a key parameter for the evaluation of the integrity of the Galileo data.

d) ***Effects of assumptions****:* most of the simulations and test are performed making assumptions on the performance of the single constellations since there are no real data to evaluate them yet.

- Phelts et al. (2014) analyse the effects of nominal signal deformation measurements, analysis technique and results previously used for GPS and SBAS on ARAIM performance.
- Macabiau et al. (2014) aim to determine the size of the nominal biases affecting the user measurements, the capacity of the ground segment to provide pertinent values and the impact on the ARAIM performance.

e) ***Comparison with other techniques and algorithm****:*

- Jiang and Wang (2011) compare ARAIM with RRAIM, showing that RRAIM, in general, provides better results but at the same time introduces complexity, increased computation burden and some other critical issues.
- Kropp et al. (2011) compare three integrity algorithms using different error over-bounding models and constellation configurations: 1) Galileo Integrity

Concept (GIC) 2) ARAIM and 3) Multiple Weighted RAIM. The first two algorithms showed a 100% availability over the whole world grid using the integrity requirement for the LPV-200 procedures, while the latter showed lower performance and higher sensitivity to the assumptions made.

- Cezon et al. (2013) compare ARAIM algorithm with a new technique, called Isotropy-Based Protection Level, which makes no assumption on the statistical behaviour or the size of individual measurements errors. It is a simple and robust solution to the multi-constellation integrity problem, without the need of a specific ground segment, as claimed by its developers. The results show that the performances of IBPL are similar to ARAIM for the selected scenarios.
- Su et al. (2012) show the results of an ARAIM algorithm developed by Thales Alenia Space Deutschland, named PORIMA, that uses IGS ultra-rapid GPS satellite orbit as additional ground monitoring information and tested on two-data years continuous data.
- Pullen et al. (2013) show how the GPS modernization could improve the performance of a GPS standalone user performance and integrity, without the need of a multi-constellation configuration.

The issue of multiple satellite faults, narrow and wide faults, stimulated the development of alternative RAIM algorithms, called Inter-Constellation Comparison Methods (ICC RAIM) and two of them deserve to be mentioned, but for further details see the related references:

- ***Optimally Weighted Average Solution (OWAS)*** method, published by Lee et al. (2005). The navigation solution of this method is not a full-set solution,

but a weighted average of the two respective solutions from the two constellations, where the weights are optimally chosen to minimize PLs

- ***Novel Integrity-Optimized RAIM (NIORAIM)***, published by Hwang and Brown (2006 and 2008). It uses a numerical ad hoc iterative search method to generate (in an offline processing) a multi-dimensional look-up table that is used to determine the PLs via interpolation (in online processing).

2.4.4. ADVANCED RAIM ALGORITHM DESCRIPTION

ARAIM technique is still in the development phase, new functions, features and optimization have presented at the conferences in the last years (e.g. a new FDE algorithm presented by Blanch et al. (2014)), while, at the same time, it is now undergoing through the experimental phase. The following section explains part of ARAIM algorithm functions developed and described by GEAS in the second report (2010), implemented in the MATLAB ARAIM Availability Simulation Tool (MAAST) (presented in Par. 3.3) and used in this research, even though it has been reckoned that some of the functions are not optimal (e.g. the error models and probability allocations are too conservative). Other functions, such as the Chi-Square test, the fault detection and exclusion or the computation of the integrity and accuracy after the detection of a fault, are not considered, since the main purpose of this research is to analyse the algorithm prediction performance in nominal conditions and evaluate the influence of other factors that might reduce the reliability of the system. As mentioned in the previous section, ARAIM technique, compared to RAIM, has the following additional features:

- Multi-constellation, to increase the number of redundant measurements
- Multi-frequency, to remove the first order component of the ionospheric delay
- Multiple faults detection capability (Blanch et al., 2011, Blanch et al., 2012, Blanch et al., 2013c, Brown and McBurney, 1987).

Additionally, the technique is based on an algorithm also developed by Stanford University, named Multiple Hypothesis Solution Separation (MHSS) (Blanch et al., 2007, Ene, 2009).

F. MULTIPLE HYPOTHESIS SOLUTION SEPARATION (MHSS)

This section presents the Multiple Hypothesis Solution Separation method, for additional information refers to the papers by Blanch et al. (2007), Ene (2007), Pervan et al. (1998) and the PhD thesis by Ene (2009).

The real-time integrity monitoring function usually includes a fault-detection (FD) function, and possible exclusion or isolation (FDE or FDI), however, in order to uncover faults, they need to be characterised and modelled, a difficult task due to their random nature. For this reason, a probabilistic conservative approach is used, through Gaussian distributions with correlated maximum biases that over-bound them. In a system that deals with multiple sources of measurements, each source could be affected by an error and more than one source could be it at the same time. In terms of number, if there are *n* pseudo-ranges, there are 2^n different cases of failure, also known as error model states or hypothesis, including single and multiple failures and the nominal case (or null hypothesis), in which the system does not present any failure.

For each single failure state, an a priori probability of failure is associated ($P_{ap,i}$, where i is the i-th state), while multiple-failures state is computed by multiplying their a priori probabilities:

$$P_{ap,tot} = \prod_1^m P_{ap,i} \left(= P_{ap}^m \ if\ all\ probabilities\ are\ equal\right) \quad (2.34)$$

Where m is the number of simultaneous faults.

For ARAIM performance prediction, two types of a priori probability of failure are considered:

- Single Satellite a priori probability of failure P_{sat}
- Single Constellation a priori probability of failure P_{const}

The analysis of all the possible combination of failure modes, composed by subsets of satellites or constellations, might require a considerable amount of computational power that clearly increase exponentially with the number of measurements *n*, though of satellites, involved. To reduce the number of subsets to be analysed by the algorithm, two parameters have been introduced: the maximum number of failed satellites ($N_{sat,max}$) and constellation ($N_{sat,const}$). Each subset has its probability given by (2.34) and the value decreases with the increase of the number of failures *m*, reaching eventually values that can be neglected and only the subsets that have a probability higher than a defined threshold are considered in the computation.

$$N_{sat,max} = \frac{\left(\sum_{k=1}^{N_{sat}} P_{sat,k}\right)^m}{m!} > P_{sat,thre} \quad (2.35)$$

With $\mathrm{m} < \mathrm{N_{sat}} - 3 - \mathrm{N_{const}}$

The $N_{sat,max}$ value is found iteratively and it will define the number of subsets will be considered in the computation and Table 2-3 (see work by Blanch et al. (2012) for

further details), provides examples of the relationship between $N_{sat,max}$, the a priori probability of failure and the number of satellite in view.

Table 2-3 $N_{sat,max}$ dependency from P_{ap} and the number of satellite in view.

P_{sat}/N_{sat}	10	15	20	25	30	35	40
10^{-5}	1	1	1	1	2	2	2
10^{-4}	2	2	2	2	2	2	2
$5x10^{-4}$	2	3	3	3	3	3	3
10^{-3}	3	3	3	3	3	4	4

However, the discarded subsets still need to be considered in the algorithm, since even though they are not analysed, the sum of all the probabilities of the not monitored modes has to be removed from the allocated probability used for the computation of the protection levels (see Eq. (2.36)):

$$P_{sat,not\_monitored} = \frac{\left(\sum_{k=1}^{N_{sat}} P_{sat,k}\right)^{N_{sat,max}+1}}{(N_{sat,max}+1)!} \tag{2.36}$$

A similar process is performed to compute the maximum number of constellations that can fail at the same time. The ARAIM algorithm is designed for multi-constellation configuration and it is capable of detecting a single constellation failure, but only if in the computation more than one constellation is included, otherwise the constellation fault is not detectable. If only one constellation is used in the analysis, the value of P_{const} needs to be set lower than the thresholds, otherwise, there is a high chance that the algorithm will generate an error, warning the user that is not possible to detect a constellation failure. First of all, the probability of no constellation is computed as:

$$P_{const,nofault} = \prod_{k=1}^{N_{const}} \left(1 - P_{const,k}\right) \quad (2.37)$$

Then, since $N_{const,max}$ depends on N_{const}, if there are more than three constellations available and the following relationship is valid:

$$1 - P_{const,nofault} - P_{const,nofault} \sum_{k=1}^{N_{const}} \frac{P_{const,k}}{1-P_{const,k}} > P_{const\_threshold} \quad (2.38)$$

The maximum number of failed constellations is two, otherwise the algorithm is going set one as maximum value.

As for the satellites faults, removing some of the possible combinations from the computation requires to remove the probability of the unmonitored ones from the budget allocated for the computation of the protection levels:

For:

$N_{const,max} = 1$

$$P_{const,not_{monitored}} = 1 - P_{const,nofault} - P_{const,nofault} \sum_{k=1}^{N_{const}} \frac{P_{const,k}}{1-P_{const,k}} \quad (2.39)$$

$N_{const,max} = 2$

$$P_{const,not\_monitored} = 1 - P_{const,nofault} \left(1 + \sum_{k=1}^{N_{const}} \frac{P_{const,k}}{1-P_{const,k}}\right) - P_{const,nofault} \sum_{k_1<k_2} \frac{P_{const,k_1}}{1-P_{const,k_1}} \frac{P_{const,k_2}}{1-P_{const,k_2}} \quad (2.40)$$

The last term in (2.40) takes in to account the different combination of the two constellations.

Once the maximum number of satellites and constellations is determined, it is possible to define the number of error models or hypothesis that the algorithm will deal with:

$$N_{hyp} = \sum_{i=1}^{N_{sat,max}} \binom{N_{sat}}{i} + \sum_{j=1}^{N_{const,max}} \binom{N_{const}}{j} \quad (2.41)$$

At this point, it is possible to generate all the required subsets and an example is shown in Table 2-4, in which a configuration with two constellations and ten satellites is used:

Table 2-4 Example of subsets with N_{sat} =10, N_{const} = 2, P_{sat} = 10^{-5} and P_{const}= 10^{-4}, 1 indicates that the satellite is included in the subset, 0 that is not included.

	GPS1	GPS2	GPS 3	GPS 4	GPS 5	Gal1	Gal2	Gal3	Gal4	Gal5
Sub#0	1	1	1	1	1	1	1	1	1	1
Sub#1	0	1	1	1	1	1	1	1	1	1
Sub#2	1	0	1	1	1	1	1	1	1	1
Sub#3	1	1	0	1	1	1	1	1	1	1
Sub#4	1	1	1	0	1	1	1	1	1	1
Sub#5	1	1	1	1	0	1	1	1	1	1
Sub#6	1	1	1	1	1	0	1	1	1	1
Sub#7	1	1	1	1	1	1	0	1	1	1
Sub#8	1	1	1	1	1	1	1	0	1	1
Sub#9	1	1	1	1	1	1	1	1	0	1
Sub#10	1	1	1	1	1	1	1	1	1	1
Sub#11 (GPS)	1	1	1	1	1	0	0	0	0	0
Sub#12 (GAL)	0	0	0	0	0	1	1	1	1	1

The first subset is the all-in-view or null hypothesis subset, subset from #1 to #11 each one excludes a single satellite at a time, while the last two subsets are the single constellation subset, used to evaluate if a failure occurred at constellation level.

For each subset, except for the null hypothesis or the fault-free mode, it is then required to compute the overall probability of occurrence, generating an a priori Probability Mass Function (PMF):

$$P(H_i) = P_{fault,i} \tag{2.42}$$

With i = 0, 1, …, N_{hyp}

Each subset of a priori probability is given by:

- For single (or multiple) satellite fault:

$$P_{fault,i} = \prod_{j \epsilon i} P_{sat,j} \tag{2.43}$$

With $i \leq \sum_{k=1}^{N_{sat,max}} \binom{N_{sat}}{k}$

- For single (or multiple) constellation fault:

$$P_{fault,i} = \prod_{j \epsilon i} P_{const,j} \tag{2.44}$$

With $i > \sum_{k=1}^{N_{sat,max}} \binom{N_{sat}}{k}$

G. Position Estimation and Solution Separation Test

The basic principle of the navigation problem has been already presented in par2.2. In this section, the main functions of the ARAIM will be further explained and summarised in the following steps, as described by Blanch et al. (2012) :

- *Covariance Matrices.* The first step of the ARAIM algorithm is the computation of the Covariance Matrices for the two error models (C_{int} for integrity and C_{acc} for accuracy model) using the signal errors and biases characterisation of each satellite:

$$C_{int}(i,i) = \sigma^2_{URA,i} + \sigma^2_{tropo,i} + \sigma^2_{user,i} \quad (2.45)$$

$$C_{acc}(i,i) = \sigma^2_{URE,i} + \sigma^2_{tropo,i} + \sigma^2_{user,i} \quad (2.46)$$

Where:

Table 2-5 Signal Error Description.

Name	***Description***
$\sigma_{URA,i}$	Standard deviation of the clock and ephemeris error of satellite *i* used for integrity
$\sigma_{URE,i}$	Standard deviation of the clock and ephemeris error of satellite *i* used for accuracy and continuity
$\sigma_{tropo,i}$	Tropospheric delay of satellite *i,* function of its elevation angle
$\sigma_{user,i}$	User contribution to the error budget function of satellite *i* elevation angle

- *Computation of All-in-view Position Solution*. Using a weighted least-squares estimation:

$$\Delta x = (G^T W G)^{-1} G^T W \Delta PR \quad (2.47)$$

Where:

Table 2-6 Weighted Least-Square Elements.

Name	***Description***
Δx	Corrections of the receiver position and clock states
G	Geometry Matrix in East North Up coordinates with a clock component for each constellation
W	Weighting matrix defined as C^{-1}_{int}

Name	***Description***
ΔPR	Vector of pseudo-range measurements minus the expected ranging values based on the location of the satellites and the position solution given by the previous iteration

- *Fault-tolerant positions and associated standard deviation and biases*. For each of the k subsets, the algorithm computes the position solution x_k, evaluates the differences with the all-in-view position solution x_0 (also known as solution separation method) and determines the standard deviations and the test thresholds.

$$\Delta x_k = x_k - x_0 = (S_k - S_0)y \quad (2.48)$$

Where

$$S_k = (G^T W_k G)^{-1} G^T W_k \quad (2.49)$$

- y: vector of pseudo-range measurements minus the expected range for an all-in-view position.
- W_k is the weighting matrix of the k-th Hypothesis in which the element corresponding to the satellite removed from the subset has been replaced by a zero (the measurement coming from that satellite has no weight in the position estimation).

The variances of $x_{k,q}$ (where index q = 1, 2 and 3 designate the East, North and Up components respectively) are given by:

$$\sigma^2_{k,q} = (G^T W_k G)^{-1}_{q,q} \quad (2.50)$$

The nominal biases of the position solutions $x_{k,q}$ are given by:

$$b_{k,q} = \Sigma_i \mid S_{k,q,i} \mid b_{nom,i} \quad (2.51)$$

The variances of the differences $\Delta x_{k,q}$ are given by:

$$\sigma^2_{ss\,k,q} = e^T_q\,(S_k - S_0) C_{acc}\,(S_k - S_0)^T\,e_q \qquad (2.52)$$

in which e_q denotes a vector whose qth entry is one and all others are zero

- *Solution Separation Threshold*. Each fault mode has three solution separation threshold tests, one for each coordinate. They are defined by:

$$T_{k,q} = K_{fa,q}\,\sigma_{ss,k,q} \qquad (2.53)$$

Where:

$$K_{fa,1} = K_{fa,2} = Q^{-1}\left(\frac{P_{fa\_hor}}{4N_{hyp}}\right) \qquad (2.54)$$

$$K_{fa,3} = Q^{-1}\left(\frac{P_{fa\_ver}}{2N_{hyp}}\right) \qquad (2.55)$$

- $Q^{-1}(p)$: it is the (1-p)-quantile of a zero-mean unit-variance Gaussian distribution
- P_{FA}: continuity budget allocated to disruptions due to false alert (distributed to the Vertical and Horizontals components).
- $\frac{P_{fa\_hor}}{N_{hyp}}$: continuity budget allocated for each hypothesis. The budget is equally shared between the number of hypotheses, a concept already proved to be inefficient by Blanch et al. (2012), since some of the failure modes might have a higher probability to occur compared to the others.

The Protection Levels can be computed only if the following relation is valid for all k and q:

$$\tau_{k,q} = \frac{|x_{k,q} - x_{0,q}|}{T_{k,q}} \leq 1 \qquad (2.56)$$

If any of the tests fail, in the full version, the algorithm must attempt the exclusion of the fault.

- *Computation of the Protection Levels (PL)*. Vertical Protection Level (VPL) and Horizontal Protection Levels (HPL) are the solutions of the following equations:

$$2Q\left(\frac{VPL - b_{0,3}}{\sigma_{0,3}}\right) + \sum_{k=1}^{N_{hyp}} P_{fault,k} Q\left(\frac{VPL - T_{k,3} - b_{k,3}}{\sigma_{k,3}}\right) = P_{HMI\_vert}\left(1 - \frac{P_{sat,not\_monitored} + P_{const,not\_monitored}}{P_{HMI\_vert} + P_{HMI\_hor}}\right) \quad (2.57)$$

$$2Q\left(\frac{HPL_q - b_{0,q}}{\sigma_{0,q}}\right) + \sum_{k=1}^{N_{hyp}} P_{fault,k} Q\left(\frac{HPL_q - T_{k,q} - b_{k,q}}{\sigma_{k,q}}\right) = \frac{1}{2} P_{HMI\_hor}\left(1 - \frac{P_{sat,not\_monitored} + P_{const,not\_monitored}}{P_{HMI\_vert} + P_{HMI\_hor}}\right) \quad (2.58)$$

with q = 1 and 2 for HPL_q. The final HPL is given by:

$$HPL = \sqrt{HPL_1^2 + HPL_2^2} \quad (2.59)$$

- P_{HMI}: total integrity budget from the requirements, shared between the HPL and VPL.
- $P_{sat/const,not\_monitored}$: removes from the PHMI budget the probability of the unmonitored fault modes.
- $P_{fault,k}$: prior probability of fault in subset k per approach

Eqs. (2.57) and (2.58) cannot be solved to directly compute VPL and HPL, an iterative process is required (see the paper by Blanch et al. (2012) for further details)

- *Accuracy, Fault-free position error bound and effective monitor threshold.* Finally, the other two parameters are computed: the accuracy and the Effective Monitoring Threshold.

$$\sigma_{v,acc} = \sqrt{e_3^T S_0 C_{acc} S_0^T e_3} \quad (2.60)$$

$$\text{EMT} = \max_k (T_{k,3}) \quad (261)$$

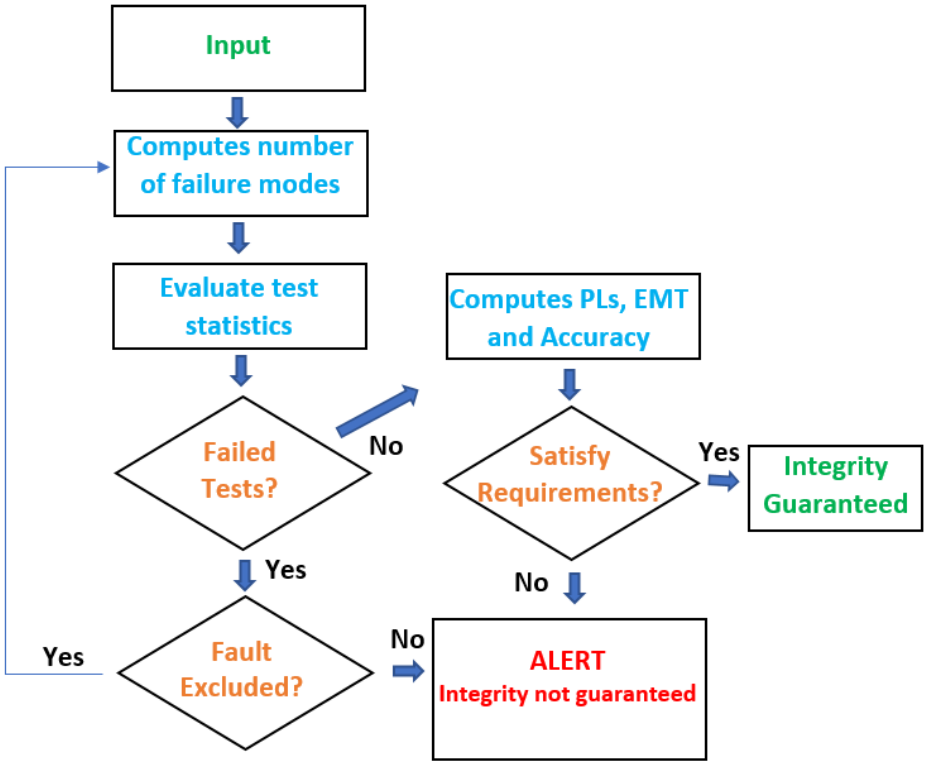

Figure 2-10 Summary of the ARAIM algorithm.

2.5. Performance Based Navigation and Localizer Performance with Vertical Guidance-200

Before the 1990's, conventional routes were defined and based on specific and certified ground navigation aids, using large protection areas and separation criteria between aeroplanes due to the limited accuracy of those systems, such as VOR/DME, NDB and ILS. Aircrafts were forced to fly over the waypoints in the proximity of which

the ground aids were located (Figure 2-11). The main drawback of this process was that it wasn't easy to upgrade the systems or to introduce new type of technologies, limiting the flexibility and the possibility of implementing new design and concepts that soon lead to a saturation of the air traffic.

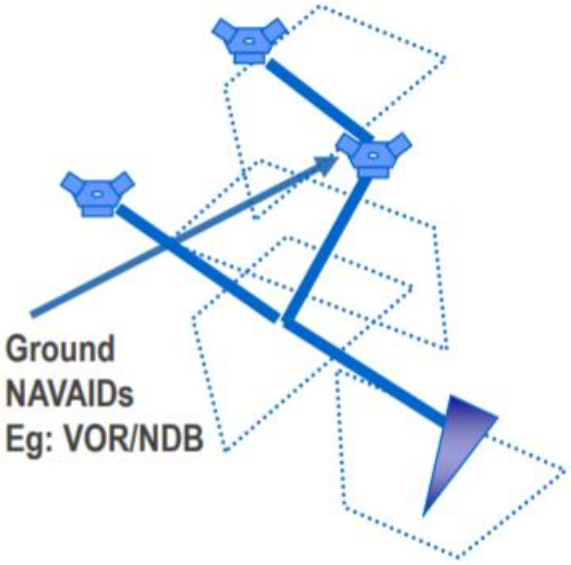

Figure 2-11 Conventional Routes Using Ground Aids (Airbus, 2015).

With the introduction of GPS for civil use, its performances immediately demonstrated the potentiality of the system in the aviation field, however, its design did not allow for a direct integration into the Instrument Flight Rules (IFR).

In the 1990's, The International Civil Aviation Organization (ICAO) recognised that the impediments generated by the regulations inhibited the industry to enhance the aircraft capabilities and the advancement of the civil aviation, for this reason, it examined and established a new standard of navigation, the Performance Based Navigation (PBN).

The main difference between the conventional routes and PBN is that the latter are focused on the level of performance required rather than a specific equipment. This was a tremendous innovation that completely transformed the concept behind the

design of the processes and procedure for the airspace, using the performances rather than the system as driving feature.

As presented in the previous sections, PBN requirements relate to the four parameters (accuracy, integrity, continuity and availability), but they take also into account the capability of the operators, the flight crew knowledge and the global safety performance of the system.

The main advantage of PBN is the flexibility in the design of routes, arrival and departure procedures, allowing tighter separations and protection areas, giving the possibility of making more direct routes and the capability to airports of managing the continuous increase in traffic.

The second main advantage is that new navigation technologies can be more easily implemented, since the procedure requirements are based on the performances of the overall system and not on the system itself.

The PBN procedures are divided in two categories, distinguished by the capability of the system of providing or not on-board performance monitoring and alerting:

- Area Navigation (RNAV), defined by ICAO as “a method of navigation which permits aircraft operation on any desired flight path within the coverage of ground-based or space-based navigation aids or within the limits of the capability of self-contained aids, or a combination of these” (Figure 2-12 Area Navigation Procedure). The introduction of “space-based navigation aids”, such as GNSS, allows defining waypoints using coordinates (latitude and longitude) of a generic point that is not correlated to a ground navaid.

  RNAV procedures are usually associated to a number that represents the lateral accuracy of the system that has to be achieved 95% of the time during

the flight (e.g. RNAV 10 used for En-Route phases requires a lateral accuracy of ±10 nm).

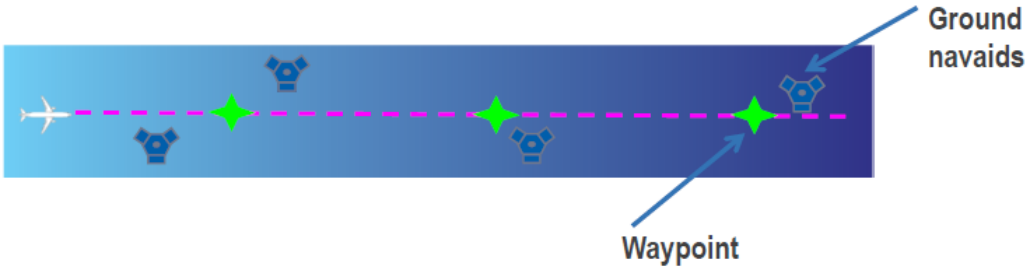

Figure 2-12 Area Navigation Procedure (Airbus, 2015).

- Required Navigation Performance (RNP), defined by ICAO as "navigation specification based on area navigation that includes the requirement for performance monitoring and alerting". As for the RNAV procedures, RNPs are associated to a number that defines two limits, the accuracy and the containment (the latter is two times the accuracy limit and it needs to be achieved 99.999% of the flight time, e.g. RNP 4 used for En-route phases requires a lateral accuracy of ±4 nm and a containment limit of ±8 nm, Figure 2-13)

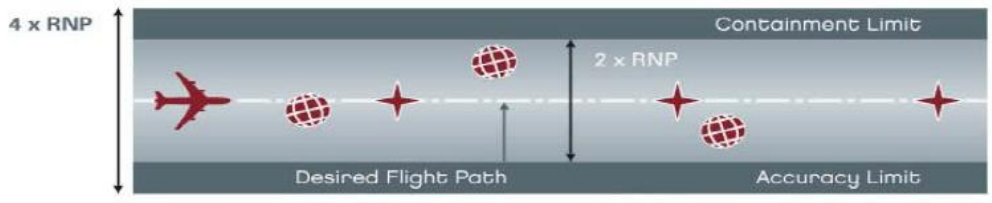

Figure 2-13 Accuracy and Containment limits for a RNP procedure (Airbus, 2015).

Figure 2-14 summarises and provides some examples of the PNB procedures categorization and Figure 2-15 shows the operational difference between RNAV,

in which the use of geographical waypoints represented an enhancement compared to the conventional navigation shown in Figure 2-11 Conventional Routes Using Ground Aids, giving more flexibility and reducing the required airspace, and RNP procedures that include an on-board performance monitoring and alerting system, optimise the use of the airspace through the containment of the flight path within a “tunnel” and introduce curved paths in the design.

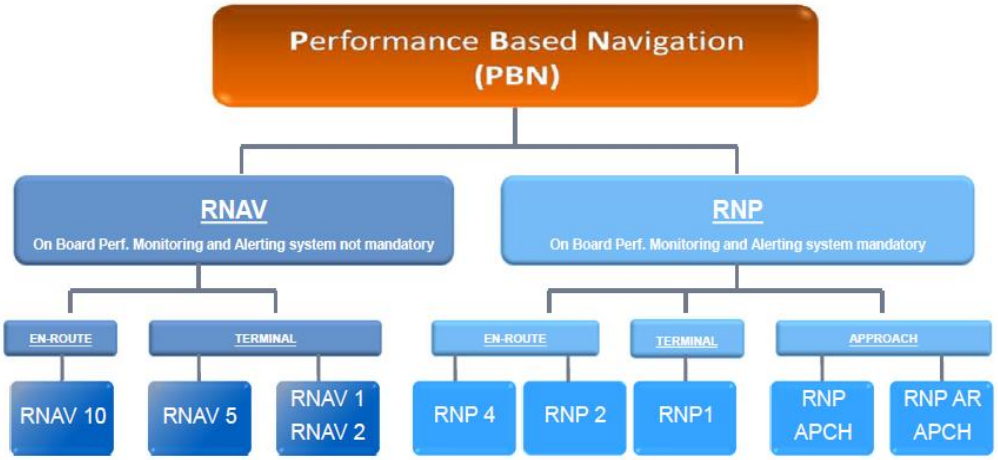

Figure 2-14 Graphical overview of PNB categorization (Airbus, 2015).

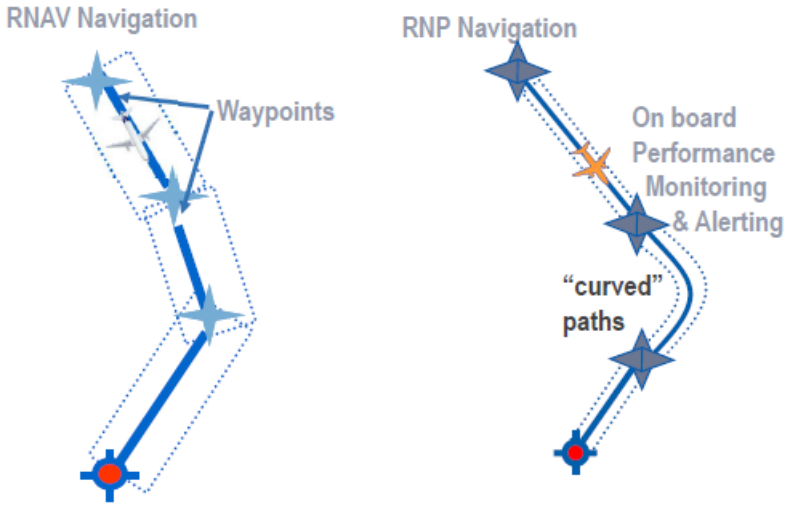

Figure 2-15 Operational difference between RNAV and RNP (Airbus, 2015).

The institution of PBN procedures lead to an optimization of the 3D trajectories that brought many benefits:

- Increased Airspace Capacity and safety, that lead to an improvement in the sequencing (arrival time more predictable), an easier management of the crossing of different flight paths and so less effort for Air Traffic Controllers (ATC) in deconflicting them (Figure 2-16).
- Increase in airport access; better sequencing and predictability of the flights allow an increase of the traffic.
- Efficiency and Environmental impact; the flexibility and higher accuracy of PBN procedures support the design of more direct routes and the implementation of Continuous Descent Operations (CDO) that reduce the flown distances (Figure 2-17), the fuel burn (CDO saves around 200kg of fuel compared to conventional arrival trajectories, Figure 2-18) and therefore reducing the environmental impact in terms of CO2 emissions and noise pollution.

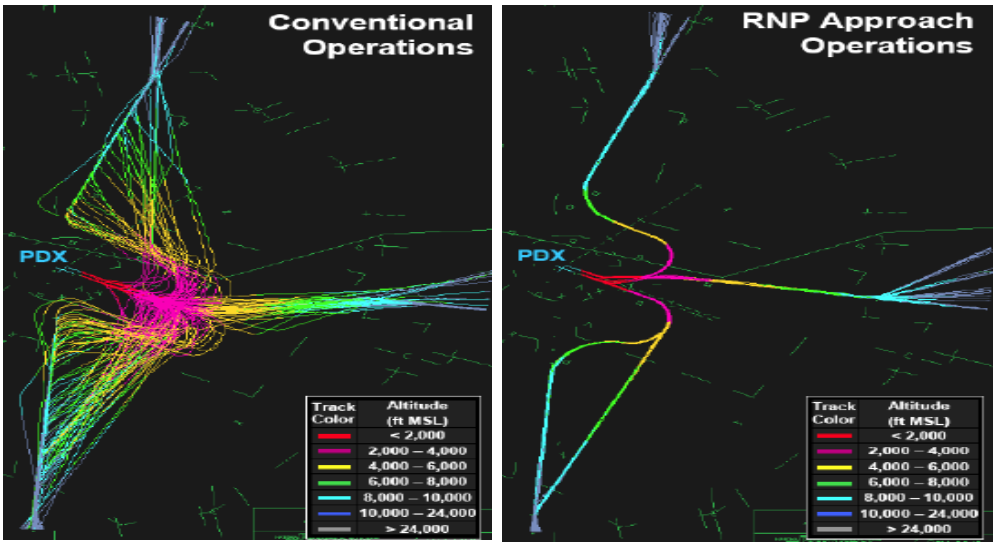

Figure 2-16 Difference in Arrival Routes between Conventional and RNP Operations (Airbus, 2015).

Figure 2-17 Example of Reduction of Flown Distance between Conventional (orange) and RNP (yellow) operations (Airbus, 2015).

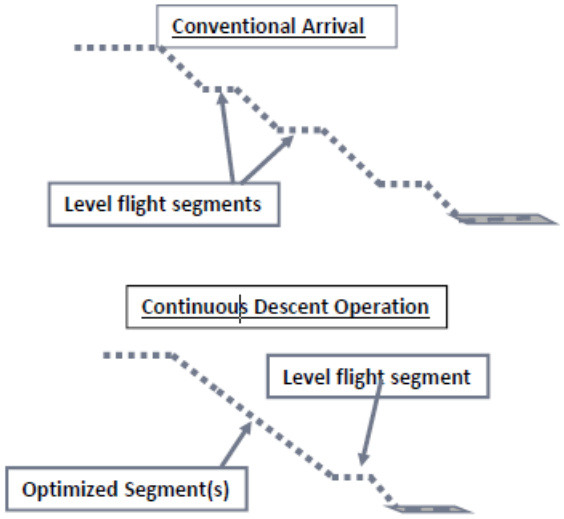

Figure 2-18 Difference Between Conventional Arrival Descent Profile (top) and Continuous Descent Operation (bottom) (Airbus, 2015).

For each category (RNAV and RNP), the Navigation Specification defines the set of requirements that aircrafts and crew members need to satisfy in order to support PNB operations:

- Performances (accuracy, integrity, continuity and availability) that the system is required to satisfy in order to perform a specific procedure.
- Functionalities that the system is required to have in order to achieve the predefined performances
- Navigation Sensors that the system is required to have installed
- Requirements required to the aircrew to achieve the performances.

2.5.1. Approach Procedure and Localizer Performance with Vertical Guidance (LPV) Review

As described in the previous sections, RNP are specified for each phase of the flight and, between all of them, the approach phase is the most demanding and important in terms of integrity requirements.

Figure 2-19 shows some examples of the requirements for the different types of approaches, such as the Minimum Descent Altitudes (MDA, a specified altitude below which the approach must be discontinued without the required visual reference) and the Alert Limit (AL). Current regulations allow GPS to only support Lateral Navigation (LNAV) approaches, while for other types it is necessary the support of other navigation aids.

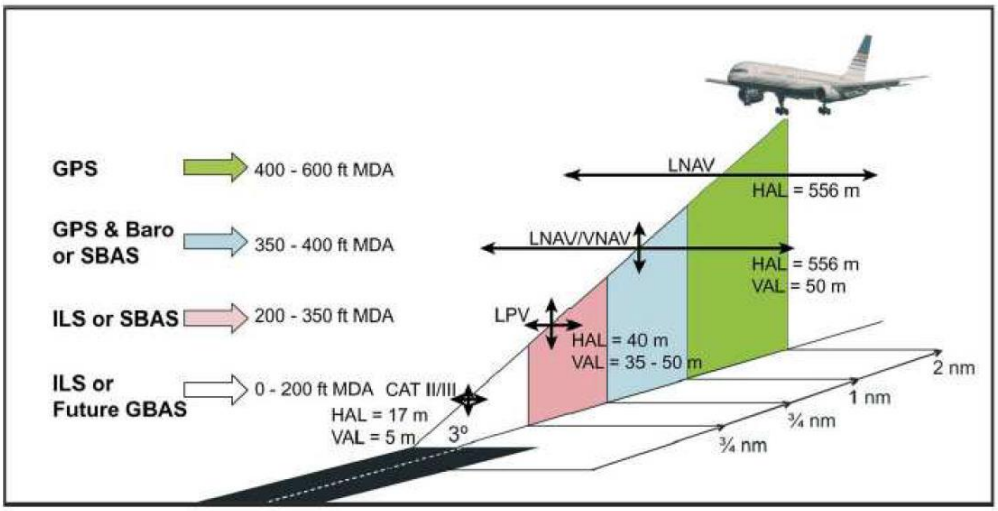

Figure 2-19 Summary of types of approach procedures and related Minimum Descent Altitudes and Alert Level (Walter et al., 2008).

The introduction of ARAIM could allow the use of GNSS for the more demanding approach and additionally the use of Optimized Profile Descent (OPD), also known as Continuous Descent Approach (CDA), instead of the conventional stair-step approach, that requires a higher workload to the pilots and ATM. Two different types of CDAs are currently utilized, standard (3° descent angle) and steep (>4.5° descent angle), implemented in few airports worldwide. They possess two main advantages compared to conventional approaches:

- minimize noise pollution

- reduce fuel consumption.

Within the SESAR project, approach procedures with new features (e.g. steeper glide slopes) have been designed and tested with the main objective of implementing in the future more efficient trajectories that reduce noise impact and fuel consumption without impacting airports traffic. As an example, Heathrow airport tested for six months steep approaches using RNAV GNSS

procedures without being fitted with a GBAS system and finding a significant reduction of noise pollution in the surrounding areas (SESAR, 2016).

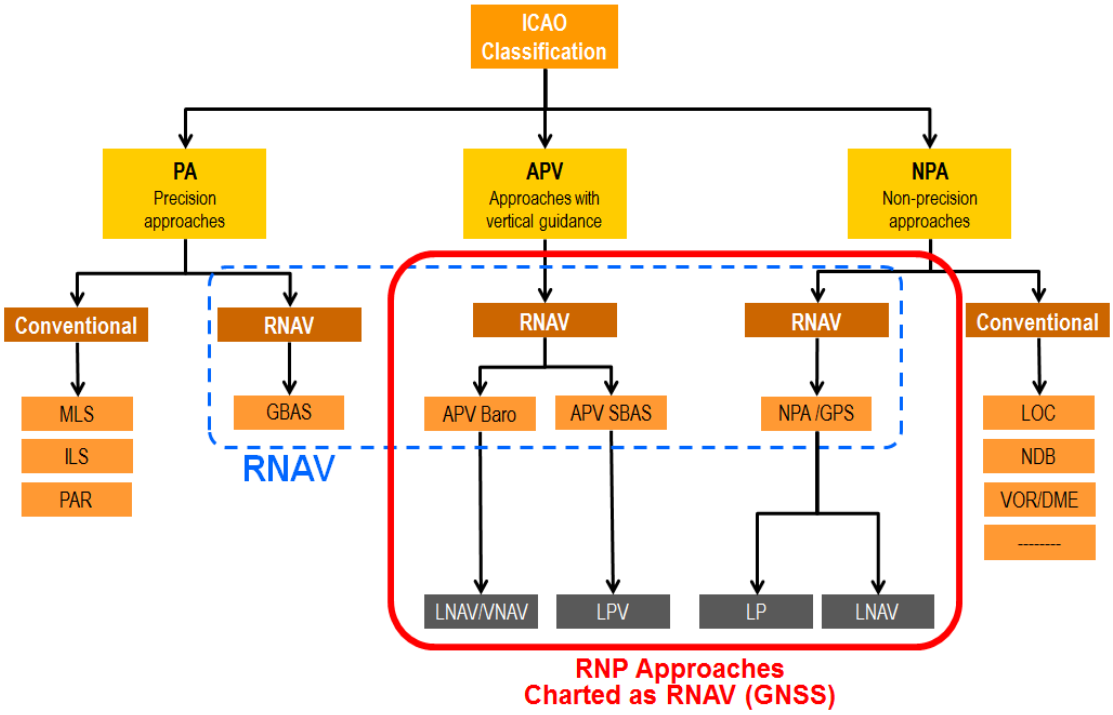

Figure 2-20 Approach Procedure Categories (Unknown, 2015).

Figure 2-20 shows the ICAO classification of the Approach procedures, divided in three main categories: Non-Precision Approach (NPA), Approaches with Vertical Guidance (APV) and Precision Approach (PA).

- **Non-Precision Approach (NPA)** only supports lateral navigation but not vertical guidance, giving information on the aircraft lateral deviation (left or right) with respect to the runway direction; it includes conventional procedures that utilise ground equipment like Localizer (LOC), Non-Directional Beacon (NDB), VHF Omni Directional Range (VOR), Distance Measuring Equipment (DME) to bring the aircraft to a point where the pilot can see the runway and perform a visual landing, but it also includes GNSS-

based RNAV approaches like Localizer Performance (LP) and Lateral Navigation (LNAV). The navigation systems provide

- **Approach with Vertical Guidance (APV)** supports both lateral and vertical guidance, however without satisfying the more stringent requirements defined for the last category, Precision Approach. For this category, vertical guidance is enabled by barometric altimeter (LNAV/VNAV) and GNSS-based systems (e.g. SBAS for LPV), guiding the aircraft along a predefined glidepath.
- **Precision Approach (PA)**, as for APV, supports both lateral and vertical guidance enabled by ground landing systems like Instrument Landing System (ILS), Precision Approach Radar (PAR), Microwave Landing System (MLS) and GBAS. Precision approaches are in turn divided in categories and defined by the Decision Altitude/Height and the Runway Visual Range (RVR):

Table 2-7 Precision Approach Categories.

PA category	DA/H	RVR (minimum)	Visibility
CAT I	60m (200ft)	550m	800m
CAT II	60 m< DA/H < 30m	350m	
CAT IIIA	DA/H < 30m or No DA/H	200m	
CAT IIIB	DA/H >15m or No DA/H	200m < RVR < 50m	
CAT IIIC	No DA/H	No limitation	

The different approaches are enabled by the implemented systems and infrastructures that can be different for each airport, depending on their capabilities and strategy, due to the fact that each system requires continuous or periodic

maintenance and calibration that might be too expensive for airports with limited traffic. Localizer performance with vertical guidance (LPV) is currently the most precise GNSS-based RNP procedures implemented, but only through the support of SBAS. This category of approach has similar requirements as CAT I instrument landing systems (ILS), such as a decision height of 200ft (equivalent to around 60m) and a minimum visibility of 800m.

As presented in the previous chapters, ARAIM aims to become an Approved Navigation System down to LPV-200 approach (Localizer Performance with Vertical Guidance, decision height of 200 feet and visibility of ½ mile). The first LPV-200 approaches have already been implemented in airports around the world with the support of SBAS (e.g. USA and Europe) bringing numerous benefits that could be further enhanced with the implementation of ARAIM:

- Reduced support from other ground systems (e.g. ILS) and reduced delays due to their malfunctioning or maintenance.
- Optimised trajectory, lower fuel consumption and reduced environmental impact
- Increased availability and capability of airports

enabling a further reduction of the ground systems effort and costs. For these reasons, this research analysed the integrity performances of ARAIM implemented to LPV-200 procedures, for which the requirements are summarised in Table 2-8.

Table 2-8 Integrity Requirements for LPV-200 Approach Procedures.

	HAL	VAL	Accuracy (vertical component)	EMT
Alert Level [m]	40	35	1.87	15

3. ARAIM PREDICTION TOOL

3.1. INTRODUCTION

As mentioned in the first chapter, one of the main objectives of the research is to investigate critical aspects to safe aircraft operations in GNSS restricted access situations, to analyse the possible use ARAIM as a safe and reliable method of autonomous integrity augmentation system and integrate it in systems and processes (e.g. into the flight management system (FMS)).

ARAIM is the technology that the GNSS community is aiming to develop and make operational by the end of this decade putting a lot of effort into it, demonstrated by the conspicuous number of papers and performed researches presented in the literature review in the previous chapter. These analyses show the interest of the scientific community but also of national and international organisation (such as FAA, CAA, Eurocontrol, ESA, EU and many other), in the development, finalisation and implementation of this new technique in Civil Aviation. Today, RAIM is an approved Navigation System only for Lateral Navigation (LNAV) in En-route, Terminal and Non-precision approach flight phases and its performance predictions are mandatory if GPS is used to solely satisfy RNAV requirements (FAA, 2007a). The main disadvantages of this technique are that at the current stage it implements only one constellation (GPS), uses a single frequency configuration and can detect only one fault at a time, limiting the performance. The new technique aims to become an Approved Navigation System down to LPV-200 approach (Localizer Performance with

Vertical Guidance, decision height of 200 feet and visibility of ½ mile) in order to reduce the ground systems effort; its strengths are the use of multiple constellations, dual frequency and multiple fault detection capability. For these reasons, ARAIM has been selected as topic of this research; the technique has reached a good level of maturity and the analyses and studies have demonstrated its capabilities, advantages and strengths but also some weaknesses that need to addressed and analysed; one of the aims and main objectives of this research is to develop a system that satisfies the future needs for the Civil Aviation. The final objective of the first phase of this research was to evaluate the influence of the attitude of the aircraft on the ARAIM performances, since previous ARAIM performance analyses were performed on selected points on the Earth surface, with full view of the sky (no obstacles that can shadow satellites).

This chapter describes in detail the ARAIM algorithm, how it works, the inputs and outputs (the integrity parameters defined by the protection levels) and the new tool developed and used in this research, the ARAIM Performance on Predicted Aircraft Trajectory Tool (APPATT). In this chapter, the functions used and integrated in the algorithm are presented, starting from the original MAAST, the MATLAB ARAIM Availability Simulation Tool (MAAST) a tool developed by Stanford University that is the basis of the APPATT, to the new functions and models that evaluate the shadowing effect of the aircraft attitude and terrain, highlighting how these functions have been modelled and implemented.

3.2. COORDINATES FRAMES AND ROTATIONS

3.2.1. COORDINATE TRANSFORMATION AND ROTATION MATRICES

The computation of the integrity performance within the aircraft Navigation systems requires the knowledge of absolute and relative position and velocity (state vector) of different elements, such as the GNSS satellites and the aircraft itself, additionally involves the use of several reference frames and the related coordinate transformation. GNSS receivers first estimate the position and velocity of the satellites in the orbital perifocal frame based on the orbital parameters provided by the YUMA almanacs (they will be described in the next sections). The state vector is then transformed to a conventional geographic coordinate system, the Earth-Centered-Earth-Fixed (ECEF) reference. This system rotates with the Earth body, allowing an easy conversion to Cartesian coordinates of geographical points expressed in term of latitude, longitude and altitude. Having both satellites and locations coordinates expressed in a common Cartesian system allows a straightforward computation of the lines of sight (LoS) between each location with all the satellites of the constellations, in particular, the unit vector of each line of sight is computed. However, the LoS unit vectors expressed in ECEF do not allow to evaluate which satellite is above the local horizon of the user's location and so in view in the GNSS receiver reference frame, they need to be transformed to an appropriate ground or local reference frame, also referred as Local Vertical Local Horizon. Two examples of these coordinate systems are the East- North-Up (ENU), used to describe measurements/observations relative to a control frame located on the ground, such

as control towers, and the North-East-Down (NED), used to describe measurements/observations from the aircraft intrinsic axes. The original ARAIM algorithm transforms the LoS unit vectors from the ECEF to ENU frame, evaluates their elevation angles and discard the satellites with negative values (below the local horizon). In this research, two more transformations have been introduced:

- From ENU to NED frame
- From NED to Body reference frame

The latter transformation allows evaluating the shadowing effect of the aircraft attitude. In the following sections, a quick description of the different reference frames and the mathematical formulas for the transformation are provided.

A. Reference Frames

- *Perifocal reference frame*

  A non-inertial frame used to define a coordinate system within an orbit. The origin of the system is the focus of the orbit in which the celestial body is located, the xy plane coincides with the orbital plane, with the x-axis pointing towards to the periapsis, the z perpendicular to the orbital plane in the direction of the satellite's angular momentum and the y-axis completing the right-hand set of co-ordinate axis (Figure 3-1)

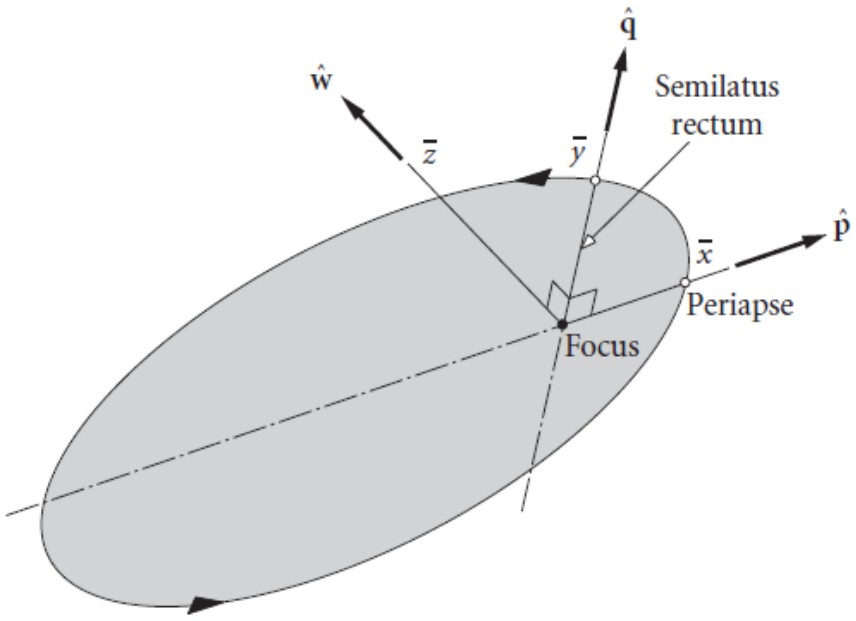

Figure 3-1 Perifocal reference frame of an orbit (adcsforbeginners, 2015).

- *Earth-Centered-Earth-Fixed reference frame*

A non-inertial reference frame fixed to the Earth body and rotating with it. The origin of the system is the center of the Earth and the equatorial plane corresponds to the XY plane with the X axis directed toward the intersection between the equatorial plane and the reference Meridian (0° Greenwich Meridian), the Z-axis passing through the international reference pole (True North or the instantaneous Earth rotation axis) and the Y completing the right-handed set of coordinate systems (Figure 3-2)

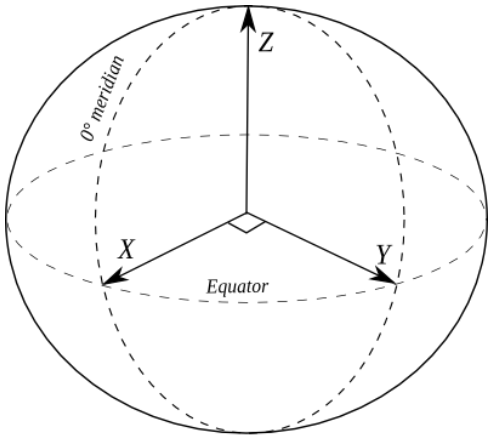

Figure 3-2 Earth-Centered-Earth-Fixed Reference Frame (ECEF) (Airdata, 2017).

- *East-North-Up (ENU) reference frame*

This non-inertial reference frame is location dependent, the origin is centred in the location itself (defined by the geographical coordinates latitude φ and longitude λ), the xy plane is the tangent plane to the geoid at the location point, with the x-axis pointing East (along the local Parallel), the y-axis pointing North (along the local Meridian) and the z-axis perpendicular to the xy plane pointing upwards (Figure 3-3)

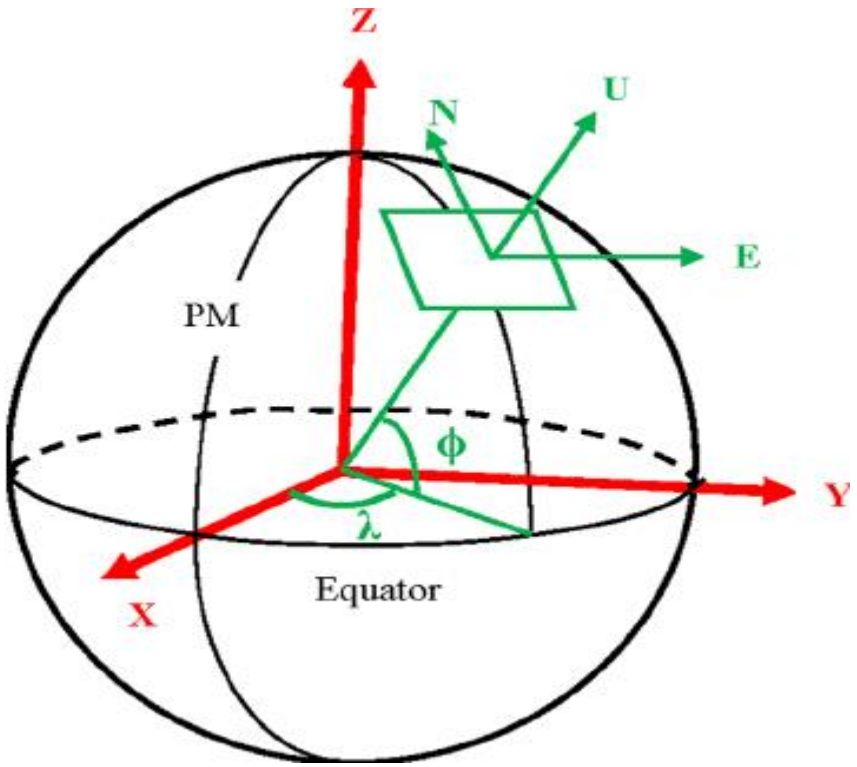

Figure 3-3 Example of East-North-Up (ENU) Reference Frame for a generic location (λ, φ) (Wang, 2013).

- *North-East-Down (NED) reference frame*

Another non-inertial reference system that is location dependent, usually used in Aerospace applications as a reference system to describe the aircraft attitude. The origin is centred with the centre of mass of the aircraft with the xy plane being tangent to the equipotential surface to the geoid. The x-axis points North (parallel to the local Meridian), the y points Eastward (along the local Parallel) and the z-axis is perpendicular to the xy plane pointing downwards (Figure 3-3)

- *Aircraft Body reference frame*

A non-inertial reference frame fixed to the aircraft body. The origin is centred in the aircraft centre of mass., the x-axis is directed along the aircraft longitudinal axis towards its nose, the z-axis is along the aircraft vertical axis towards the

upward direction and the y-axis along the aircraft lateral axis completing the right-handed set of coordinate systems (Figure 3-4). The rotations around the body axes also define the attitude angles roll, pitch and yaw, respectively to the x, y and z axes.

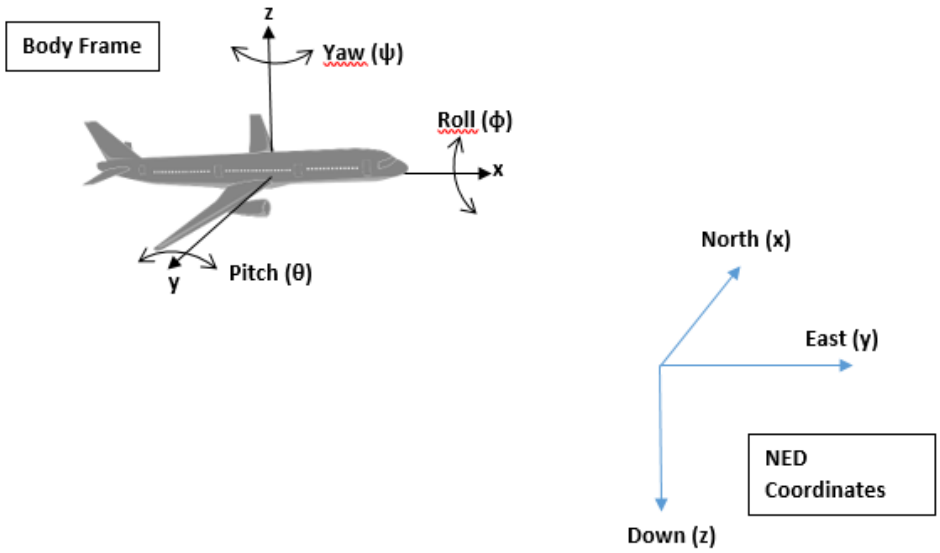

Figure 3-4 NED and Body Reference Frames.

B. Cartesian Representation of Vector

Cartesian representation of a vector can be found in texts by Curtis (2013) and Colasurdo (2010). A vector can be represented in different Cartesian frames. Given two coordinate frames *a* [X,Y,Z] and *b* [x,y,z] oriented differently in space, with orthogonal unit vectors a_X , a_Y , a_Z and b_x , b_y , b_z (a_1 , a_2 , a_3 and b_1 , b_2 , b_3 in a generic coordinate system), a vector $\vec{v}$ can be represented with respect to any of the systems a and b.

This is written as:

$$v = \sum_{i=1}^{3} v_{a,i}\hat{a}_i \qquad \text{and} \qquad v = \sum_{i=1}^{3} v_{b,i}\hat{b}_i \tag{3.1}$$

where:

$$v_{a,i} = v \cdot \hat{a}_i \quad \text{and} \quad v_{b,i} = v \cdot \hat{b}_i \tag{3.2}$$

are the coordinates of $\overset{\nu}{v}$ in a and b respectively. The relation between the two vectors v_a and v_b in frames a and b is given by the following calculation:

$$v_{a,i} = v \cdot \hat{a}_i = \left(v_{b,1}\hat{b}_1 + v_{b,2}\hat{b}_2 + v_{b,3}\hat{b}_3\right) = \sum_{j=1}^{3} v_{a,j}\left(\hat{a}_i \cdot \hat{b}_j\right) \tag{3.3}$$

The coordinate transformation from b to a is given by:

$$v_a = A_{ab} v_b \tag{3.4}$$

where:

$$A_{ab} = \left\{\hat{a}_i \cdot \hat{b}_j\right\} \tag{3.5}$$

is the rotation matrix from a to b. The elements of the rotation matrix are called the direction cosines.

C. Properties of the rotation matrix

In this section, a few properties of the rotation matrix will be listed. For more details on these properties refer to the paper by Egeland and Gravdahl (2002).

The rotation/transformation matrix from b to a can be found in the same way as from a to b by interchanging a and b in the expressions which gives:

$$A_{ba} = \left\{\hat{b}_j \cdot \hat{a}_i\right\} \tag{3.6}$$

The rotation matrix is orthogonal and satisfies:

$$A_{ba} = (A_{ab})^{-1} = (A_{ab})^T \tag{3.7}$$

D. Euler Angles

The orientation between a rigid body [x,y,z] and a fixed reference frame [X,Y,Z] can be represented as the composition of three consecutive elemental rotations, the order of which is important, about the axes of one of the two reference frames.

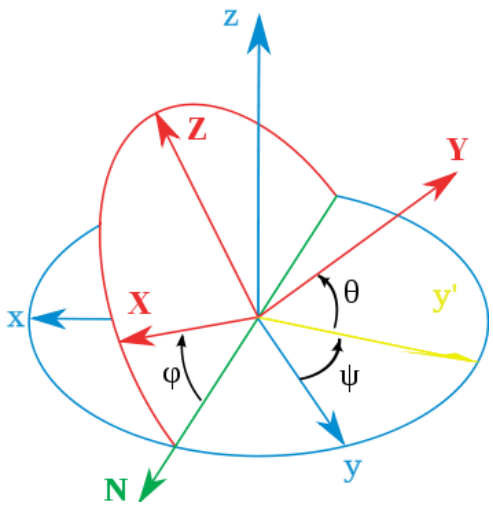

Figure 3-5 Representation of Euler Angles between two Reference Frames (X,Y,Z) and (x,y,z) (Brits, 2008).

The angles that define the rotations are called Euler Angles and their combination generates in total 12 sets that can be divided in 2 different categories:

- Proper or Classic Euler Angles, that use only two axes (symmetric: 3-1-3, 1-2-1, 2-3-2, 1-3-1, 3-2-3, 2-1-2)
- Tait-Bryan Angles, that uses all the three axes (1-2-3, 2-3-1, 3-1-2, 1-3-2, 3-2-1, 2-1-3)

The latter category is normally used in the Aerospace field, as for the Heading-elevation-bank angles (Figure 3-6) and the yaw-pitch-roll angles (Figure 3-7), both usually denoted as (φ, θ, ψ). They are used to represent the position and orientation of aircrafts (and satellite as well) with respect to ground positions in a local or terrestrial reference frame, such as the North-East-Down (NED) and the East-North-Up (ENU), presented in the previous section.

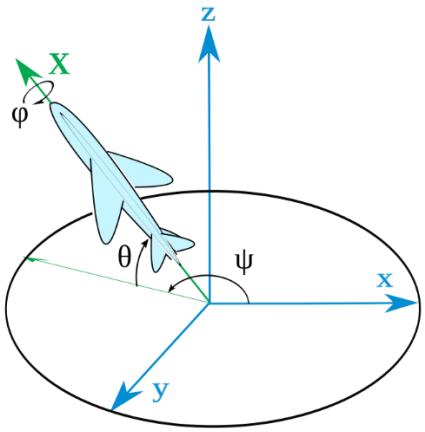

Figure 3-6 Heading-elevation-bank angles (Sempere, 2009).

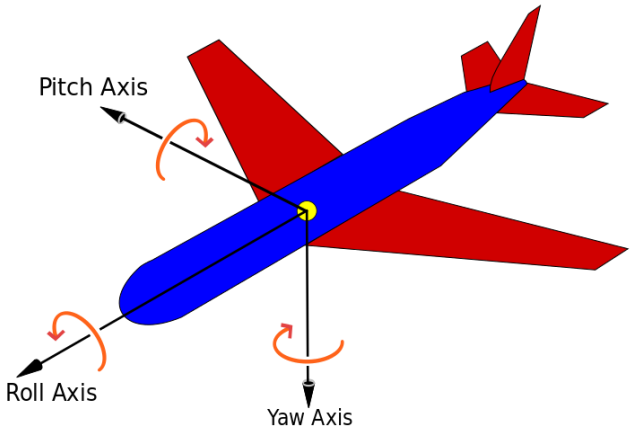

Figure 3-7 yaw-pitch-roll angles (Auawise, 2010).

The rotations can also be divided in extrinsic and intrinsic, based on which of the two reference frames rotates respect to the other ([x,y,z] respect to [X,Y,Z] or vice versa).

E. Elemental Rotations

Elemental rotations, which are rotation around a fixed axis, using Tait-Bryan Angles as parameters, are defined in the following way:

$$A_x(\phi)=\begin{pmatrix}1 & 0 & 0\\ 0 & \cos\phi & -\sin\phi\\ 0 & \sin\phi & \cos\phi\end{pmatrix}$$

$$A_y(\theta)=\begin{pmatrix}\cos\theta & 0 & \sin\theta\\ 0 & 1 & 0\\ -\sin\theta & 0 & \cos\theta\end{pmatrix} \quad (3.8)$$

$$A_z(\psi)=\begin{pmatrix}\cos\psi & -\sin\psi & 0\\ \sin\psi & \cos\psi & 0\\ 0 & 0 & 1\end{pmatrix}$$

where x, y and z are the axes' which the angles ϕ, θ and ψ revolves around.

As mentioned in the previous section, there are twelve possible sets of Euler angles, six symmetric and six asymmetric sets.

In each label, the first (leftmost) integer denotes the first rotation axis.

For example, the rotation matrix given by the set 3-2-1 is given by:

$$A_{3-2-1}=A_z(\psi)A_y(\theta)A_x(\phi)=\begin{pmatrix}c\psi\, c\theta & c\psi\, s\phi\, s\theta-c\phi\, s\psi & s\phi\, s\psi+c\phi\, c\psi\, s\theta\\ c\theta\, s\psi & c\phi\, c\psi+s\phi\, s\psi\, s\theta & c\phi\, s\psi\, s\theta-c\psi\, s\phi\\ -s\theta & c\theta\, s\phi & c\phi\, c\theta\end{pmatrix} \quad (3.9)$$

For additional information on Euler Angles and element rotations, the reader can refer to the texts by Curtis (2013) and Colasurdo (2010).

3.3. THE MATLAB ALGORITHM AVAILABILITY SIMULATION TOOL (MAAST)

MAAST is a set of MATLAB functions developed by the University of Stanford for SBAS, RAIM and ARAIM availability analysis that is intended for use as a fast, accurate and highly customizable experimental testbed for algorithm development. The tool is open source and the original version and its related guides can be

downloaded from the University of Stanford website (Standford, 2014). The University of Stanford has also developed the ARAIM algorithm used in MAAST and it is based on the published paper by Blanch et al. (2012).

The MAAST has the main objective of computing the four parameter indices of the reliability of the navigation solution provided by GNSS; these parameters are:

- The Horizontal Protection Level (HPL),
- The Vertical Protection Level (VPL),
- The Accuracy
- The Effective Monitoring Threshold (EMT).

The tool takes as input:

- A 2D map of the area of interest and density of the points on it to be analysed
- The YUMA Almanac files. These contain the orbital parameters for each satellite of the constellation (GPS/Galileo/GLONASS). GPS YUMA almanacs are downloaded from the CelesTrak website (Kelso, 2015), which in turn are obtained from the US Coast Guard Navigation Center (NavCen, 1997). Galileo and GLONASS YUMA almanacs are provided with the MAAST and are based on the nominal constellation orbits.
- The Required Navigation Performance (RNP). In order to use GNSS as the primary source for navigation in aviation, stringent requirements have to be met, the so-called Required Navigation Performance (RNP) for civil aviation, a concept endorsed by the ICAO (1999) and (2000). RNP are specified for the different flight phases in terms of the four parameters: accuracy, integrity, continuity of service and availability.

Table 3-1 Required Navigation Performance (ICAO, 2000).

<table>
<tr><th rowspan="3">Operation</th><th colspan="2">Accuracy</th><th colspan="2">Integrity</th><th rowspan="2"></th></tr>
<tr><th colspan="2">95% (2 σ)</th><th colspan="2">Alert Limit (4-5σ)</th><th rowspan="2">TTA</th></tr>
<tr><th>Vertical</th><th>Horizontal</th><th>Vertical</th><th>Horizontal</th></tr>
<tr><td>Oceanic</td><td rowspan="3">N/A</td><td>3.7 km or more</td><td rowspan="3">N/A</td><td>7.4 km or more</td><td>1-5 min</td></tr>
<tr><td>En-route</td><td rowspan="2">0.22-0.74 km</td><td rowspan="2">1.85-3.7 km</td><td rowspan="2">10-15 s</td></tr>
<tr><td>Terminal</td></tr>
<tr><td>NPA</td><td>20 m</td><td>220 m</td><td rowspan="2">50 m</td><td>556 m</td><td rowspan="3">10 s</td></tr>
<tr><td>LNAV/VNAV</td><td rowspan="3">16 m</td><td rowspan="4">40 m</td></tr>
<tr><td>LPV</td><td>35 m</td></tr>
<tr><td>APV I</td><td>8 m</td><td>20 m</td><td rowspan="3">6 s</td></tr>
<tr><td>APV II</td><td rowspan="2">4 m</td><td>35 m</td></tr>
<tr><td>LPV-200</td><td>10 m</td></tr>
<tr><td>CAT I</td><td rowspan="2">< 2.0 m</td><td rowspan="2">< 6.9 m</td><td rowspan="2">5.3 m</td><td rowspan="2"><15.5 m</td><td rowspan="2">< 2 s</td></tr>
<tr><td>CAT II</td></tr>
<tr><td>CAT III</td></tr>
</table>

Operation	Max Probabilities of Failure		Availability
	Integrity (1-risk)	Continuity (1-risk)	
Oceanic, En-route	10^{-7}/hr	10^{-4}/hr	10^{-2} to 10^{-5}
Terminal, NPA			
LNAV/VNAV	1.2×10^{-7}/ 150 s	4.8×10^{-6}/ 15 s	
LPV			
APV I			
APV II			
LPV-200			
CAT I			
CAT II	< 10^{-9}/ 150 s	< 4×10^{-6}/ 15 s	
CAT III			

- Signal errors and biases characterisation. They can be specified for each satellite of the different constellation and expressed in terms of:

- User Range Error (URE) and Signal-in-Space-Error for Galileo (SISE).
- User-Range-Accuracy (URA) and Signal-in-space-accuracy, for Galileo (SISA).
- Two levels of bias magnitudes for the range measurements: one is the magnitude of a bias in a nominal condition (b_{nom}), used for the evaluation of accuracy and continuity, the other is the maximum bias magnitude used or the evaluation of integrity (b_{int}).

- Probability of failure for each satellite and constellation (P_{sat} and P_{const}).

3.4. THE ARAIM PERFORMANCE ON PREDICTED AIRCRAFT TRAJECTORY TOOL (APPATT)

For the purpose of this research, MAAST has been selected and modified in order to analyse the ARAIM performance along aircraft trajectories considering the shadowing effect of the aircraft attitude and surrounding environments.

Based on the information provided by the researchers at the Stanford University, the algorithm in which MAAST is based was extensively reviewed by the bilateral EU- US working group that is developing the concept (WG-C). In addition, the tool was cross-checked against three other similar availability simulation tools (not been made publicly available), to make sure that the formulas were correctly implemented, developed by:

- the University of the Federal Armed Forces UFAF (Dr Kropp's thesis project will be available some time later in 2018)
- DLR
- ESA

The newly developed algorithm, named APPATT, has the same objective as MAAST, to compute the four parameters indices of the reliability of the navigation solution provided by GNSS but with three main differences:

- The tool takes two additional inputs with respect to the MAAST, txt files that include the trajectory (position and attitude) and terrain data (latitude, longitude and altitude)

- The tool compares the results of the integrity analysis computed including and not the shadowing effects of the aircraft attitude and surrounding environment, in order to highlight the differences.
- The parameters are predicted for a specific point and time; they are not averaged values, but instantaneous, only valid for that well-defined configuration of the satellites constellations and signal errors and bias characterisation.

The following sections will give a more detailed overview of the modified algorithm, the functions and processes that perform to compute the integrity performances of the selected trajectory.

The overall tool is composed of several functions or sub-functions, each with a specific task, and Figure 3-8 summarises the overall flow chart of the APPATT algorithm.

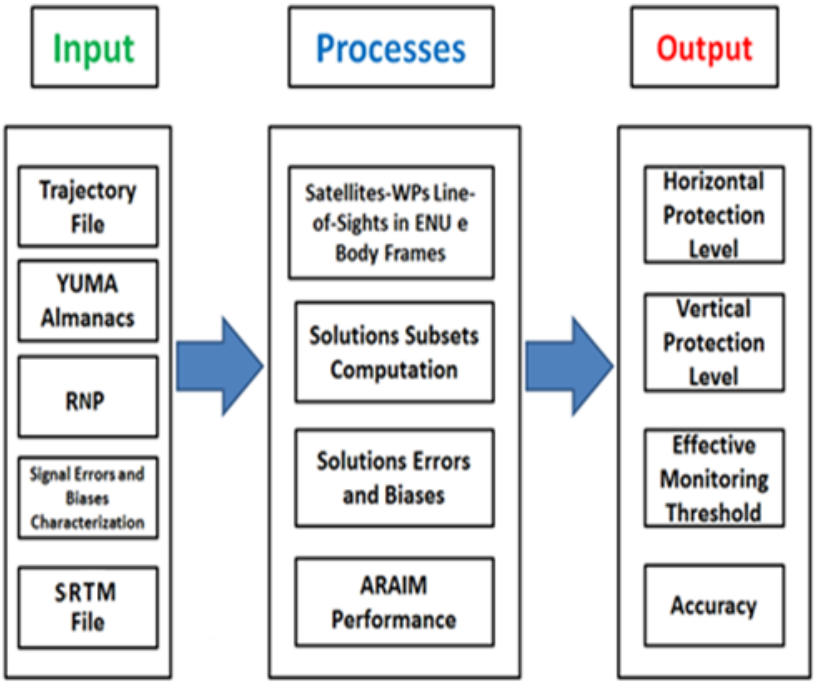

Figure 3-8 APPATT Scheme.

In this chapter, the first part is focused on the different elements and functions of the APPATT and an overview of the processes and algorithms integrated in the tool is provided, while the next chapter presents the selected scenario and related results.

3.4.1. INPUT

There is a primary function that is the main configuration function with which is possible to set up and select the inputs and the parameters needed for the ARAIM performance computation, summarised in Table 3-2 and Table 3-3.

Table 3-2 Standard MAAST input.

Parameter	Definition
URA and BIAS	Standard deviation and bias of the clock and ephemeris error used for the computation of the integrity performance
URE and $Bias_{cont}$	Standard deviation of the clock and ephemeris used for the accuracy and continuity performance
P_{sat} and P_{const}	The a priori probabilities of failure per approach for the single satellite and constellation.
$PHMI_{vert}$ and $PHMI_{hor}$	Integrity budget for the vertical and horizontal components
P_{sat_thres} and P_{const_thres}	Threshold for the integrity risk coming from unmonitored satellite and constellation faults
P_{fa}	Continuity budget allocated to disruptions due to false alert.
P_{fa_vert} and P_{fa_hor}	Continuity budget allocated to the vertical and horizontal mode

PL_{tol}	Tolerance for the computation of the Protection Level
P_{EMT}	Probability used for the calculation of the Effective Monitor Threshold
HPL, VPL, EMT and accuracy	The Thresholds Limits of the four ARAIM parameters for the specific phase of the flight (e.g. LPV-200 approach).
YUMA almanacs	The input file for the constellation (single/dual/tri constellations configuration); the YUMA almanacs are categorized by week; therefore, it is necessary to select the suitable files for the trajectory that will be analysed.

The new tool takes as additional input respect to the standard MAAST:

Table 3-3 Additional APPATT input.

Trajectory	The input file for the trajectory
t_{reset}	Reset time (flight start time respect to the YUMA week time that starts every Sunday at 0:00)
t_{int}:	Interpolation time (the trajectory files usually provide data every 5 seconds, but the data can be further linearly interpolated by using a user-defined time step)
Environment Database	High-resolution topographic data generated from NASA's Space Shuttle Radar Topography Mission (SRTM)

3.4.2. YUMA ALMANACS

The YUMA almanacs contain the elements of each GNSS satellite necessary to propagate the orbit of the satellite, such elements are presented in Table 3-4:

Table 3-4 YUMA Almanacs Element Description (Kelso, 2015).

Element	Description
ID	Unique number (PRN) that defines the satellite (SV)
Health	Flag that sets the usability of the satellite (000=usable)
Eccentricity (e)	Amount by which an orbit deviates from a perfect circle. It is the distance between the foci divided by the length of the semi-major axis.
Time of Applicability [s]	A time tag indicating the number of seconds in the orbit when the almanac was generated.
Orbital Inclination (i) [rad]	Angle between the axis perpendicular to the orbital plane and the Earth rotation axis.
Rate of Right Ascension $(\dot{\Omega})$ **[rad/s]**	Rate of change in the measurement of the angle of right ascension as defined in the Right Ascension mnemonic.
Square Root of Semi-Major Axis $\left(\sqrt{a}\right)$ **[m]**	This is defined as the measurement from the centre of the orbit to either the point of apogee or the point of perigee.
Right Ascension (Ω_0) at Time of Almanac (TOA) [rad]	Right Ascension is an angular measurement on the equatorial plane from the vernal equinox to the point where the spacecraft crosses the fundamental plane while moving in the northerly direction
Argument of Perigee [rad]	An angular measurement along the orbital path measured from the ascending node to the point of perigee, measured in the direction of the SV's motion.

Mean Anomaly [rad]	Angle (arc) travelled past the longitude of ascending node (value = 0±180 degrees).
a_{f0} [s]	SV clock bias in seconds.
a_{f1} [s/s]	SV clock drift in seconds per seconds.
Week	GPS week (0000–1023), every 7 days since 1999 August 22.

The YUMA almanac includes the six classical orbital elements that fully define an orbit (size, shape, direction and orientation) and the position of the satellite on it:

1) Eccentricity (e)
2) Semi-major axis (a)
3) Inclination (i)
4) Longitude of the Ascending Node (Ω)
5) Argument of perigee (ω)
6) True Anomaly (v), substituted by the Mean Anomaly (M) in the almanac

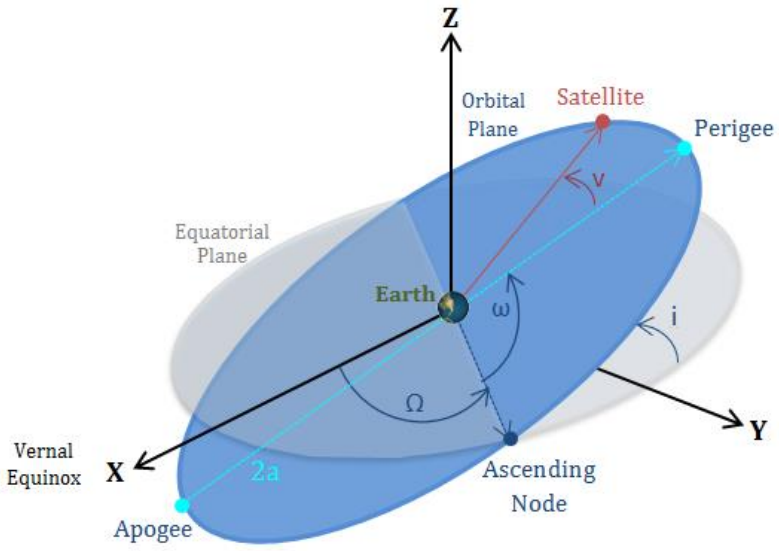

Figure 3-9 Orbital Elements (GSC-EUROPA, 2017).

From the orbital elements, it is possible to compute the satellite state vector (position [X,Y,Z] and velocity [Vx, Vy, Vz]) in the ECEF reference frame applying the algorithm that will be presented in Par. 3.4.5.

3.4.3. AIRCRAFT TRAJECTORY

The aircraft trajectory file is a text file generated by the RNAV Validation Tool (RVT) software developed by the DW International Ltd (now NavBlue); it is a desktop application, developed for EUROCONTROL, to help procedure designers in the ground validation of new or modified Radio Navigation (RNAV) Standard Instrument Departures (SIDs) and Standard Terminal Arrival Routes (STAR). Ground validation is a key step between the design and the implementation of RNAV procedures (Figure 3-10).

One of the RVT software features is the simulation of the aircraft dynamics along the defined trajectory. After each simulation, the software generates an output file in which the flight path is defined in terms of waypoints, providing information related to position, attitude, velocity and aircraft performance such as:

- Latitude, Longitude and Altitude
- Bank and Heading angles
- Time (in seconds since trajectory started)
- Calibrated and True Airspeed (CAS and TAS), Vertical Speed (VS) and Acceleration
- Fuel Consumption and Thrust (based on the performance of the selected aircraft used for the simulation)

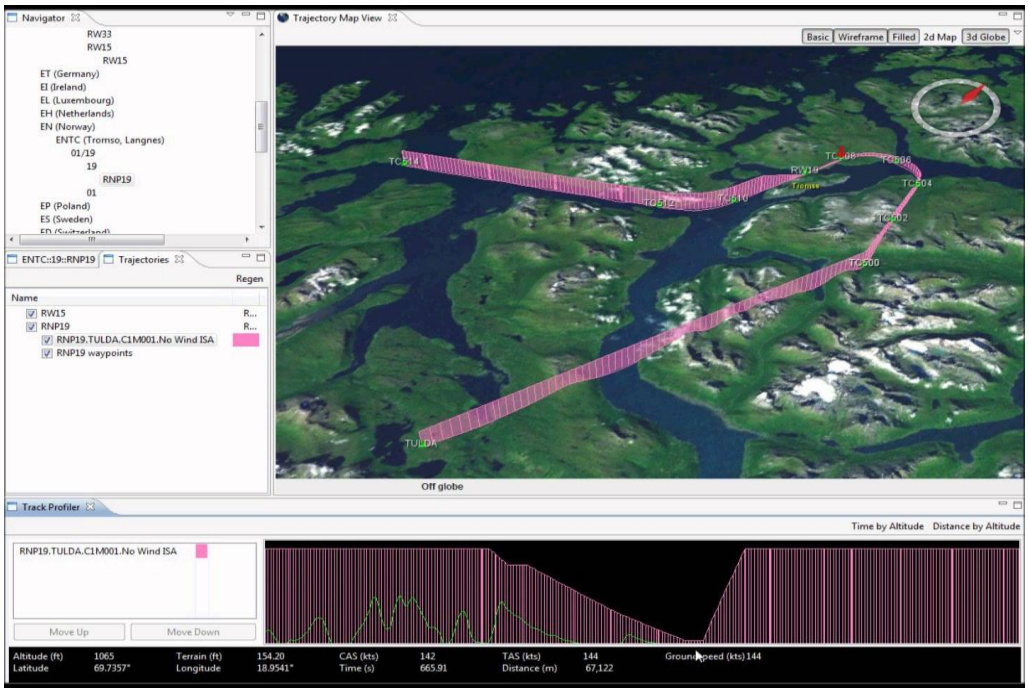

Figure 3-10 RTV GUI and results (DWint, 2013).

The trajectory parameters are recorded every 5 seconds in level flight, while the time step is reduced during manoeuvres; however, the APPATT also includes a function that linearly interpolates the data in order to have a user defined time step between WPs that have a time interval higher than the one sets by the user (e.g. 1 second, like the update frequency of GNSS position estimation). Additionally, as an input parameter, the user can set a flight starting time, expressed in days, hours, minutes and seconds since the beginning of the week (the YUMA almanacs are provided weekly with starting time on Monday 12:00 am), allowing the user to select the preferred or expected starting day and time.

The main limitation of the RVT output file is that, regarding the aircraft attitude, it only provides the bank and heading angles; for this reason, the following hypotheses have been considered:

- Bank angle = Roll angle

- Heading angle = Yaw angle
- Ramp angle = Pitch angle

The first and second hypotheses are valid if there is “no wind” or “no trim” condition during the flight. The third is a worst-case approximation, since the RVT software doesn’t provide the ramp angle. In the APPATT, the ramp angle is taken as equal to the angle between the aircraft local horizon and the trajectory between two waypoints (Figure 3-11) (ramp angle = pitch angle, not always true since the altitude of the airplane can change even if the pitch angle is null or it can be constant even if the pitch angle is not zero).

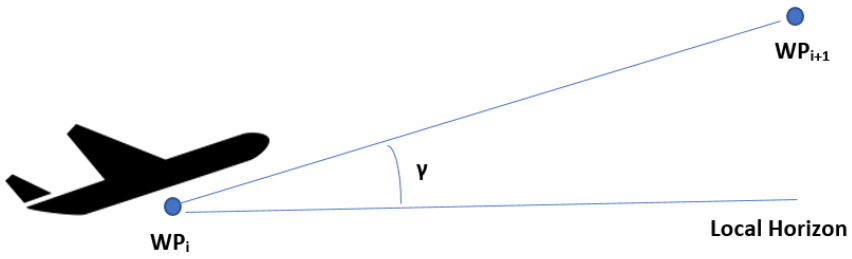

Figure 3-11 Ramp Angle.

3.4.4. Environment Database

The surrounding environment along the flight path is extracted from the high-resolution topographic data generated from NASA’s Space Shuttle Radar Topography Mission (SRTM) (NASA, 2000b).

The SRTM was developed through an international collaboration with the objective of obtaining the most complete high-resolution digital topographic database of Earth on a near-global scale from 56° S to 60° N. In February 2000, the Space Shuttle

Endeavour carried the special radar system, a modified version of the Spaceborne Imaging Radar-C/X-band Synthetic Aperture Radar (SIR-C/X-SAR) already used in a previous mission to acquire topographic data. The payload consisted of two radar antennas, one located in the Shuttle's payload bay, the other on the end of a 60-meter mast extended from the payload bay.

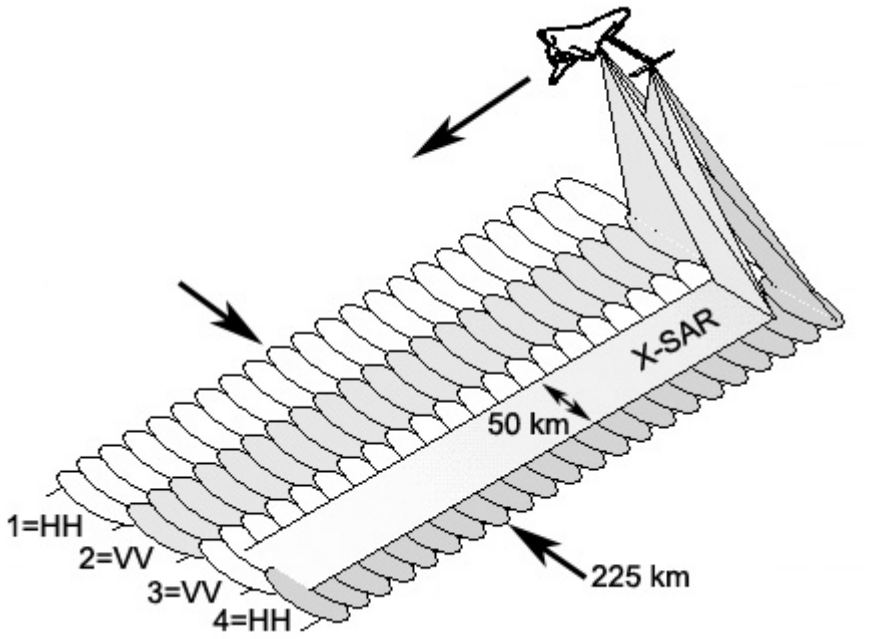

Figure 3-12 Measurement Pattern of the Space Shuttle Radar Topography Mission (NASA, 2007).

The elevation data are organised into tiles, each covering one degree of latitude and one degree of longitude. The resolution of the raw data is one arcsecond (30 m) over United States territory and three arcseconds (90 m) for the rest of the world. The arcsecond tiles have 3,601 rows, each consisting of 3,601 16-bit bigendian cells, while the three arcsecond tiles have 1201 rows and 1201 columns. Originally, the WGS84 ellipsoid was used as a reference for the elevation model, but lately the EGM96 geoid separation values were also introduced to facilitate the conversion of the related products.

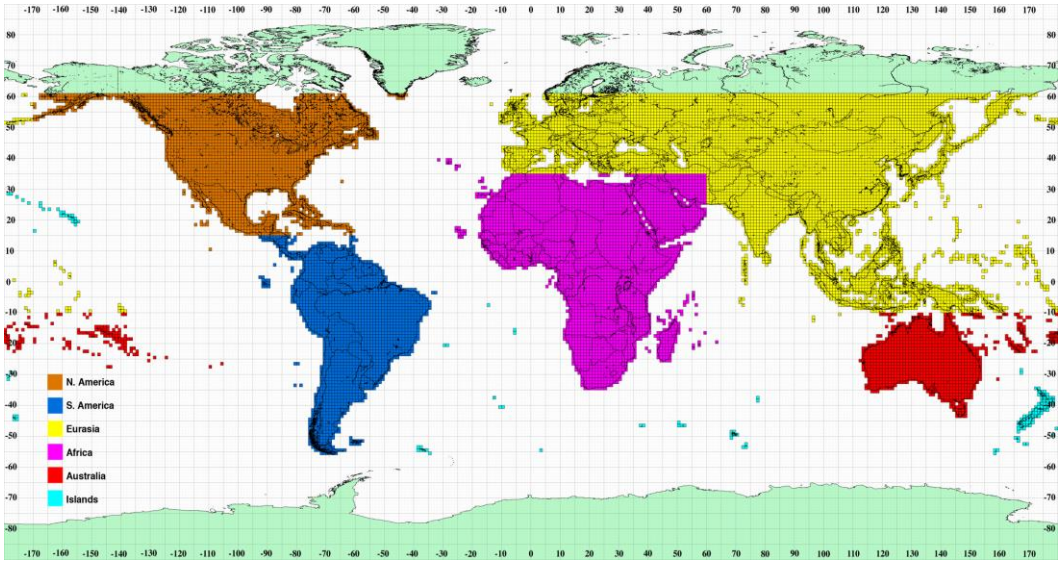

Figure 3-13 Map of the Covered Areas by SRTM (NASA, 2001a).

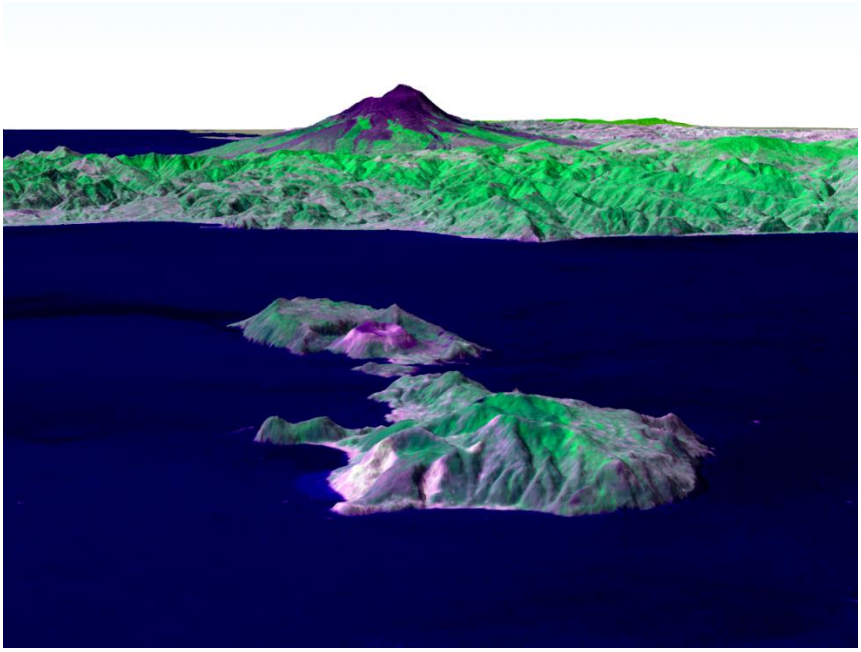

Figure 3-14 Example of 3D Terrain Reconstruction using SRTM data (NASA, 2000a).

3.4.5. INPUT ELABORATION AND INTEGRATION

The previous section presented the main inputs that the APPATT tool takes and uses to evaluate the integrity performance of the provided aircraft trajectory. In this section, it is presented how the different inputs are elaborated and integrated (for the orbit propagation method and coordinate transformation the user can refer to the text by Curtis (2013)).

A. SATELLITE POSITION AND PROPAGATION ON THE ORBIT: COMPUTATION OF THE TRUE ANOMALY, THE STATE VECTOR IN THE PERIFOCAL AND ECEF REFERENCE FRAMES

The YUMA almanac provides all the required information to define the position of the GNSS satellites at a specific time (TOA). Given the Mean anomaly, it is necessary to compute the true anomaly (ν), through the Eccentric anomaly (E), following an iterative procedure, due to the fact that the relation between Mean and Eccentric anomaly is non-linear:

$$M = E - e \sin E \tag{3.10}$$

Newton's method is one of the methods that could be used to find the root of the equation using the following equation:

$$E_{i+1} = E_i - \frac{f(E_i)}{f'(E_i)} \tag{3.11}$$

Where:

$$f(E_i) = E_i - e \sin E_i - M \tag{3.12}$$

$$f'(E_i) = 1 - e\cos E_i \tag{3.13}$$

Using as initial estimate for the Eccentric anomaly:

- If $M < \pi$, $E_0 = M + e/2$
- If $M > \pi$, $E_0 = M - e/2$

The iterative process stops when the ratio $\mathrm{f(E_i)/f'(E_i)}$ is less than the set tolerance (e.g. 10^{-8}).

Once the Eccentric anomaly is obtained, the true anomaly is computed using the following equation:

$$\tan\frac{\nu}{2} = \sqrt{\frac{1+e}{1-e}}\tan\frac{E}{2} \tag{3.14}$$

From the true anomaly, it is straightforward to define the satellite state vector in the perifocal reference frame (position [x, y, z] and velocity [v_x, v_y, v_z]):

$$\{r\}_x = \begin{Bmatrix} x \\ y \\ z \end{Bmatrix} = a(1 - e\cos E)\begin{Bmatrix} \cos\nu \\ \sin\nu \\ 0 \end{Bmatrix} \tag{3.15}$$

$$\{v\}_x = \begin{Bmatrix} v_x \\ v_y \\ v_z \end{Bmatrix} = \frac{\mu}{\sqrt{a\mu(1-e^2)}}\begin{Bmatrix} -\sin\nu \\ e + \cos\nu \\ 0 \end{Bmatrix} \tag{3.16}$$

Where μ is the gravitational constant of Earth and a is the semi-major axis of the orbit.

At this point, the satellite state vector is expressed in the orbital perifocal frame and a sequence of three rotations is required to transform its components in the ECEF reference frame (Figure 3-15). Given the definition of the two reference frames and the coordinate transformation given in Section 1093.2, the sequence starts with a rotation around the $\hat{k}$ of an angle equal to the argument of perigee ω that brings the $\hat{\imath}$ axis in the Earth equatorial (XY) plane, in the position $\hat{\imath}'$ along the node line, the $\hat{\jmath}$ axis in $\hat{\jmath}'$, and the associated orthogonal transformation matrix is:

$$A_3(\omega) = \begin{bmatrix} \cos\omega & \sin\omega & 0 \\ -\sin\omega & \cos\omega & 0 \\ 0 & 0 & 1 \end{bmatrix} \tag{3.17}$$

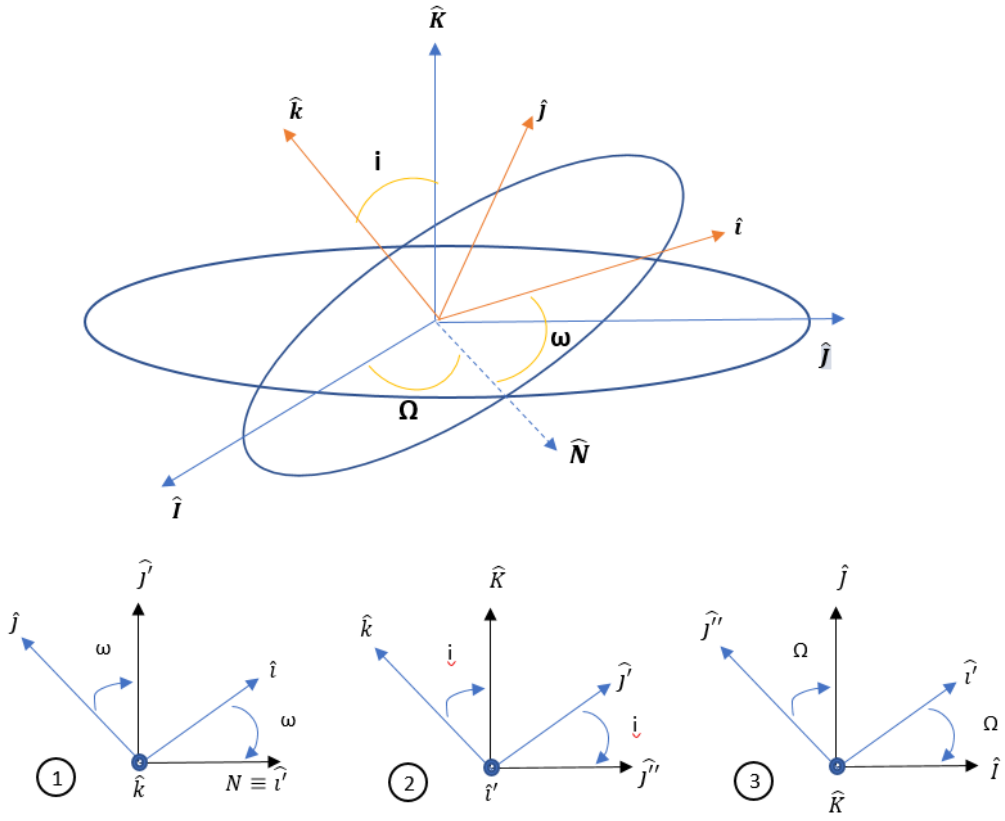

Figure 3-15 Change of Reference Frame: from Orbital to ECEF.

The second rotation is around the new $\hat{\imath}'$ axis, through the orbit inclination angle i, bringing the orbital plane parallel to the equatorial plane ($\hat{\jmath}'$ becomes $\hat{\jmath}''$ in the XY plane) and aligning the perifocal $\hat{k}$ axis with the ECEF $\hat{K}$. The related rotation matrix is:

$$A_1(\mathrm{i}) = \begin{bmatrix} 1 & 0 & 0 \\ 0 & \cos\mathrm{i} & \sin i \\ 0 & -\sin i & \cos\mathrm{i} \end{bmatrix} \tag{3.18}$$

The final rotation is again around the $\hat{k}$ through the right ascension angle Ω that will eventually align the $\hat{\imath}'$ and $\hat{\jmath}''$ axes with $\hat{I}$ and $\hat{J}$. The correspondent transformation matrix is:

$$A_3(\Omega) = \begin{bmatrix} \cos\Omega & \sin\Omega & 0 \\ -\sin\Omega & \cos\Omega & 0 \\ 0 & 0 & 1 \end{bmatrix} \tag{3.19}$$

The final transformation matrix from xyz to XYZ is given by the product of the three rotation matrices:

$$A_{xX} = A_3(\Omega)A_1(\mathrm{i})A_3(\omega) =$$

$$=$$

$$\begin{bmatrix} \cos\Omega\cos\omega - \sin\Omega\sin\omega\cos\mathrm{i} & -\cos\Omega\sin\omega - \sin\Omega\cos\mathrm{i}\cos\omega & \sin\Omega\sin\mathrm{i} \\ \sin\Omega\cos\omega + \cos\Omega\cos\mathrm{i}\sin\omega & -\sin\Omega\sin\omega + \cos\Omega\cos i\cos\omega & -\cos\Omega\sin\mathrm{i} \\ \sin\omega\sin\mathrm{i} & \sin\mathrm{i}\cos\omega & \cos\mathrm{i} \end{bmatrix} \tag{3.20}$$

The satellite state vector in the ECEF reference frame is given then by:

$$r_X = A_{xX}r_x \qquad\qquad v_X = A_{xX}v_x \tag{3.21}$$

The algorithm presented above is also used to propagate the satellite position along the orbit with some additional steps. Given the Δt respect to a specific time in which the satellite position is known (e.g. the YUMA Time of Applicability), it is possible to compute the Mean anomaly (M) through the Mean motion (n) given by:

$$n = \frac{2\pi}{T} = \sqrt{\frac{\mu}{a^3}} \tag{3.22}$$

Where T is the period of the orbit.

Then the Mean anomaly is:

$$M = M_0 + n\Delta t \tag{3.23}$$

Where:

- M_0 is the input of the YUMA almanac

And:

$$\boldsymbol{\Delta t = t_{res} + t_{traj} - TOA} \tag{3.24}$$

defines the time respect to the beginning of the YUMA week in which:

- t_{res} is the time between the beginning of the week and the trajectory starting time, expressed in the input function in days, hours, minutes and seconds and all converted in seconds.
- t_{traj} is the time since the beginning of the trajectory; the tool analyses one waypoint at a time, each with its own time stamp.
- TOA is one of the parameters provided in the YUMA almanacs representing the time between the beginning of the week.

Given the new Mean anomaly, it is possible to compute the true anomaly following the steps presented before to compute the state vector in the perifocal frame, but before projecting the state vector into the ECEF reference frame, it is necessary to update the right ascension of the node by using its rate $(\dot{\Omega})$**:**

$$\Omega_i = \Omega_0 + (\dot{\Omega} - \dot{\Omega}_E)\boldsymbol{\Delta t} - \dot{\Omega}_E mod\left(\frac{TOA}{604800}\right) \qquad (3.25)$$

Where:

- TOA is the Time of Applicability
- Ω_0 is the Right Ascension at Time of Almanac
- $\dot{\Omega}$ is the Rate of Right Ascension
- $\dot{\Omega}_{\mathrm{E}}$ is the Earth's angular velocity
- *mod* returns the remainder after the division of TOA and 604800 (number of seconds in a week).

B. Flight Path Waypoints Transformation and Computation of the Line of Sight

As it was introduced in the previous sections, the trajectory file describes the flight path in terms of geodetic latitude, longitude and altitude, however, in order to compute the line of sights, the geographical coordinates [φ, λ, h] (latitude, longitude and altitude) need to be converted in the ECEF reference frame [X,Y,Z]. The transformation is given by the following relations:

$$\begin{aligned} X &= (R_N + h)\cos\varphi\cos\lambda \\ Y &= (R_N + h)\cos\varphi\sin\lambda \\ Z &= [R_N + (1 - e^2)h]\sin\varphi \end{aligned} \tag{3.26}$$

Where:

$$R_N = \frac{R_e}{\sqrt{1-e^2\sin^2\varphi}} \tag{3.27}$$

$$e^2 = 2f - f^2 \tag{3.28}$$

- e is the WGS-84 first eccentricity
- R_e is the equatorial radius = 6378137.0 [m]
- f is the Earth Flattering, which inverse value is $1/\mathrm{f} = 298.257223563$

At this step, both satellites and aircraft positions are expressed in the ECEF reference system and it is now possible to compute the line of sight (LoS) between each aircraft position and all the satellites of the different constellations included in the analysis. The lines of sight are computed and stored in a matrix in terms of components of the unit vector between each pair of points:

$$LoS_{ij} = \frac{[X_j - X_i \quad Y_j - Y_i \quad Z_j - Z_i]}{\sqrt{(X_j - X_i)^2 + (Y_j - Y_i)^2 + (Z_j - Z_i)^2}} \tag{3.29}$$

Where

- *1 < i <* n_waypoints, the number of position of the aircraft along the trajectory
- $[X_i \quad Y_i \quad Z_i]$ waypoint coordinates in the ECEF
- *1 <* j < n_sat, the total number of satellites included in the computation
- $[\mathrm{X_j} \quad \mathrm{Y_j} \quad \mathrm{Z_j}]$ satellite coordinates in the ECEF

The stored unit vectors include all the LoS of the considered satellites, however, not all of them are effectively in view from the GNSS receiver point of view. A screening criterion needs to be implemented in order to discard the satellites that are below the receiver's local horizon, for this reason, the LoSs have to be transformed in the aircraft body reference frame using the transformation matrix presented in Section 3.4.5 . The components of the unit vectors need to be transformed three times:

a) From ECEF to ENU reference frame. Figure 3-3 shows the relative position between the ENU reference frame and the ECEF; a counter-clock rotation of (90° + λ) along the Z axis is required to align the X and East axes and a counter-clock rotation of (90° - φ) along the new X-axis is required to align the Z to the Up axis. The final transformation matrix is:

$$\widehat{LoS}_{ENU} = A_{ECEF-ENU}\widehat{LoS}_{ECEF} = A_1[\pi/2 - \varphi]A_3[\pi/2 + \lambda]\widehat{LoS}_{ECEF}$$
$$= \begin{pmatrix} -\sin\lambda & \cos\lambda & 0 \\ -\cos\lambda\sin\varphi & -\sin\lambda\sin\varphi & \cos\varphi \\ \cos\lambda\cos\varphi & \sin\lambda\cos\varphi & \sin\varphi \end{pmatrix}\widehat{LoS}_{ECEF} \qquad (3.30)$$

b) From ENU to NED reference frame. Fig. shows the relative position between the ENU and NED reference frames. The two systems have a fixed relative position that doesn't depend on the geographical coordinates, in which the East direction corresponds to the x-axis in ENU and the y-axis in the NED, the

North direction corresponds to the y-axis in ENU and the x-axis in the NED, while the z-axis corresponds to the Up direction in ENU and Down direction for the NED reference. There are two fixed rotations that transforms the ENU in NED, a 90° rotation around the Up direction, that leads x-axis in the North direction and the y-axis in the West direction, and a 180° degrees rotation around the x-axis, that leads the y-axis to point in the East direction and the z-axis in the Down direction. Another difference between the reference frame is the positive direction of the heading angle (the angle between the direction of motion and the North direction, represented as the East direction in Figure 3-16) that is measured clockwise in the NED reference frame and counter-clockwise in the ENU.

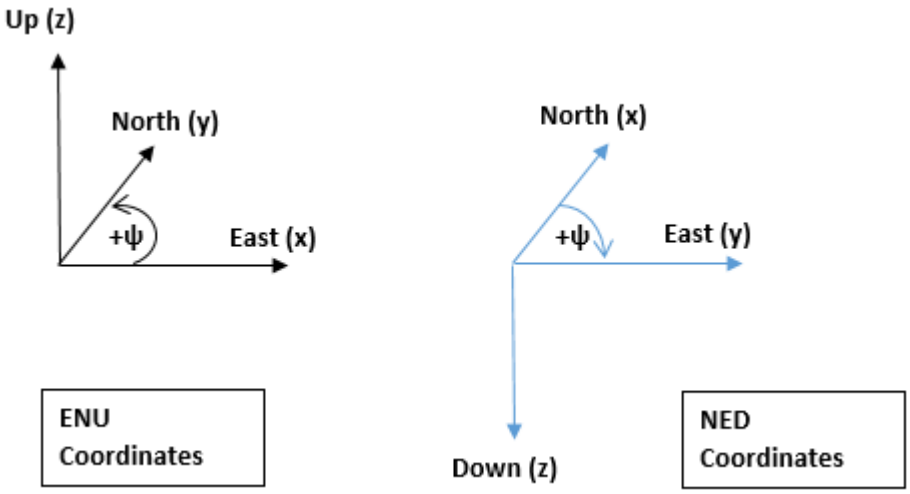

Figure 3-16 Difference between ENU and NED Reference Frames.

The equation that transforms the LoS from the ENU to the NED reference point is:

$$\widehat{LoS}_{NED} = A_{ENU-NED}\widehat{LoS}_{ENU} = A_1[\pi]A_3[\pi/2]\widehat{LoS}_{ENU}$$

$$= \begin{pmatrix} -\sin\lambda & \cos\lambda & 0 \\ -\cos\lambda\sin\varphi & -\sin\lambda\sin\varphi & \cos\varphi \\ \cos\lambda\cos\varphi & \sin\lambda\cos\varphi & \sin\varphi \end{pmatrix} \widehat{LoS}_{ENU} \qquad (3.31)$$

c) From NED to Body reference frame. The final transformation brings the LoS from the NED reference frame to the Body reference frame, which attitude is defined by the three angles roll, pitch and yaw. Therefore, in this case, three rotations are required

- Along the NED Z axis of an angle equal to the yaw angle, in order to align the NED X axis with the Body x-axis along the same direction.
- Along the NED Y axis of an angle equal to the pitch angle, in order to fully align the NED X and Z axes with the Body x and z axes.
- Along the NED X-axis of an angle equal to the roll angle, to complete the alignment of the axes of the two reference frames.

The last transformation matrix is then expressed by:

$$\widehat{LoS}_{BODY} = A_{NED-BODY}\widehat{LoS}_{NED} = A_1[\phi]A_2[\theta]A_3[\psi]\widehat{LoS}_{NED} =$$

$$\begin{pmatrix} \cos\theta\cos\psi & \cos\theta\sin\psi & -\sin\theta \\ \sin\phi\sin\theta\cos\psi - \cos\phi\sin\psi & \sin\phi\sin\theta\sin\psi + \cos\phi\cos\psi & \sin\phi\cos\theta \\ \cos\phi\sin\theta\cos\psi + \sin\phi\sin\psi & \cos\phi\sin\theta\sin\psi - \sin\phi\cos\psi & \cos\phi\cos\theta \end{pmatrix}\widehat{LoS}_{NED} \quad (3.32)$$

3.4.6. COMPUTATION OF THE SHADOWING EFFECT OF THE AIRCRAFT ATTITUDE

The APPATT algorithm uses the waypoints coordinates, the time information and the orbital elements provided by the YUMA almanacs to compute the aircraft and satellites positions respect to the Earth Centered Earth Fixed (ECEF) reference system, as described in Section 3.4.5. Afterwards, it computes the Line-of-Sight (LoS) unit vectors between each aircraft position and all the satellites of the considered

constellations. Then the LoS unit vectors are then converted in the local East, North and Up (ENU) reference frame for each location and the satellites below the horizon (with the z component of the LoS being negative) are removed from the computation, since they are below the local horizon. In order to evaluate the effect of the attitude of the aircraft, the LoSs are assessed in the NED (North-East-Down) and Body reference frame (Roll, Pitch and Yaw axes). NED coordinates to describe observations made from an aircraft are normally given relative to its intrinsic axes, but normally using as positive the coordinate pointing downwards, where the interesting points are located. At each change of reference frame, the algorithm computes and uses the corresponding rotation matrix to transform the LoS unit vectors.

Once the LoSs are expressed in the Body reference frame, the same filter used to remove from the computation the satellites below the local horizon in the ECEF filter is applied, but this time all the LoS with z components positive are removed, due to the fact that the z-axis in the Body reference frame is pointing downward (considering a standard attitude for commercial airplane and not acrobatic or jetfighters).

Figure 3-17 shows an example of the result of a specific point of the trajectory of an aircraft with banking angle of 20 degrees; there are the three different reference systems presented in Section 3.2, blue is the ENU, yellow the NED and magenta is the Body reference system. The red dots are the satellite in view in the ENU reference system, while the green circle is the aircraft horizontal plane (x-y or roll-pitch plane) and on the right side of the picture it is easy to see that there are three satellites below the GNSS receiver's field of view, reducing the number of satellites in view and affecting the ARAIM performance as will be shown in the following chapters.

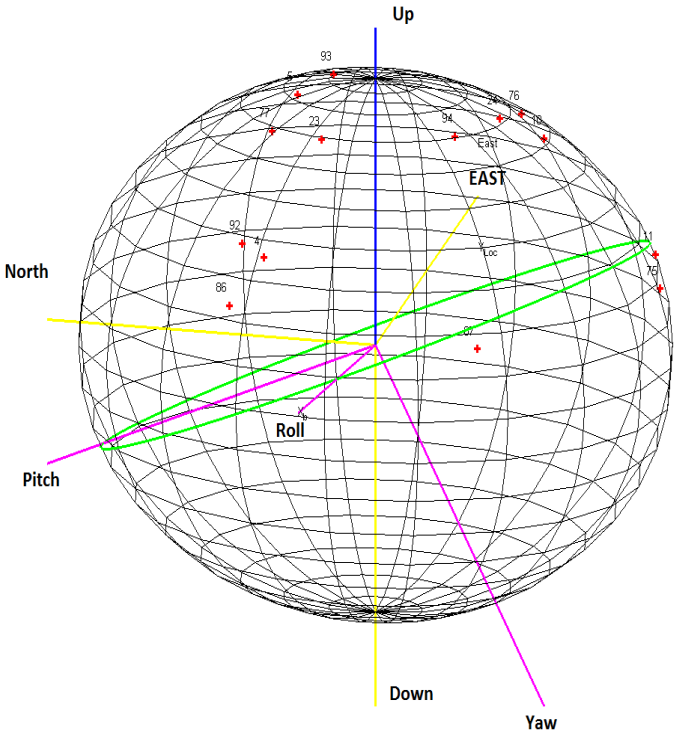

Figure 3-17 Example of Shadowing Effect due to the Aircraft Attitude.

3.4.7. COMPUTATION OF THE SHADOWING EFFECT OF THE SURROUNDING ENVIRONMENT

The APPATT reads and loads a txt file, generated from the conversion of the SRTM data, containing the geographical information (latitude, longitude and altitude) of the terrain surrounding the trajectory.

Figure 3-18 SRTM Data Tiles over the Map of Europe (NASA, 2001b).

Figure 3-18 shows that the SRTM data is organized per tiles of dimension 1°latitude x 1° longitude containing around 1.4 million sample points and for each point in the dataset, latitude, longitude and altitude is stored.

Then, the data passes through a series of filters and checks in order reduce the computational load and with the main objective of finding the satellites that are shadowed by the terrain.

Figure 3-19 shows an example of a horizon mask, a 2D representation of the local skyline view; the circle centre is the local zenith and each circle is the elevation angle with respect to the local horizon represented by the external circumference. The spokes are the directions (also defined as azimuth or heading angles) with respect to the North direction. The red line and dots are the local terrain profile that could shadow one or more satellites.

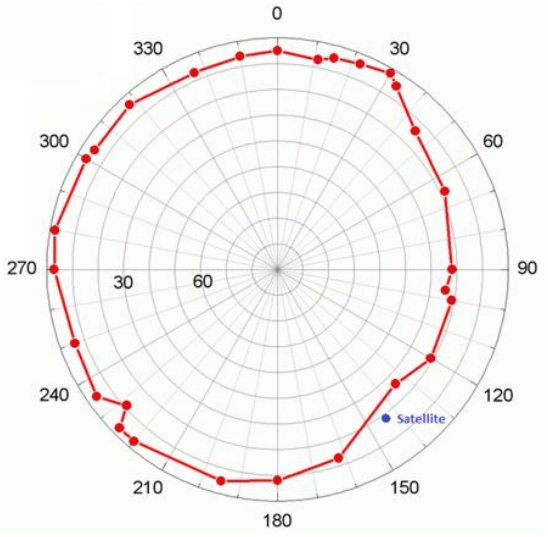

Figure 3-19 Example of Horizon Mask with Satellite in Shadow.

The objective of the terrain shadowing function is to evaluate which satellite lays behind the local skyline and its algorithm is quite straightforward and performs the following steps and checks:

- Remove all the terrain points with altitude $\mathrm{h_{terr}}$ lower than the aircraft $\mathrm{h_{aircraft}}$ (an approximation that does not consider the Earth curvature).

$$if\ h_{terr,i} < h_{aircraft}$$

Terrain point *i* is discarded

- Compute the LoS of the points left for each aircraft position and compute their elevation and heading angles with respect to the ENU reference system.

- Compute LoS in the ENU reference frame using Eqs. (3.29) and (3.30).
- Compute elevation (α) and azimuth (ψ, that correspond to the heading angle) of the LoS as:

$$\alpha = \sin^{-1}(LoS_{ENU,z}) \tag{3.33}$$

$$\psi = \tan^{-1}\left(\frac{LoS_{ENU,x}}{LoS_{ENU,y}}\right) \tag{3.34}$$

- Remove from the computation the satellites with elevation angles higher than the highest elevation angle of the sample points (it further reduces the number of satellites to check)

$$if\ \alpha_{sat,i} > \alpha_{max,terrain} \quad (3.35)$$

Satellite *i* is removed

- Find the terrain points that have elevation angle higher than the lowest satellite elevation.

$$if\ \alpha_{terrain,i} < \alpha_{min,sat} \quad (3.36)$$

Terrain *i* is removed

The following steps are repeated for each of remaining satellites:

- Find the terrain points that have the heading angles within a predefined range β (Figure 3-20).

$$\psi_{sat,i} - \beta \leq \psi_{terrain,i} \leq \psi_{sat,i} + \beta \quad (3.37)$$

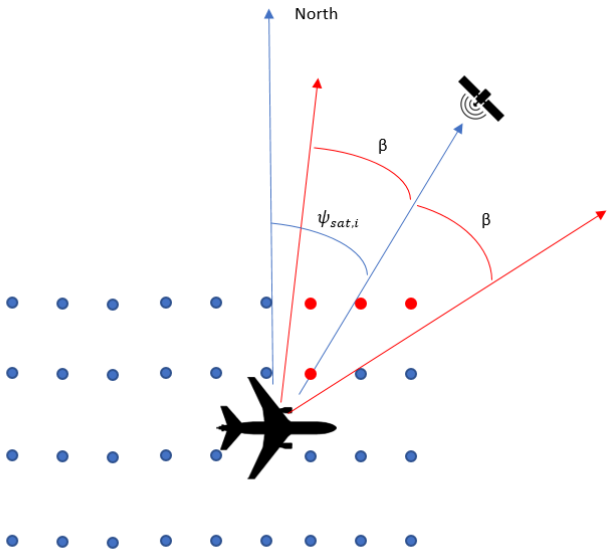

Figure 3-20 Filtered Terrain Data in the Satellite Direction.

- For each point that passed the filter, the algorithm takes the eight adjacent points and checks for each pair of points (central + one of the adjacent) if the LoS between aircraft and satellite lays in between (comparing the azimuth angles) (Figure 3-21).

$$if\ sign(\psi_{terrain,central} - \psi_{sat}) = sign(\psi_{terrain,i} - \psi_{sat}) \quad (3.38)$$

Terrain *i* is removed

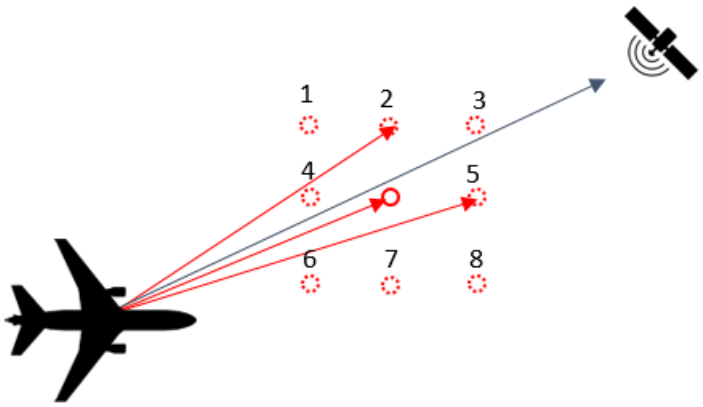

Figure 3-21 Points number 1, 2, 3 and 4 satisfy the filter condition.

- For the remaining pairs, the algorithm interpolates the elevation values between the main central point and the adjacent ones to create a profile of the terrain data and compares the elevation value of the point that has the same azimuth angle of the satellite (Figure 3-22).

$$\alpha_{int} = \frac{(\psi_{sat} - \psi_i)(\alpha_C - \alpha_i)}{(\psi_C - \psi_i)} + \alpha_i \quad (3.39)$$

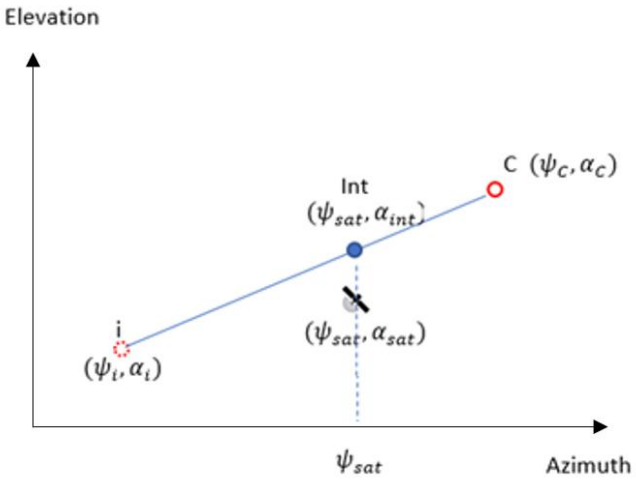

Figure 3-22 Interpolation between Pair of Terrain Data.

- If the elevation angle of the interpolated point is higher than the satellite, the satellite is declared shadowed and the algorithm repeats the previous steps for the remaining satellites.
- If the elevation angle of the interpolated point is not higher than the satellite, the algorithm continues to check all the pair of points.
- If none of the pairs satisfies the criteria, the algorithm selects the next central point from the list of the points that satisfied the condition (3.37) until it checks all the points for all the satellite that satisfied the condition (3.35).

One of the limits of this algorithm is that the detection capability is strictly related to the resolution of the terrain data; higher is the resolution better will be the capability of the algorithm of identifying shadowed satellites and avoiding erroneous configurations, while at the same time a higher resolution also increases the computational effort.

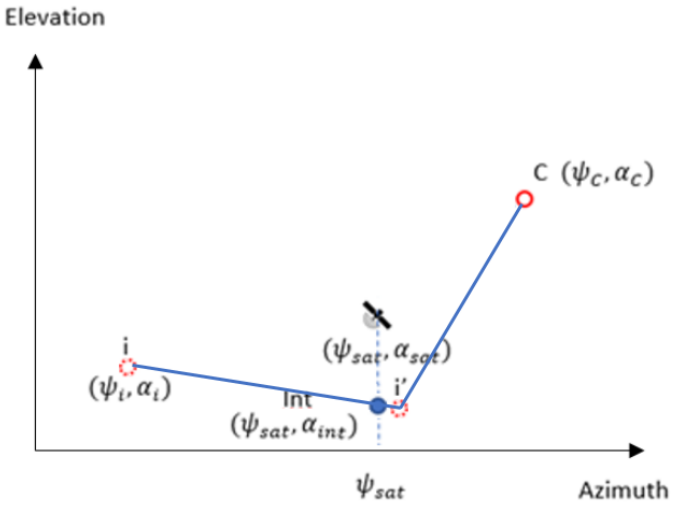

Figure 3-23 Possible configuration with higher resolution data.

Figure 3-24 shows an approach and related missed approach flight path integrated in the terrain data of the Alps area around Innsbruck airport, Austria, one of the airports selected for the ARAIM performance analysis in this research for its peculiar position within the mountains, a perfect scenario to test the algorithm capabilities and the effect of the terrain.

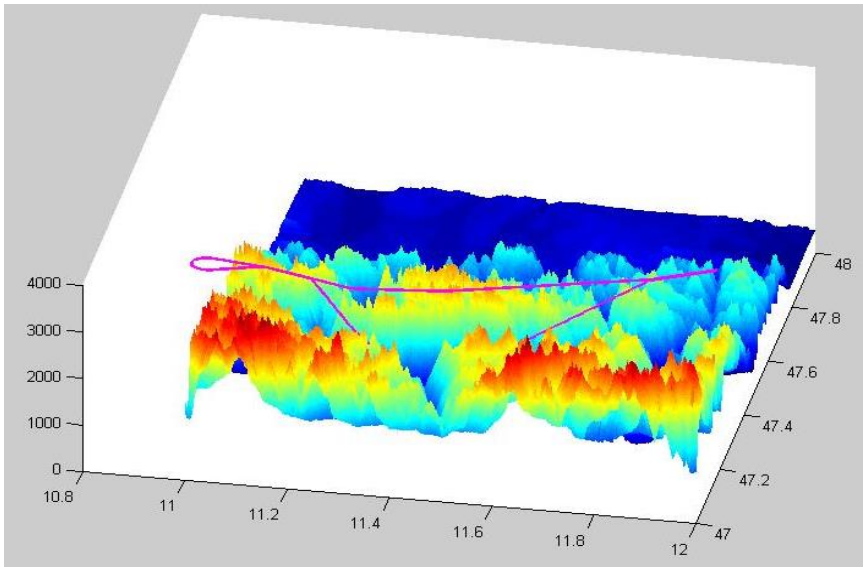

Figure 3-24 Graphical View of an Approach and Missed Approach Trajectory Integrated in the Terrain Data.

3.4.8. OUTPUT

At this stage, the algorithm has all the required input to analyse the integrity performances of the ARAIM algorithm described in Section 2.4.4 based on the remaining satellite in view.

The APPATT tool provides as output for each trajectory waypoint:

- Predicted ARAIM Performance with respect to the East North Up (ENU) reference frame (no shadow effect included, full view of the sky)
- Predicted ARAIM Performance with respect to the aircraft body reference frame (both attitude and environment shadowing effect included)
- Number of satellites in view in the two reference systems
- Number of satellites lost due to the shadowing effects.

In this chapter, a full overview of the APPATT algorithm has been provided, with a particular focus on the description of the shadowing effect functions. In the next chapter, the selected scenarios, parameters and configurations will be presented together with the results of the analysis of the integrity performances.

4. INTEGRITY ANALYSIS OF SIMULATED AIRCRAFT TRAJECTORIES

As it has been presented in the previous chapters, the current RAIM technique is an approved civil aviation navigation system for Lateral Navigation (LNAV) in the En-route, Terminal and Non-precision approach flight phases and RAIM prediction is required if GPS is to be used to solely satisfy the RNAV requirements (FAA, 2007a). The main drawbacks of the RAIM technique are:

- uses a single constellation
- uses a single frequency
- detects a single fault,

and these factors dramatically limit the performance.

However, the new advanced version aims to become an approved navigation system down to the LPV-200 approach level in order to reduce the ground systems effort, to increase air traffic in minor airports and to allow curved and parallel approaches with reduced or limited visibility. The main strengths of ARAIM are

- use multiple GNSS constellations
- use dual frequency data
- multiple fault detection capability

For these reasons, one of the aims and main objectives of this research is to develop a system that satisfies the future needs of civil aviation.

In this chapter, ARAIM performance are evaluated in simulated operational configurations: aircraft flights can last for hours and on-board receivers don't always have a full view of the sky, attitude changes from manoeuvres, obscuration by the

aircraft body and shadowing from the surrounding environment could all affect the incoming signal from the GNSS constellations, leading to configurations that could adversely affect the real performance. For this reason, the main objective of the algorithm developed in this research project is to analyse these shadowing effects and compute the performance of the ARAIM technique when integrated with a predicted flight path using different combinations of three constellations (GPS, GLONASS and Galileo), considered as fully operational, since previous ARAIM performance analysis was mostly performed on selected points on the Earth's surface, with full view of the sky, showing the potential of Advanced RAIM architectures to provide the Required Navigation Performance and achieve a global coverage of LPV-200 using, at least, two constellations.

4.1. Current Status of ARAIM Performance Analysis

Figure 4-1 and Figure 4-2 show an example of the analyses performed by Stanford University with the MATLAB Algorithm Availability Simulation Tool (MAAST) considering a single constellation configuration (Galileo) and dual-constellation (GPS and Galileo) (Standford, 2014). In Figure 4-1 map there are the average Vertical Protection Levels in a 24-hour time interval using a single constellation configuration, in this case, Galileo in the 27 satellites configuration. The light green areas present a VPL value close to 35 m, the requirements for the LPV-200 approach, while the yellow areas have an average VPL of around 40 m, above the alert limit. Figure 4-2 instead represents the LPV-200 approach availability around the world using a dual constellation configuration (GPS and Galileo). Violet areas represent an availability of

more than 99.9%, in which the 99,9th VPL percentile means that for each location the VPL has been selected in order to have 99,9% of availability for the selected simulation time (Blanch et al., 2011).

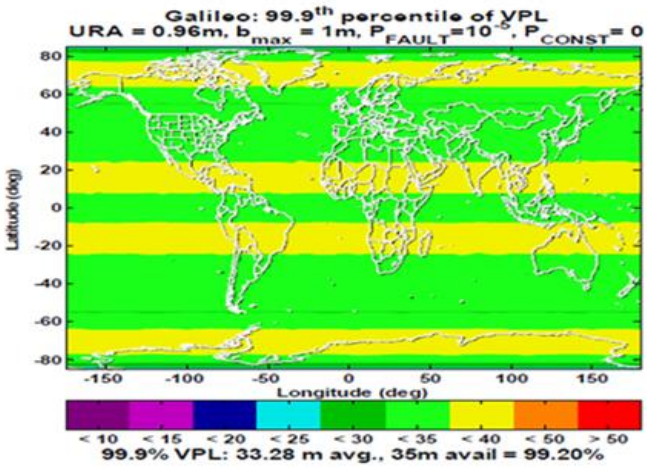

Figure 4-1 99.9th VPL percentile for ARAIM using the 27SV Galileo Constellation (Blanch et al., 2011).

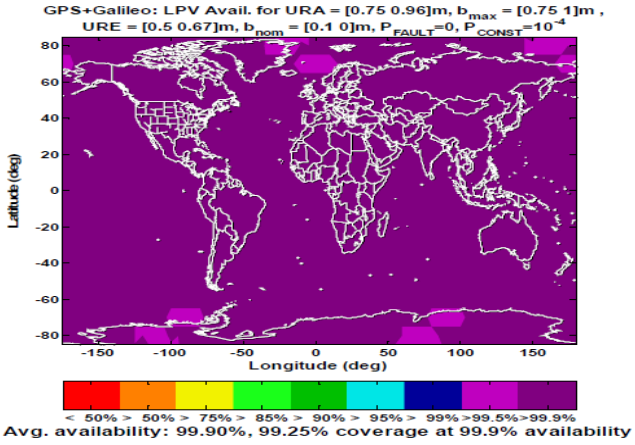

Figure 4-2 Combined Availability for GPS + Galileo (Blanch et al., 2011).

However, in a real configuration, the aircraft attitude and the terrain and objects in the surrounding environment could shadow a certain number of satellites (Figure 4-3), especially during a safety critical phase (take-off, maneuverings and landing

phases), leading to a possible degradation of the integrity performance of the ARAIM algorithm.

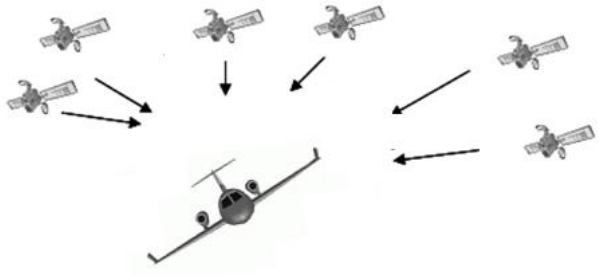

Figure 4-3 Attitude shadowing effect.

None of the previous analysis considered and integrated into the system the effects of these two factors, only Rippl et al. (2014) noticed an effect on the ARAIM performance during flight tests.

This research has extended this requirement for a generic situation, analysing ARAIM performance prediction for different approach routes in several airports around the World in order to prove the concept. For the purpose of this research, the MAAST has been selected and modified in order to analyse ARAIM performance along aircraft trajectories considering the shadowing effect of the aircraft attitude and surrounding environments. The newly developed algorithm, named APPATT (ARAIM Performance on Predicted Trajectories Tool) and described in the previous chapter, has the main objective of computing the four parameter indices of the reliability of the navigation solution provided by GNSS.

4.2. APPATT SHORT-TERM (ST) ALGORITHM AND SCENARIOS

The APPATT algorithm presented in the previous chapter has been designed to analyse the integrity performance along aircraft trajectories considering the shadowing effect of the aircraft attitude and surrounding environments (if enabled in the tool).

The newly developed algorithm has the same objective as the MAAST, to compute the four parameters indices of the reliability of the navigation solution provided by GNSS but with two main differences:

- The tool compares the integrity parameters computed including and not including the shadowing effects of the aircraft attitude and the surrounding environment, with the main purpose of highlighting the impact of the loss of satellites on the performances.
- The predicted parameters are valid for that specific trajectory and time that completely defines the configuration of the satellites constellations together with their expected signal errors and bias characterisation (see

  Table 4-2).

For the purpose of this research, three different RNAV (RNP) approach procedures have been selected for the ARAIM prediction analysis:

- Fairbanks (Alaska) (Figure 4-5) and Cairns (Australia) (Figure 4-6) due to their positions in areas of low ARAIM performance according to the analysis computed by the University of Stanford using a single constellation configuration (Figure 4-4).

- Innsbruck (Austria) (Figure 4-7) due to its peculiar location, where the environment shadowing effect could increase the number of the satellites not available.

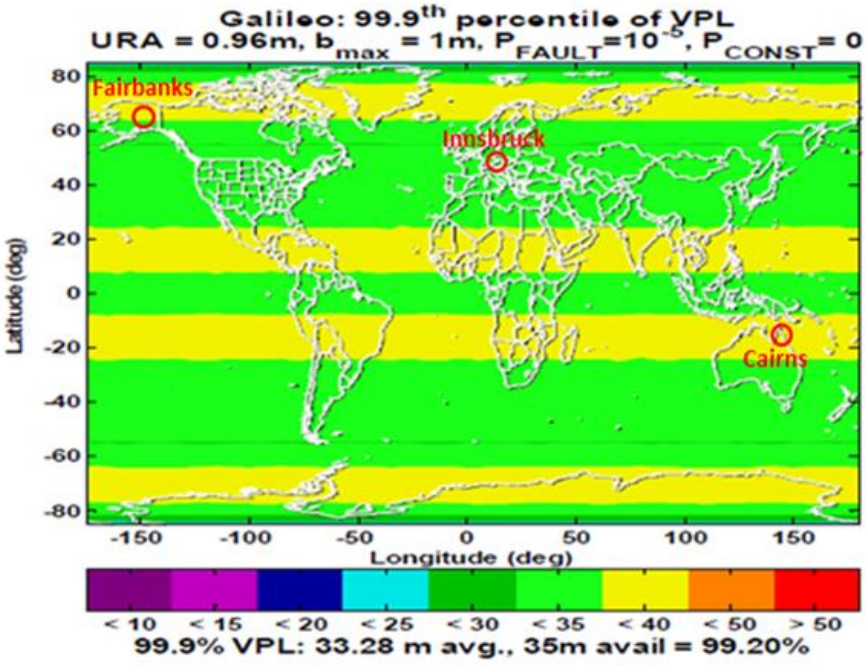

Figure 4-4 Selected Airport Locations.

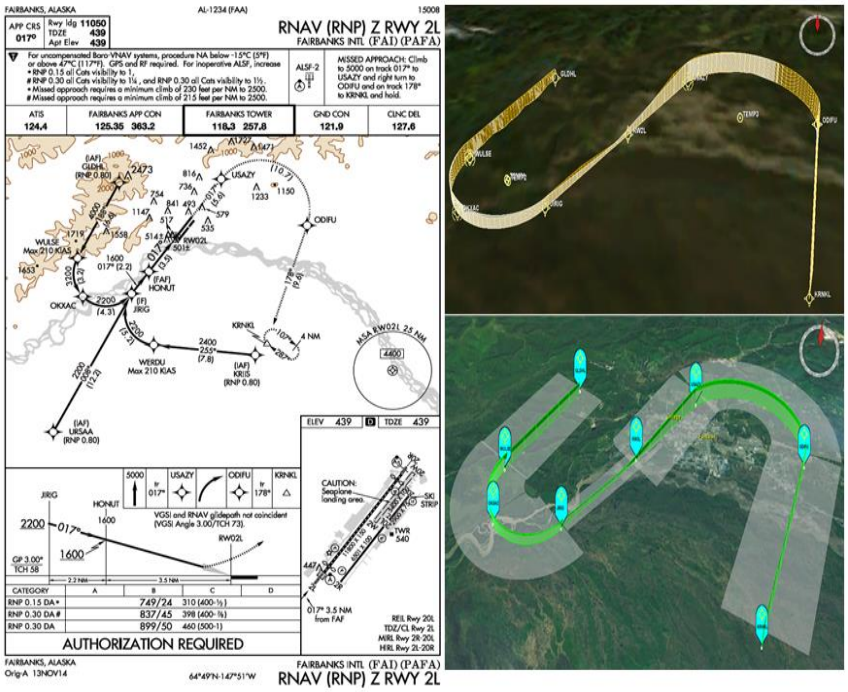

Figure 4-5 Fairbanks Approach Procedure.

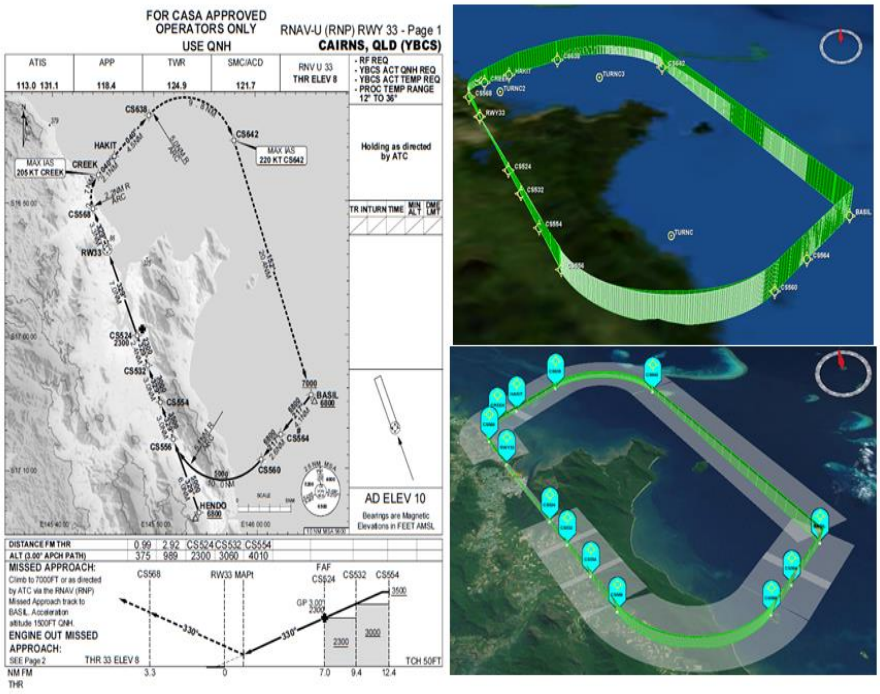

Figure 4-6 Cairns Approach Procedure.

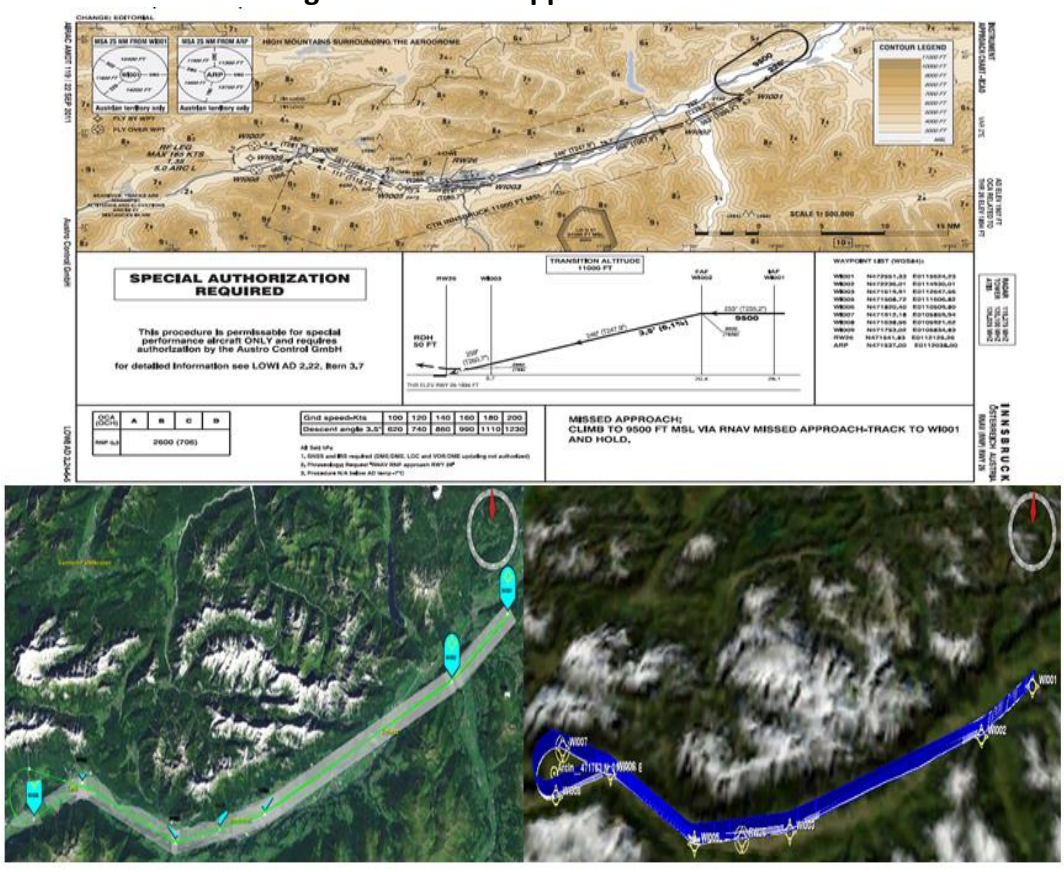

Figure 4-7 Innsbruck Approach Procedure.

The other main advantage of these three approaches is that they include a wide variety of manoeuvres (90, 180 and 270 degrees manoeuvres).

The three trajectories have been defined using the details provided in the approach charts and inserted in the RVT software (Figure 4-8), that generates as output a txt file (Figure 4-9) with the information required for the ARAIM analysis (coordinates, time and attitude). The generated trajectories also include the missed approach manoeuvre that the aircrafts are expected to execute in case the landing is aborted. Additionally, for the simulation it has been selected as aircraft an Airbus A320, the software allows to select the aircraft category and model since the characterisation of the trajectory depends on the aircraft performances. All the manoeuvres along the trajectories satisfy the standard limitations imposed by the regulations for commercial flights that are (values depend on the aircraft model and approach type):

- Max bank angle between 25-33°
- Max pitch angles: 15-20° positive pitch (take-off) and 5° negative pitch (landing).

The Innsbruck missed approach is of particular interest, it is a 270° manoeuvre above a valley surrounded by mountains that brings the aircraft to fly again over the runway before leaving the airport area in the North-East direction. Innsbruck airport is a perfect example of how a reliable and accurate navigation system could make the difference in a location in which aircrafts can proceed on only one route, limiting the airport capabilities and driving the safety requirements.

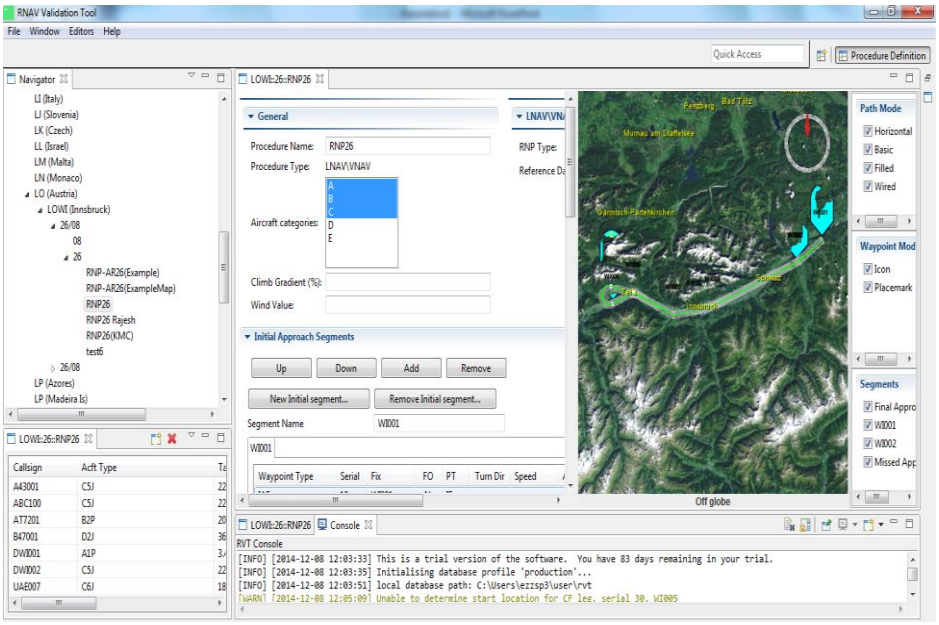

Figure 4-8 Trajectory definition in the RVT software.

Tracks

Time (s)	Latitude	Longitude	X (nm)	Y (nm)	Altitude (ft)	Bank (dg)	Heading (dg)	CAS (kt)	TAS (kt)	Accel (kt/s)	VS (ft/m)	FF (kg/h)	THRUST (daN)	POWER (%)	Dist (nm)	Interv (s)
0.00	47.4309250	11.9400639	27.6804	10.3646	9500.0	0.0	234.76	146.5	168.7	0.0000	0	3132	23398	37.5	0.000	0.00
5.00	47.4287007	11.9353373	27.4890	10.2294	9500.0	0.0	234.76	146.5	168.7	0.0000	0	3132	23398	37.5	0.234	5.00
10.00	47.4264763	11.9306112	27.2977	10.0942	9500.0	0.0	234.76	146.5	168.7	0.0000	0	3132	23398	37.5	0.469	5.00
15.00	47.4242516	11.9258854	27.1063	9.9590	9500.0	0.0	234.76	146.5	168.7	0.0000	0	3132	23398	37.5	0.703	5.00
20.00	47.4220267	11.9211601	26.9149	9.8238	9500.0	0.0	234.76	146.5	168.7	0.0000	0	3132	23398	37.5	0.937	5.00
25.00	47.4198017	11.9164351	26.7235	9.6886	9500.0	0.0	234.76	146.5	168.7	0.0000	0	3132	23398	37.5	1.172	5.00
															1.406	5.00

Figure 4-9 Extract of the RVT trajectory output.

4.3. RESULTS AND ANALYSIS

The three trajectories have been analysed in different scenarios (single, dual and tri-constellation), combining the different constellations: GPS, Galileo (24 and 27 satellites nominal configuration) and GLONASS (23 satellites nominal configuration). The tool takes as input:

- Trajectory and environment files
- Satellites mask angle; receivers automatically screen-out (mask) the satellites that are below a defined elevation angle (e.g. 5°). In this research, different

mask angles have been used to evaluate if the inclusion of masked satellites could improve the performances.

- Integrity parameters
- Signal error and bias characterization.
- Reset time. Trajectory starting time respect to the GPS week time
- YUMA Almanacs

The tool provides as output several graphs:

- Aircraft attitude along the trajectory: Roll, Pitch and Yaw angles.
- Number of satellites in view in the ENU and Body reference system, distinguishing the one. Satellites are removed from the computation following the criteria described in Section 3.4.6 and Section 3.4.7.
- Horizontal and Vertical Protection Level (HPL and VPL), Accuracy and Effective Monitoring Threshold in the ENU and Body reference frame respect to the Alert Limit.

Table 4-1 and

Table 4-2 summarises the values used by Stanford University for the integrity parameters and used as reference for the trajectory analysis, but tests using different values for the signal errors, bias characterisation and probability of satellite/constellation failure are going to be presented as well.

Table 4-1 Parameter Definitions.

Name	**Description**	**Value**
P_{sat}	Probability of satellite failure of the single satellite	10^{-5}
P_{const}	Probability of constellation failure	10^{-4}

Name	Description	Value
PHMI	Total integrity budget	10^{-7}
$PHMI_{VERT}$	Integrity budget for the vertical component	$9.8x10^{-8}$
$PHMI_{HOR}$	Integrity budget for the horizontal component	$2x10^{-9}$
P_{FA}	Continuity budget allocated to disruptions due to false alert.	$4x10^{-6}$
P_{FA_VERT}	Continuity budget allocated to the vertical mode	$3.9x10^{-6}$
P_{FA_HOR}	Continuity budget allocated to the horizontal mode	$9x10^{-8}$
P_{EMT}	Probability used for the calculation of the Effective Monitor Threshold	10^{-5}

Table 4-2 Signal Errors and Bias Characterisation.

	GPS	Galileo	GLONASS
URA (m)	1	1	0.75
URE (m)	0.5	0.5	0.5
b_{nom} (m)	0	0	0
b_{int} (m)	0.75	0.75	0.75

4.3.1. INNSBRUCK AIRPORT

This section is dedicated to the analysis of the integrity performance of the RNAV (RNP) approach procedure (including the missed approach phase) for the airport of

Innsbruck. The trajectory is going to be analysed using different combinations of three GNSS constellations (GPS, Galileo in the 24SV and 27SV configuration and GLONASS) and mask angles. The terrain data included in the computation covers the area between 47-48° latitude and 11-13° longitude.

Figure 4-10 shows the aircraft attitude along the trajectory expressed in terms of Roll (red), Pitch (green) and Yaw (blue) angles; on the X-axis there are the waypoints along the trajectory and on the Y axis the values of the attitude angles in degrees. It is easy to reconstruct the different phases of the flight from the values of the angles:

- Between WPs 100 and 550 the final descent to the runway (pitch angle negative)
- Between WPs 550 and 850 the initial phase of the missed approach with the aircraft gaining altitude (pitch angle positive) and following the valley
- Between WP 850 and 1000 the 250° manoeuvre to go back in the direction of the airport
- Between WP 1000 and 1800, the aircraft follows the valley and flies over the runaway going back on the same path travelled in the first phase (to be noticed in particular the symmetry between WP 1100-1800 and WP 0-550).

The aircraft attitude angles, in particular the bank and pitch angles, respect the standard values

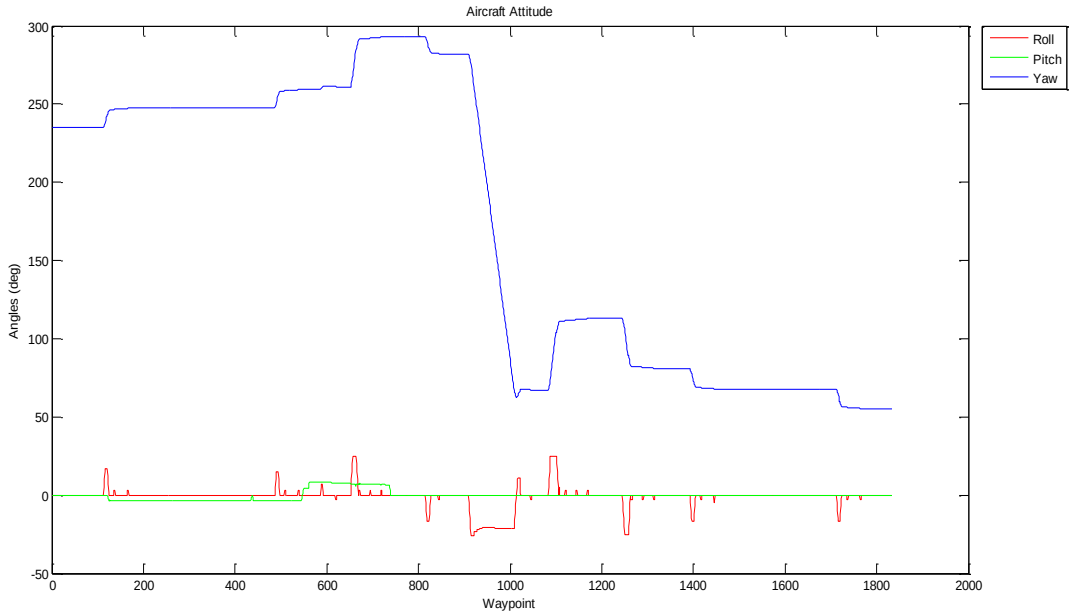

Figure 4-10 Aircraft Attitude along the trajectory: Roll (red), Pitch (green) and Yaw (blue) angles.

A. SINGLE CONSTELLATION CONFIGURATION

- ***Single constellation GPS: Yuma almanac week 703 (TOA 319488s), reset time [0d 0h 0m 0s], mask angle 5°***

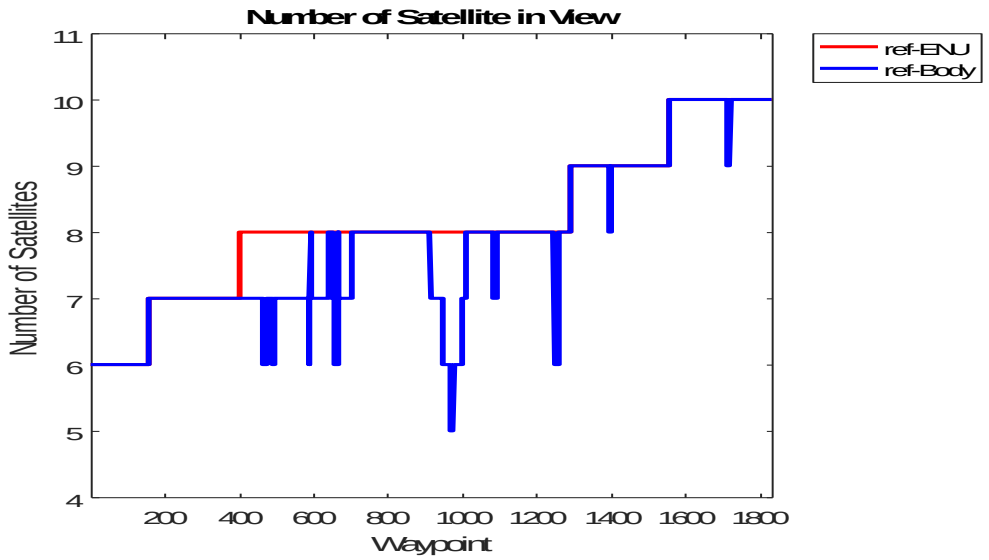

Figure 4-11 Number of Satellites in view in the ENU (red) and Body (blue) Reference Frames along the Trajectory.

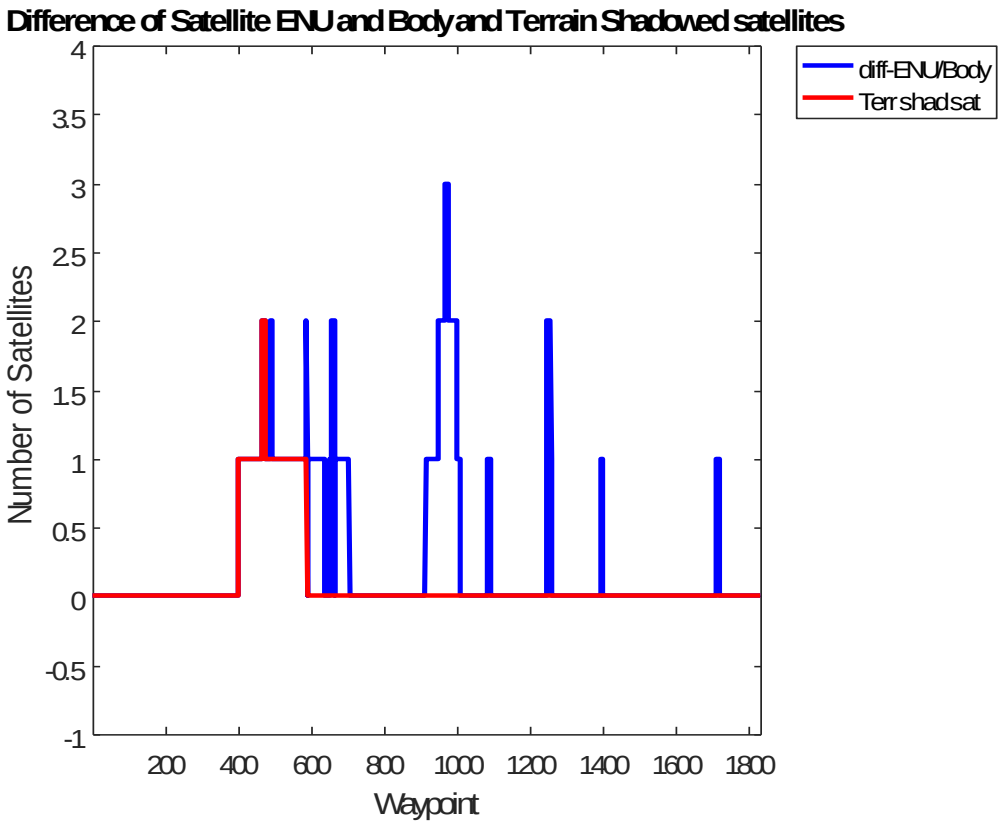

Figure 4-12 Number of Shadowed Satellites by Aircraft Attitude (blue) and Terrain (red).

Figure 4-11 shows the number of satellites in view along the trajectory in the two reference frames (Body and ENU), while Figure 4-12 shows the number of satellites that have been shadowed by the aircraft attitude and by the surrounding environment (to be noticed that the two numbers in the graph are cumulative, for example at WP 500 one satellite is shadowed by the terrain, in red, and one by the aircraft attitude, in blue, for a total of two loss of LoS). Another thing to be noticed is that in Figure 4-12 and in all the subsequent graphs, the environmental shadowing effect is mainly affecting the system between WP400 and WP600, in this section of the trajectory the aircraft altitude is low enough to be affected by the mountains surrounding the area around Innsbruck airport.

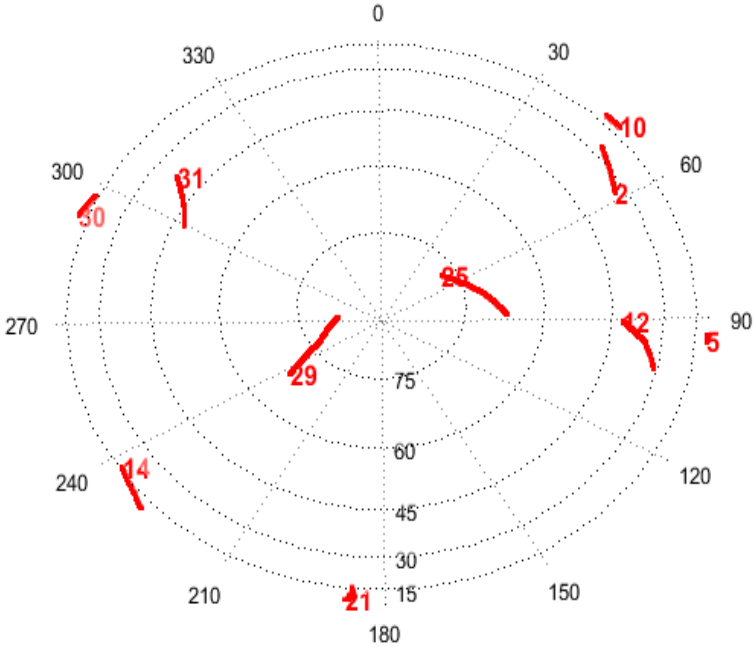

Figure 4-13 Satellites in View Skyplot in the ENU Reference Frame.

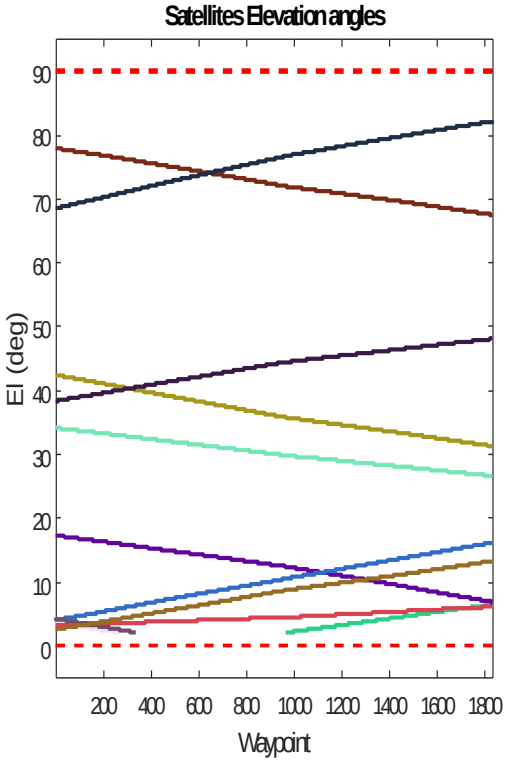

Figure 4-14 Satellites Elevation.

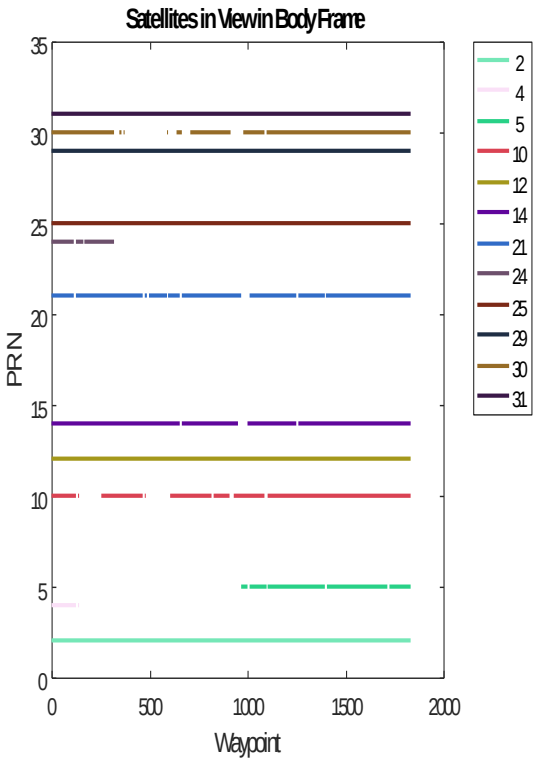

Figure 4-15 Satellites visibility by PRN.

Figure 4-13 shows the sky view of the path and the number of the GPS satellites in view in the ENU reference frame.

Figure 4-14 shows the elevation angle of all the satellites along the path. This figure makes easy to identify which satellites were lost due to the shadowing effect or because it set below the horizon, e.g. satellite number 24 (the grey descending line on the bottom left side of the picture) sets below the horizon between WP 300 and 400, reducing the number of satellite in view.

Figure 4-14 instead shows the visibility of the satellites, ordered by PRN number on the y-axis, along the trajectory in the body reference frame. Each gap in the line represents a waypoint in which that specific satellite was lost due to the shadowing effect of the aircraft during the manoeuvre or due to the shadowing effect of the surrounding environment.

Figure 4-10 shows that along the 250° turn of the missed approach phase, the aircraft heading angle goes from almost 300° to around 50° with a roll angle of 25°. Along these part of the trajectory, the GNSS receiver loses three satellites, as displayed in Figure 4-11 and by comparing Figure 4-13, Figure 4-14 and Figure 4-14, it is easy to define that the GPS satellites with PRN 14, 21 and 30 are the one below the receiver's local horizon and the following graphs show the impact on the integrity performances.

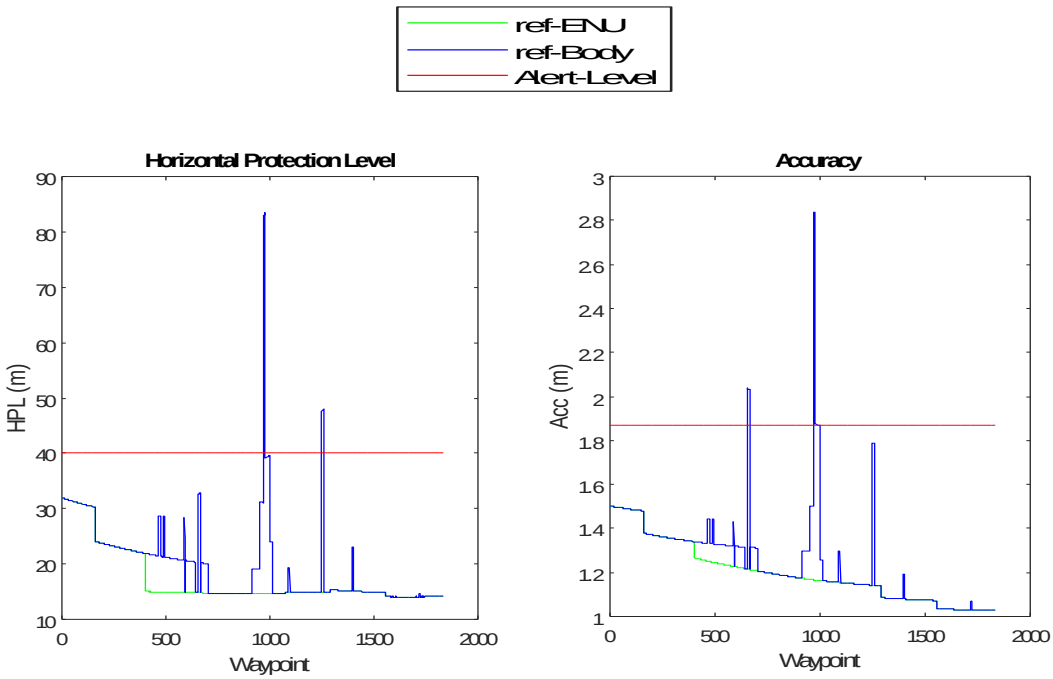

Figure 4-16 HPL in the ENU (green) and Body (blue) Reference Frames compared with the Alert Level (red).

Figure 4-17 VPL in the ENU (green) and Body (blue) Reference Frames compared with the Alert Level (red).

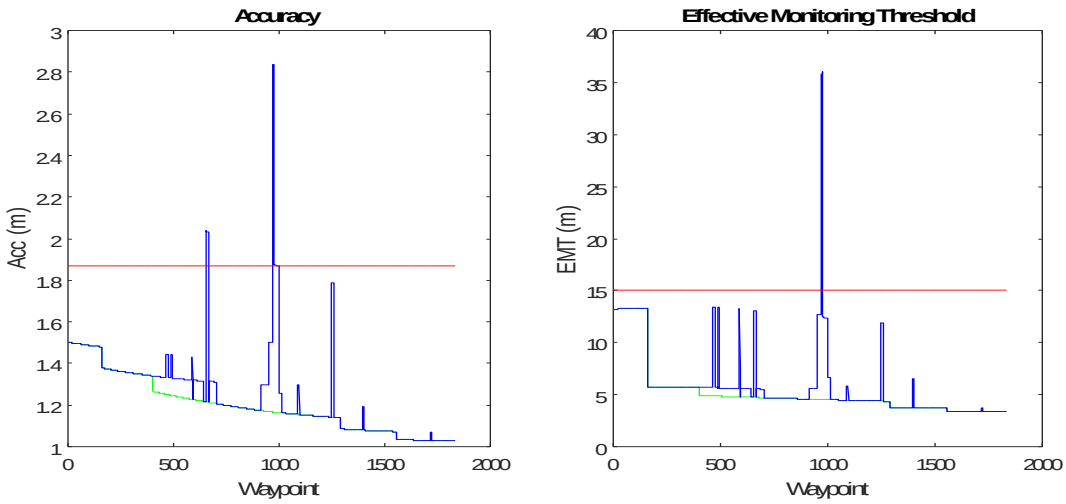

Figure 4-18 Accuracy in the ENU (green) and Body (blue) Reference Frames compared with the Alert Level (red).

Figure 4-19 EMT in the ENU (green) and Body (blue) Reference Frames compared with the Alert Level (red).

Figure 4-16, Figure 4-17, Figure 4-18 and Figure 4-19 show that with the current configuration (single constellation, GPS) and at the current flight time, all the integrity parameters overcome the alert of level due to the limited availability of satellites in

view at around WP 977 (969 for accuracy). Table 4-3 shows the max values that each parameter reaches and in which WP for both the reference frame (ENU and body) and the value that the parameters reach in the ENU reference frame in correspondence of the WP in which the body reference frame reaches the max values. The values below the Alert level (last column on the right) are highlighted in green, the values close but below the AL in yellow and in red are highlighted the values above the AL.

Table 4-4 shows the difference in percentage between the maximum values in the body reference frame and the correspondent values in the ENU reference frame together with the difference in percentage between the Body max values and the Alert Level. All the parameters in the Body frame overtake that Alert Levels with a minimum of 50% of their values to up to a maximum of 140%.

Table 4-3 Values Comparison between ENU and Body Reference Frames.

Performance Parameter	Max_{ENU}	WP_{Max_ENU}	Max_{Body}	WP_{Max_Body}	ENU at WP_{Max_Body}	AL
HPL (m)	30.1	1	79.31	977	13.58	**40**
VPL (m)	29.5	130	79.02	977	12.56	**35**
EMT (m)	13.35	158	36.08	977	4.54	**15**
Accuracy (m)	1.5	1	2.84	969	1.17	**1.87**

Table 4-4 Percentage Differences between Max Values in Body Reference Frame, related ENU values and Alert Level.

Performance Parameter	Δ% between Body and ENU at WP_{Max_Body}	Δ% between Max_{Body} and AL
HPL (m)	484.01	98.27
VPL (m)	528.87	125.78
EMT (m)	694.83	140.55
Accuracy (m)	143.21	51.75

- ***Single constellation GPS: Yuma almanac week 703 (TOA 319488s), reset time [0d 0h 0m 0s], mask angle 2°***

For this case, there is only a slight variation respect to the previous scenario. The constellation considered is still GPS, what is changed is the mask angle that has been reduced to 2° in order to evaluate that effects generate the introduction of new satellites in the configuration, even though their elevation angle is very low and so having bigger biases.

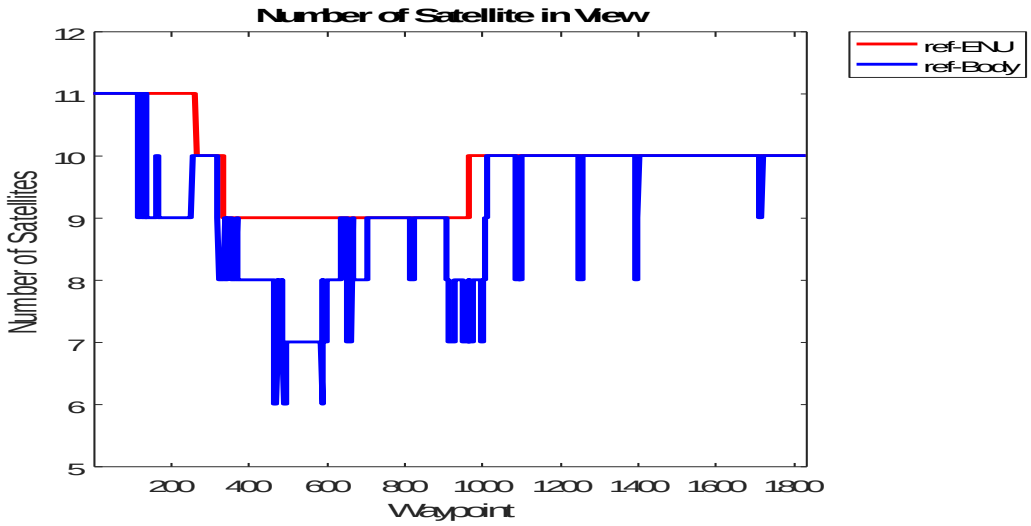

Figure 4-20 Number of Satellites in view in the ENU (red) and Body (blue) Reference Frames along the Trajectory.

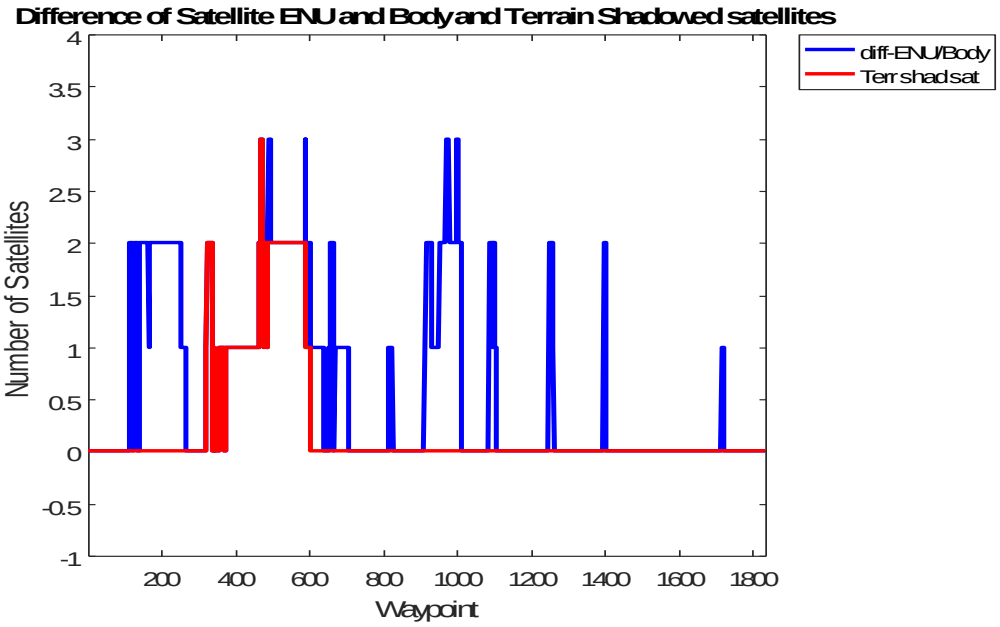

Figure 4-21 Number of Shadowed Satellites by Aircraft Attitude (blue) and Terrain (red)

By comparing Figure 4-20 and Figure 4-11, it is already clear how the reduction of the mask angle has changed the scenario along the flight path, in particular in the first part, in which the number of satellites in view has increased from 6 to 11, due to the fact that 5 satellites are below the 5° degree elevation angle, that are satellite 4, 10, 21, 24 and 29. By checking Figure 4-23 it is clear that the elevation angles of satellites 4 and 24 are decreasing and eventually fall below the 2° mask angle around WP 400, while for satellites 10, 21 and 29, the elevation angle is increasing but starting from a very low value and for this reason filtered out in the previous case.

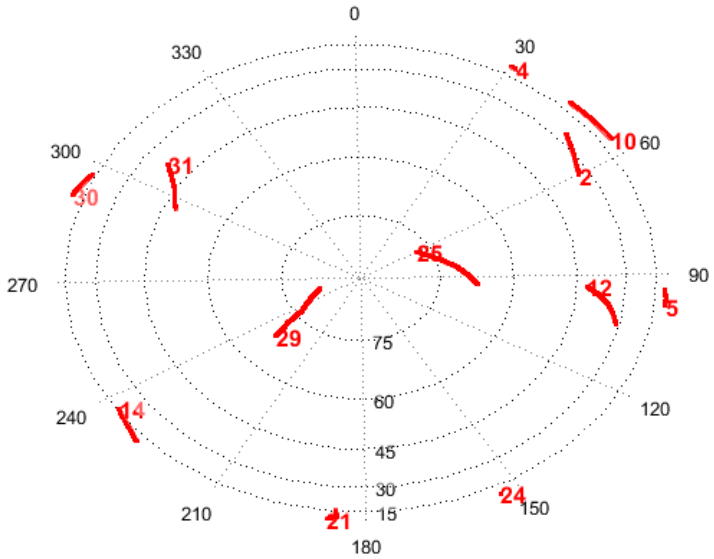

Figure 4-22 Satellites in View Skyplot in the ENU reference frame.

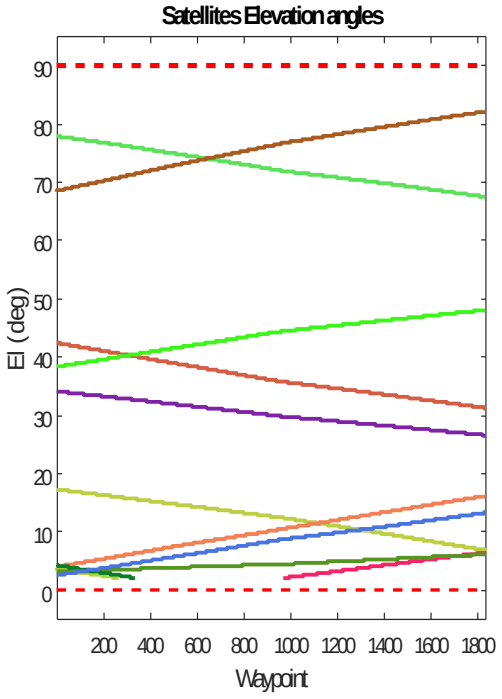

Figure 4-23 Satellites Elevation.

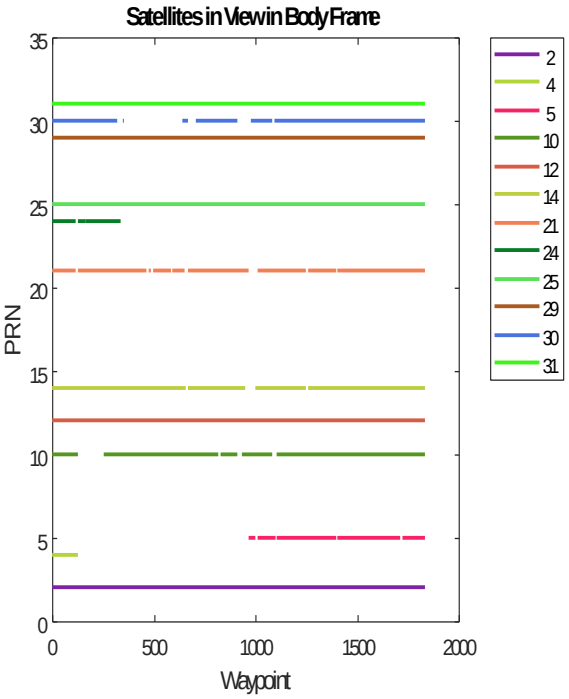

Figure 4-24 Satellites visibility by PRN.

Figure 4-20 and Figure 4-21 also show that decreasing the mask angle has increased the occurrences of LoSs since each manoeuvre performed by the aircraft and the surrounding environment easily shadow the satellites with low elevation.

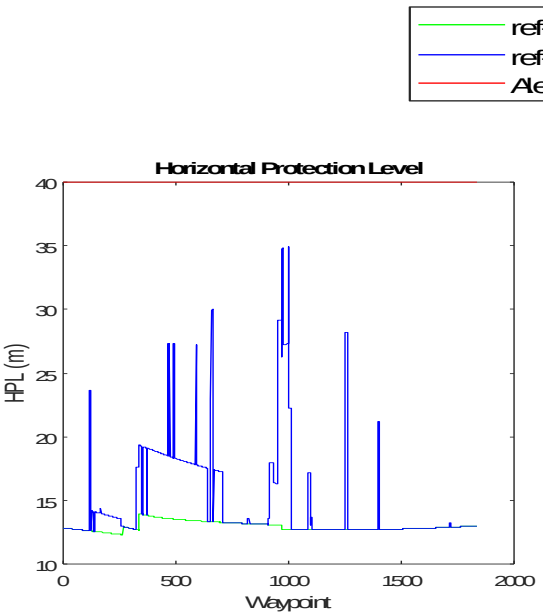

Figure 4-25 HPL in the ENU (green) and Body (blue) Reference Frames compared with the Alert Level (red).

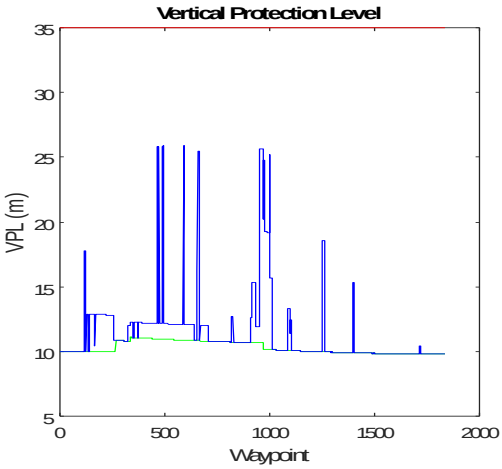

Figure 4-26 VPL in the ENU (green) and Body (blue) Reference Frames compared with the Alert Level (red).

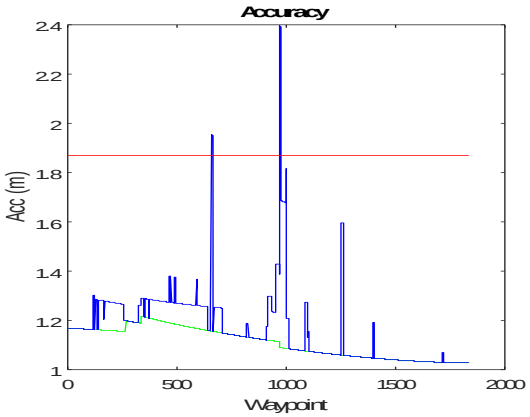

Figure 4-27 Accuracy in the ENU (green) and Body (blue) Reference Frames compared with the Alert Level (red).

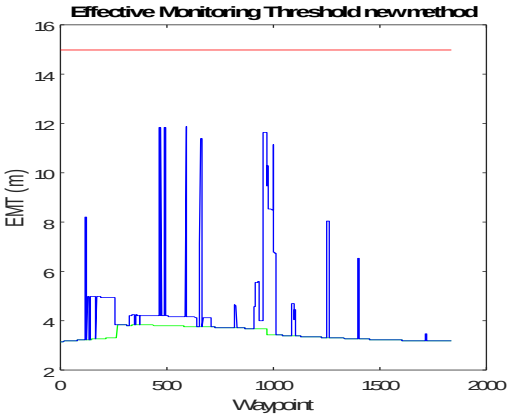

Figure 4-28 EMT in the ENU (green) and Body (blue) Reference Frames compared with the Alert Level (red).

Comparing the graphs from Figure 4-20 to Figure 4-27 with the graphs of the previous scenario, it is possible to see that the increase of number of satellites in view has decreased the average values of the performance parameters that now do not overtake the alert level, except for the accuracy. In the previous case, around WP

1000, the number of satellite in view dropped to five, limiting the redundancy in the system and bringing the integrity parameters above the alert levels. With the reduced mask angle, the number of satellites in view for this specific location and scenario has increased to seven, positively affecting the results.

Table 4-5 Values Comparison between ENU and Body Reference Frames.

Performance Parameter	Max_{ENU}	WP_{Max_ENU}	Max_{Body}	WP_{Max_Body}	ENU at WP_{Max_Body}	AL
HPL (m)	13.98	337	34.97	1001	12.73	**40**
VPL (m)	11.09	337	29.29	467	10.96	**35**
EMT (m)	3.85	337	13.37	467	3.8	**15**
Accuracy (m)	1.21	337	2.4	969	1.09	**1.87**

Table 4-6 Percentage Differences between Max Values in Body Reference Frame, related ENU values and Alert Level.

Performance Parameter	Δ% between Body and ENU at WP_{Max_Body}	Δ% between Max_{Body} and AL
HPL (m)	174.63	-12.58
VPL (m)	138.61	-16.3
EMT (m)	214.63	-10.85
Accuracy (m)	119.73	28.08

Table 4-5 and Table 4-6 confirm that the integrity parameters improved with the addition of new redundant satellites (as expected) aside for the accuracy that is still above the alert level and the other PLs are very close to the ALs (10-16% lower), giving limited margin in case of a sudden increase or change in the values of signal errors and biases. For completeness of the analysis, in Appendix D it has been included the single constellation configuration (GPS) with receiver's mask angle equal to 0°.

- ***Single constellation Galileo 24SV: Yuma almanac provided with MAAST, reset time [0d 0h 0m 0s], mask angle 5°***

For this case, the single constellation using the Galileo configuration with 24 satellites has been considered together with the mask angle of 5°.

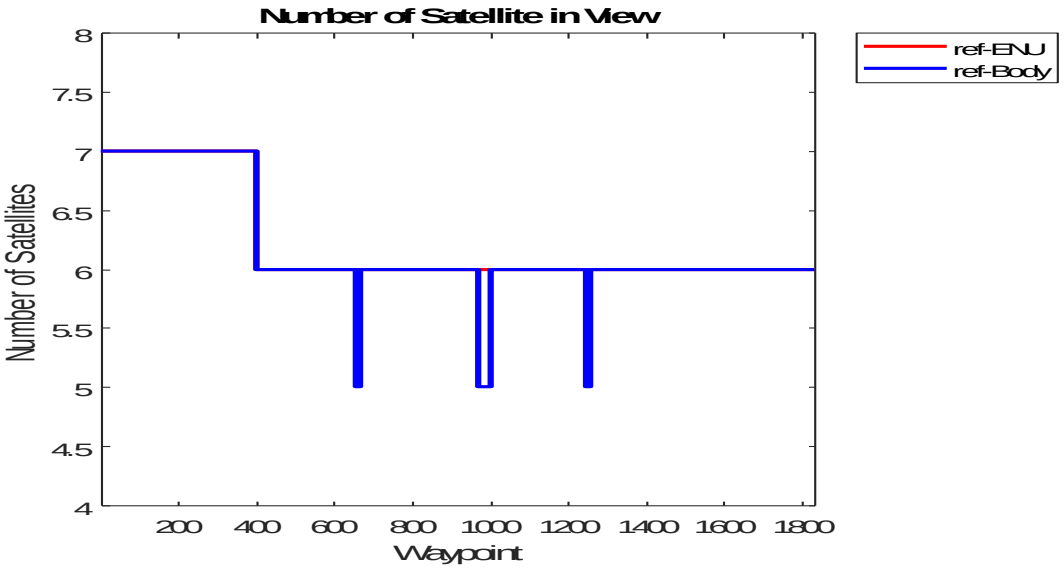

Figure 4-29 Number of Satellites in view in the ENU (red) and Body (blue) Reference Frames along the Trajectory.

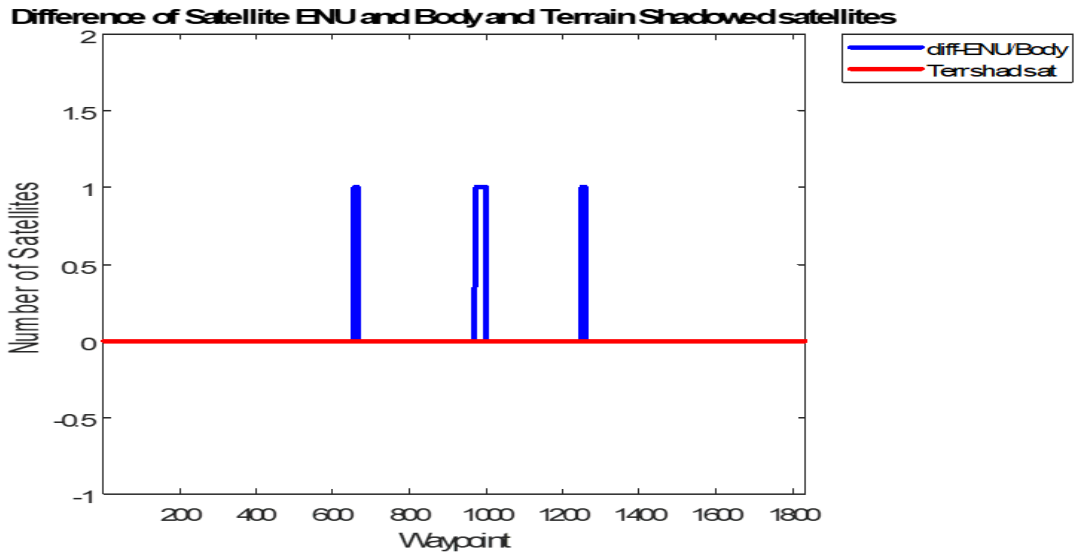

Figure 4-30 Number of Shadowed Satellites by Aircraft Attitude (blue) and Terrain (red).

Figure 4-29, Figure 4-30 and Figure 4-31 show that in this particular configuration, there are few satellites that are shadowed along the flight path and none of them Galileo satellites is shadowed by the surrounding environments but only by the attitude of the aircraft. Due to the reduced size of the picture, it is not easy to spot in Figure 4-32 that the satellite lost three times along the trajectory in three different WP is the PRN n. 76, between WP 600-700, around 1000 and between 1200-1300. In these three manoeuvres the aircraft is banking with an angle of 20-25° in a direction that generates a mask on satellite 76.

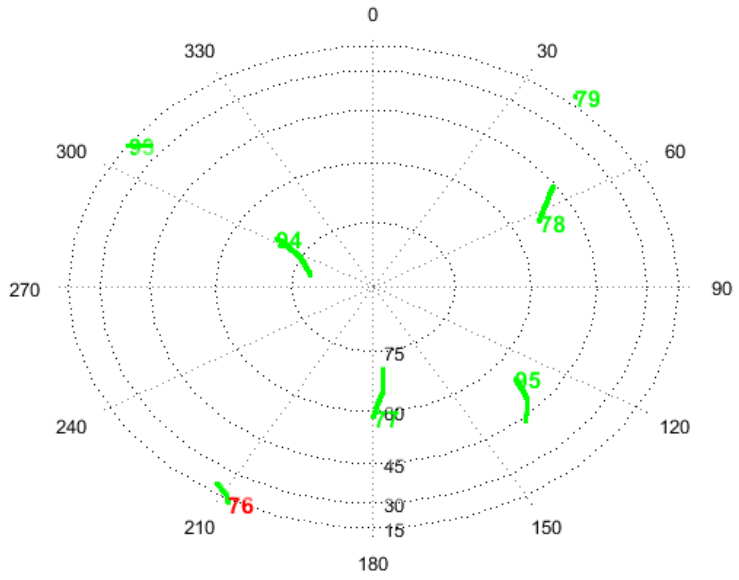

Figure 4-31 Satellites in View Skyplot in the ENU reference frame.

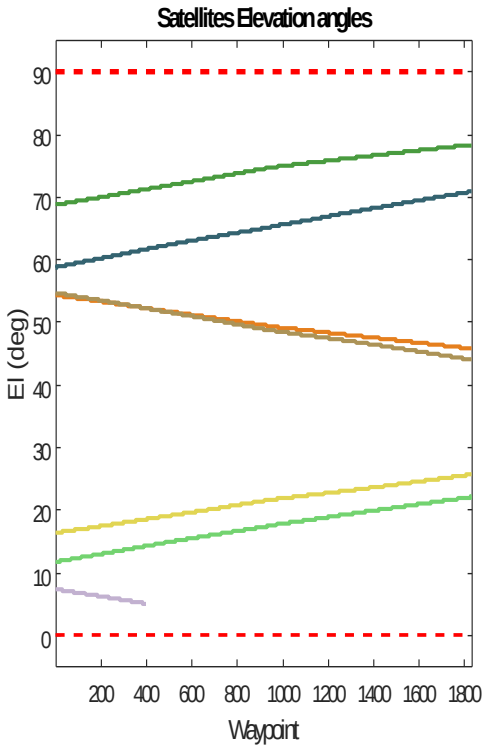

Figure 4-32 Satellites Elevation.

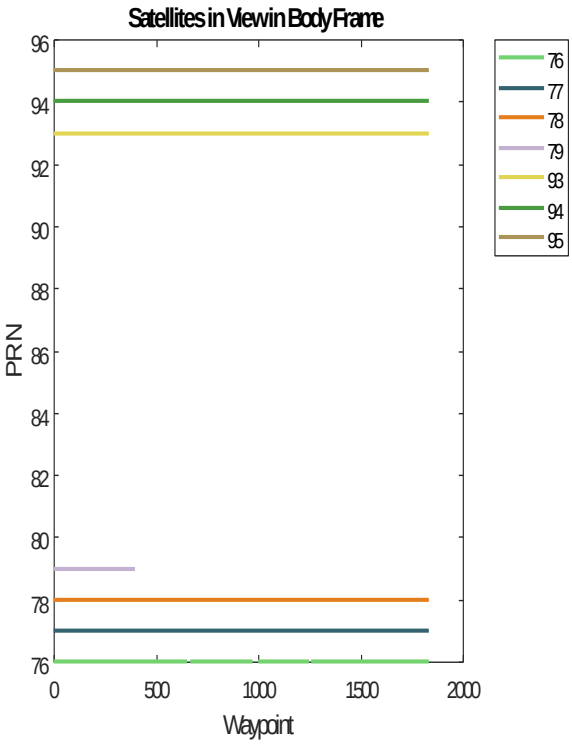

Figure 4-33 Satellites visibility by PRN.

Figure 4-34 to Figure 4-37 show that each event of a loss of a satellite generates a peak in the integrity parameters, in particular due to the fact that each satellite lost reduces the number of available ones to five, limiting the redundancy of the system and affecting the performances of the technique. The only parameter that remains within the Alert Level is the accuracy.

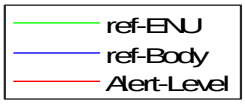

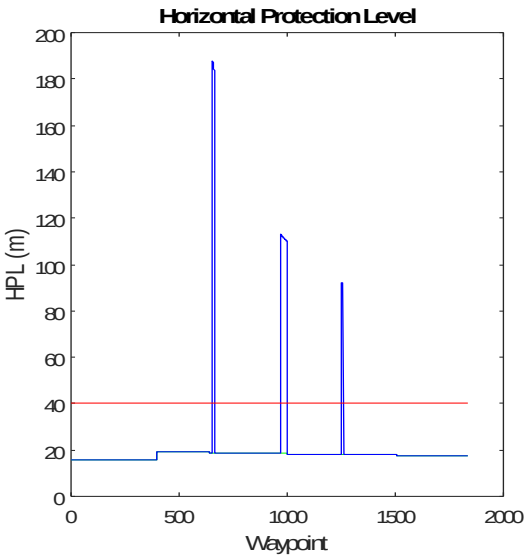

Figure 4-34 HPL in the ENU (green) and Body (blue) Reference Frames compared with the Alert Level (red).

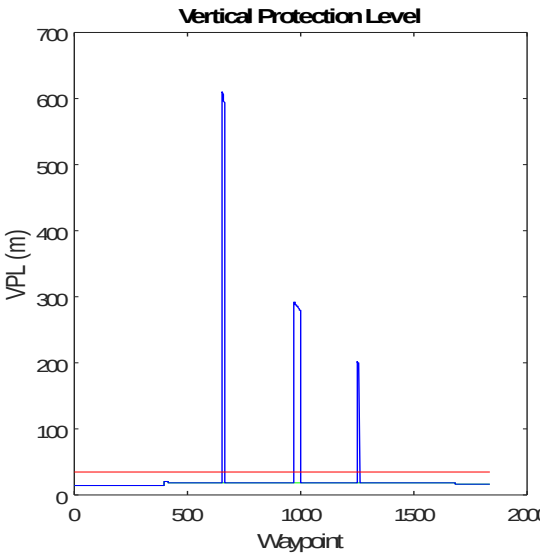

Figure 4-35 VPL in the ENU (green) and Body (blue) Reference Frames compared with the Alert Level (red).

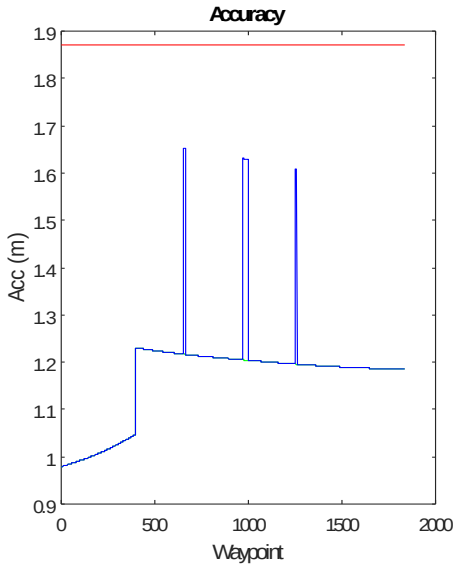

Figure 4-36 Accuracy in the ENU (green) and Body (blue) Reference Frames compared with the Alert Level (red).

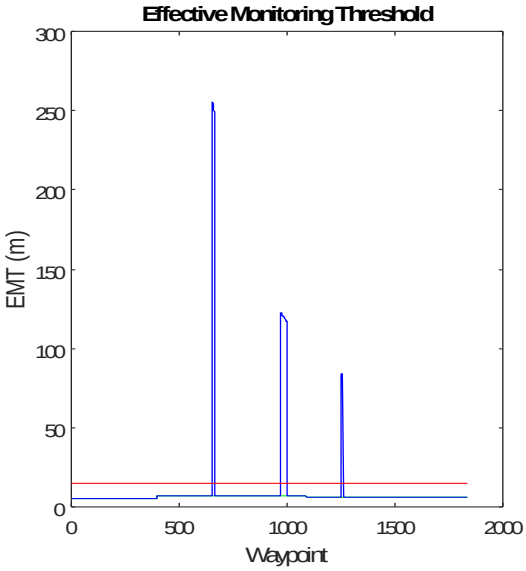

Figure 4-37 EMT in the ENU (green) and Body (blue) Reference Frames compared with the Alert Level (red).

Table 4-7 and Table 4-8 show the maximum values reached by the parameters in the two reference frame and their difference in percentage, in particular the maximum values in the body reference frame respect to the Alert levels, that in this case range between the 370% for the HPL to up to the 1600% of VPL and EMT.

Table 4-7 Values Comparison between ENU and Body Reference Frames.

Performance Parameter	Max_{ENU}	WP_{Max_ENU}	Max_{Body}	WP_{Max_Body}	ENU at WP_{Max_Body}	AL
HPL (m)	19.39	399	187.54	655	18.96	40
VPL (m)	19.55	399	609.43	655	19.06	35
EMT (m)	7.36	399	255.16	655	7.05	15
Accuracy (m)	1.23	399	1.65	655	1.22	1.87

Table 4-8 Percentage Differences between Max Values in Body Reference Frame, related ENU values and Alert Level.

Performance Parameter	Δ% between Body and ENU at WP_{Max_Body}	Δ% between Max_{Body} and AL
HPL (m)	889.34	368.86
VPL (m)	3097.7	1641.2
EMT (m)	3518.2	1601.1
Accuracy (m)	35.77	-11.65

- ***Single constellation Galileo 27SV: Yuma almanac provided with MAAST, reset time [0d 0h 0m 0s], mask angle 5°***

The main difference of this scenario respect to the previous one is that analyses the Galileo constellation configuration with 27 satellites in orbit.

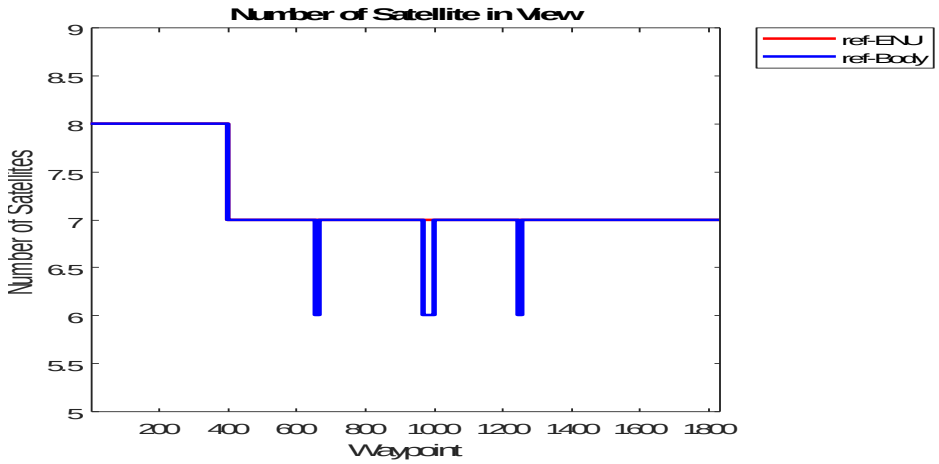

Figure 4-38 Number of Satellites in view in the ENU (red) and Body (blue) Reference Frames along the Trajectory.

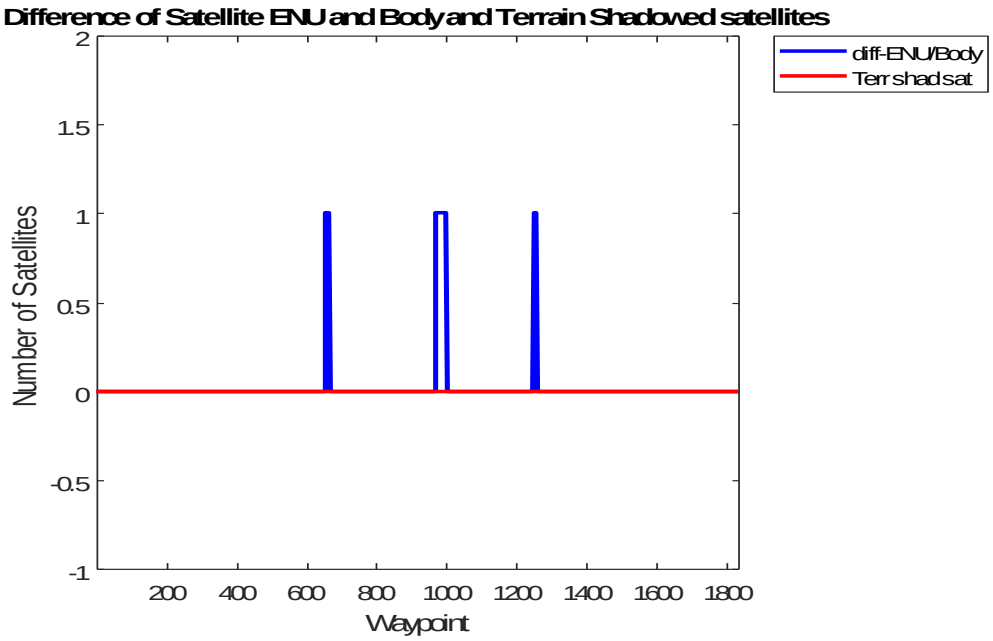

Figure 4-39 Number of Shadowed Satellites by Aircraft Attitude (blue) and Terrain (red).

Figure 4-38 Number of Satellites in view in the ENU (red) and Body (blue) Reference Frames along the Trajectory. and Figure 4-39 show that the overall shadowing effect hasn't changed respect to the 24SV configuration, but the increase on number of satellite in orbit has actually helped this particular scenario, since the number of total satellite in view has increased of one unity, bringing the minimum number reached in the body reference frame to six and providing support to the integrity performances. By comparing Figure 4-31 Satellites in View Skyplot in the ENU reference frame. with Figure 4-40 Satellites in View Skyplot in the ENU reference frame.it is easy to define that the added satellite is PRN 101, that having a high elevation angle in this specific scenario, it remains visible for the whole trajectory.

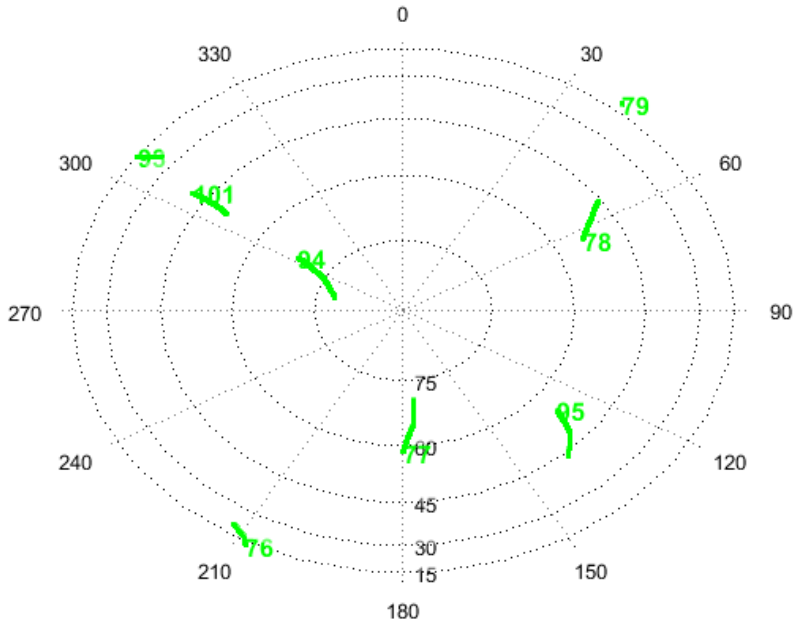

Figure 4-40 Satellites in View Skyplot in the ENU reference frame.

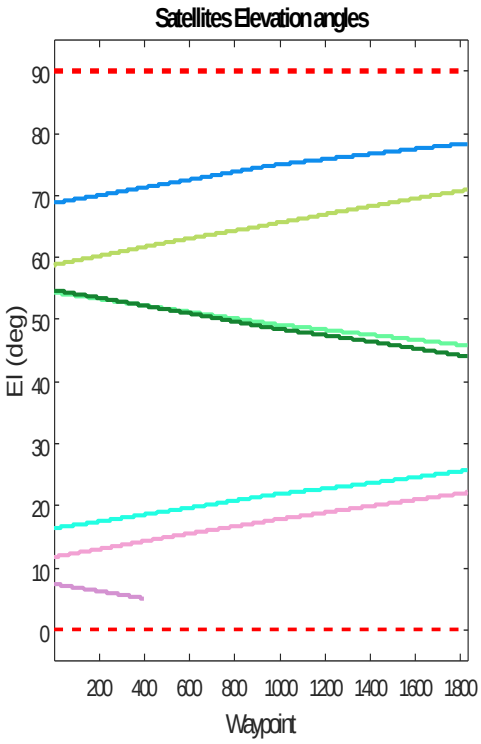

Figure 4-41 Satellites Elevation.

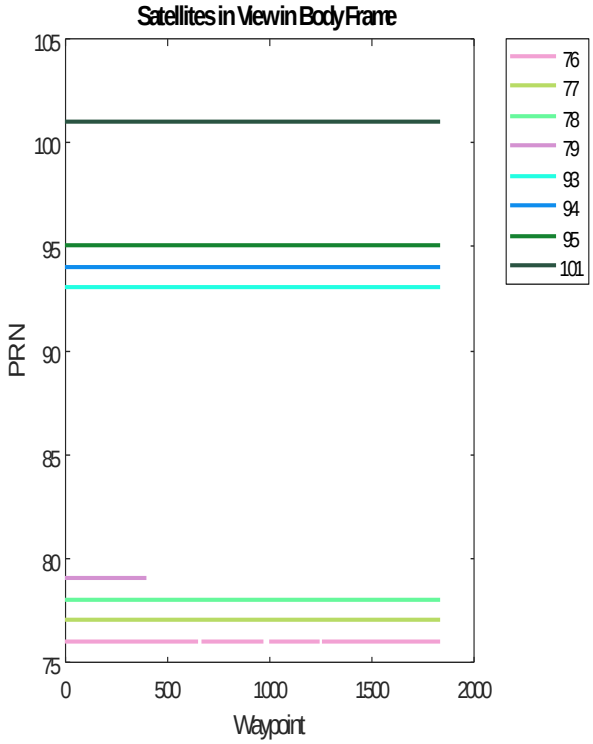

Figure 4-42 Satellites visibility by PRN.

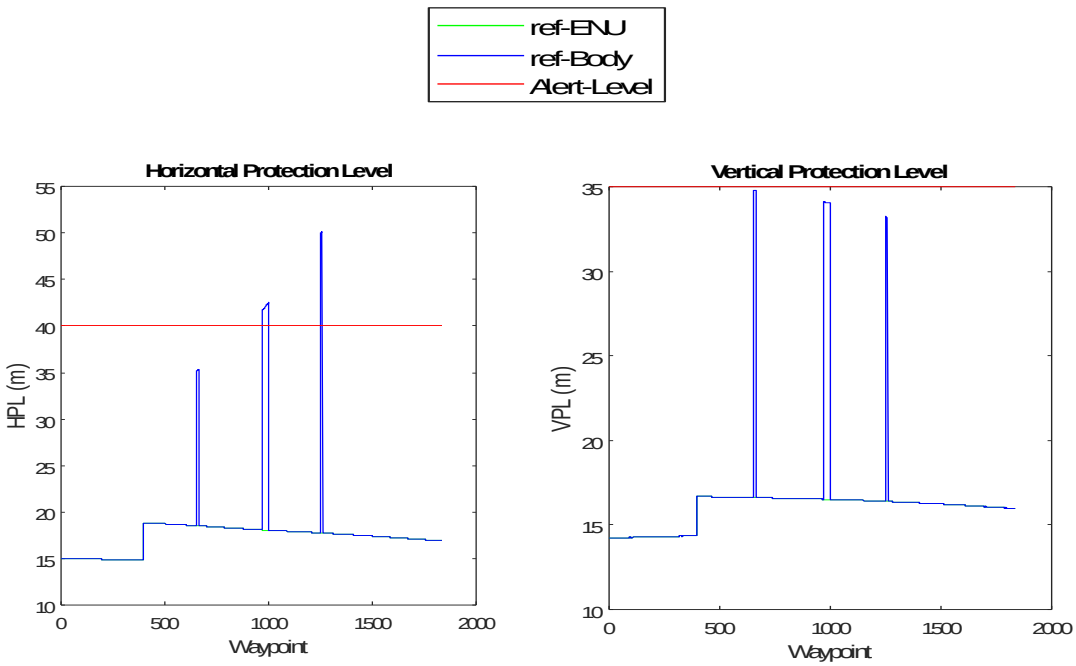

Figure 4-43 HPL in the ENU (green) and Body (blue) Reference Frames compared with the Alert Level (red).

Figure 4-44 VPL in the ENU (green) and Body (blue) Reference Frames compared with the Alert Level (red).

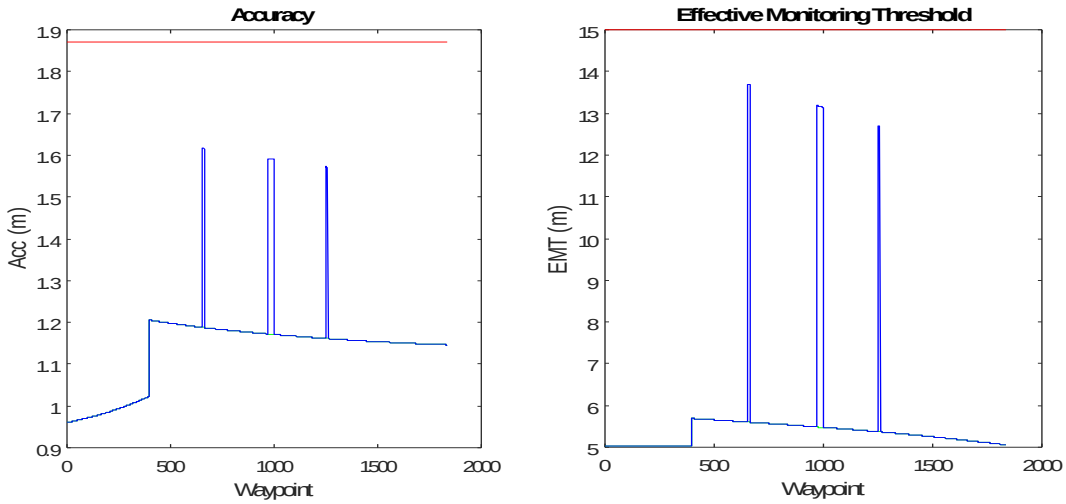

Figure 4-45 Accuracy in the ENU (green) and Body (blue) Reference Frames compared with the Alert Level (red).

Figure 4-46 EMT in the ENU (green) and Body (blue) Reference Frames compared with the Alert Level (red).

Figure 4-43 to Figure 4-46 show that even the addition of a single satellite can drastically improve the performances; in this scenario, only the HPL is overtaking the Alert levels on two occasions. However, it needs to be noticed that both the VPL and EMT are very close to the limits, so it is enough a slight deviation of the parameters

used in this simulation that these parameters could generate an integrity outage (that in this case is already triggered by the HPL).

Table 4-9 and Table 4-10 show the values reached by the different parameters. The latter one in particular shows that VPL, EMT and accuracy are few percentages below the alert levels.

Table 4-9 Values Comparison between ENU and Body Reference Frames.

Performance Parameter	Max_{ENU}	WP_{Max_ENU}	Max_{Body}	WP_{Max_Body}	ENU at WP_{Max_Body}	AL
HPL (m)	18.86	399	50.18	1258	17.75	**40**
VPL (m)	16.69	400	34.82	655	16.63	**35**
EMT (m)	5.69	399	13.69	655	5.6	**15**
Accuracy (m)	1.20	399	1.62	655	1.18	**1.87**

Table 4-10 Percentage Differences between Max Values in Body Reference Frame, related ENU values and Alert Level.

Performance Parameter	Δ% between Body and ENU at WP_{Max_Body}	Δ% between Max_{Body} and AL
HPL (m)	182.71	25.45
VPL (m)	109.4	-0.53
EMT (m)	144.39	-8.71
Accuracy (m)	36.08	-13.55

This case clearly shows the difference between having a full operational Galileo constellation (27SV) and a quasi-full operational constellation (24SV). In this configuration, the aircraft has an additional satellite in view along the trajectory that allows keeping some of the parameters below the alert levels, the only exception is the HPL

- ***Single constellation GLONASS: Yuma almanac provided with MAAST, reset time [0d 0h 0m 0s], mask angle 5°***

After having analysed the performances of the single constellation with GPS and Galileo (with two different configuration), it is worth to analyse the performances of the Russian constellation, due to its particular configuration, in particular of the orbit. The almanac used in this research considers the GLONASS constellation with 23 operational satellite.

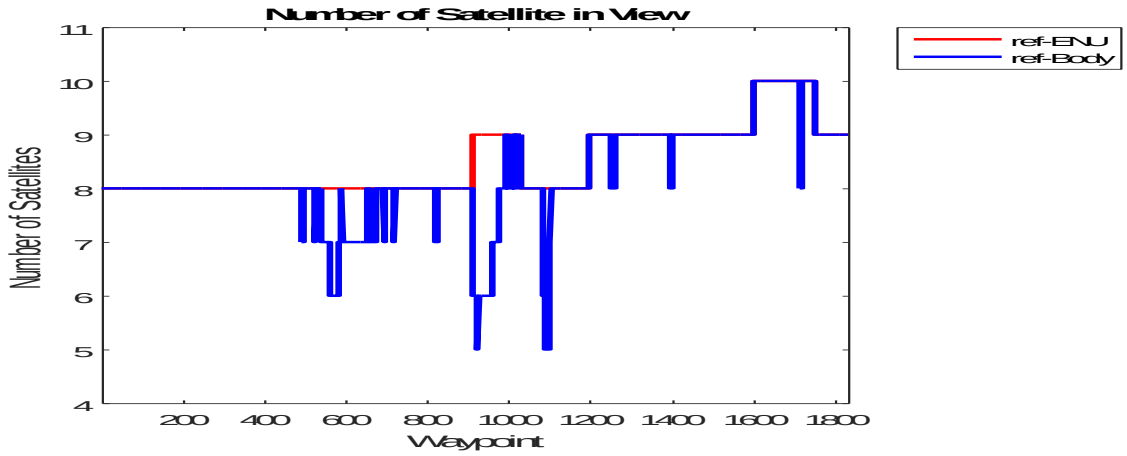

Figure 4-47 Number of Satellites in view in the ENU (red) and Body (blue) Reference Frames along the Trajectory.

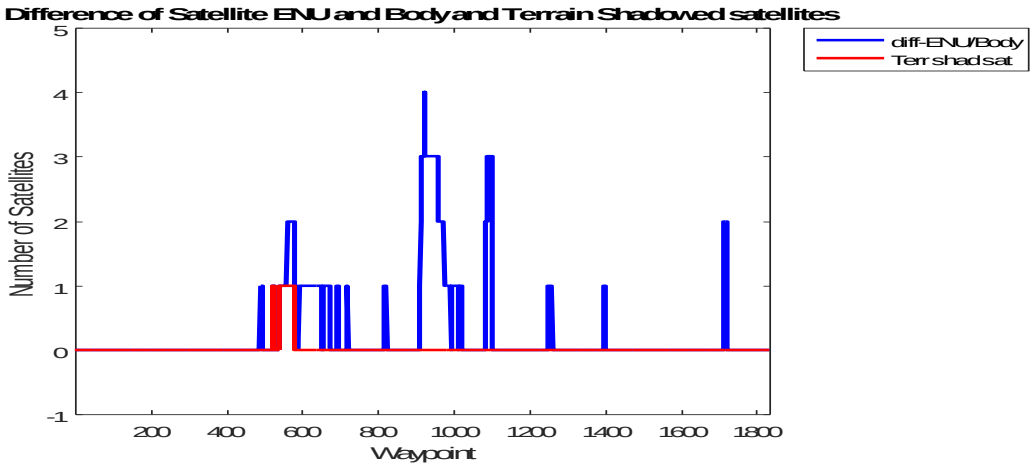

Figure 4-48 Number of Shadowed Satellites by Aircraft Attitude (blue) and Terrain (red).

Figure 4-49 shows that in this particular simulation, the GLONASS constellation presents several satellites with low elevation angle, in particular in the second half of the trajectory, as it can be seen in the bottom right part of Figure 4-50, making them much easier to be shadowed. Figure 4-47, Figure 4-48 confirm this concern and the aircraft loses the LoS with the satellites multiple times along the trajectory and losing up to a maximum of four satellites around WP900.

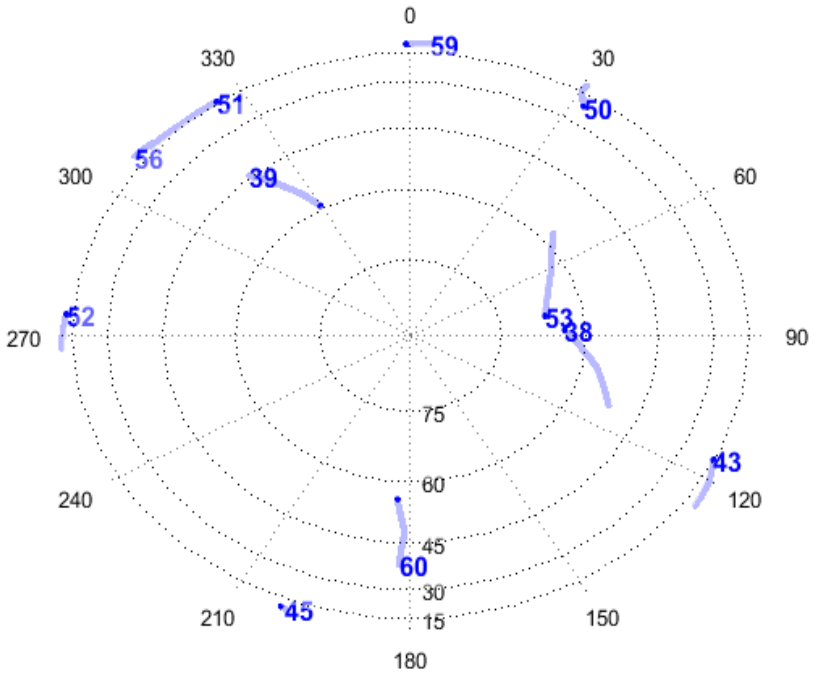

Figure 4-49 Satellites in View Skyplot in the ENU reference frame.

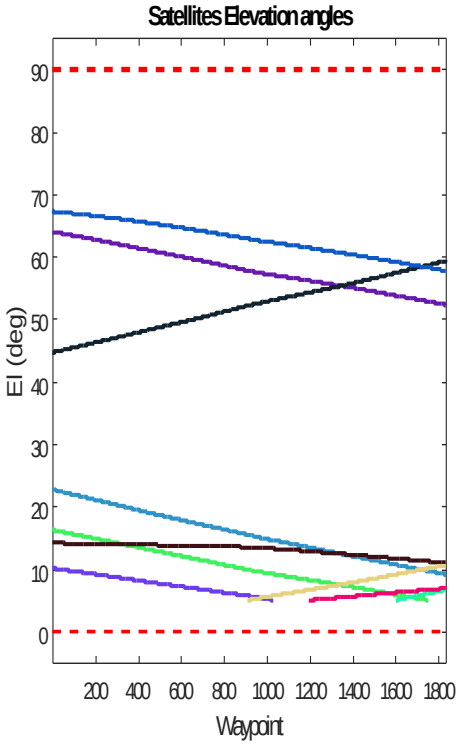

Figure 4-50 Satellites Elevation.

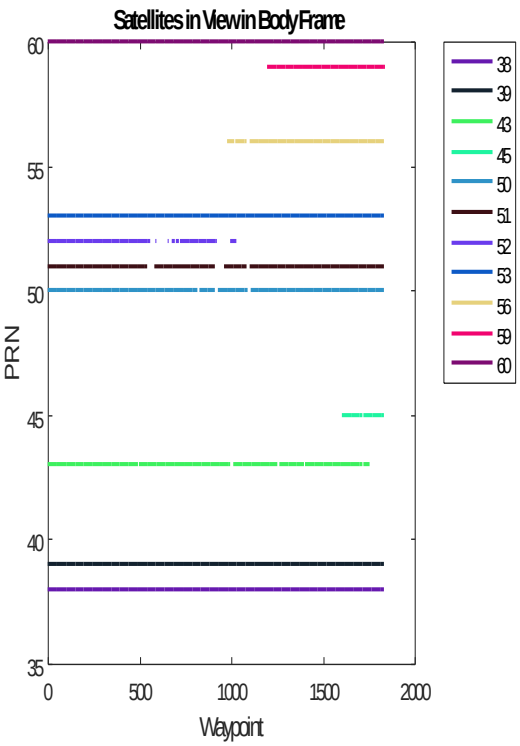

Figure 4-51 Satellites visibility by PRN.

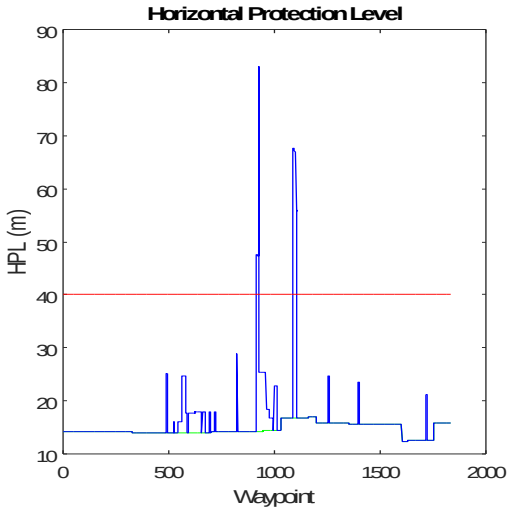

Figure 4-52 HPL in the ENU (green) and Body (blue) Reference Frames compared with the Alert Level (red).

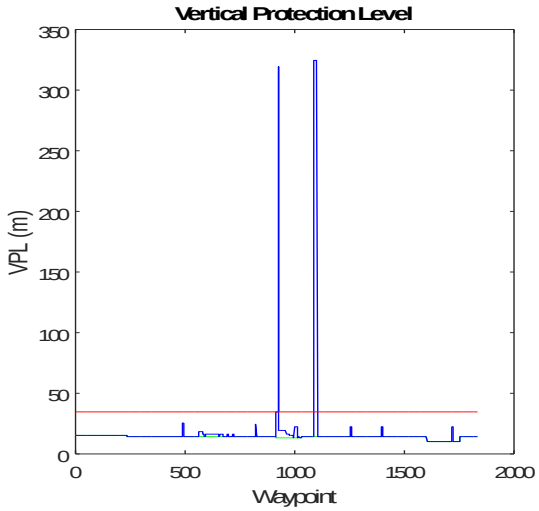

Figure 4-53 VPL in the ENU (green) and Body (blue) Reference Frames compared with the Alert Level (red).

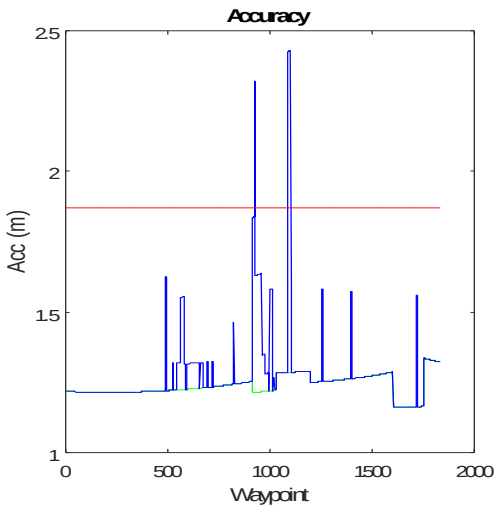

Figure 4-54 Accuracy in the ENU (green) and Body (blue) Reference Frames compared with the Alert Level (red).

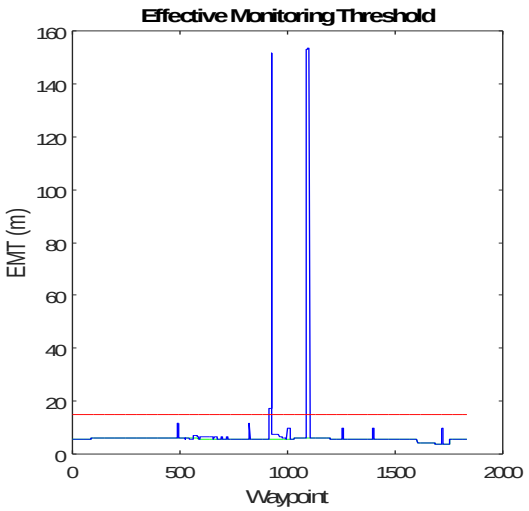

Figure 4-55 EMT in the ENU (green) and Body (blue) Reference Frames compared with the Alert Level (red).

Figure 4-52 to Figure 4-55 confirm the behaviour seen in the previous cases, with the parameters reaching very high values in particular when the number of satellite in view drop below 6 (around WP900 and WP1100).

Table 4-11 and Table 4-12 show that maximum values in the body reference frame reach values as little as 30% higher than the alert level (accuracy) to up to a maximum of 10 times (VPL and EMT)

Table 4-11 Values Comparison between ENU and Body Reference Frames.

Performance Parameter	Max_{ENU}	WP_{Max_ENU}	Max_{Body}	WP_{Max_Body}	ENU at WP_{Max_Body}	AL
HPL (m)	16.9	1195	83.09	924	14.3	40
VPL (m)	15.09	1	324.43	1101	14.79	35
EMT (m)	6.19	1195	153.32	1101	6.18	15
Accuracy (m)	1.33	1753	2.43	1101	1.28	1.87

Table 4-12 Percentage Differences between Max Values in Body Reference Frame, related ENU values and Alert Level.

Performance Parameter	Δ% between Body and ENU at WP_{Max_Body}	Δ% between Max_{Body} and AL
HPL (m)	480.85	107.72
VPL (m)	2093	826.93
EMT (m)	2379.7	922.15
Accuracy (m)	89.12	30.04

The single constellation scenarios analysed so far show that overall the algorithm performs very well if the shadowing effect is not taken into account, all the values in the ENU reference frame are within the alert levels since the satellite geometry is good enough to keep the values low. However, the implemented shadowing effect shows that the loss a satellite generates a peak in the parameters that could lead to an integrity outage, depending on the satellite geometry and the number of satellites in view left.

The above analyses seem to confirm the necessity of integrating more than one constellation, in order to avoid at least cases in which the number of satellites in view drops below six.

In the next section, the different combination of dual-constellation configuration will be analysed.

B. Dual-Constellation Configuration

In this section, different combinations of the three constellations, taken two by two, are analysed.

- GPS and Galileo 24SV
- GPS and Galileo 27SV

- GPS and GLONASS
- Galileo 24SV and GLONASS
- Galileo 27SV and GLONASS

- ***Dual-constellation GPS and Galileo 24SV: Yuma almanac week 703 for GPS, provided with MAAST for Galileo, reset time [0d 0h 0m 0s], mask angle 5°***

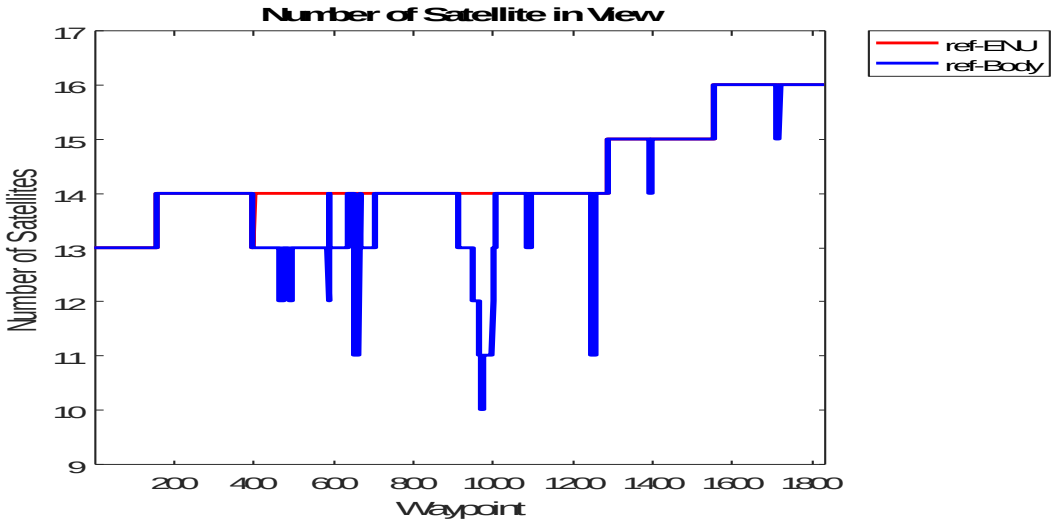

Figure 4-56 Number of Satellites in view in the ENU (red) and Body (blue) Reference Frames along the Trajectory.

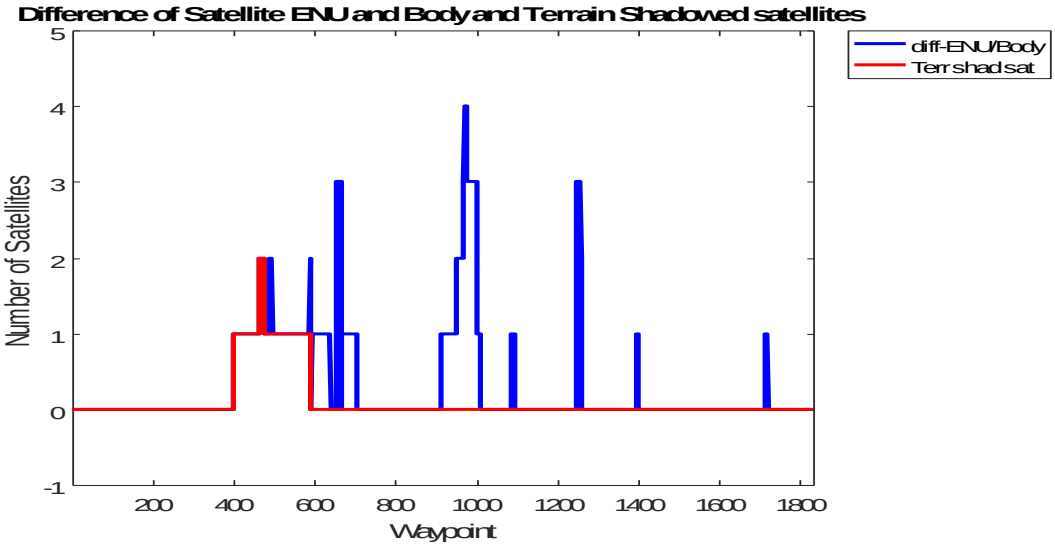

Figure 4-57 Number of Shadowed Satellites by Aircraft Attitude (blue) and Terrain (red).

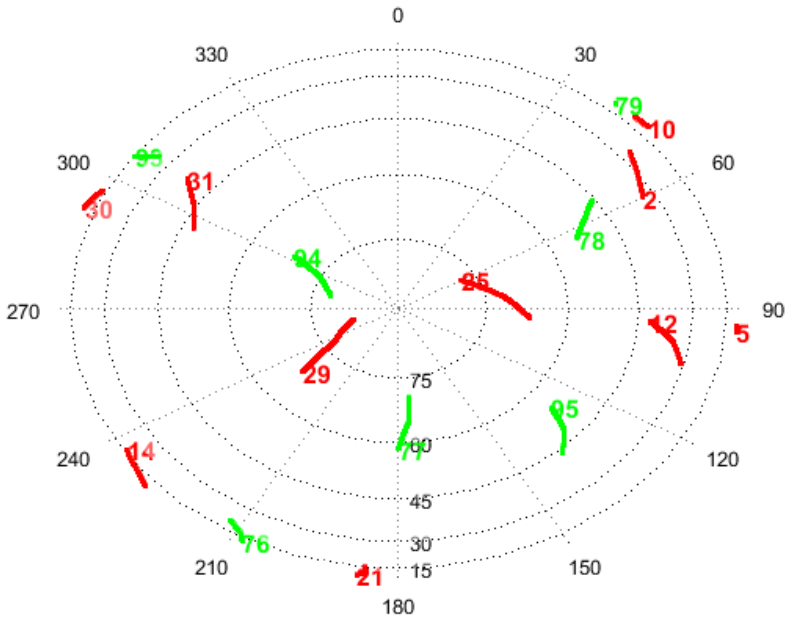

Figure 4-58 Satellites in View Skyplot in the ENU reference frame (GPS in red and Galileo in green).

Figure 4-56 and Figure 4-57 show that the implementation of a dual-constellation system has obviously increased the average number of satellite in view as well as the number of loss of LoS. Figure 4-58 shows in red the GPS satellites and in green the Galileo ones and how the combination of the two constellations improve the variety of positions and geometry, confirmed by Figure 4-59 in which it is possible to see that many ranges of elevation angles are covered along the trajectory

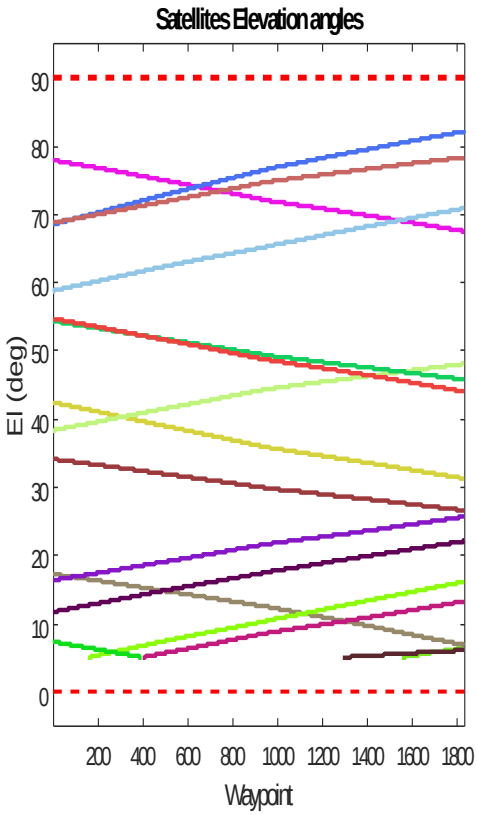

Figure 4-59 Satellites Elevation.

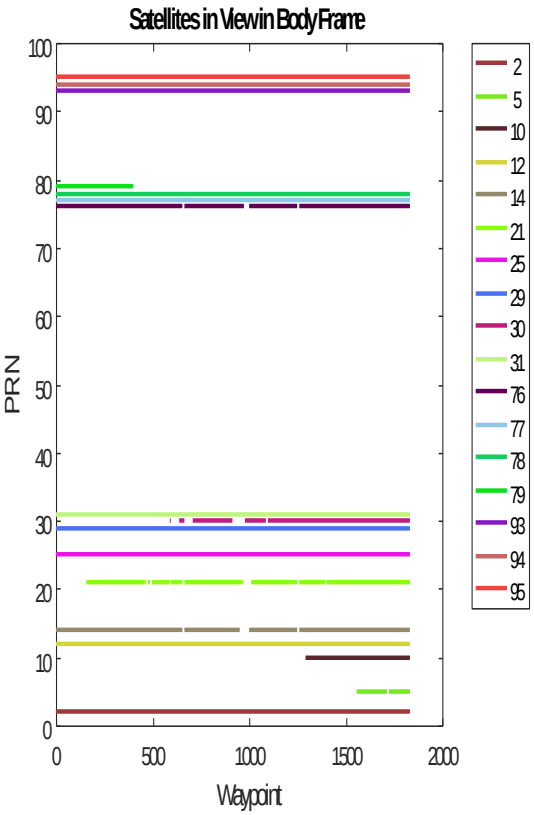

Figure 4-60 Satellites visibility by PRN.

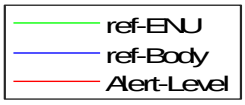

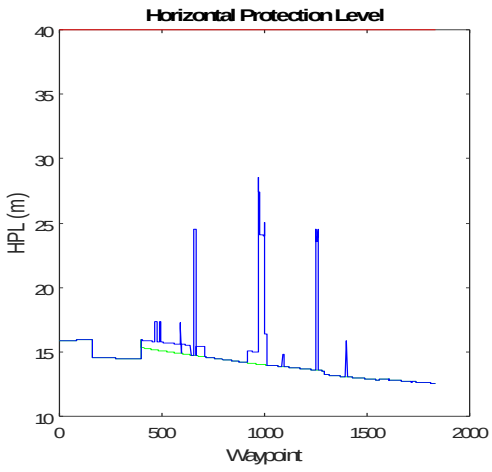

Figure 4-61 HPL in the ENU (green) and Body (blue) Reference Frames compared with the Alert Level (red).

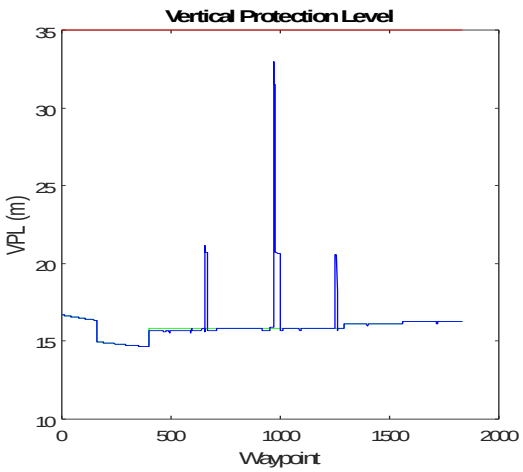

Figure 4-62 VPL in the ENU (green) and Body (blue) Reference Frames compared with the Alert Level (red).

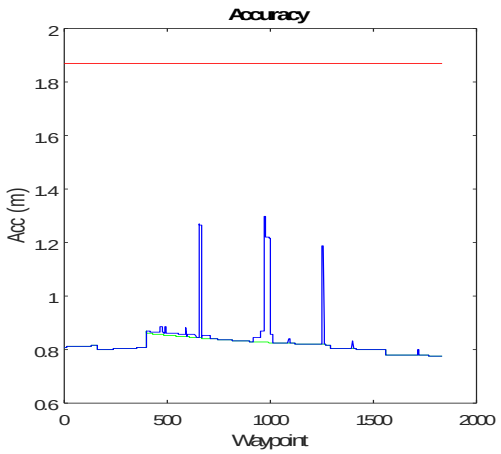

Figure 4-63 Accuracy in the ENU (green) and Body (blue) Reference Frames compared with the Alert Level (red).

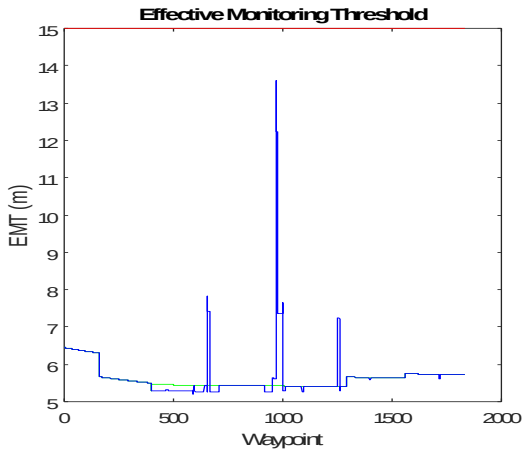

Figure 4-64 EMT in the ENU (green) and Body (blue) Reference Frames compared with the Alert Level (red).

Figure 4-61 to Figure 4-64 confirm that using two different constellations enhances the capabilities of the ARAIM technique, all the parameters that in the previous single-constellation cases were overtaking the limit (at least one of them), in this case all of them stayed within the alert limits. It has to be noticed, however, that for the VPL and the EMT, the values are close to the limits (only 5-10% below as shown in Table 4-14).

Table 4-13 Values Comparison between ENU and Body Reference Frames.

Performance Parameter	Max_{ENU}	WP_{Max_ENU}	Max_{Body}	WP_{Max_Body}	ENU at WP_{Max_Body}	AL
HPL (m)	15.95	158	28.53	969	14.05	**40**
VPL (m)	16.7	1	33	969	15.86	**35**
EMT (m)	6.45	1	13.6	969	5.43	**15**
Accuracy (m)	0.87	399	1.3	971	0.83	**1.87**

Table 4-14 Percentage Differences between Max Values in Body Reference Frame, related ENU values and Alert Level.

Performance Parameter	Δ% between Body and ENU at WP_{Max_Body}	Δ% between Max_{Body} and AL
HPL (m)	103.03	-28.67
VPL (m)	107.82	-5.81
EMT (m)	150.39	-9.4
Accuracy (m)	56.98	-30.52

- ***Dual-constellation GPS and Galileo 27SV: Yuma almanac week 703 for GPS, provided with MAAST for Galileo, reset time [0d 0h 0m 0s], mask angle 5°***

As for the single constellation, also for the dual configuration the Galileo 27SV is considered. As in the previous exanimated cases, the introduction of the 27SV configuration adds only one more satellite to the simulation, as it can be noticed by comparing Figure 4-65 with Figure 4-47 (max number is seventeen in this former picture, against the sixteen of the latter). But considering that the added satellite, number 101, has a high elevation angle, nothing has changed in the number of satellite lost.

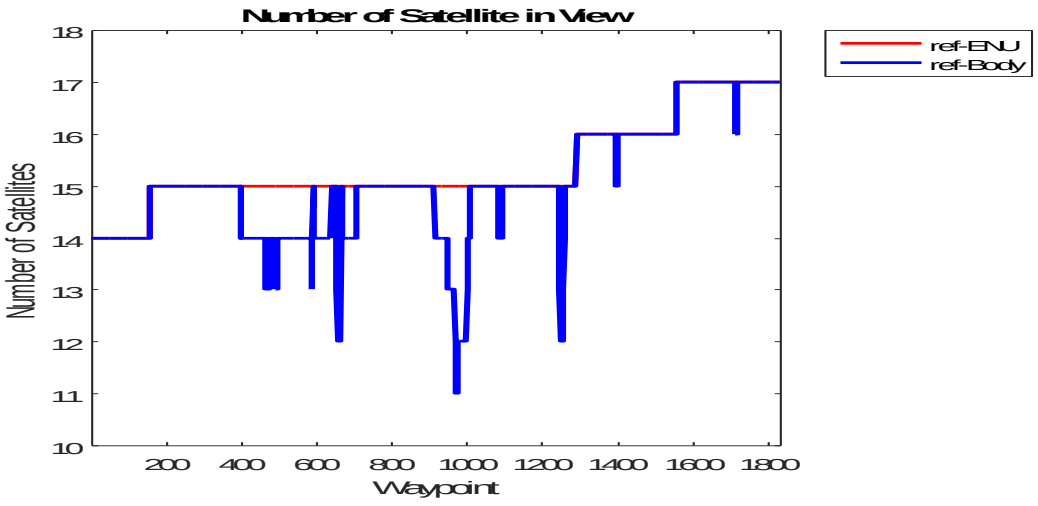

Figure 4-65 Number of Satellites in view in the ENU (red) and Body (blue) Reference Frames along the Trajectory.

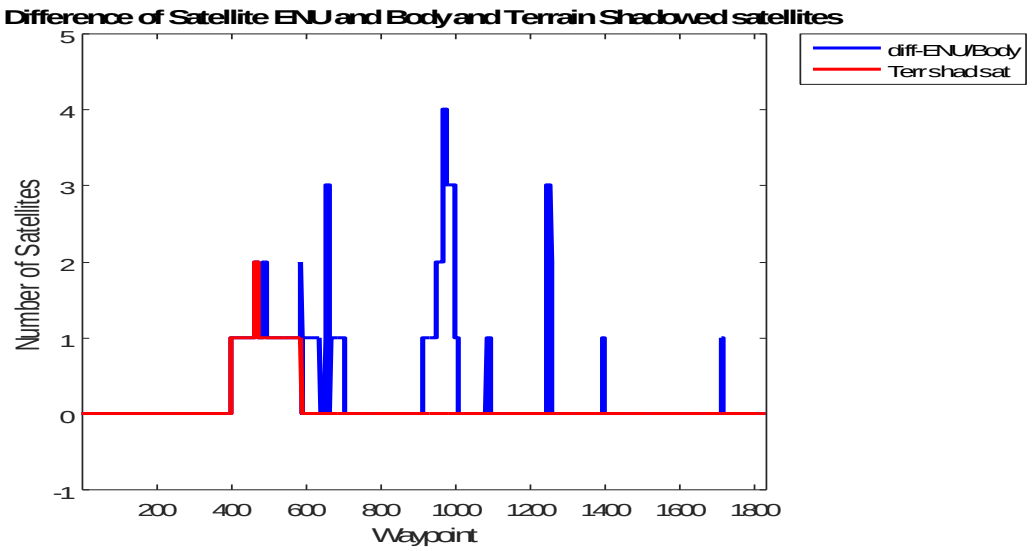

Figure 4-66 Number of Shadowed Satellites by Aircraft Attitude (blue) and Terrain (red).

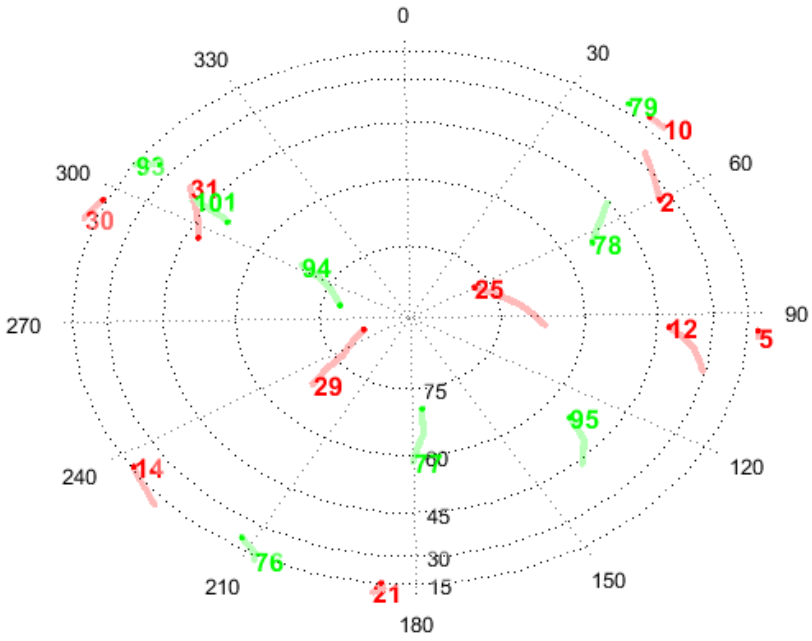

Figure 4-67 Satellites in View Skyplot in the ENU reference frame (GPS in red and Galileo in green).

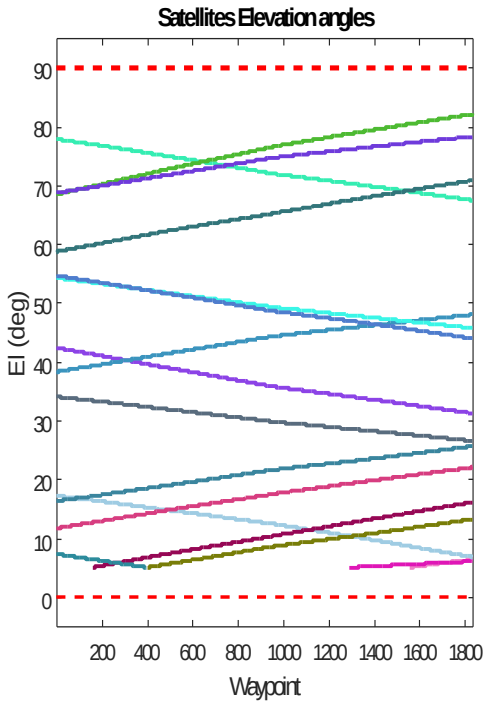

Figure 4-68 Satellites Elevation.

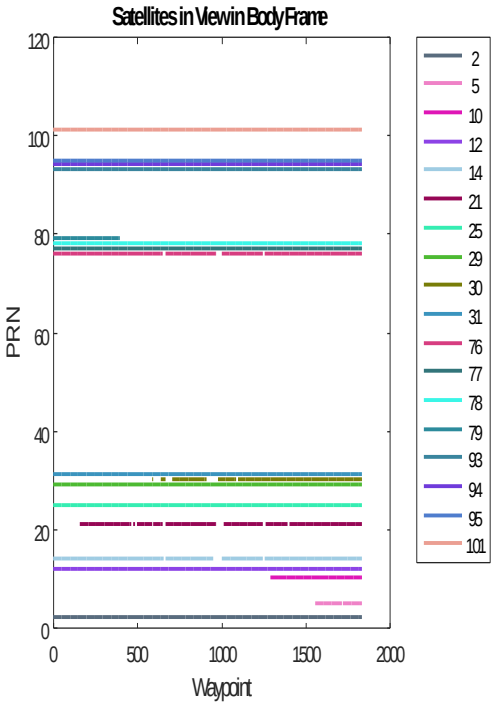

Figure 4-69 Satellites visibility by PRN.

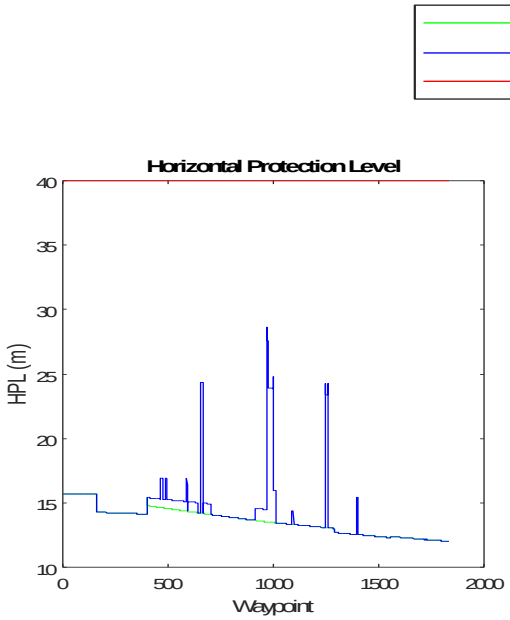

Figure 4-70 HPL in the ENU (green) and Body (blue) Reference Frames compared with the Alert Level (red).

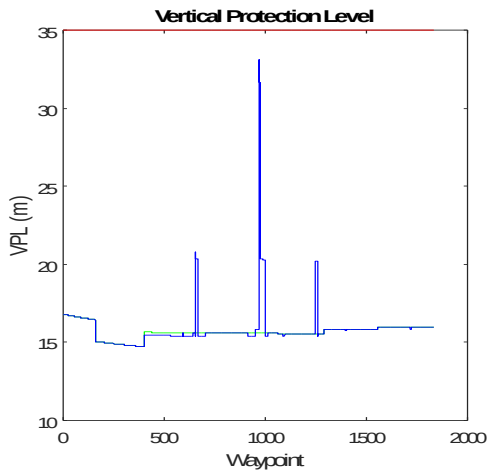

Figure 4-71 VPL in the ENU (green) and Body (blue) Reference Frames compared with the Alert Level (red).

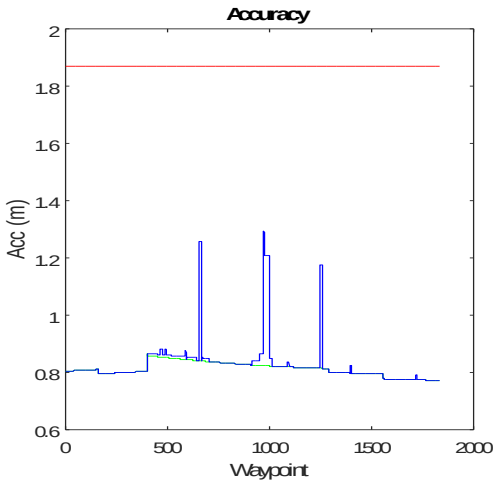

Figure 4-72 Accuracy in the ENU (green) and Body (blue) Reference Frames compared with the Alert Level (red).

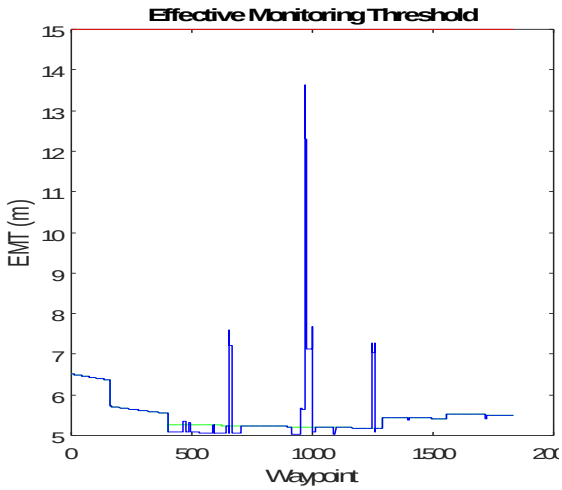

Figure 4-73 EMT in the ENU (green) and Body (blue) Reference Frames compared with the Alert Level (red).

Despite the increase in the number of satellite available, Figure 4-70 to Figure 4-73 and Table 4-15 and Table 4-16 show that almost nothing has changed from the performances point of view, probably due to the fact that the added satellite is in a position in the sky where there is already another satellite and so not bringing a variation in the overall geometry of the scenario, or at least nothing has changed in the geometry of the worst subset .

Table 4-15 Values Comparison between ENU and Body Reference Frames.

Performance Parameter	Max_{ENU}	WP_{Max_ENU}	Max_{Body}	WP_{Max_Body}	ENU at WP_{Max_Body}	AL
HPL (m)	15.73	158	28.65	969	13.52	**40**
VPL (m)	16.8	1	33.08	969	15.59	**35**
EMT (m)	6.51	1	13.64	969	5.21	**15**
Accuracy (m)	0.87	399	1.29	971	0.82	**1.87**

Table 4-16 Percentage Differences between Max Values in Body Reference Frame, related ENU values and Alert Level.

Performance Parameter	Δ% between Body and ENU at WP_{Max_Body}	Δ% between Max_{Body} and AL
HPL (m)	111.9	-28.36
VPL (m)	112.15	-5.48
EMT (m)	161.77	-9.03
Accuracy (m)	56.85	-30.9

- ***Dual-constellation GPS and GLONASS: Yuma almanac week 703 for GPS and provided with MAAST for GLONASS, reset time [0d 0h 0m 0s], mask angle 5°***

The next case includes the combination of the American and Russian systems.

Figure 4-74 shows that the satellites available in this scenario ranges between 12 and 20, so between 2-3 times the average values in the single constellation scenarios.

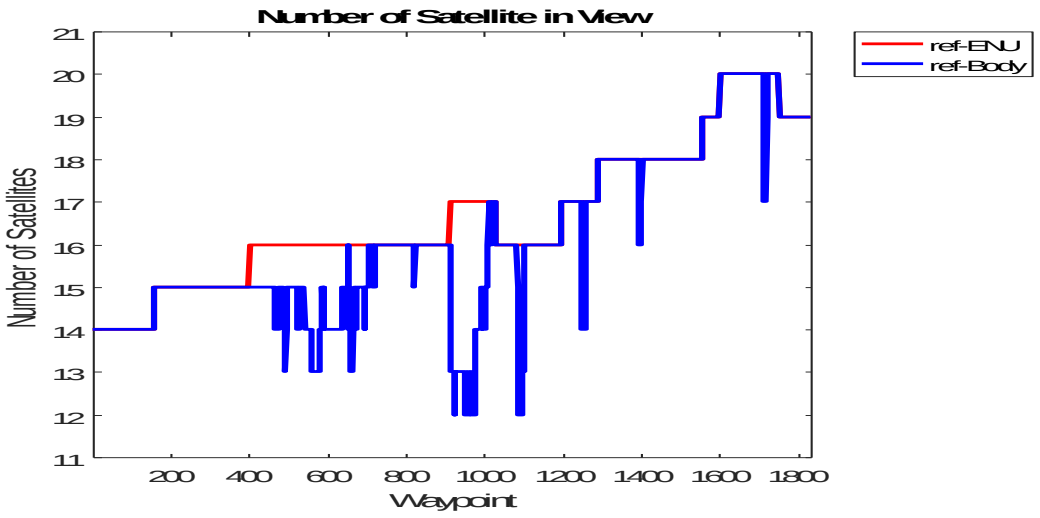

Figure 4-74 Number of Satellites in view in the ENU (red) and Body (blue) Reference Frames along the Trajectory.

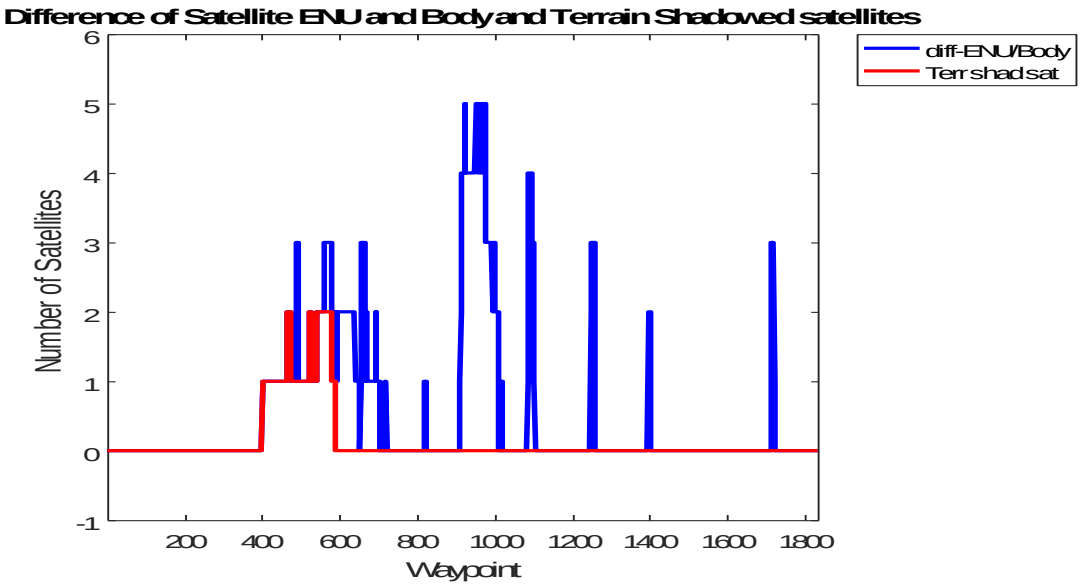

Figure 4-75 Number of Shadowed Satellites by Aircraft Attitude (blue) and Terrain (red).

Figure 4-75 and Figure 4-76 shows as for the previous case that the number of loss of LoS has increased due to the increased number of satellites available and the increased variety and range of their locations and elevations, in particular for elevation below 25° and Figure 4-77 confirms that half of them is in that range.

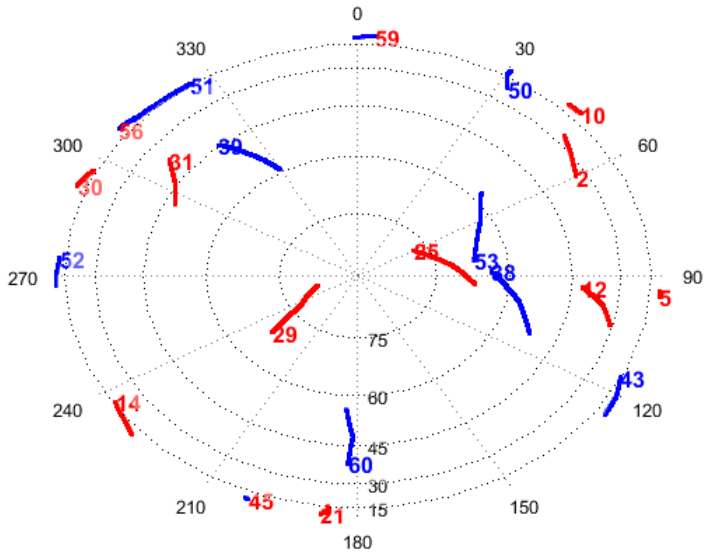

Figure 4-76 Satellites in View Skyplot in the ENU reference frame (GPS in red and GLONASS in blue).

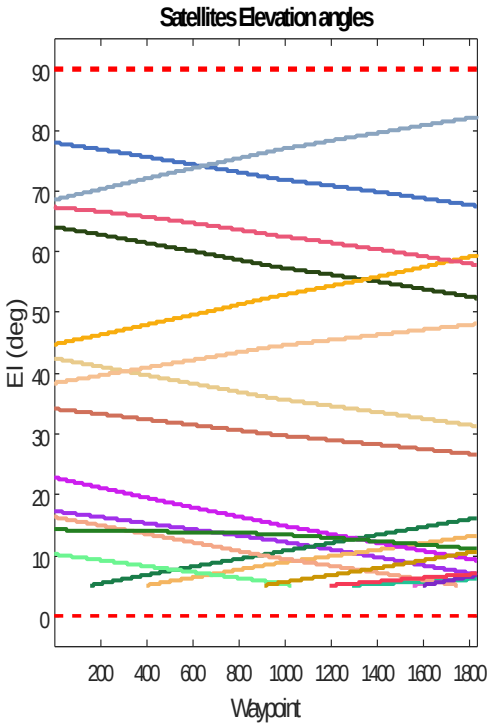

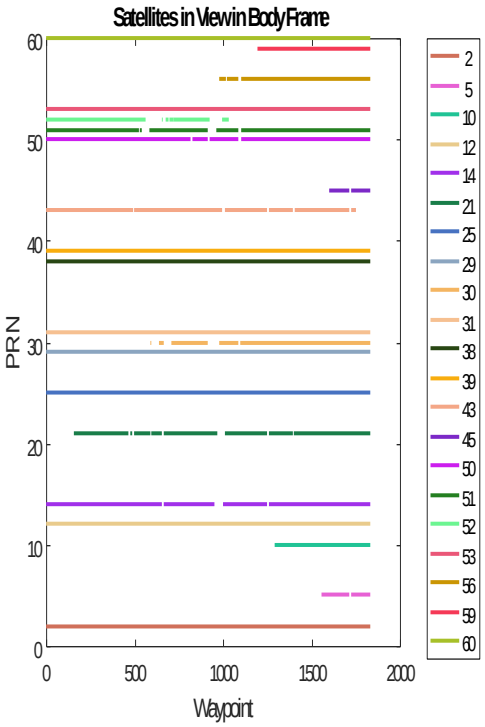

Figure 4-77 Satellites Elevation. **Figure 4-78 Satellites visibility by PRN.**

Figure 4-79 to Figure 4-82 shows as for the previous case that the use of two constellations provides enough redundancy to reduce the impact on the performances. None of the integrity parameters exceeds the alert level, but two of them (VPL and EMT) are close to the alert levels, they are only 4-6% below (see Table 4-17 and Table 4-18 for further details). This means that a slight change in the biases or probabilities that characterise the system could generate an outage.

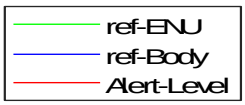

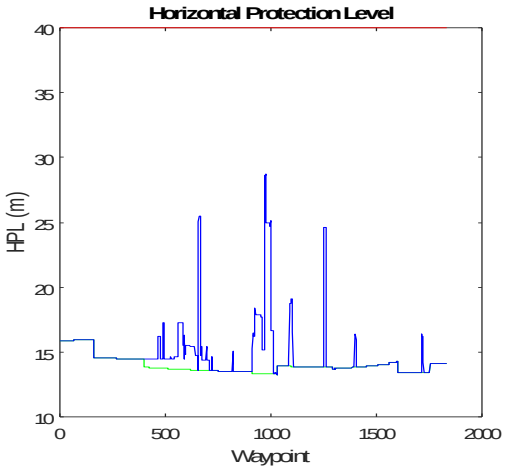

Figure 4-79 HPL in the ENU (green) and Body (blue) Reference Frames compared with the Alert Level (red).

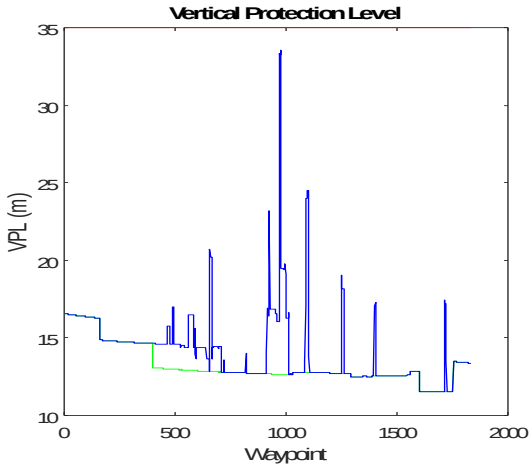

Figure 4-80 VPL in the ENU (green) and Body (blue) Reference Frames compared with the Alert Level (red).

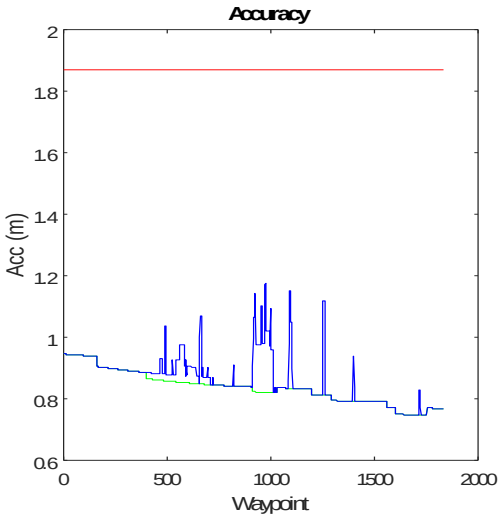

Figure 4-81 Accuracy in the ENU (green) and Body (blue) Reference Frames compared with the Alert Level (red).

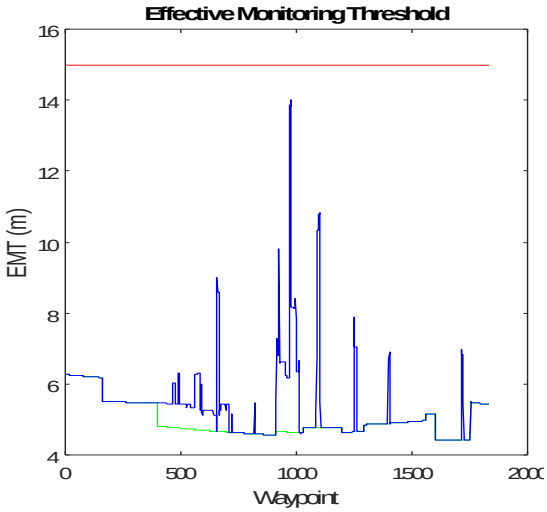

Figure 4-82 EMT in the ENU (green) and Body (blue) Reference Frames compared with the Alert Level (red).

Table 4-17 Values Comparison between ENU and Body Reference Frames.

Performance Parameter	Max_{ENU}	WP_{Max_ENU}	Max_{Body}	WP_{Max_Body}	ENU at WP_{Max_Body}	AL
HPL (m)	15.97	158	28.74	976	13.3	40
VPL (m)	16.55	1	33.52	976	12.64	35
EMT (m)	6.26	1	14.02	976	4.65	15
Accuracy (m)	0.95	1	1.17	975	0.82	1.87

Table 4-18 Percentage Differences between Max Values in Body Reference Frame, related ENU values and Alert Level.

Performance Parameter	Δ% between Body and ENU at WP_{Max_Body}	Δ% between Max_{Body} and AL
HPL (m)	116.1	-28.16
VPL (m)	165.2	-4.23
EMT (m)	201.91	-6.5
Accuracy (m)	43.01	-37.23

- ***Dual-constellation Galileo 24SV and GLONASS: Yuma almanac provided with MAAST, reset time [0d 0h 0m 0s], mask angle 5°***

It is now the turn to analyse the combination of the European and Russian systems. As for the GPS-GLONASS case, Figure 4-83 and Figure 4-84 show the number of satellite in view along the trajectory and the ones lost, while Figure 4-85 and Figure 4-86 show the location and elevation of the satellites. To be noticed that respect to the previous case, there a less homogeneous distribution of the satellites along the range of elevation values, leaving a gap between 25° and 40°.

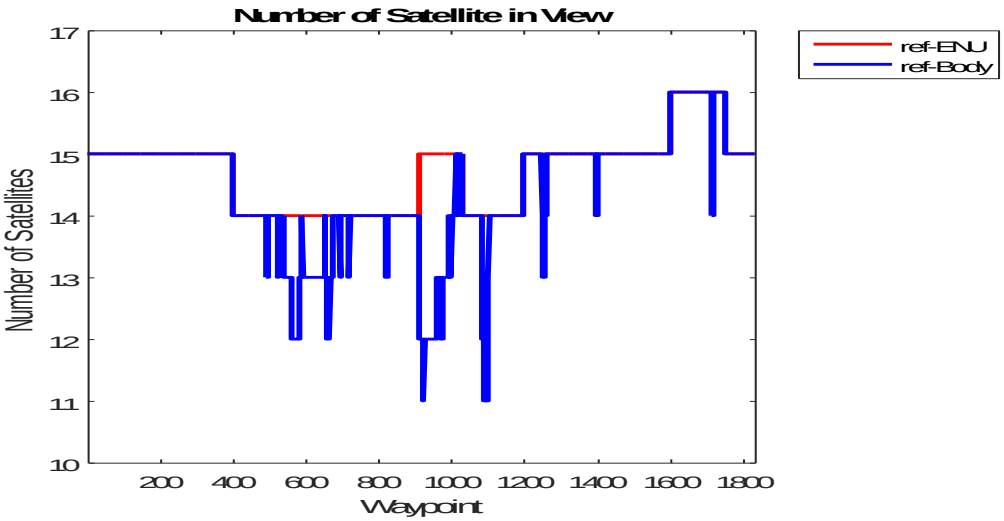

Figure 4-83 Number of Satellites in view in the ENU (red) and Body (blue) Reference Frames along the Trajectory.

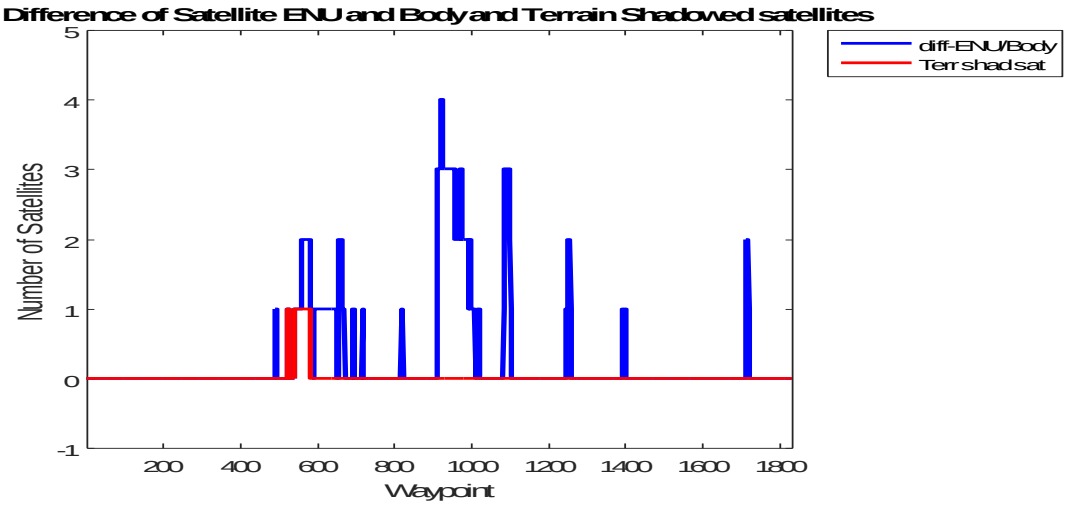

Figure 4-84 Number of Shadowed Satellites by Aircraft Attitude (blue) and Terrain (red).

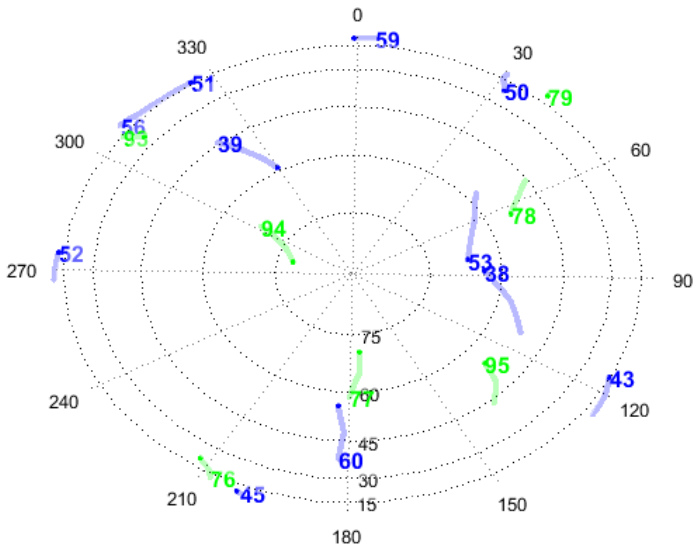

Figure 4-85 Satellites in View Skyplot in the ENU reference frame (GLONASS in blue and Galileo in green).

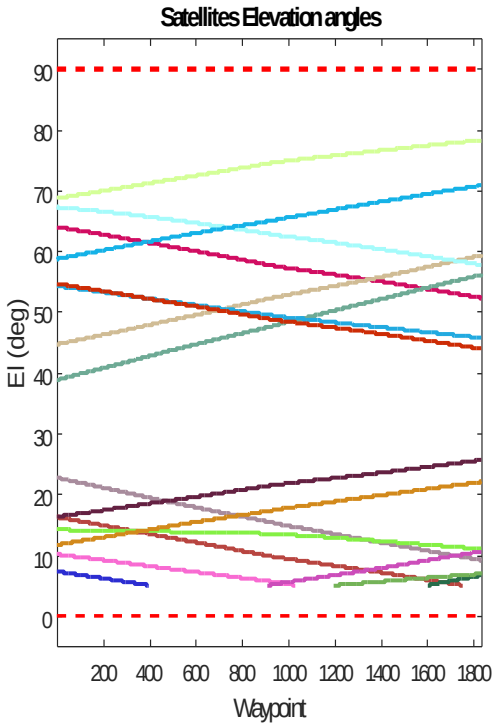

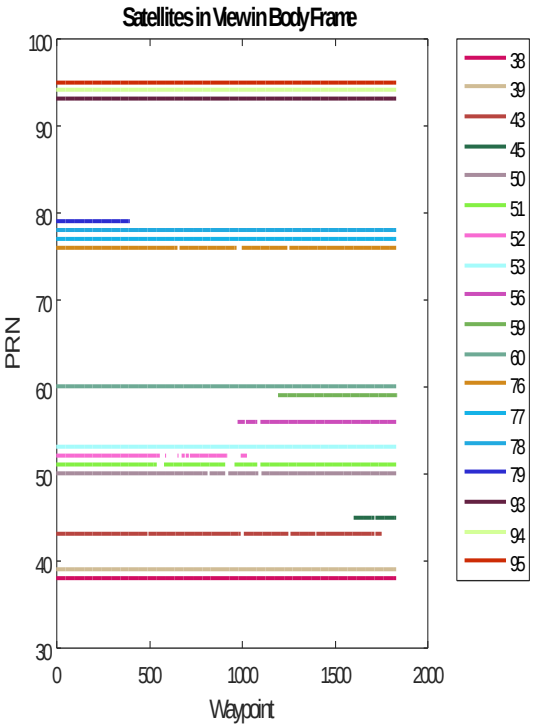

Figure 4-86 Satellites Elevation.

Figure 4-87 Satellites visibility by PRN.

Figure 4-88 to Figure 4-91 show the results of this particular scenario that combines the Galileo 24SV constellation and GLONASS has better performances compared to the GPS-GLONASS and GPS-Galileo. Values of the parameters are far from the alert levels, all the values are actually 50% less than them.

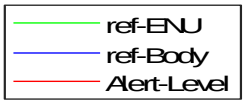

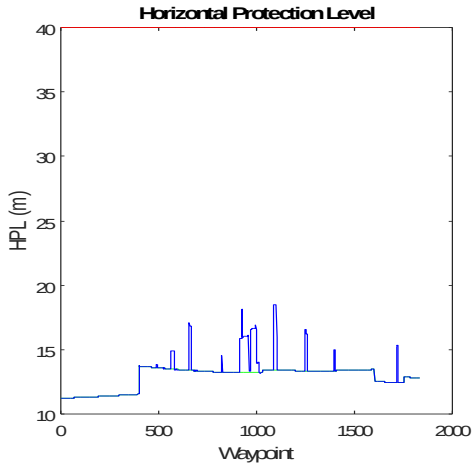

Figure 4-88 HPL in the ENU (green) and Body (blue) Reference Frames compared with the Alert Level (red).

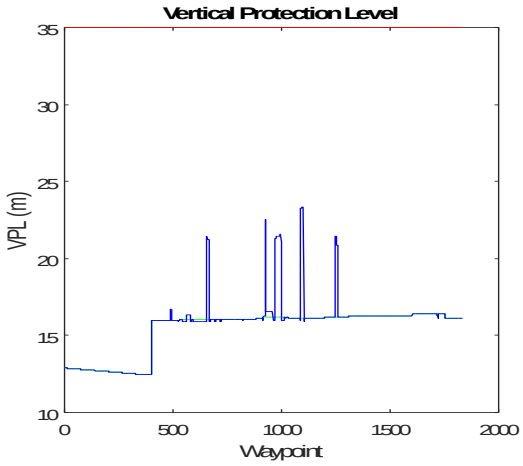

Figure 4-89 VPL in the ENU (green) and Body (blue) Reference Frames compared with the Alert Level (red).

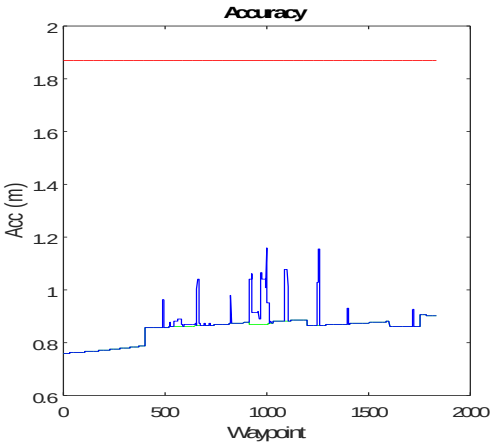

Figure 4-90 Accuracy in the ENU (green) and Body (blue) Reference Frames compared with the Alert Level (red).

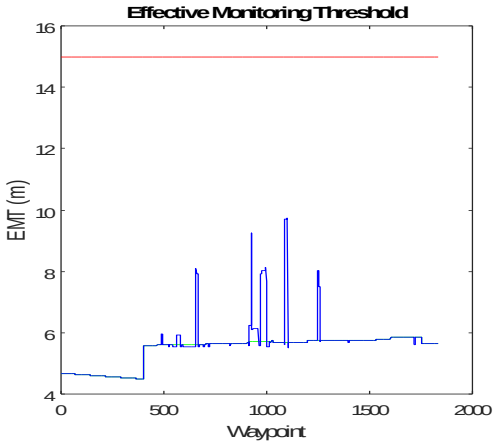

Figure 4-91 EMT in the ENU (green) and Body (blue) Reference Frames compared with the Alert Level (red).

Table 4-19 Values Comparison between ENU and Body Reference Frames.

Performance Parameter	Max_{ENU}	WP_{Max_ENU}	Max_{Body}	WP_{Max_Body}	ENU at WP_{Max_Body}	AL
HPL (m)	11.73	158	20.16	976	10.31	40
VPL (m)	10.54	1	17.32	976	10.09	35
EMT (m)	3.77	1753	6.48	976	3.34	15
Accuracy (m)	0.71	399	0.95	975	0.68	1.87

Table 4-20 Percentage Differences between Max Values in Body Reference Frame, related ENU values and Alert Level.

Performance Parameter	Δ% between Body and ENU at WP_{Max_Body}	Δ% between Max_{Body} and AL
HPL (m)	95.61	-49.59
VPL (m)	71.56	-50.51
EMT (m)	94	-56.8
Accuracy (m)	38.41	-49.44

- ***Dual-constellation Galileo 27SV and GLONASS: Yuma almanac provided with MAAST, reset time [0d 0h 0m 0s], mask angle 5°***

As for the previous cases, implementing the 27SV configuration introduces one more satellite in view, as it can be easily seen by comparing Figure 4-92 and Figure 4-83. However, results presented in Figure 4-97 to Figure 4-100 show that the addition of one satellite it actually degrades the integrity of the performances. Respect to the previous case, the percentage difference between the performances computed in the body reference frame and the alert level has increased by 10-20%.

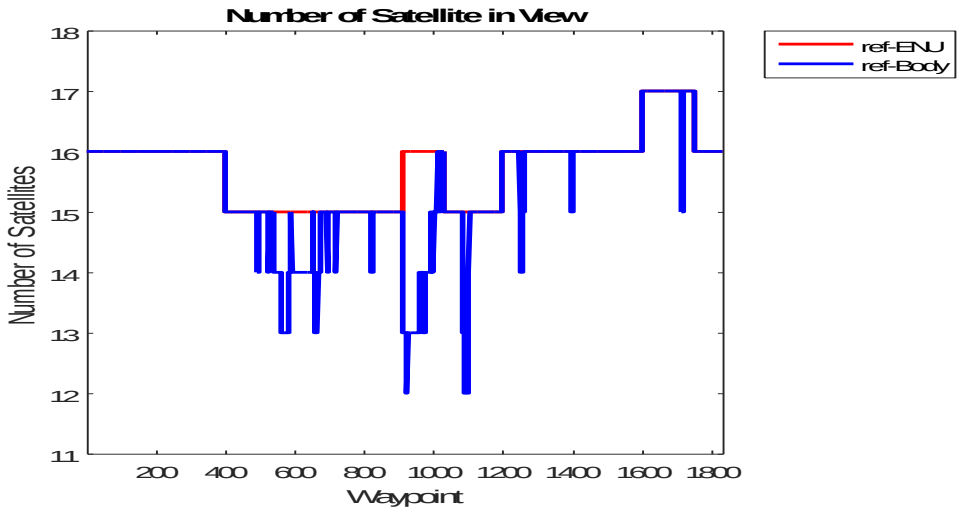

Figure 4-92 Number of Satellites in view in the ENU (red) and Body (blue) Reference Frames along the Trajectory.

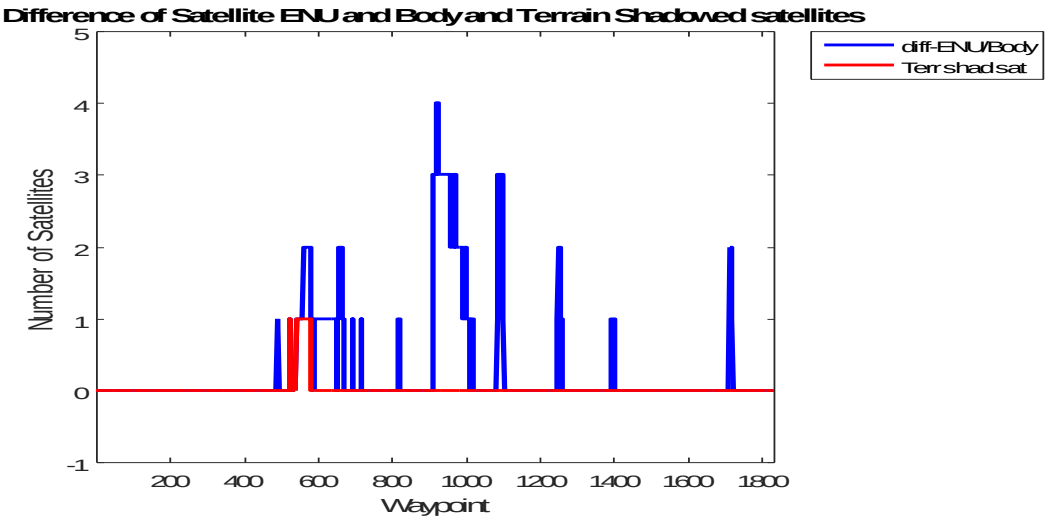

Figure 4-93 Number of Shadowed Satellites by Aircraft Attitude (blue) and Terrain (red).

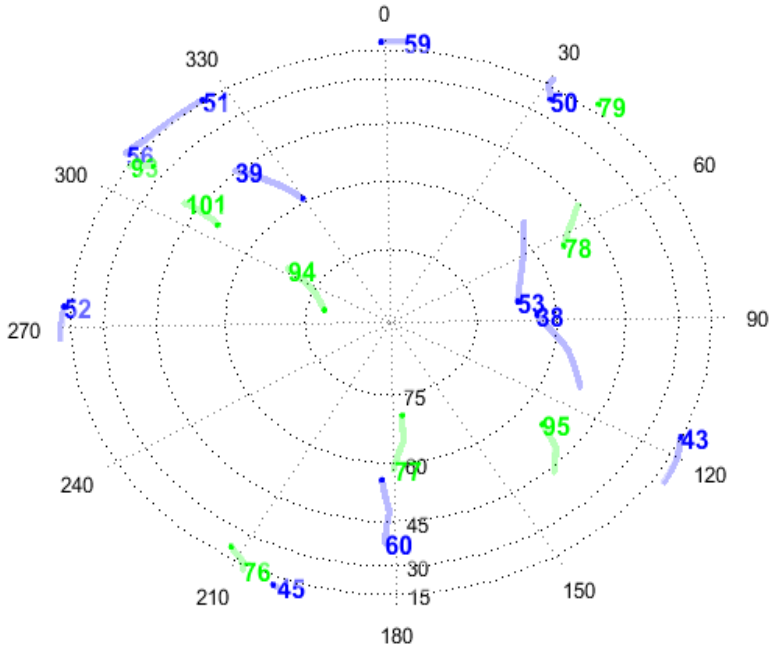

Figure 4-94 Satellites in View Skyplot in the ENU reference frame (GLONASS in blue and Galileo in green).

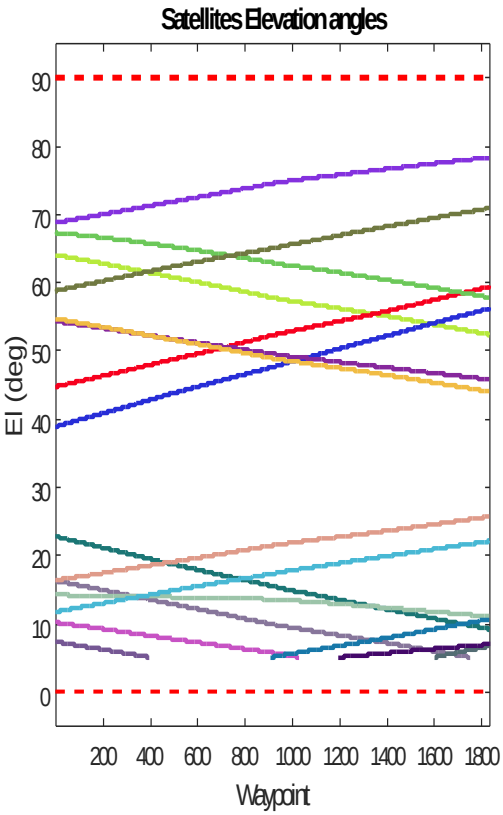

Figure 4-95 Satellites Elevation.

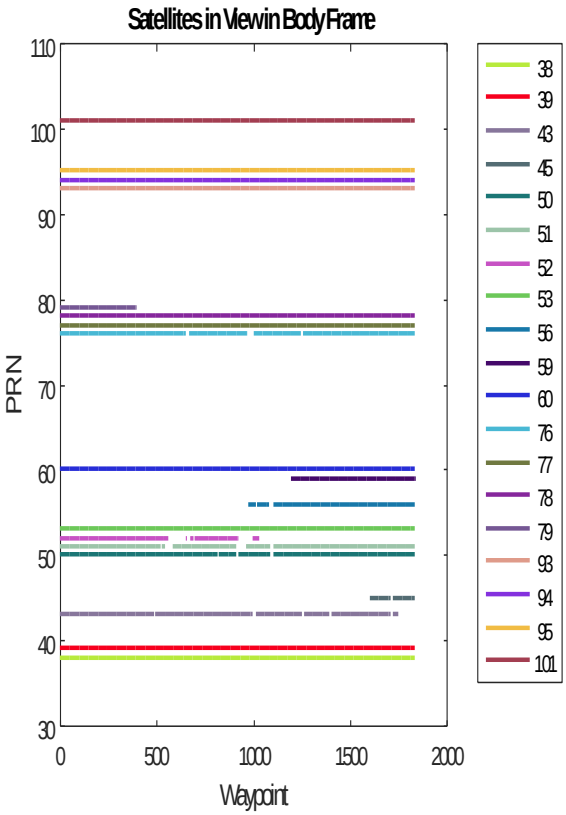

Figure 4-96 Satellites visibility by PRN.

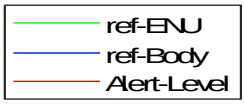

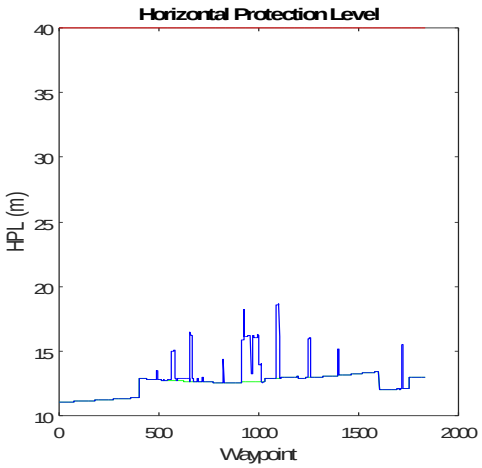

Figure 4-97 HPL in the ENU (green) and Body (blue) Reference Frames compared with the Alert Level (red).

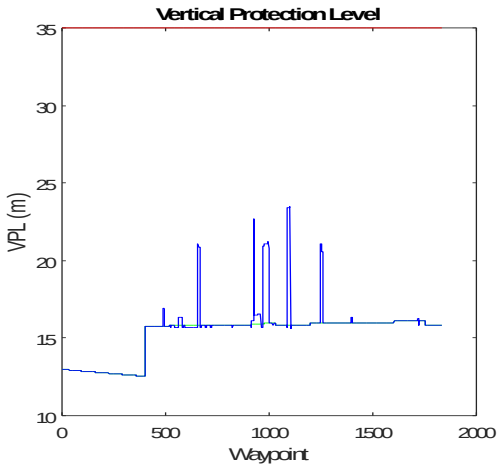

Figure 4-98 VPL in the ENU (green) and Body (blue) Reference Frames compared with the Alert Level (red).

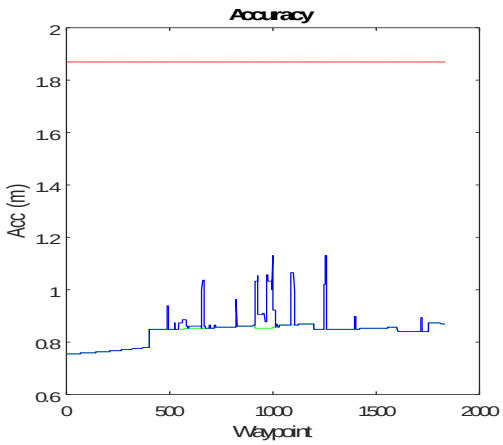

Figure 4-99 Accuracy in the ENU (green) and Body (blue) Reference Frames compared with the Alert Level (red).

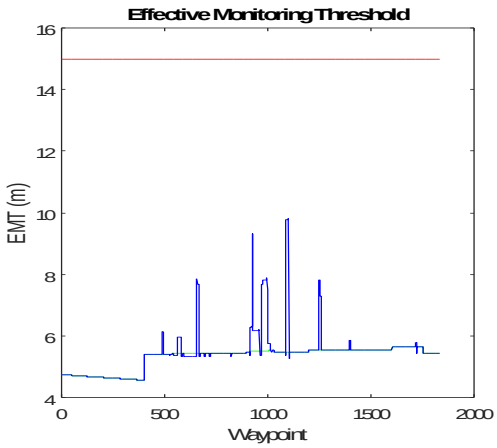

Figure 4-100 EMT in the ENU (green) and Body (blue) Reference Frames compared with the Alert Level (red).

Table 4-21 Values Comparison between ENU and Body Reference Frames.

Performance Parameter	Max_{ENU}	WP_{Max_ENU}	Max_{Body}	WP_{Max_Body}	ENU at WP_{Max_Body}	AL
HPL (m)	13.41	1601	18.62	1101	12.93	40
VPL (m)	16.09	1602	23.45	1101	15.85	35
EMT (m)	5.63	1602	9.79	1101	5.47	15
Accuracy (m)	0.87	1753	1.13	997	0.86	1.87

Table 4-22 Percentage Differences between Max Values in Body Reference Frame, related ENU values and Alert Level.

Performance Parameter	Δ% between Body and ENU at WP_{Max_Body}	Δ% between Max_{Body} and AL
HPL (m)	44.02	-53.44
VPL (m)	47.97	-32.99
EMT (m)	79.01	-34.68
Accuracy (m)	32.27	-39.5

The combination of two constellations has increased the number of satellites in view, improving the performances of the integrity parameters. None of the analysed configurations presents an outage, however, in some cases, the protection levels are close to the alert levels (less than 20%) leaving short margins to a sudden change in the nominal values used for the characterisation of the signal errors and biases.

Additionally, it is interesting to notice how the loss or addition of a satellite can generate an effect that is opposite to the expected. Examples are the two combinations that use the two different Galileo configurations (24SV and 27SV, for which the only difference is the addition of the satellite n.101), both the GPS and GLONASS present better performances for some of the parameters when they are combined with the 24SV configuration (e.g. the VPL goes from 17m in the GLONASS+Galileo 24SV to 23m in the GLONASS+Galileo 27SV, while the difference between the combinations GPS+Galileo 24SV and GPS+Galileo 27SV is much less relevant, only 0.08m), the same effect is found in the tri-constellation configuration (see next section). At the same time, the loss of a satellite in all the combinations that involve the Galileo constellation sometimes generates an improvement in the performances; for examples in Figure 4-71 VPL in the ENU (green) and Body (blue) Reference Frames compared with the Alert Level (red) of the GPS+Galileo 27SV case, around WP-500, the performances (mainly VPL and EMT) in the ENU reference frame (green line) is above the one from the Body reference frame (blue line). In this part of the trajectory, satellite n. 30 (a GPS satellite) has just arisen from the horizon (Figure 4-68) and above the mask angle in the ENU reference point, but due to the aircraft manoeuvre (banking and pitching) the satellite is not visible in the Body reference frame until it is ended.

A similar situation can be seen in the GLONASS+Galileo 27SV at around WP-600, in which the satellite n. 52 (a GLONASS satellite) is on the way to set below the local horizon and due to the aircraft manoeuvre, this satellite is shadowed and missing in the Body reference. In this case as well, the VPL and EMT values in the Body reference frames are below the ones in the ENU reference frame. It is believed that cause of this unexpected behaviour resides in the satellites geometry that influences the value of S_0 in eq. (2.30), a variable that depends from the geometry G and the weight matrix W, that in cascades determines the values of T (Eq. 2.31) σ_{ss} (Eq. 2.34) and then HPL and VPL.

C. TRI-CONSTELLATION CONFIGURATION

This section analyses the effect of the simultaneous integration of the three GNSS constellation in the receiver. Two different configurations are considered:

- GPS, Galileo 24SV and GLONASS
- GPS, Galileo 27SV and GLONASS

- ***Tri-constellation GPS, Galileo 24SV and GLONASS: Yuma almanac week 703 for GPS and provided with MAAST for Galileo and GLONASS, reset time [0d 0h 0m 0s], mask angle 5°***

With a tri constellation configuration, the total number of satellites in view reaches the maximum value of 26 units, while the minimum does not go below 17. This implementation presents optimal performances, with values that stay below by 50% of the alert limits (as shown in Table 4-23 and Table 4-24).

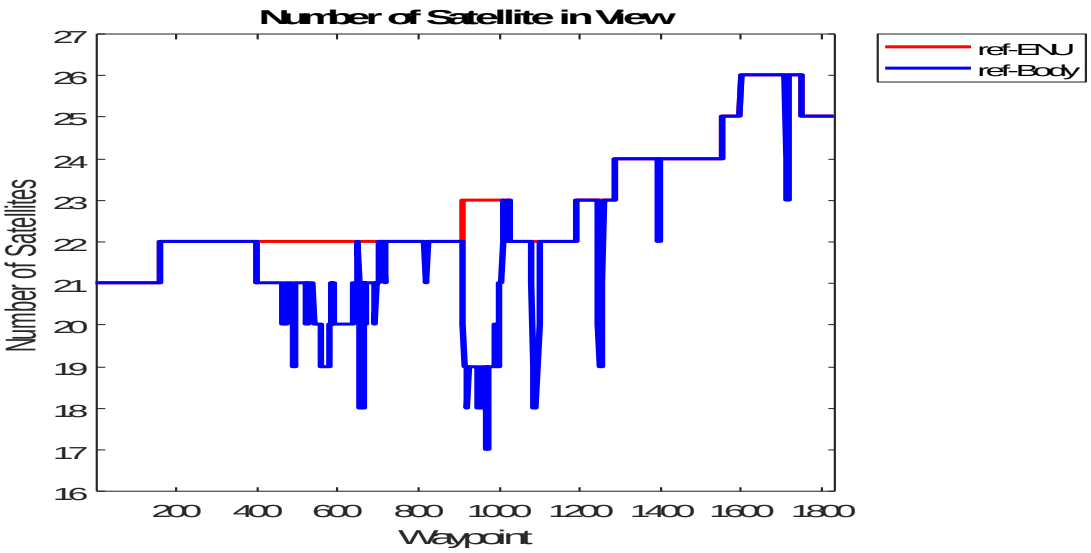

Figure 4-101 Number of Satellites in view in the ENU (red) and Body (blue) Reference Frames along the Trajectory.

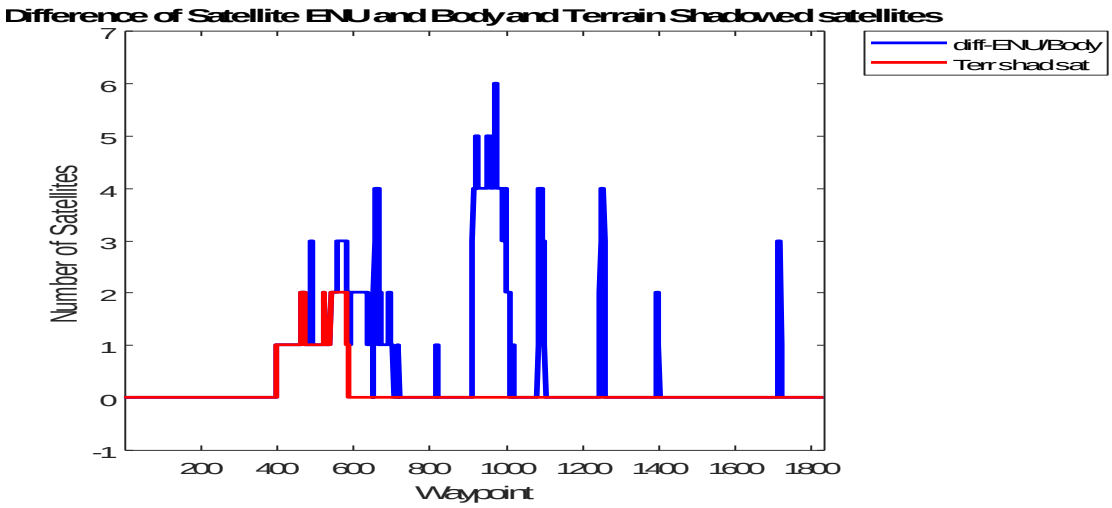

Figure 4-102 Number of Shadowed Satellites by Aircraft Attitude (blue) and Terrain (red).

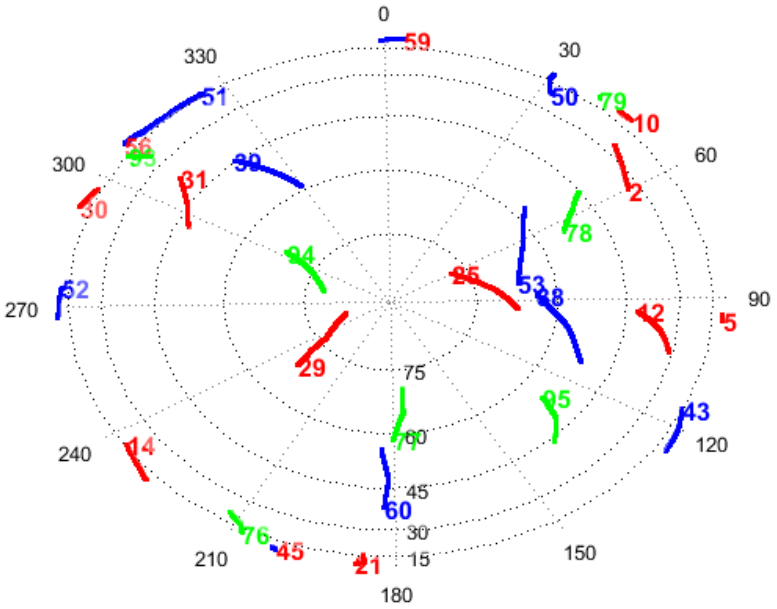

Figure 4-103 Satellites in View Skyplot in the ENU reference frame (GPS in red, GLONASS in blue and Galileo in green).

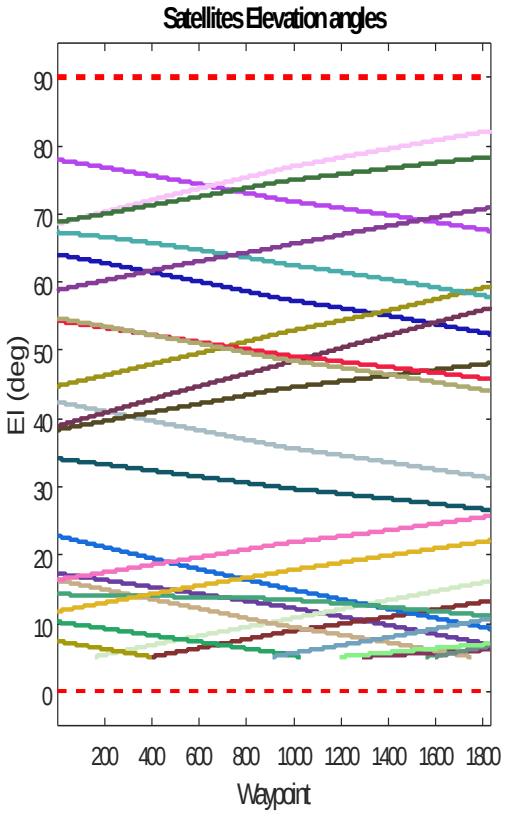

Figure 4-104 Satellites Elevation.

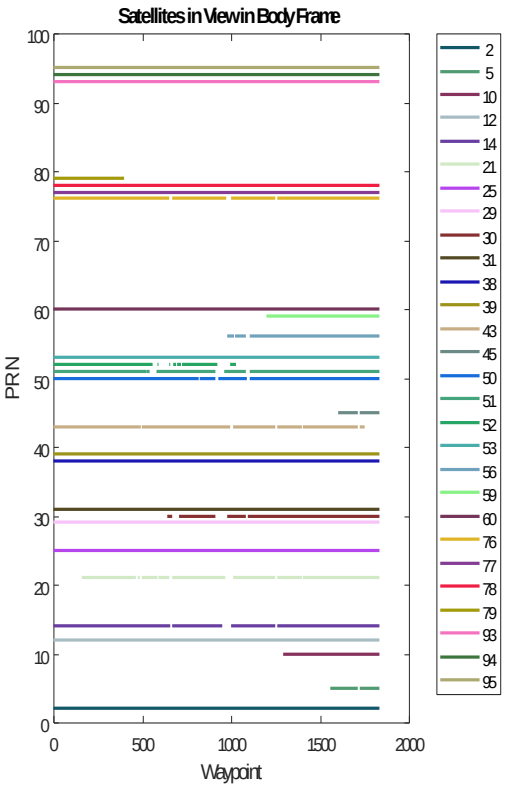

Figure 4-105 Satellites visibility by PRN.

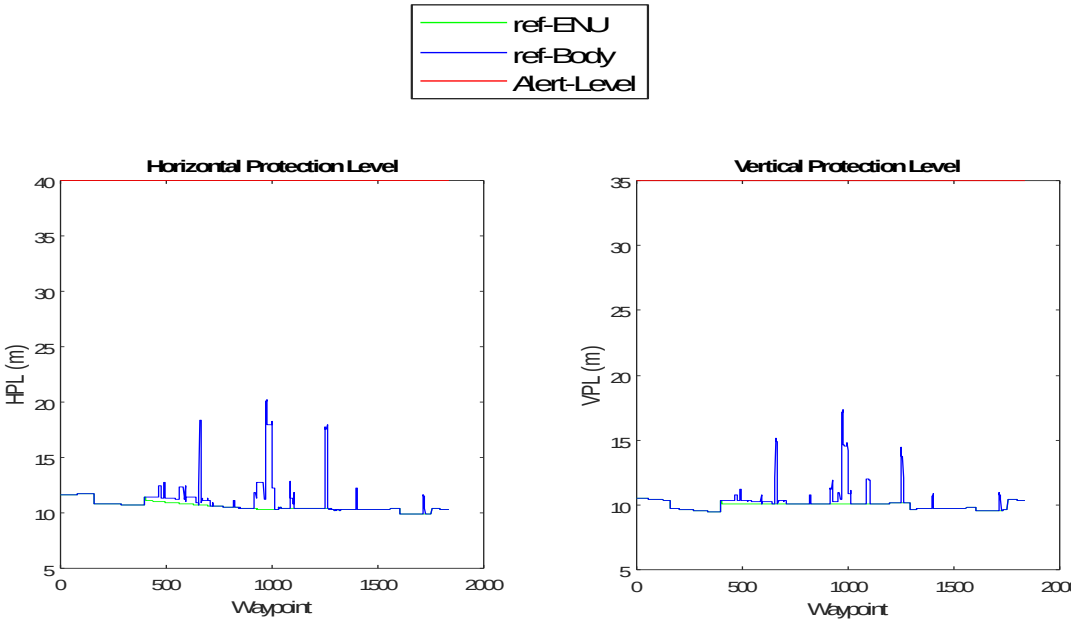

Figure 4-106 HPL in the ENU (green) and Body (blue) Reference Frames compared with the Alert Level (red).

Figure 4-107 VPL in the ENU (green) and Body (blue) Reference Frames compared with the Alert Level (red).

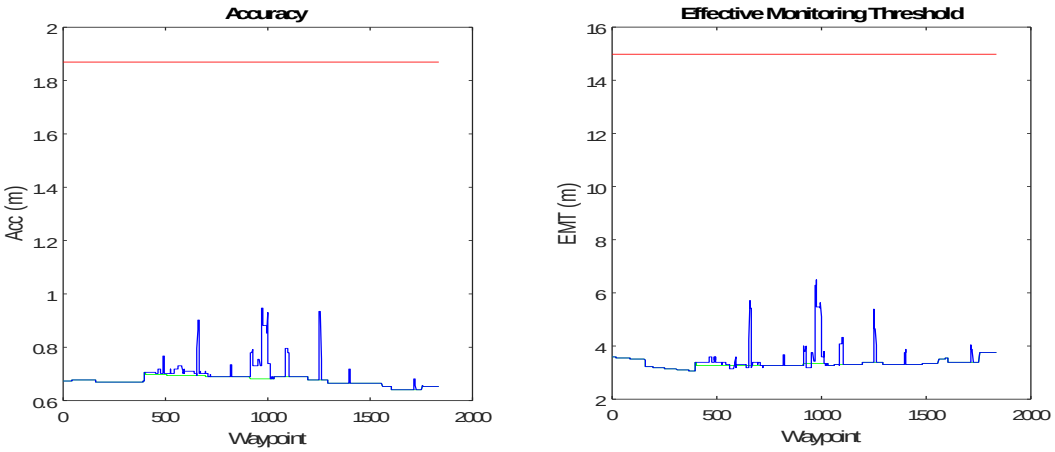

Figure 4-108 Accuracy in the ENU (green) and Body (blue) Reference Frames compared with the Alert Level (red).

Figure 4-109 EMT in the ENU (green) and Body (blue) Reference Frames compared with the Alert Level (red).

Table 4-23 Values Comparison between ENU and Body Reference Frames.

Performance Parameter	Max_{ENU}	WP_{Max_ENU}	Max_{Body}	WP_{Max_Body}	ENU at WP_{Max_Body}	AL
HPL (m)	11.73	158	20.16	976	10.31	40
VPL (m)	10.54	1	17.32	976	10.1	35
EMT (m)	3.77	1753	6.48	976	3.34	15
Accuracy (m)	0.71	399	0.95	975	0.68	1.87

Table 4-24 Percentage Differences between Max Values in Body Reference Frame, related ENU values and Alert Level.

Performance Parameter	Δ% between Body and ENU at WP_{Max_Body}	Δ% between Max_{Body} and AL
HPL (m)	95.61	-49.59
VPL (m)	71.56	-50.51
EMT (m)	94	-56.8
Accuracy (m)	38.41	-49.44

- ***Tri-constellation GPS, Galileo 27SV and GLONASS: Yuma almanac week 703 for GPS and provided with MAAST for Galileo and GLONASS, reset time [0d 0h 0m 0s], mask angle 5°***

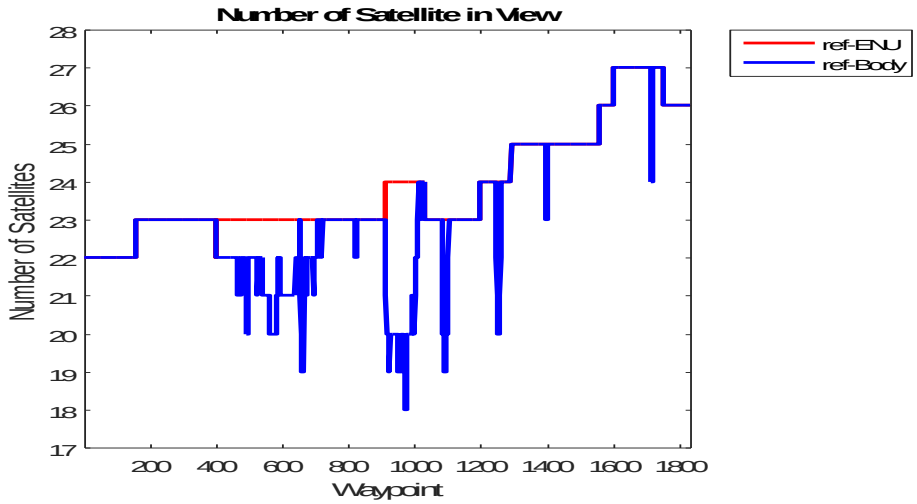

Figure 4-110 Number of Satellites in view in the ENU (red) and Body (blue) Reference Frames along the Trajectory.

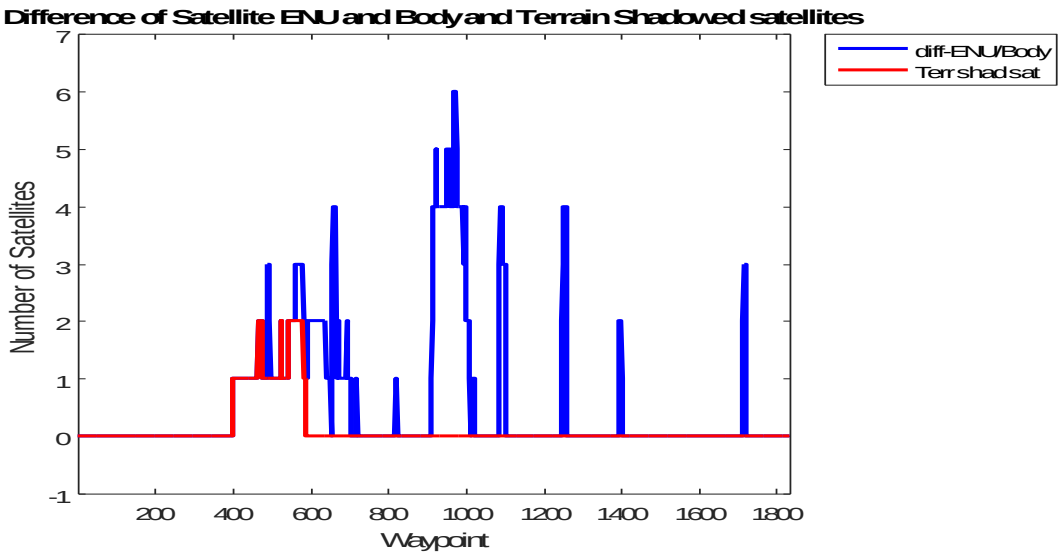

Figure 4-111 Number of Shadowed Satellites by Aircraft Attitude (blue) and Terrain (red).

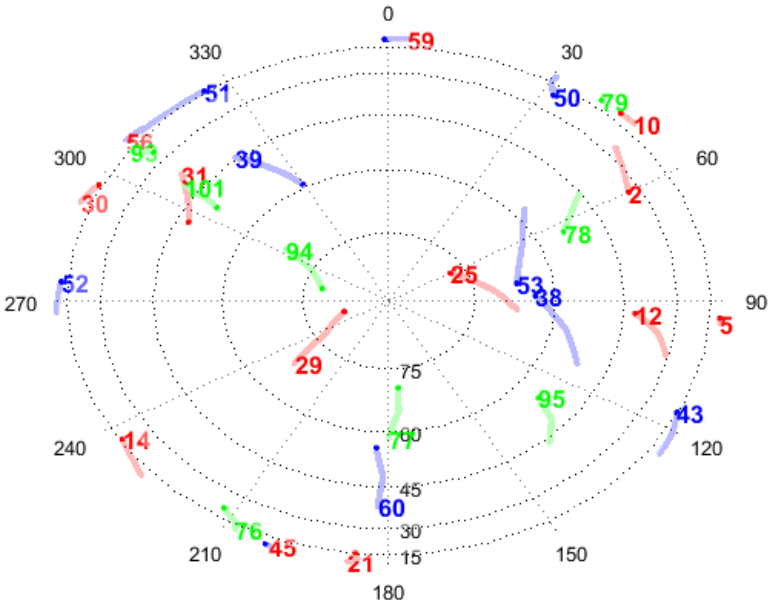

Figure 4-112 Satellites in View Skyplot in the ENU reference frame, (GPS in red, GLONASS in blue and Galileo in green).

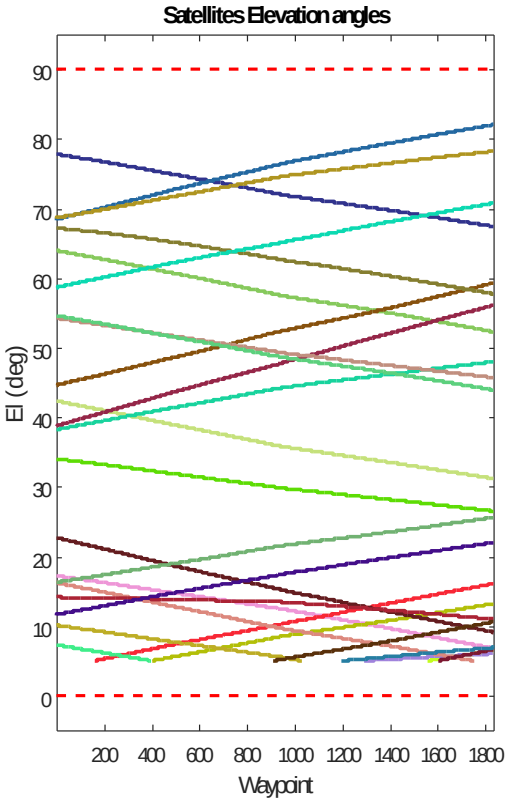

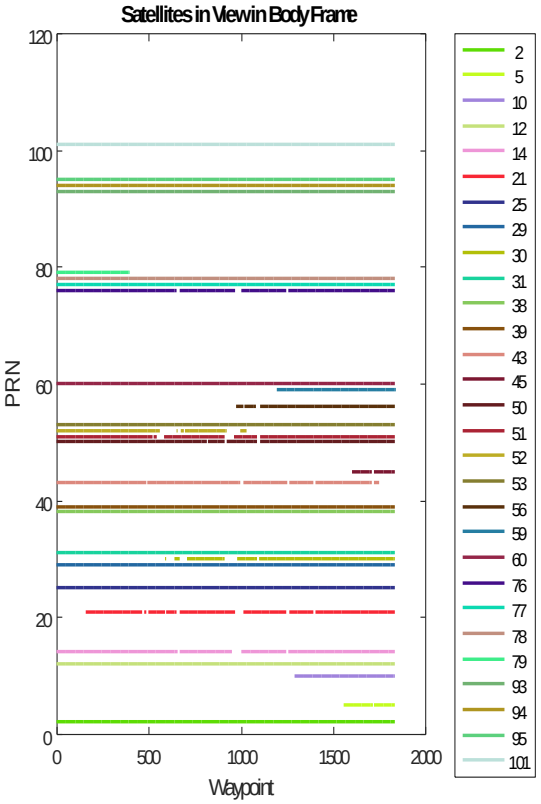

Figure 4-113 Satellites Elevation. **Figure 4-114 Satellites visibility by PRN.**

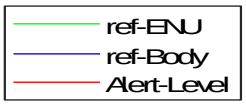

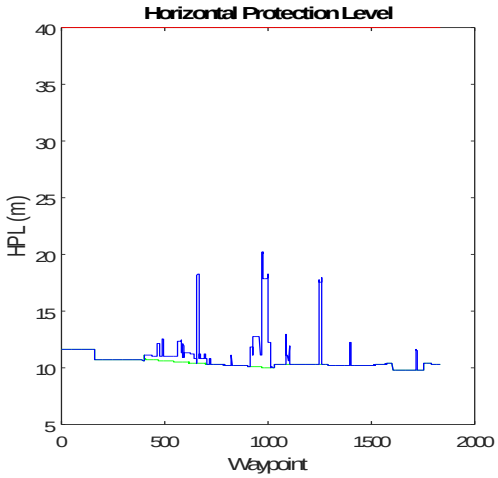

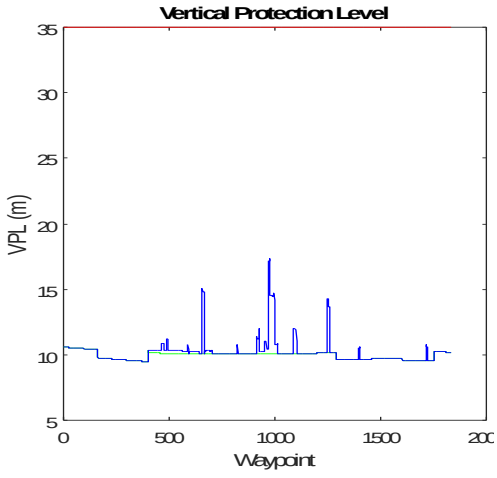

Figure 4-115 HPL in the ENU (green) and Body (blue) Reference Frames compared with the Alert Level (red).

Figure 4-116 VPL in the ENU (green) and Body (blue) Reference Frames compared with the Alert Level (red).

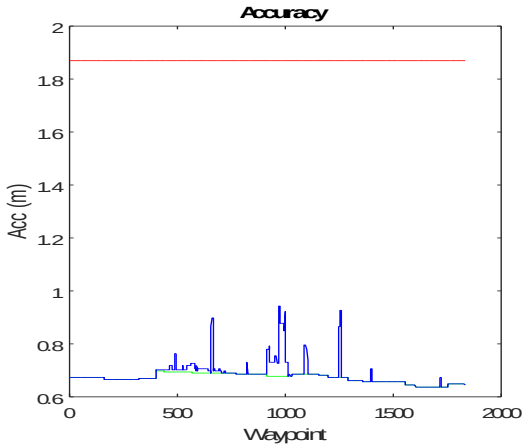

Figure 4-117 Accuracy in the ENU (green) and Body (blue) Reference Frames compared with the Alert Level (red).

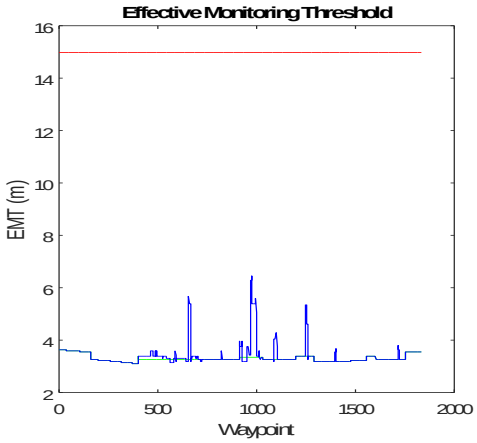

Figure 4-118 EMT in the ENU (green) and Body (blue) Reference Frames compared with the Alert Level (red).

Table 4-25 Values Comparison between ENU and Body Reference Frames.

Performance Parameter	Max_{ENU}	WP_{Max_ENU}	Max_{Body}	WP_{Max_Body}	ENU at WP_{Max_Body}	AL
HPL (m)	11.66	158	20.17	976	10.05	40
VPL (m)	10.59	1	17.36	976	10.11	35
EMT (m)	3.63	1	6.45	976	3.33	15
Accuracy (m)	0.7	399	0.94	975	0.67	1.87

Table 4-26 Percentage Differences between Max Values in Body Reference Frame, related ENU values and Alert Level.

Performance Parameter	Δ% between Body and ENU at WP_{Max_Body}	Δ% between Max_{Body} and AL
HPL (m)	100.65	-49.57
VPL (m)	71.64	-50.4
EMT (m)	93.45	-57
Accuracy (m)	39.11	-49.51

Using three constellations further improves the capabilities of the ARAIM algorithm of satisfying the required navigation performance for the LPV-200. All the PLs are well below the ALs with a margin of around 50%.

4.3.2. CAIRNS AND FAIRBANKS AIRPORTS

In this section, a quick overview of the other selected airports is presented, since the results are comparable with what has been already presented in the previous section related to the Innsbruck airport. Figure 4-5 and Figure 4-6 showed the chosen approach procedures and Figure 4-119 and Figure 4-120 the aircraft angles along the trajectories.

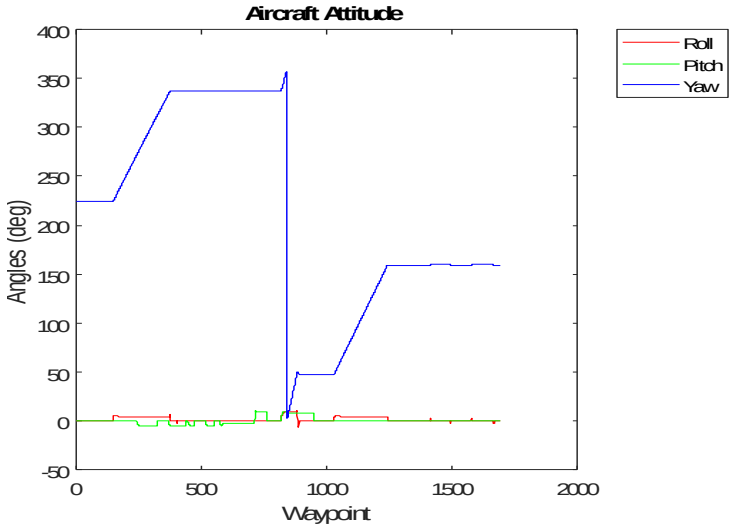

Figure 4-119 Aircraft Attitude Angles along the Approach Procedure for Cairns Airport.

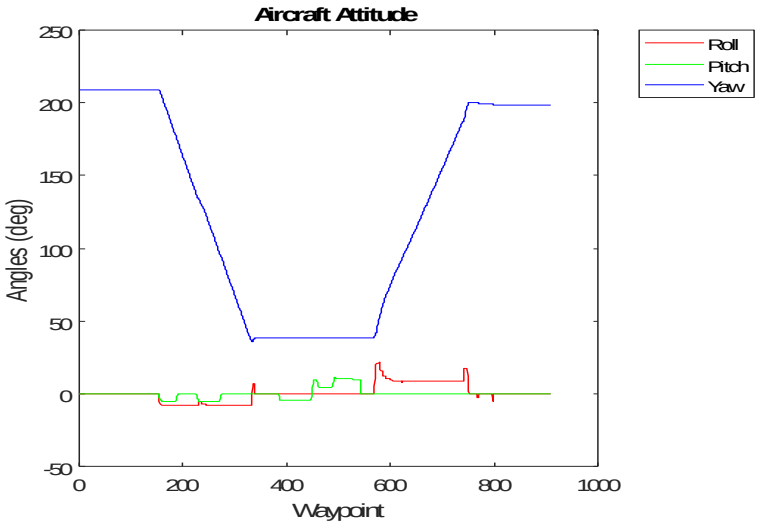

Figure 4-120 Aircraft Attitude Angles along the Approach Procedure for Fairbanks Airport.

As for Innsbruck airport, the performance parameters are analysed in different configurations and combinations of the three constellations, but they are summarised in tables and graphs for few cases to show that comparable results are found for other approach procedures.

- ***Single Constellation GPS: Yuma almanac week 703 for GPS, reset time [0d 1h 0m 0s] for Cairns and [0d 3h 0m 0s] for Fairbanks, mask angle 5°***

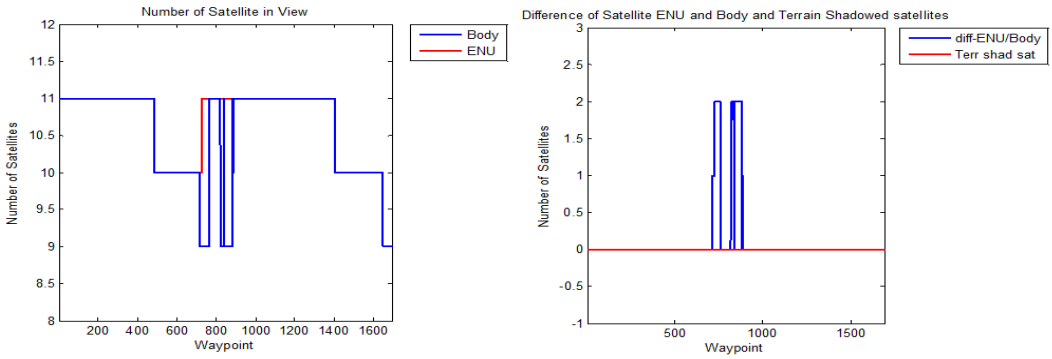

Figure 4-121 Number of Satellites in view (left) and difference (right) in the ENU (red) and Body (blue) Reference Frames for the Approach Procedure to the Airport of Cairns.

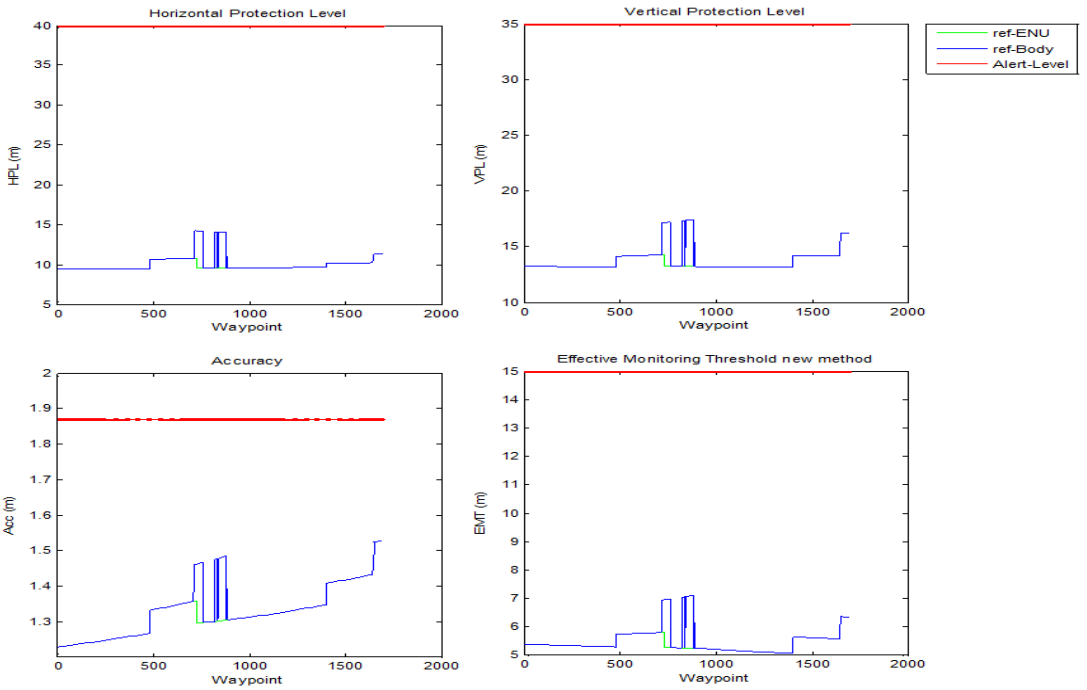

Figure 4-122 PLs in the ENU (green) and Body (blue) Reference Frames compared with the Alert Level (red) for the Approach Procedure to the Airport of Cairns.

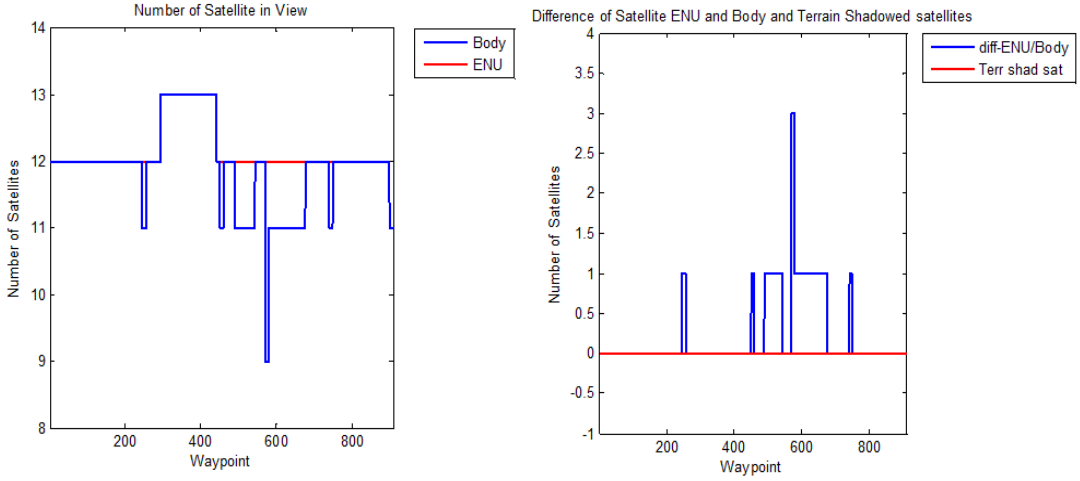

Figure 4-123 Number of Satellites in view (left) and difference (right) in the ENU (red) and Body (blue) Reference Frames for the Approach Procedure to the Airport of Fairbanks.

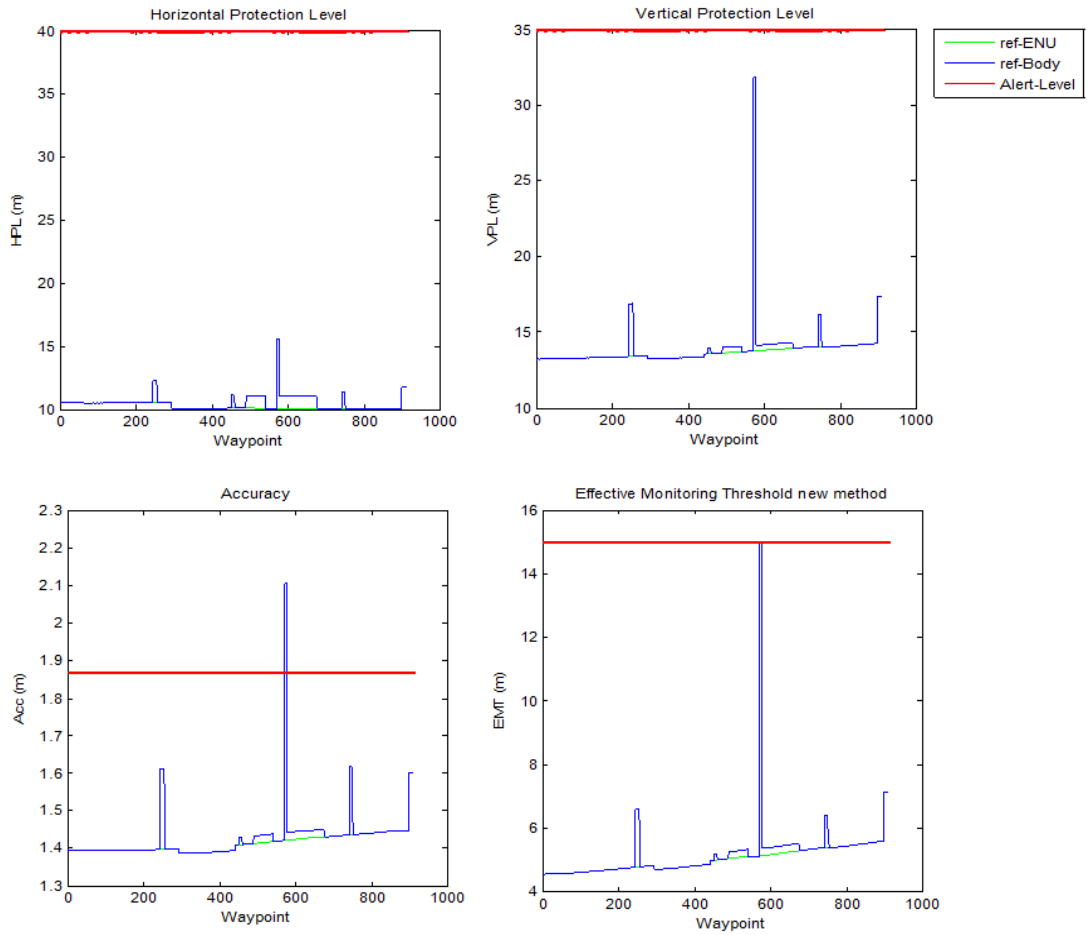

Figure 4-124 PLs in the ENU (green) and Body (blue) Reference Frames compared with the Alert Level (red) for the Approach Procedure to the Airport of Fairbanks.

Table 4-27 Values Comparison and Percentage Differences between ENU and Body Reference Frames for Cairns and Fairbanks Airports.

Performance Parameters	Location	Max Body	ENU value	ΔBody-ENU%	ΔAL%	AL
HPL (m)	Cairns	14.2	10.8	31.8	-64.4	40
	Fairbanks	15.6	10.1	54.5	-61.1	
VPL (m)	Cairns	17.4	13.2	31.9	-50.2	35
	Fairbanks	31.84	13.8	131.4	-9.0	
EMT (m)	Cairns	7.1	5.2	35.7	-52.7	15
	Fairbanks	14.97	5.1	191.7	-0.2	
Acc (m)	Cairns	1.53	1.5	0.02	-18.3	1.87
	Fairbanks	2.11	1.4	48.2	12.6	

- ***Single Constellation Galileo 24SV: Yuma almanac week 703 for GPS, reset time [0d 1h 0m 0s] for Cairns and [0d 3h 0m 0s] for Fairbanks, mask angle 5°***

-

Table 4-28 Values Comparison and Percentage Differences between ENU and Body Reference Frames for Cairns and Fairbanks Airports.

Performance Parameters	Location	Max Body	ENU value	ΔBody-ENU%	ΔAL%	AL
HPL (m)	Cairns	14.6	8.6	68.9	-63.6	40
	Fairbanks	16.4	10.9	47.7	-59.9	
VPL (m)	Cairns	23.1	13.6	70.0	-34.0	35
	Fairbanks	14.4	12.7	13.8	-58.8	
EMT (m)	Cairns	9.0	5.1	75.5	-40.1	15
	Fairbanks	5.5	4.8	14.1	-63.6	
Acc (m)	Cairns	1.92	1.3	52.6	2.5	1.87
	Fairbanks	1.2	1.1	5.9	-38.0	

- ***Single Constellation Galileo 27SV: Yuma almanac week 703 for GPS, reset time [0d 1h 0m 0s] for Cairns and [0d 3h 0m 0s] for Fairbanks, mask angle 5°***

Table 4-29 Values Comparison and Percentage Differences between ENU and Body Reference Frames for Cairns and Fairbanks Airports.

Performance Parameters	Location	Max Body	ENU value	ΔBody-ENU%	ΔAL%	AL
HPL (m)	Cairns	14.6	8.6	68.9	-63.6	40
	Fairbanks	14.4	10.3	39.9	-63.9	
VPL (m)	Cairns	23.1	13.6	70.0	-34.0	35
	Fairbanks	13.5	12.3	9.2	-61.6	
EMT (m)	Cairns	9.0	5.1	75.5	-40.1	15
	Fairbanks	5.7	4.7	10.9	-64.9	
Acc (m)	Cairns	1.92	1.3	52.6	2.5	1.87
	Fairbanks	1.1	1.1	0.0	-41.0	

- ***Single Constellation GLONASS: Yuma almanac week 703 for GPS, reset time [0d 1h 0m 0s] for Cairns and [0d 3h 0m 0s] for Fairbanks, mask angle 5°***

Table 4-30 Values Comparison and Percentage Differences between ENU and Body Reference Frames for Cairns and Fairbanks Airports.

Performance Parameters	Location	Max Body	ENU value	ΔBody-ENU%	ΔAL%	AL
HPL (m)	Cairns	26.1	26.1	0.0	-34.8	40
	Fairbanks	18.6	11.7	58.5	-53.6	
VPL (m)	Cairns	36.3	36.3	0.0	3.7	35
	Fairbanks	14.8	19.4	31.5	-44.5	
EMT (m)	Cairns	16.6	11.5	43.8	10.5	15
	Fairbanks	9.2	6.0	52.3	-38.6	
Acc (m)	Cairns	3.2	3.2	0.0	67.8	1.87
	Fairbanks	1.6	1.4	14.6	-13.9	

- ***Dual-Constellation GPS + Galileo 24SV: Yuma almanac week 703 for GPS and provided with MAAST for Galileo, reset time [0d 1h 0m 0s] for Cairns and [0d 3h 0m 0s] for Fairbanks, mask angle 5°***

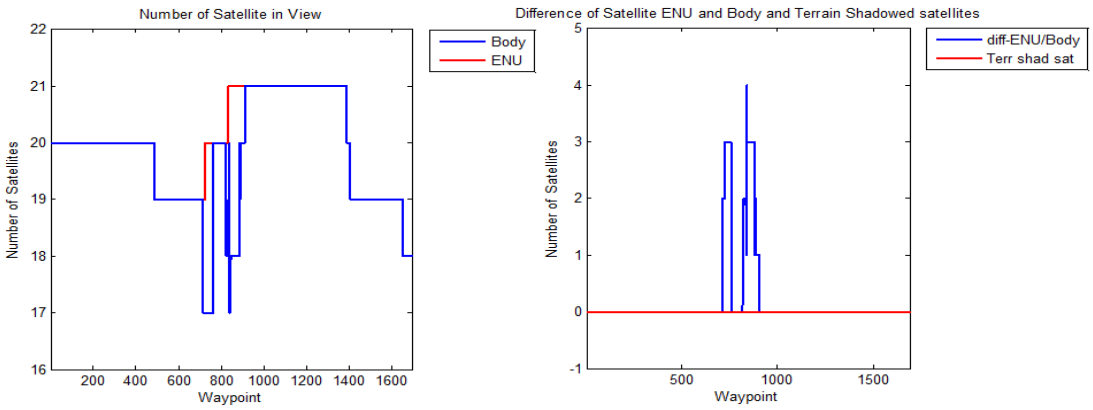

Figure 4-125 Number of Satellites in view (left) and difference (right) in the ENU (red) and Body (blue) Reference Frames for the Approach Procedure to the Airport of Cairns.

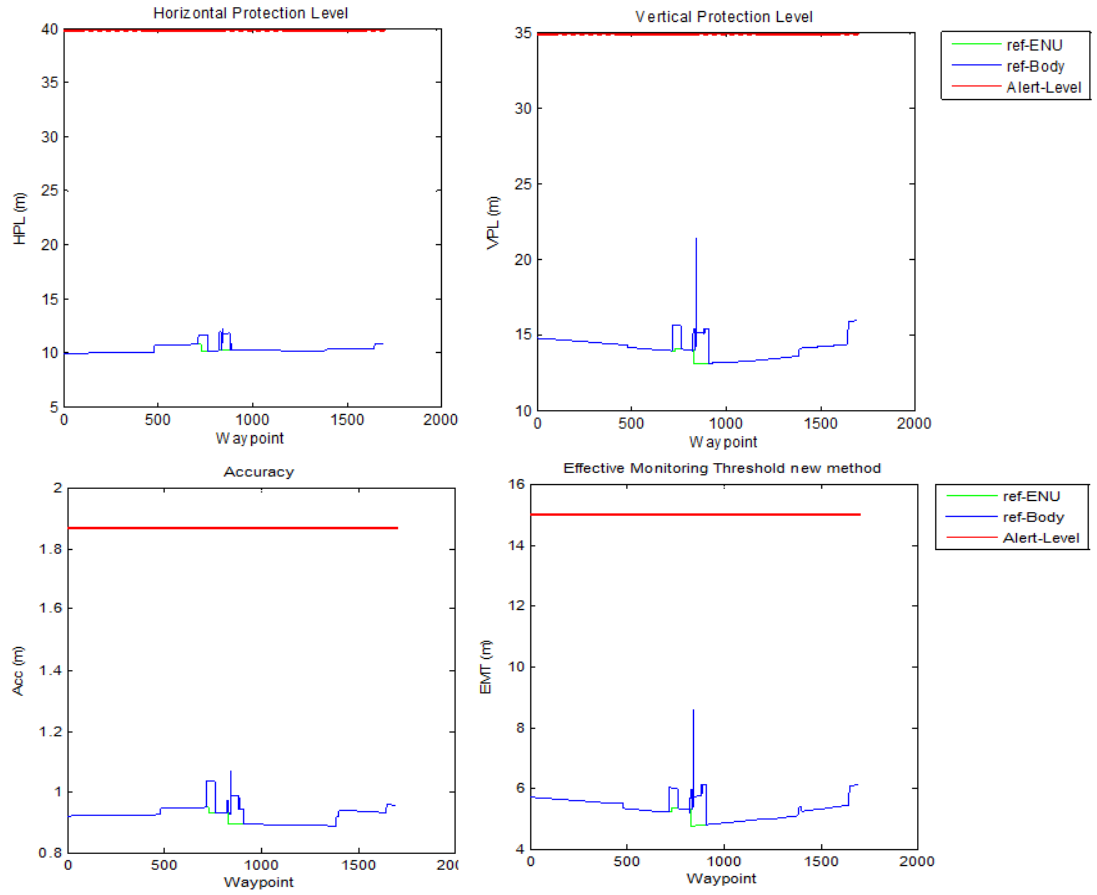

Figure 4-126 PLs in the ENU (green) and Body (blue) Reference Frames compared with the Alert Level (red) for the Approach Procedure to the Airport of Cairns.

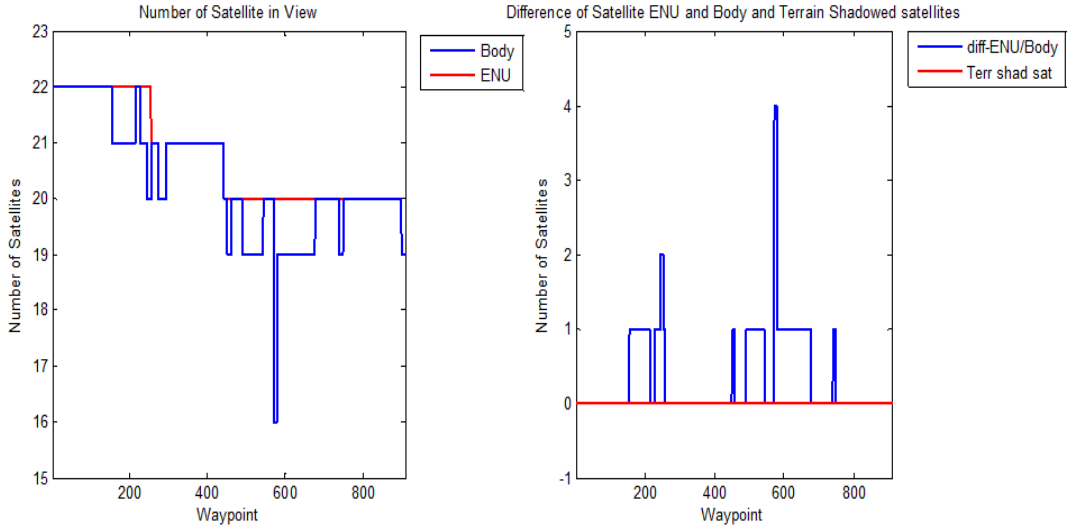

Figure 4-127 Number of Satellites in view (left) and difference (right) in the ENU (red) and Body (blue) Reference Frames for the Approach Procedure to the Airport of Fairbanks.

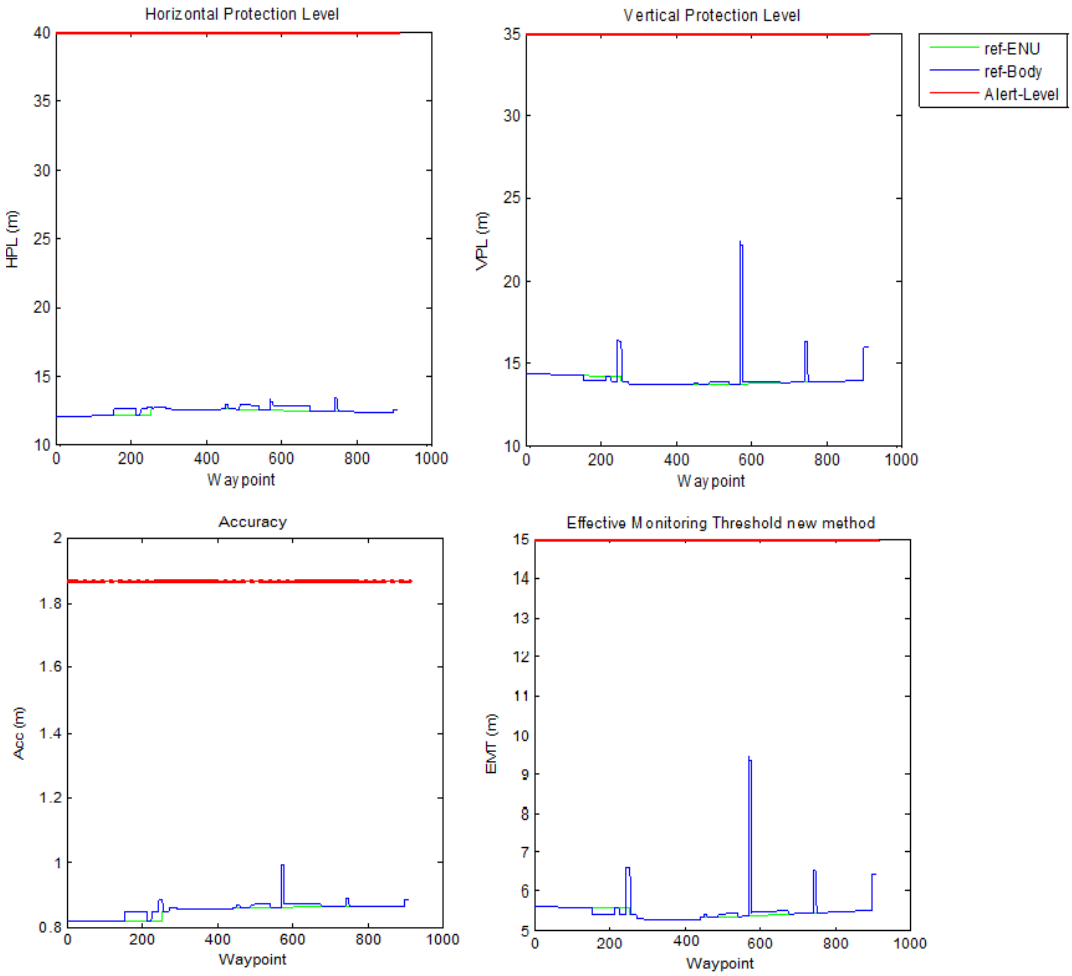

Figure 4-128 PLs in the ENU (green) and Body (blue) Reference Frames compared with the Alert Level (red) for the Approach Procedure to the Airport of Fairbanks.

Table 4-31 Values Comparison and Percentage Differences between ENU and Body Reference Frames for Cairns and Fairbanks Airports.

Performance Parameters	Location	Max Body	ENU value	ΔBody-ENU%	ΔAL%	AL
HPL (m)	Cairns	12.3	10.3	19.3	-69.3	40
	Fairbanks	13.4	12.5	7.5	-66.4	
VPL (m)	Cairns	21.4	13.1	63.2	-38.8	35
	Fairbanks	22.4	13.8	62.4	-36.0	
EMT (m)	Cairns	8.6	4.8	79.7	-42.9	15
	Fairbanks	9.5	5.4	76.5	-37.0	
Acc (m)	Cairns	1.1	0.9	19.6	-42.8	1.87
	Fairbanks	1.0	0.9	15.0	-46.9	

- ***Dual-Constellation GPS + Galileo 27SV: Yuma almanac week 703 for GPS and provided with MAAST for Galileo, reset time [0d 1h 0m 0s] for Cairns and [0d 3h 0m 0s] for Fairbanks, mask angle 5°***

Table 4-32 Values Comparison and Percentage Differences between ENU and Body Reference Frames for Cairns and Fairbanks Airports.

Performance Parameters	Location	Max Body	ENU value	ΔBody-ENU%	ΔAL%	AL
HPL (m)	Cairns	12.3	10.3	19.3	-69.3	40
	Fairbanks	13.5	12.2	10.1	-66.3	
VPL (m)	Cairns	21.4	13.1	63.2	-38.8	35
	Fairbanks	22.6	14.0	61.4	-35.5	
EMT (m)	Cairns	8.6	4.8	79.7	-42.9	15
	Fairbanks	9.6	5.5	74.4	-36.3	
Acc (m)	Cairns	0.9	1.07	19.6	-42.8	1.87
	Fairbanks	1.0	0.8	14.0	-48.4	

- ***Dual-Constellation GPS + GLONASS: Yuma almanac week 703 for GPS and provided with MAAST for Galileo, reset time [0d 1h 0m 0s] for Cairns and [0d 3h 0m 0s] for Fairbanks, mask angle 5°***

Table 4-33 Values Comparison and Percentage Differences between ENU and Body Reference Frames for Cairns and Fairbanks Airports.

Performance Parameters	Location	Max Body	ENU value	ΔBody-ENU%	ΔAL%	AL
HPL (m)	Cairns	11.8	11.1	6.3	-70.5	40
	Fairbanks	14.9	12.9	15.5	-62.8	
VPL (m)	Cairns	29.5	29.5	0.0	-15.8	35
	Fairbanks	21.9	14.5	51.4	-37.4	
EMT (m)	Cairns	13.2	13.2	0.0	-12.8	15
	Fairbanks	9.0	5.6	62.2	-39.9	
Acc (m)	Cairns	1.3	1.1	10.3	-32.7	1.87
	Fairbanks	1.2	1.0	24.9	-36.2	

- ***Dual-Constellation Galileo 24SV + GLONASS: Yuma almanac week 703 for GPS and provided with MAAST for Galileo, reset time [0d 1h 0m 0s] for Cairns and [0d 3h 0m 0s] for Fairbanks, mask angle 5°***

Table 4-34 Values Comparison and Percentage Differences between ENU and Body Reference Frames for Cairns and Fairbanks Airports.

Performance Parameters	Location	Max Body	ENU value	ΔBody-ENU%	ΔAL%	AL
HPL (m)	Cairns	11.5	11.5	0.0	-71.2	40
	Fairbanks	12.7	11.0	14.4	-68.2	
VPL (m)	Cairns	29.3	29.3	0.0	-16.4	35
	Fairbanks	15.9	13.9	14.4	-54.7	
EMT (m)	Cairns	13.1	13.1	0.0	-13.0	15
	Fairbanks	6.5	5.3	21.5	-56.7	
Acc (m)	Cairns	1.5	1.1	35.3	-18.3	1.87
	Fairbanks	0.92	0.9	7.5	-50.5	

- ***Dual-Constellation Galileo 27SV + GLONASS: Yuma almanac week 703 for GPS and provided with MAAST for Galileo, reset time [0d 1h 0m 0s] for Cairns and [0d 3h 0m 0s] for Fairbanks, mask angle 5°***

Table 4-35 Values Comparison and Percentage Differences between ENU and Body Reference Frames for Cairns and Fairbanks Airports.

Performance Parameters	Location	Max Body	ENU value	ΔBody-ENU%	ΔAL%	AL
HPL (m)	Cairns	11.5	11.5	0.0	-71.2	40
	Fairbanks	12.7	11.0	14.4	-68.2	
VPL (m)	Cairns	29.3	29.3	0.0	-16.4	35
	Fairbanks	15.9	13.9	14.4	-54.7	
EMT (m)	Cairns	13.1	13.1	0.0	-13.0	15
	Fairbanks	6.5	5.3	21.5	-56.7	
Acc (m)	Cairns	1.5	1.1	35.3	-18.3	1.87
	Fairbanks	0.9	0.8	8.0	-51.9	

- ***Tri-constellation GPS, Galileo 24SV and GLONASS: Yuma almanac week 703 for GPS and provided with MAAST for Galileo and GLONASS, reset time [0d 1h 0m 0s] for Cairns and [0d 3h 0m 0s] for Fairbanks, mask angle 5°***

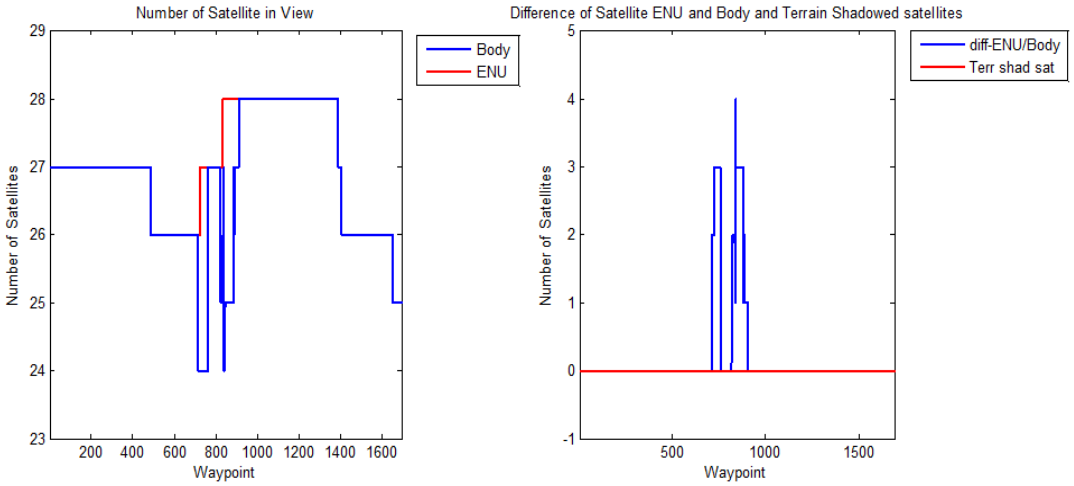

Figure 4-129 Number of Satellites in view (left) and difference (right) in the ENU (red) and Body (blue) Reference Frames for the Approach Procedure to the Airport of Cairns.

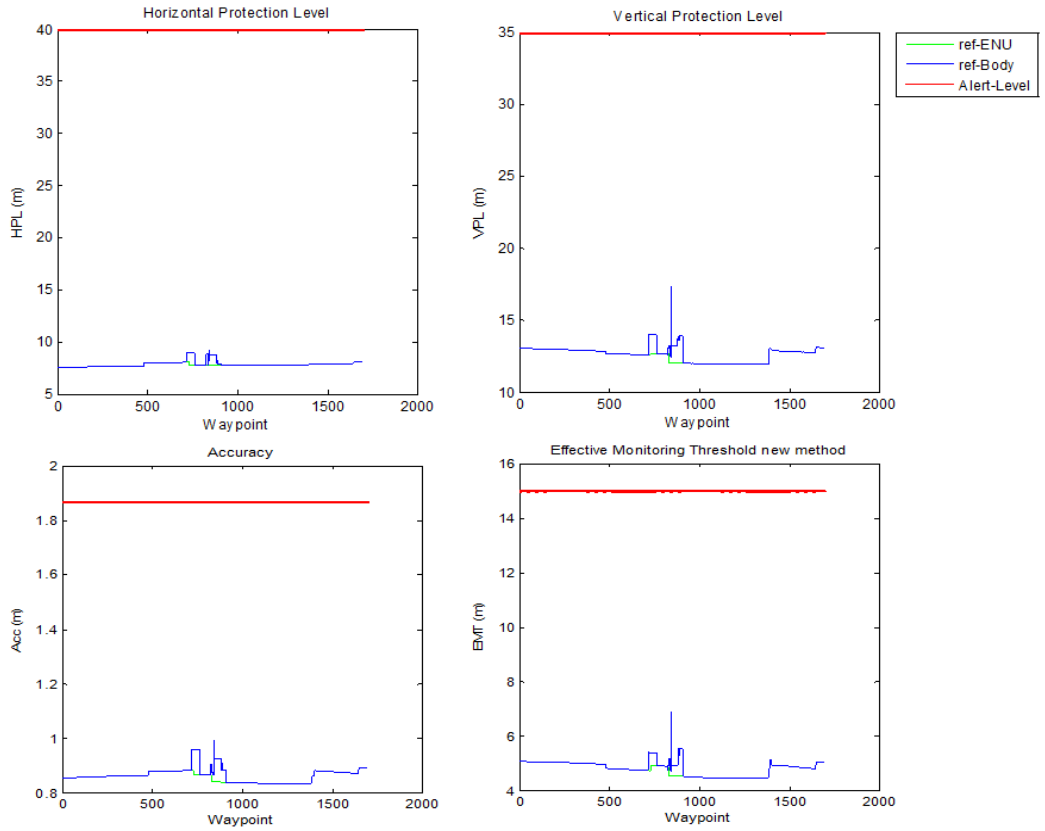

Figure 4-130 PLs in the ENU (green) and Body (blue) Reference Frames compared with the Alert Level (red) for the Approach Procedure to the Airport of Cairns.

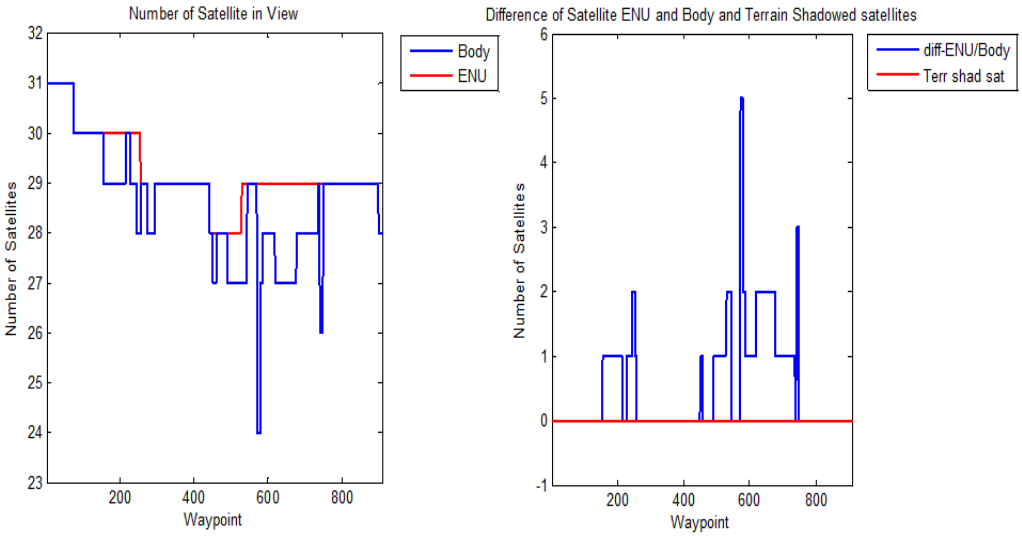

Figure 4-131 Number of Satellites in view (left) and difference (right) in the ENU (red) and Body (blue) Reference Frames for the Approach Procedure to the Airport of Fairbanks.

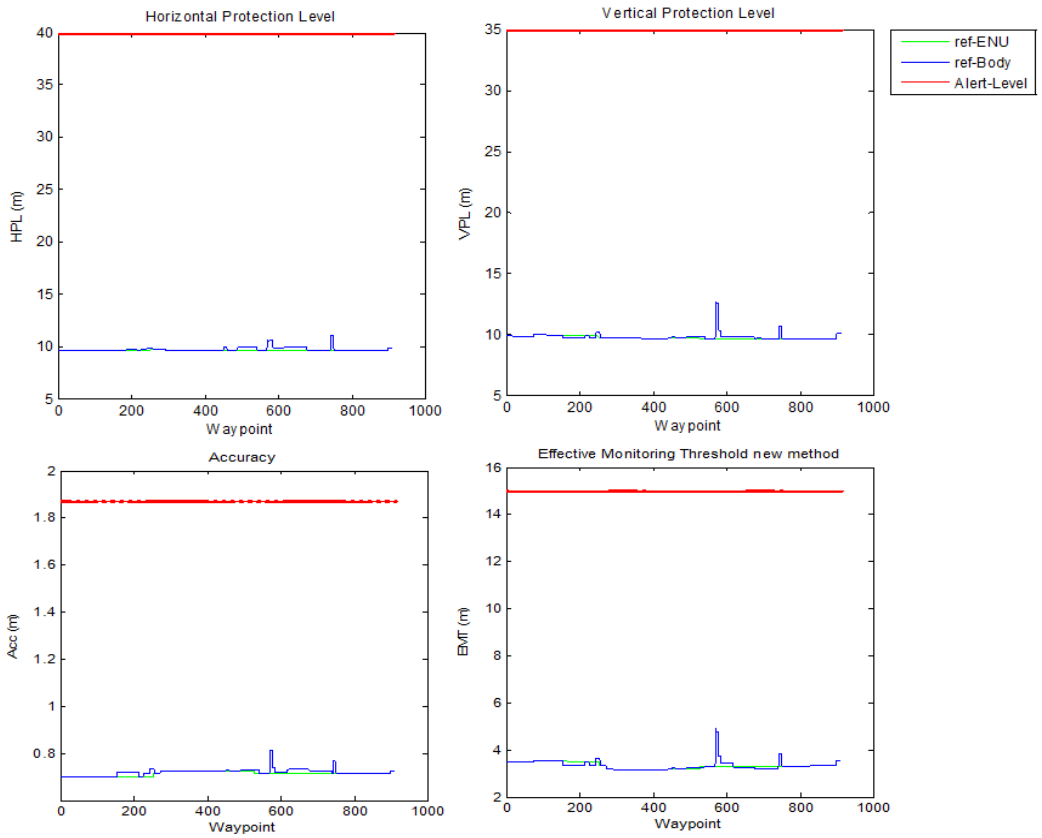

Figure 4-132 PLs in the ENU (green) and Body (blue) Reference Frames compared with the Alert Level (red) for the Approach Procedure to the Airport of Fairbanks.

Table 4-36 Values Comparison and Percentage Differences between ENU and Body Reference Frames for Cairns and Fairbanks Airports.

Performance Parameters	Location	Max Body	ENU value	ΔBody-ENU%	ΔAL%	AL
HPL (m)	Cairns	9.2	7.7	19.5	-77.0	40
	Fairbanks	11.1	9.7	15.1	-72.2	
VPL (m)	Cairns	17.3	12.0	44.3	-50.5	35
	Fairbanks	12.5	9.7	29.6	-64.3	
EMT (m)	Cairns	6.9	4.5	51.6	-54.0	15
	Fairbanks	4.8	3.1	50.8	-68.4	
Acc (m)	Cairns	1.0	0.8	18.5	-46.8	1.87
	Fairbanks	0.8	0.7	14.2	-55.8	

- ***Tri-constellation GPS, Galileo 27SV and GLONASS: Yuma almanac week 703 for GPS and provided with MAAST for Galileo and GLONASS, reset time [0d 1h 0m 0s] for Cairns and [0d 3h 0m 0s] for Fairbanks, mask angle 5°***

Table 4-37 Values Comparison and Percentage Differences between ENU and Body Reference Frames for Cairns and Fairbanks Airports.

Performance Parameters	Location	Max Body	ENU value	ΔBody-ENU%	ΔAL%	AL
HPL (m)	Cairns	9.2	7.7	19.5	-77.0	40
	Fairbanks	11.4	9.7	15.3	-72.2	
VPL (m)	Cairns	17.3	12.0	44.3	-50.5	35
	Fairbanks	12.6	9.6	31.4	-63.9	
EMT (m)	Cairns	6.9	4.5	51.6	-54.0	15
	Fairbanks	4.9	3.3	47.7	-67.5	
Acc (m)	Cairns	1.0	0.8	18.5	-46.8	1.87
	Fairbanks	0.8	0.7	13.6	-56.7	

4.3.3. FINAL COMMENTS AND REMARKS

It is clear from the graphs and the tables that the aircraft attitude and the surrounding environment affect the performance of the ARAIM algorithm; each satellite lost generates a peak in the performance parameters that depends on the total number of satellites in view, their relative geometry and on the number of satellites lost at the same time. The single GPS constellation configuration could not be enough to comply with the necessary requirements for LPV-200 approaches (the same results were obtained with GLONASS and Galileo individually). The dual constellation configuration seems to satisfy the requirements, but in some cases with limited margin with respect to the thresholds, which means that even a small variation in the nominal conditions could trigger an alarm. The main outcome of this research is the identification that the ideal scenario would be to have a tri-constellation system that provides at the same time high redundancy, reliability and increased safety margin.

However, further analysis showed that a single constellation could sometimes satisfy the LPV-200 RNP, since the performances are strongly dependent on both the satellite geometry, as one can easily deduce, and the models which are used to estimate signal errors and biases (e.g. ionospheric and tropospheric delays). Consequently, even the same trajectory, performed with a different starting time, could lead to completely different results. At the same, it has been highlighted that in some cases the loss of a satellite could, to a lesser extent, lead to a lower values in the PLs, indicating the need of an additional strategy of selecting the set of satellites that provides the best performances, as it has been proposed and discussed in (InsideGNSS, 2016).

In general, these results show that a dedicated system, that evaluates the effects of the attitude and the surrounding environment in an operational configuration, needs to be developed and integrated into the flight management system if the ARAIM technique is to be used as an on-board system for integrity monitoring. The integration of such system could support the pilots, together with the ATM, in the pre-flight operations for the definition of the path to be followed to reach the arrival location. The system could highlight possible outages along the trajectory, giving the possibility to the pilots to define a mitigation strategy, such as selecting an alternative approach procedure or requesting the support of other navigation systems, if available.

Moreover, the results show that a dual-constellation GNSS receiver might not be sufficient for all the possible scenarios, supporting the need for an international collaboration for the development of multi-GNSS applications.

4.4. APPATT LONG-TERM (LT) ALGORITHM AND SCENARIOS

The second algorithm is a variation of the APPATT ST that analyses the trend of the integrity parameters along the aircraft trajectory, showing their fluctuations within a predefined time interval. The objective is to provide the approach designers with innovative equipment for the evaluation of the availability of new procedures, together with their limits and safety. The tool enables the user to set the time interval, allowing the analysis of the expected trajectory during the selected time frame, such as the repeat pattern of the different GNSS constellations (1 day for GPS, 10 days for Galileo and 8 days for GLONASS). Currently, only a 90 degrees turn

manoeuvre (Figure 4-133 90° turn manoeuvre used for the APPAT LT tool) with 25 degrees bank angle from a STAR procedure for the airport of Cairns has been analysed and results show that also a tri-constellation configuration cannot fully satisfy the LPV-200 approach requirements all the time. However, the tool is designed to help procedures designers to define manoeuvre attitude constraints or ATM and Airlines to schedule the flights in a timeframe that do not present integrity outages.

The curved path is generated using the algorithm that is presented in the next chapter, the Flight Path Generator (FPG), that takes as input a list of waypoints of the selected approach procedure and based on the category of the points (fly-by or turn point), the trajectory parameters (e.g. aircraft speed, bank angle and turn radius or rate of turn) and it generates the possible path (further details on the algorithm are provided in the next chapter).

It has been selected a simple 90° turn manoeuvre and not the full flight path for two main reasons:

- The computational load required for the computation. The analysis of a short part of the trajectory for 2 days with the current algorithm could requires from several days to up to a month, depending on the number of constellations considered, since the tool is analysing it for a long period time and with a very short time step (1 second, the standard update rate of GNSS receivers)
- It has been highlighted in the previous sections that the manoeuvres are the most critical part of a trajectory.

However, with the support of an enhanced and optimised algorithm, the performances of the tool could be improved, enabling the possibility of analysing the full trajectory and reducing the simulation time.

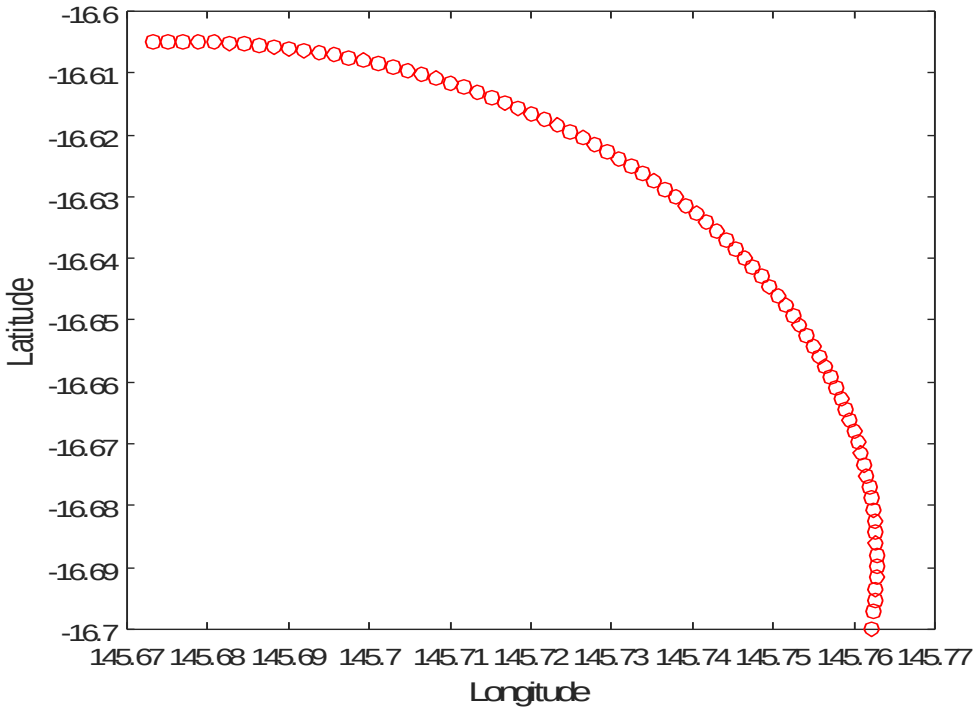

Figure 4-133 90° turn manoeuvre used for the APPAT LT tool.

4.5. RESULTS AND ANALYSIS

As for the analyses performed for the APPATT ST, different cases and combinations of the three constellations are considered in this research. Due to the high computational load, the cases presented span a timeframe of 2 days.

Figure 4-134 to Figure 4-137 show the results of the trajectory using the APPAT ST tool

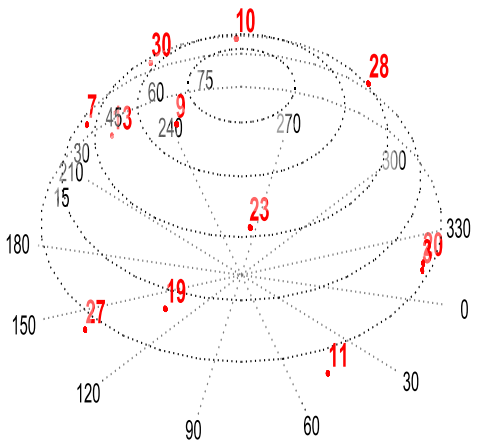

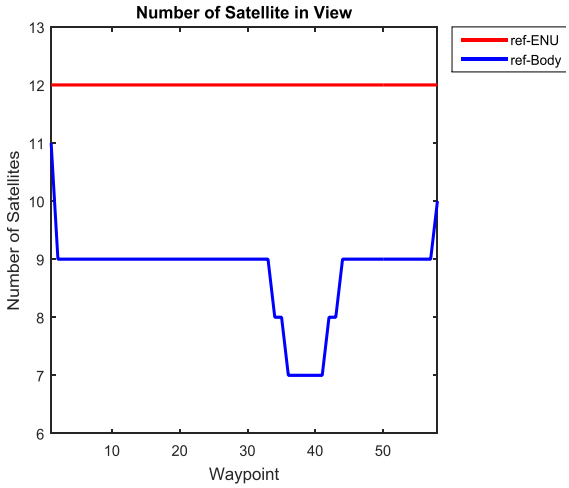

Figure 4-134 Satellites in View Skyplot in the ENU reference frame.

Figure 4-135 Number of Satellites in view in the ENU (red) and Body (blue) Reference Frames along the Trajectory.

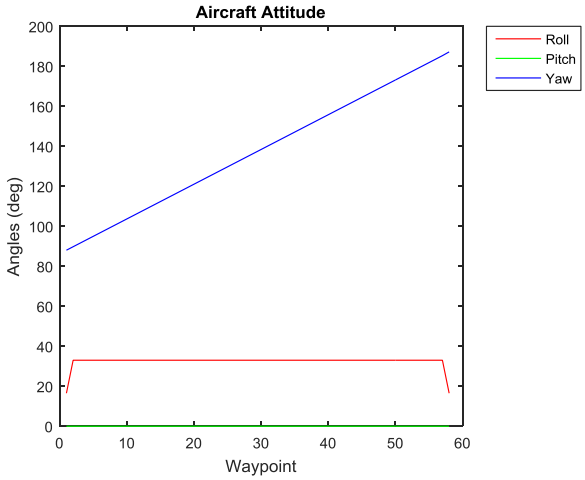

Figure 4-136 Aircraft Attitude Angles along the Approach Procedure for Cairns Airport.

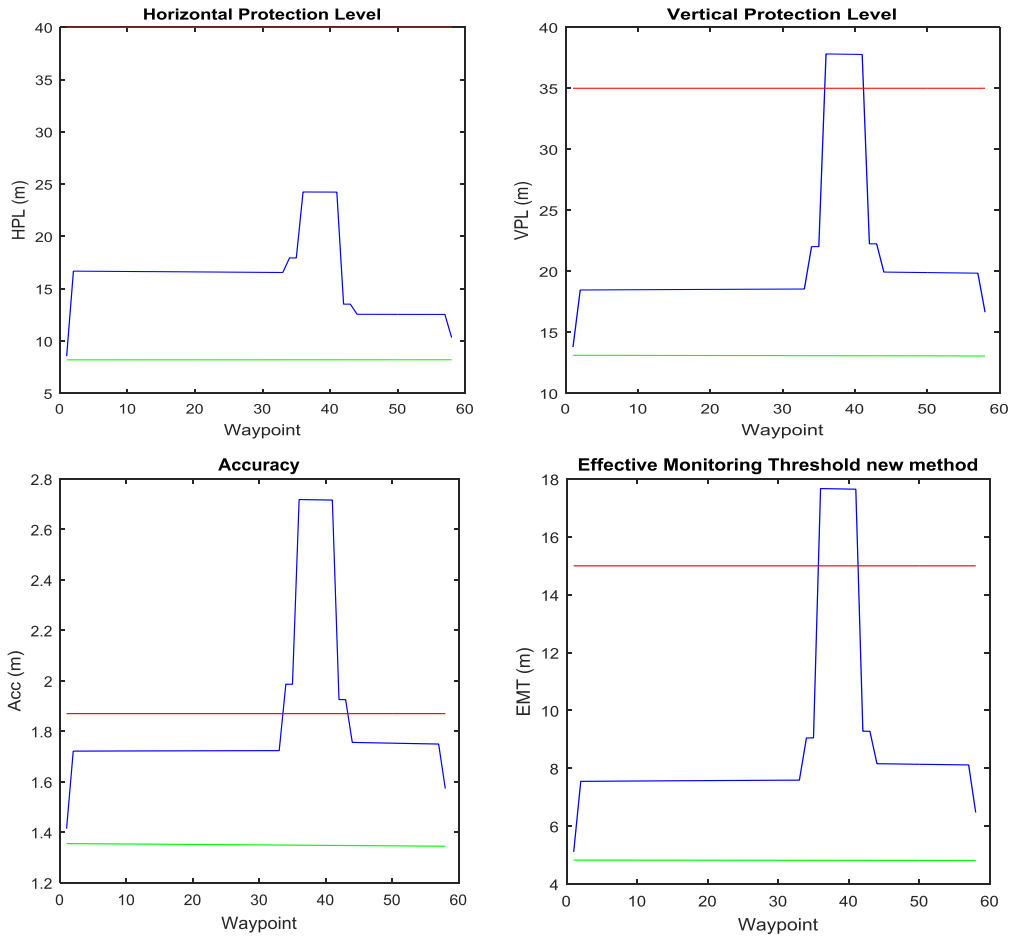

Figure 4-137 PLs in the ENU (green) and Body (blue) Reference Frames compared with the Alert Level (red) for the 90° turn manoeuvre in the short term.

- <u>Single Constellation GPS</u>

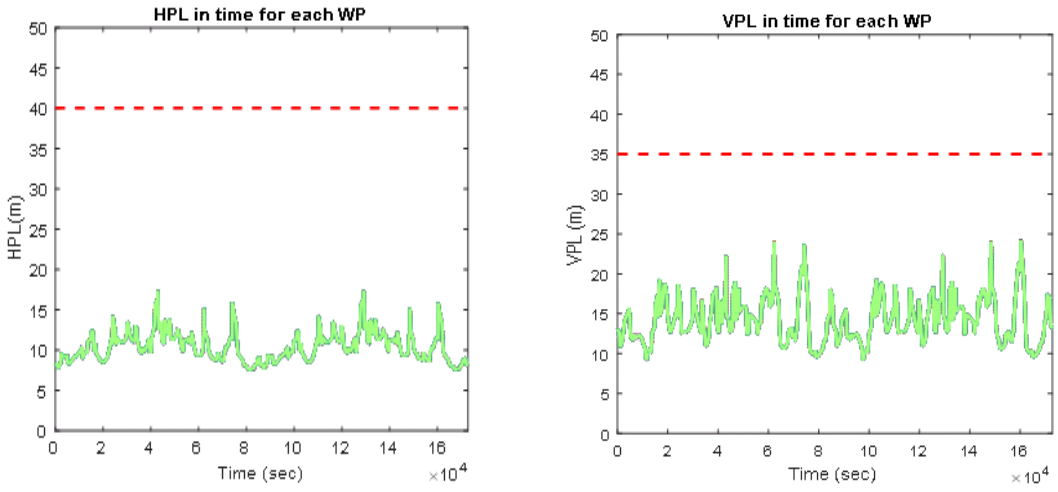

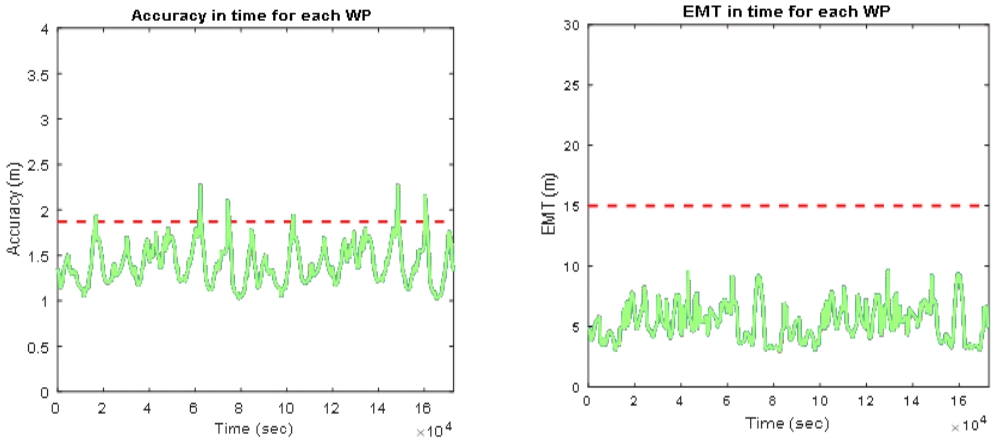

Figure 4-138 PLs in the ENU Reference Frames (no attitude effect) compared with the Alert Level (red) for the 90° turn manoeuvre in the long term (2 days) for the single constellation configuration (GPS).

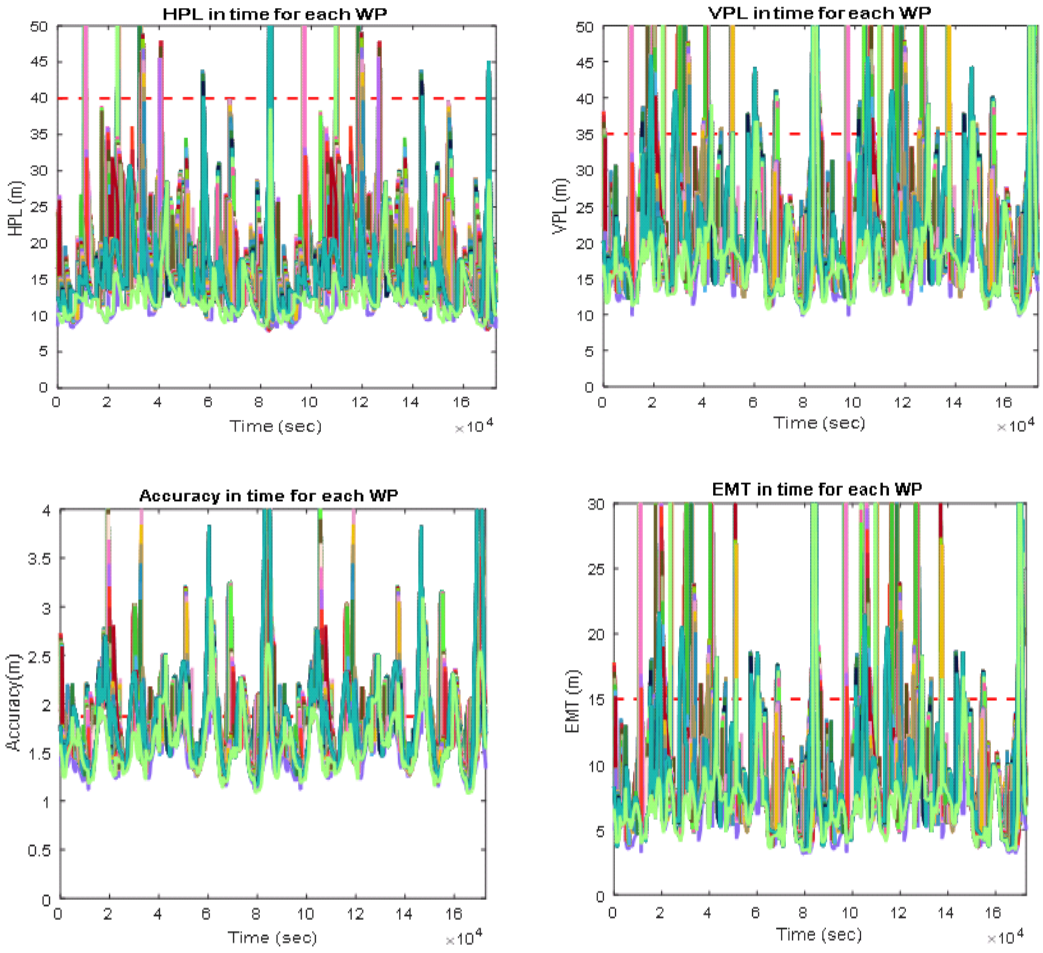

Figure 4-139 PLs in the Body Reference Frames (with attitude effect) compared with the Alert Level (red) for the 90° turn manoeuvre in the long term (2 days) for the single constellation configuration (GPS). Each colour represents a single WP.

As we may expect, for each waypoint, represented by a different colour, the integrity parameters behave in the same manner, since they benefit from the same number of satellite in view for the entire time interval. However, the single constellation configuration in the ENU reference frame already presents situations in which the RNP for LPV-200 are not satisfied, in particular the accuracy overtakes the protection level (red dashed line).

In the Body reference frame, all the parameters repeatedly overtake the limits, confirming their high time dependency found in the previous results with the APPATT ST and that a single constellation configuration does not always satisfy the LPV-200 requirements even in nominal conditions (no faults or failure).

- Dual Constellation GPS-Galileo 24SV

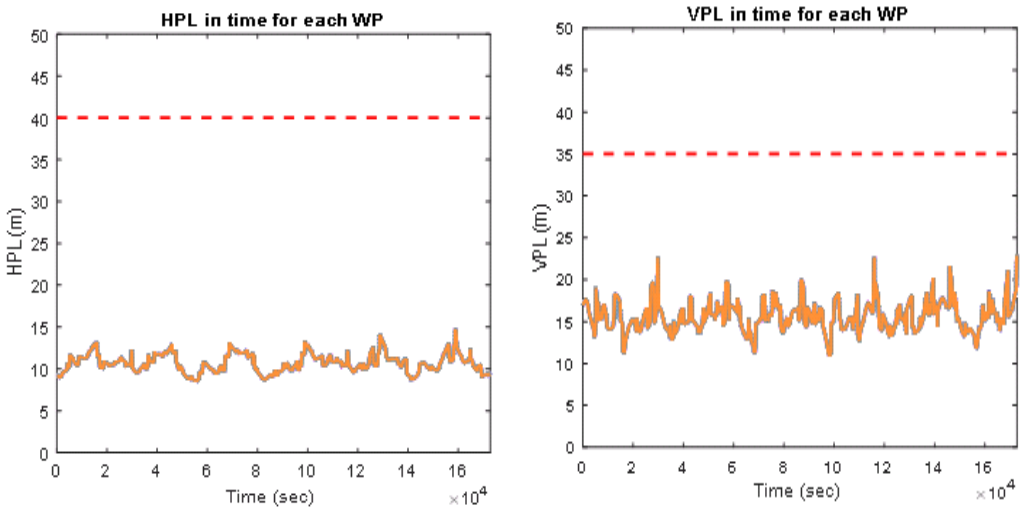

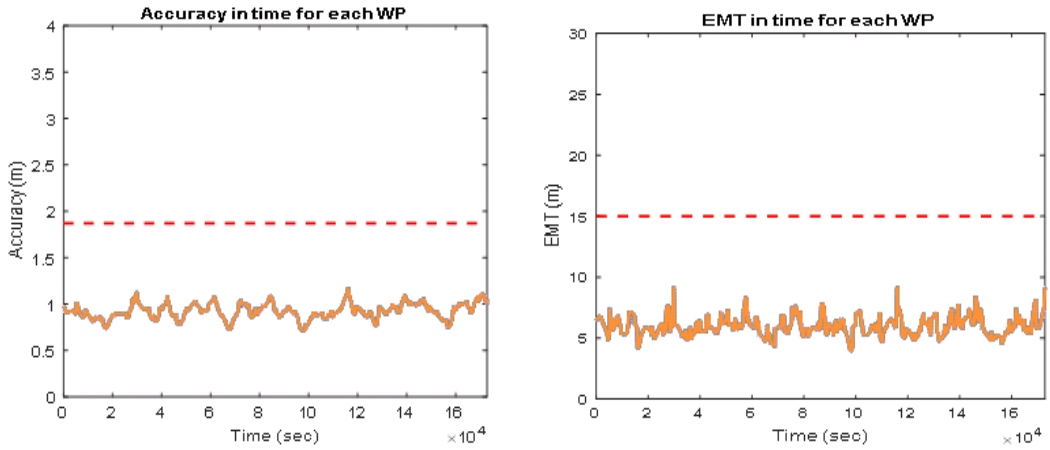

Figure 4-140 PLs in the ENU Reference Frames (no attitude effect) compared with the Alert Level (red) for the 90° turn manoeuvre in the long term (2 days) for the dual constellation configuration (GPS+Galileo 24SV).

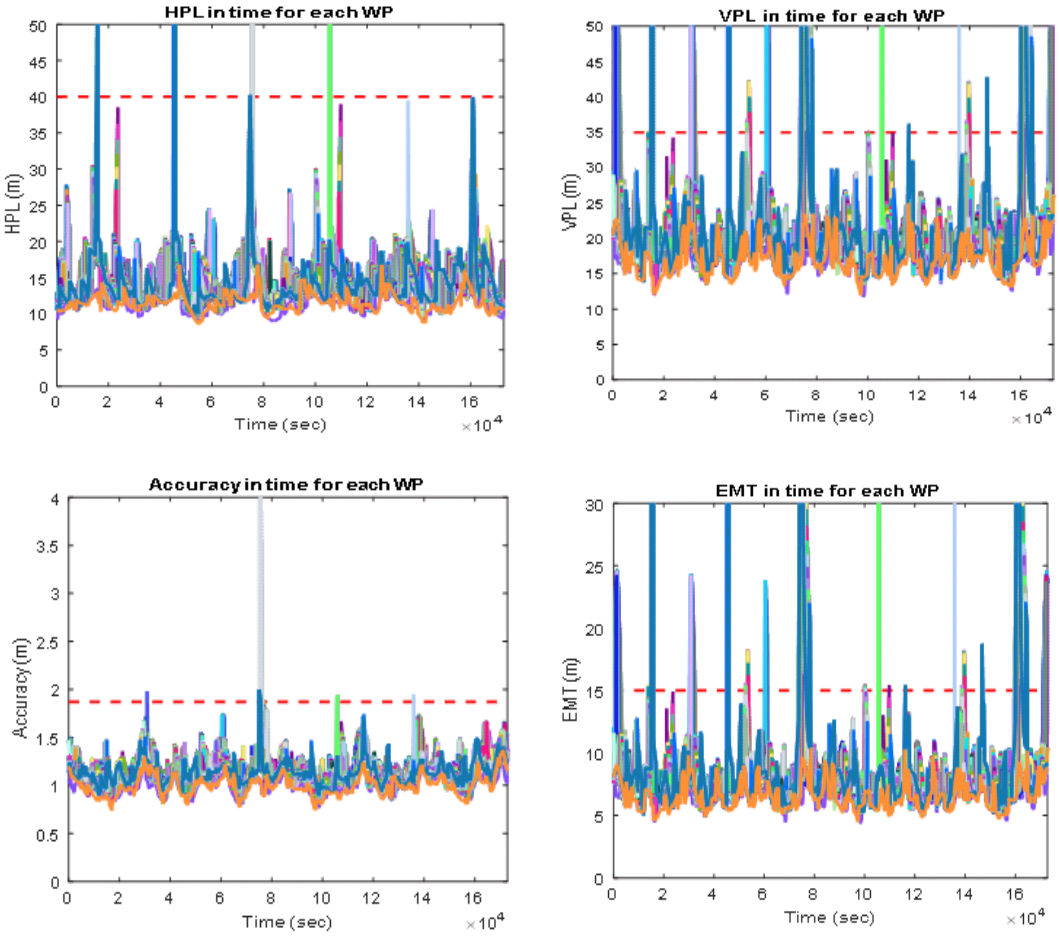

Figure 4-141 PLs in the Body Reference Frames (with attitude effect) compared with the Alert Level (red) for the 90° turn manoeuvre in the long term (2 days) for the single constellation configuration (GPS). Each colour represents a single WP.

- Dual Constellation GPS-GLONASS

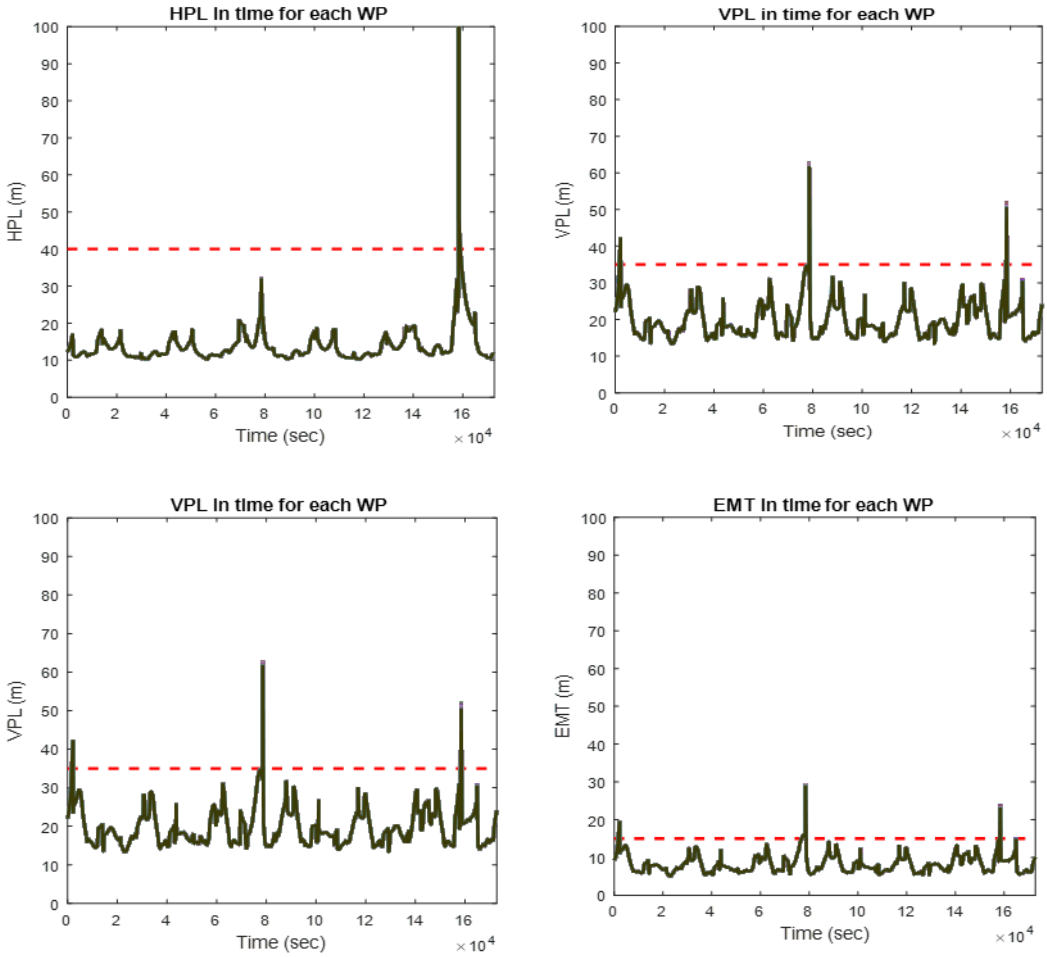

Figure 4-142 PLs in the ENU Reference Frames (no attitude effect) compared with the Alert Level (red) for the 90° turn manoeuvre in the long term (2 days) for the dual constellation configuration (GPS+Galileo 24SV).

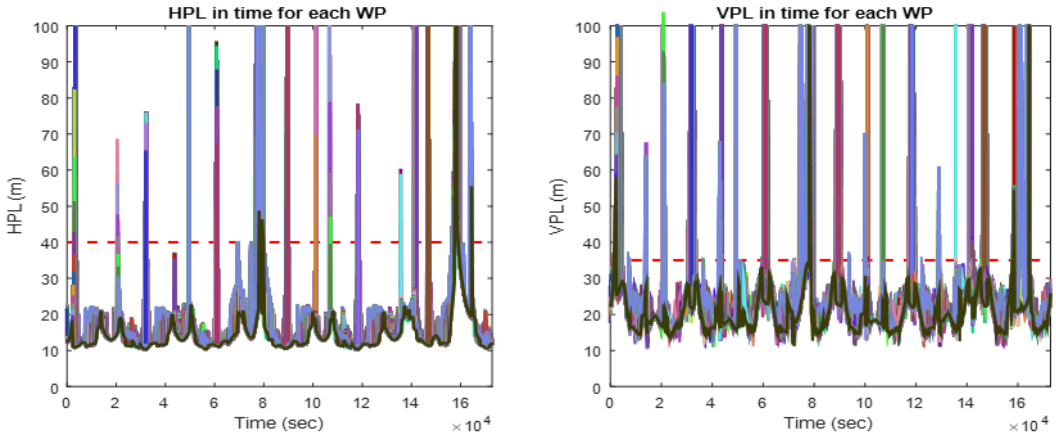

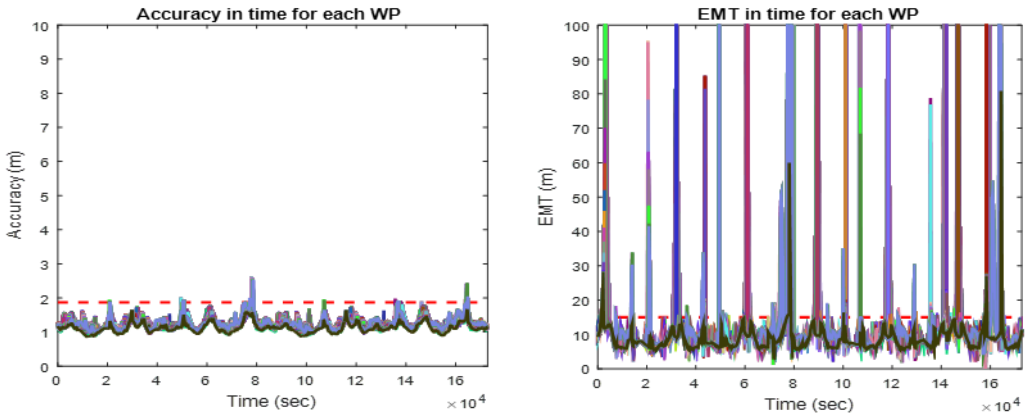

Figure 4-143 PLs in the Body Reference Frames (with attitude effect) compared with the Alert Level (red) for the 90° turn manoeuvre in the long term (2 days) for the single constellation configuration (GPS). Each colour represents a single WP.

Figure 4-140 to Figure 4-143 show that the introduction of a second constellation reduces drastically the average values and the number of peaks that break the alert levels, but it is still evident that a duel-constellation integrity monitoring system does still not guarantee full reliability.

- Tri-Constellation GPS-GLONASS-Galileo 24SV

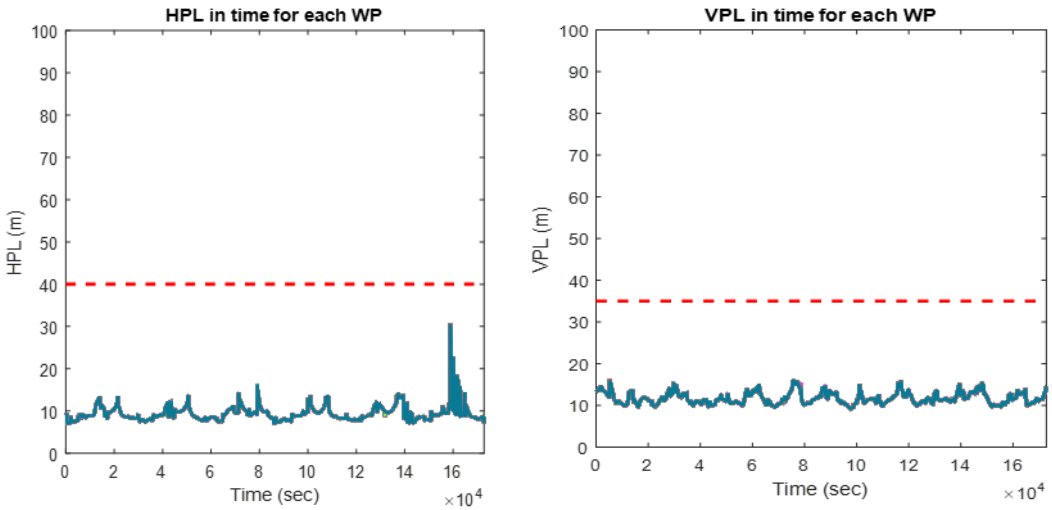

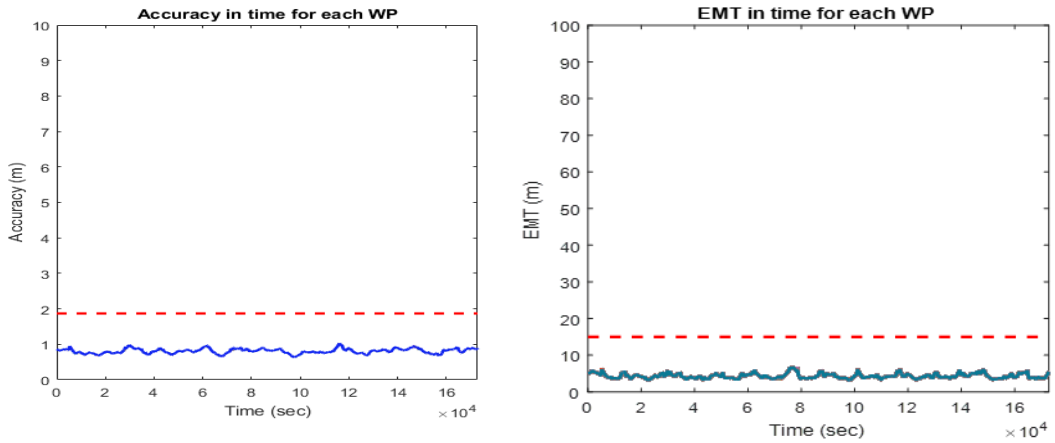

Figure 4-144 PLs in the ENU Reference Frames (no attitude effect) compared with the Alert Level (red) for the 90° turn manoeuvre in the long term (2 days) for the dual constellation configuration (GPS+Galileo 24SV).

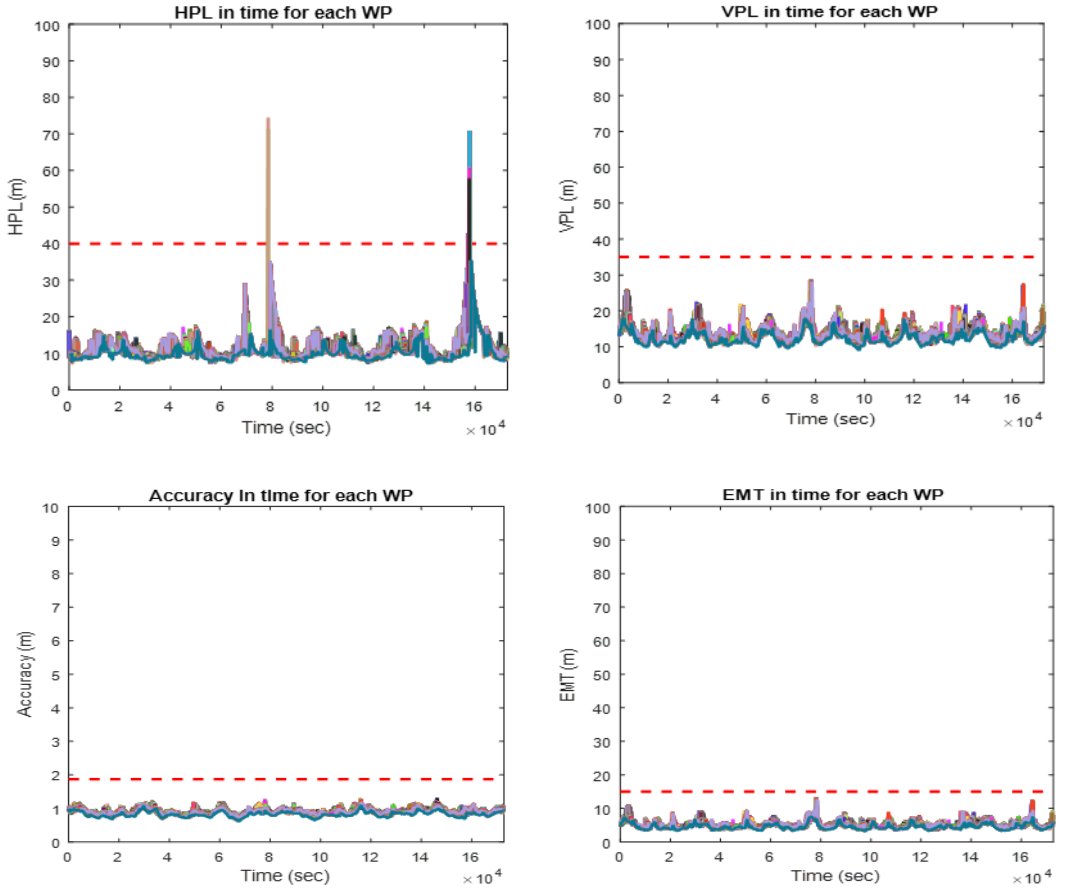

Figure 4-145 PLs in the Body Reference Frames (with attitude effect) compared with the Alert Level (red) for the 90° turn manoeuvre in the long term (2 days) for the single constellation configuration (GPS). Each colour represents a single WP.

The graphs in Figure 4-145 show how effective is the integration of three constellations in a GNSS receiver, almost all the peaks in the protection levels are mitigated with the few exceptions of two peaks in the HPL at around 22h and 42h.

In particular, analysing the first peak with the APPATT ST tool, it is possible to investigate the reason behind the integrity outage; Figure 4-146 to Figure 4-154 present the results as already seen in the APPAT ST and they show that the integrity outage is determinate by the loss in the body reference frame of the 8 satellites with low elevation angle (below 25°) and in the range of 0°-180° azimuth angle (8 is the maximum number of satellite lost between WP 60 and 65). To be noticed that in the HPL, the peak is generated by the loss of satellite n. 3 between WP 58 and WP 59, while the loss of the satellite n.40 brings back the HPL value below the HAL, showing a behaviour already examined in the previous section. The same sequence of satellite loss doesn't have the same effect on the other integrity parameters, that instead have a double sudden increase between WP58-60.

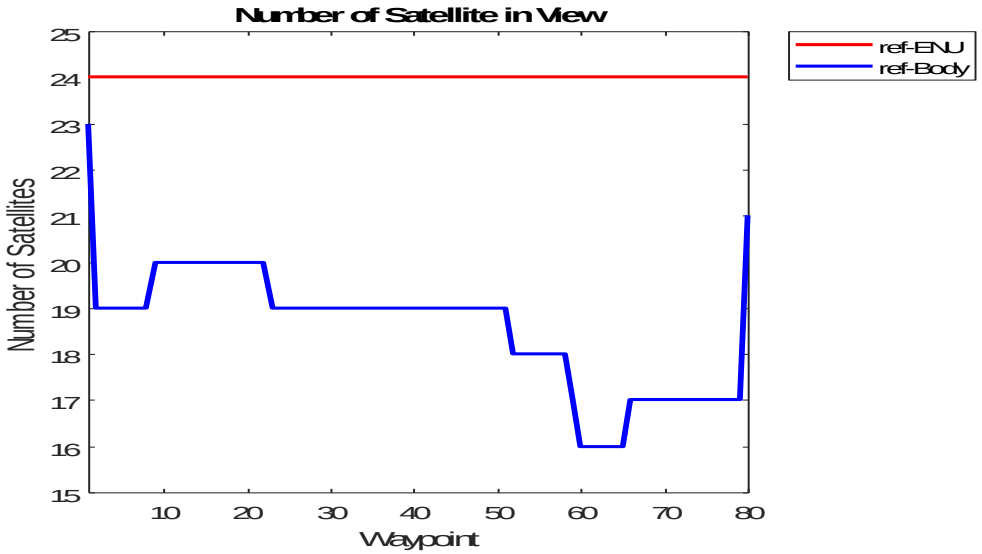

Figure 4-146 Number of Satellites in view in the ENU (red) and Body (blue) Reference Frames along the Trajectory.

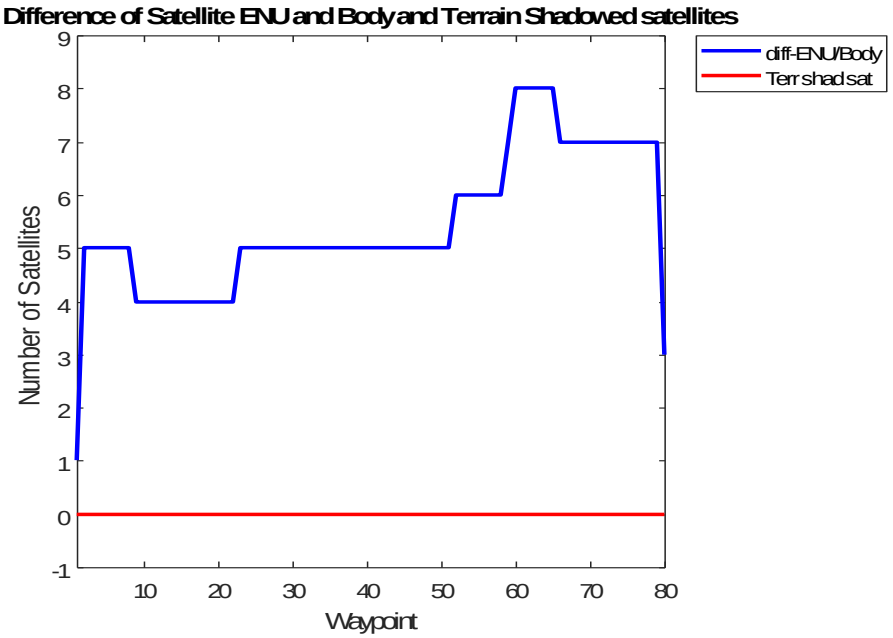

Figure 4-147 Number of Shadowed Satellites by Aircraft Attitude (blue) and Terrain (red).

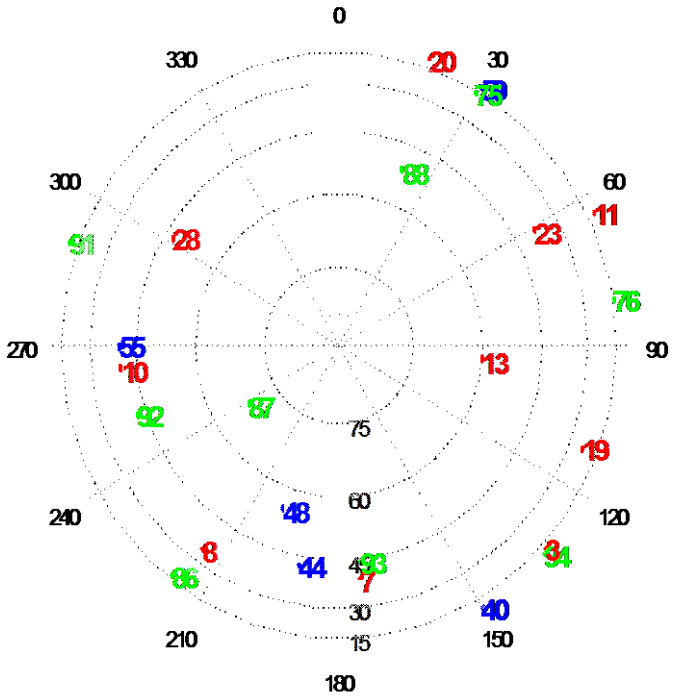

Figure 4-148 Satellites in View Skyplot in the ENU reference frame, (GPS in red, GLONASS in blue and Galileo in green).

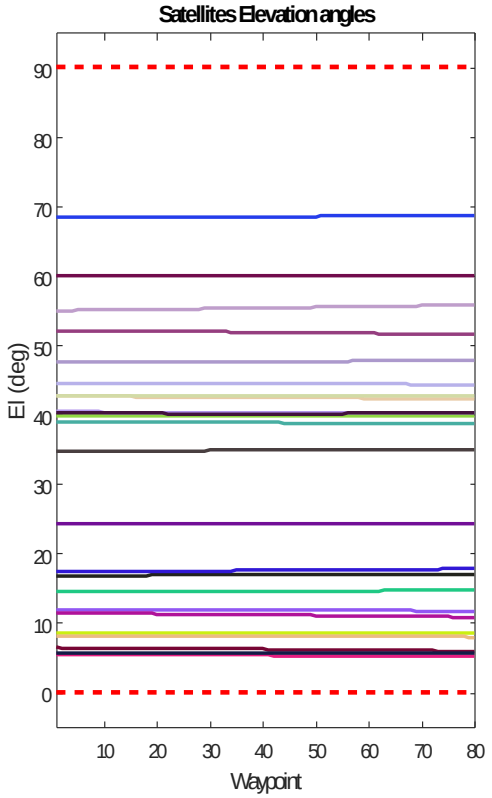

Figure 4-149 Satellites Elevation.

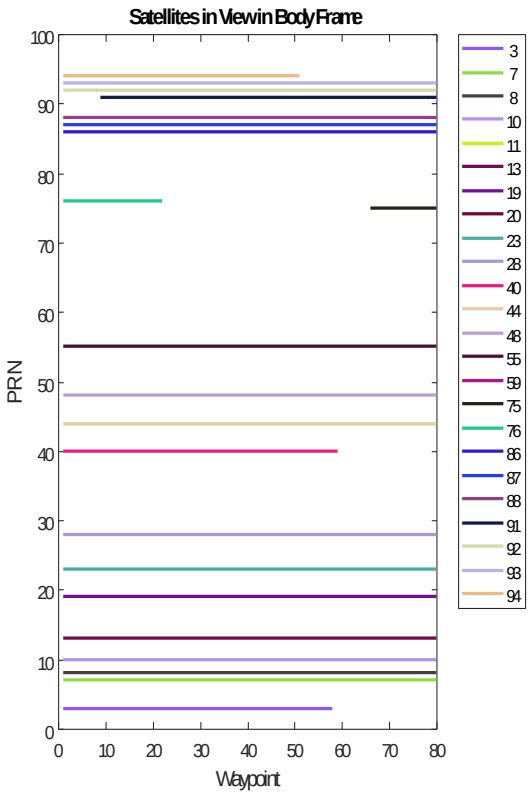

Figure 4-150 Satellites visibility by PRN.

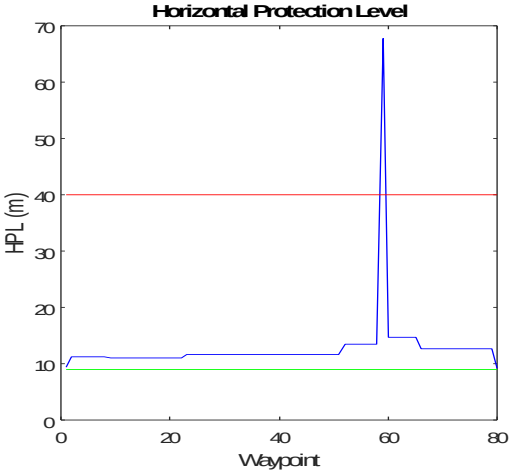

Figure 4-151 HPL in the ENU (green) and Body (blue) Reference Frames compared with the Alert Level (red).

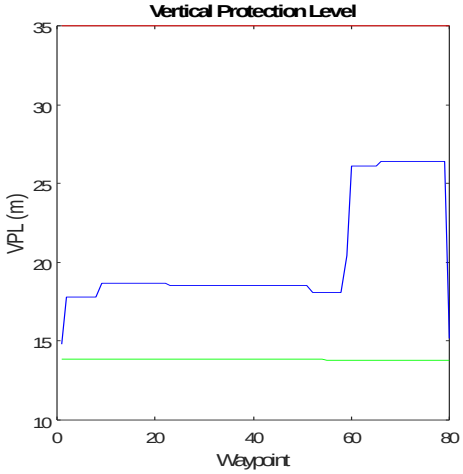

Figure 4-152 VPL in the ENU (green) and Body (blue) Reference Frames compared with the Alert Level (red).

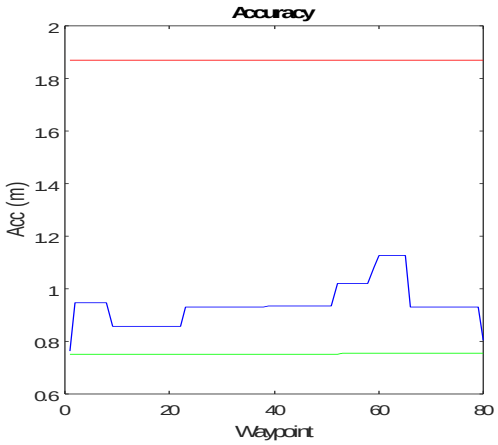

Figure 4-153 Accuracy in the ENU (green) and Body (blue) Reference Frames compared with the Alert Level (red).

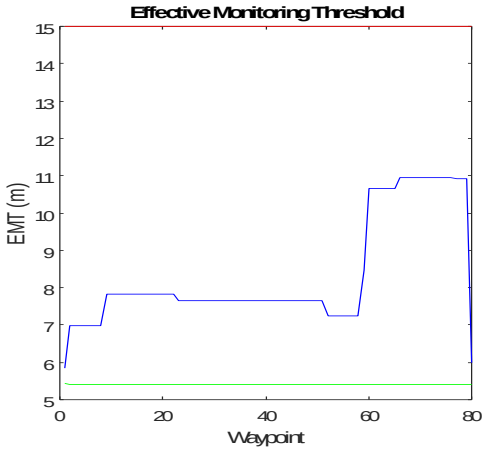

Figure 4-154 EMT in the ENU (green) and Body (blue) Reference Frames compared with the Alert Level (red).

Table 4-38 Values Comparison between ENU and Body Reference Frames.

Performance Parameter	Max_{ENU}	WP_{Max_ENU}	Max_{Body}	WP_{Max_Body}	ENU at WP_{Max_Body}	AL
HPL (m)	8.98	80	67.69	59	8.97	**40**
VPL (m)	13.86	1	26.40	66	13.82	**35**
EMT (m)	5.42	1	10.95	66	5.40	**15**
Accuracy (m)	0.75	80	1.13	60	0.75	**1.87**

Table 4-39 Percentage Differences between Max Values in Body Reference Frame, related ENU values and Alert Level.

Performance Parameter	Δ% between Body and ENU at WP_{Max_Body}	Δ% between Max_{Body} and AL
HPL (m)	654.47	69.57
VPL (m)	91	-24.55
EMT (m)	102.86	-27
Accuracy (m)	49.33	-39.81

The results of the LT version confirm that a dual-constellation GNSS receiver might not be sufficient for all the possible scenarios, supporting the need for an international collaboration for the development of multi-GNSS applications.

The implementation of these new algorithms may allow the users to assess the benefits and limits of a selected or new procedure whether they are procedures' designer, tester or pilots.

Both the results of the APPATT ST and LT tools demonstrate that dedicated systems, that predicts the effects of the attitude and the surrounding environment, need to be developed and implemented into the current processes and operations, such as integrated into the flight management system of the aircraft, if the ARAIM technique is going to be used as main on-board system for integrity monitoring.

5. AIRCRAFT TRAJECTORY MODIFIER

The Flight Path Generator and Modifier tools are introduced in this chapter; the concept behind these new functions is to introduce the integrity as a new parameter in the design and optimisation of flight path.

These two functions are designed to generate a trajectory based on the inputs provided by the user (a list of waypoints that defines the expected flight path), to analyse the integrity parameters using the APPATT ST and to attempt to modify the trajectory in order to satisfy the integrity requirements for the selected procedure. These two functions can be used as an intermediate step between the current procedures development and testing process, in which trajectories design is based on fixed waypoints where terrestrial navigational aids (NAVAIDs) may be located, and the introduction of GNSS based procedures, in which the trajectories will not be any longer based on static procedures but a more dynamic and flexible process might be introduced that could further optimise them on a multi-aspects base (such as costs, environmental impact, safety and integrity).

5.1. THE FUTURE CONCEPT

One of the main concept pursued and analysed within the SESAR project is the Trajectory Based Operations (TBO) that has the objective of enabling the management of performance-based 4D trajectories (3D position + time) by fully

sharing information related to the trajectories between all the ATM actors (SESAR, 2014).

In the future, ATM will work on a time-based system, rather than a radar-surveillance system, in which aircrafts will be required to reach a specific point of the path at a specific time with the main objective of optimising trajectories, improving safety and efficiency and reducing distances and environmental footprint. In a world where airports are getting increasingly congested, time optimization is strictly related to high-quality trajectory prediction and to an adequate description of the status of the aircraft (attitude and velocity), a crucial input for the prediction and resolution of possible conflicts along the numerous trajectories.

Currently, different trajectories for the same flight can be computed by various entities that use different constraints and sources of information, however, due to a lack of coordination, these trajectories co-exist in different locations and they are not conveyed and integrated in a single product, limiting the possibility of improving the traffic management efficiency in the execution phase. The Air Traffic Management Requirements and Performance Panel (ATMRPP) analysed a possible architecture for trajectory information sharing and listed the entities that generate the predicted trajectories (ATMRPP, 2014):

- The Flight Operation Centre (FOC) generates an optimal trajectory using information and constraints coming from Meteorological model, aircraft type and specification and airline rules, but without using local constraints applied by the Air Traffic Management (ATM). The trajectory optimisation is based on a cost index that satisfies all the economic criteria.

- The aircraft Flight Management System (FMS) generates an optimal trajectory just using a limited set of information and constraints and as for the FOC, the initial estimate usually does not consider downstream information and constraints coming from the ATM that are usually implemented at a later stage.
- The ATM generates a trajectory using the local conditions and constraints.

The objective for the future is to define a process that integrates and standardises all the processes, sources of information and to enable pilots and dispatchers to select their own flight path that is then transmitted and shared with all the parties involved. The TBO concept enhances the interoperability between the different actors while maintaining a dynamic process, since not all the constraints can be identified upfront and so often new ones need to be integrated and assessed in real time.

The ATMRPP listed some of the constraints that need to be considered and implemented in the trajectory optimisation and sharing process:

- Minimum and maximum Estimated Arrival Time (ETA)
- Cost index and speed regime
- Operational Constraints linked to ATC
- No-fly airspace (e.g. due to Military areas/operations)
- Weather conditions
- Noise abatement procedures
- Traffic synchronization

In this chapter, a basic concept of trajectory modification is introduced to cope with what we believe could be an additional constraint in the future: GNSS integrity along the flight path.

5.2. INTRODUCTION TO FLIGHT PROCEDURES

Flight procedures are defined as the planned routes from take-off to touchdown used by pilots and ATC to manage the air traffic and ensure the safety and integrity of the operations, while satisfying constraints (such as minimum clearance towards terrain, obstacles and other traffic) and meeting criteria (such as performances and environments limitation).

The design and review of flight procedures is a difficult and highly regulated process. Conditions and configurations (e.g. routes, runways, navigation aids…) in the airports around the world are in continuous evolution, for these reasons it is required to constantly review and update the procedure; the review of existing procedures is performed every 28 days following the Aeronautical Information Regulation and Control (AIRAC) cycle and then are re-distributed to the utilization entities (fleets and ATCs).

The development of a new instrument approach at a given airport can greatly enhance the airport's value to the aviation community by increasing the variety of aircraft which can use the airport, or the conditions in which it can operate. Historically, most instrument approaches have been based on terrestrial navigational aids (NAVAIDs) requiring a considerable investment in equipment and resources.

However, with the proliferation of GNSS technologies, the infrastructure required to support traditional ground-based facilities may no longer be necessary in order to obtain an instrument approach.

GNSS can be used to shorten routes, save time and fuel, reduce traffic delays, increase capacity, and permit controllers to monitor and manage aircraft with increased safety.

Although GNSS has the potential to support instrument flight procedures at hundreds of facilities, the development and implementation of a new approach are far from a simple undertaking; it is a complex, multi-disciplinary effort requiring the collaboration of many professionals within the Federal Aviation Administration (FAA). The proposal of a new procedure must first undergo the scrutiny of a cost/benefit analysis before its development will be considered. In addition, the development of an instrument approach procedure must consider factors such as obstruction evaluations, airport requirements/capacity, compatibility with the existing airport master plan, noise and environmental issues, impact to the Air Traffic Control (ATC) system, airspace change, effects on other instrument approaches, and location of existing and proposed NAVAIDs and their limitations.

One of the main phases of the evaluation process for an instrument approach is the flight inspection, where criteria such as signal availability, integrity, and accuracy are all validated. Once this has been passed, the instrument flight procedure is forwarded for publication.

In this research, an algorithm has been developed with integrated ARAIM function that could be used to reduce the time, effort and cost of the flight inspection phase and help the procedures' designer and tester to assess the benefits and limits respect

to the integrity point of you. It can also help in increasing the automation in the design of possible alternative routes or improvements to the existing routes.

5.3. MERCATOR MAP PROJECTION

It is a set of mathematical-geometrical rules that transform a 3D model of the Earth in a plane representation. It is usually used to design atlas and navigation charts that are much handier to use than a globe and the computation of the route is simpler on a flat surface rather than a curved one. However, these projections are not able to fully represents the reality, distorting some part of the maps, but one of the main advantages is that courses can be represented as straight segments with constant angles with respect to the meridians, that corresponds to have a path with a constant bearing angle (also called rhumb lines).

Map projections are divided in groups depending on the surfaces used for the projection (plane, cone or cylinder), if they are tangential or secant to the Earth surface (Figure 5-1 and Figure 5-2) and from the relative direction of their axes respect to the Earth (normal, transverse or oblique, Figure 5-3).

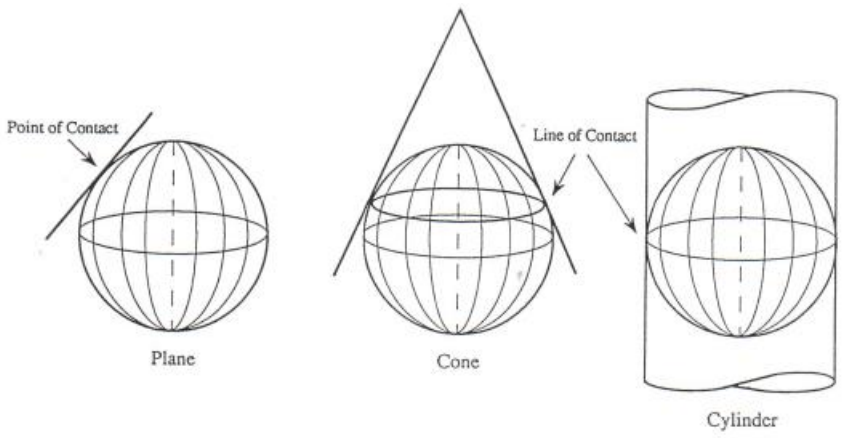

Figure 5-1 Tangential Projection Surfaces (Moore, 1992).

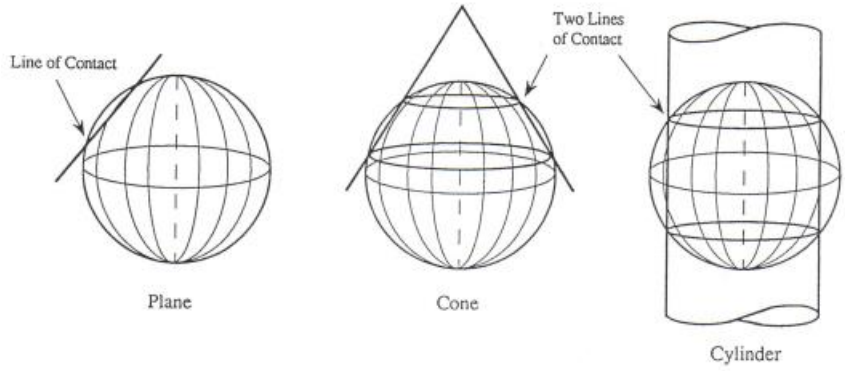

Figure 5-2 Secant Projection Surfaces (Moore, 1992).

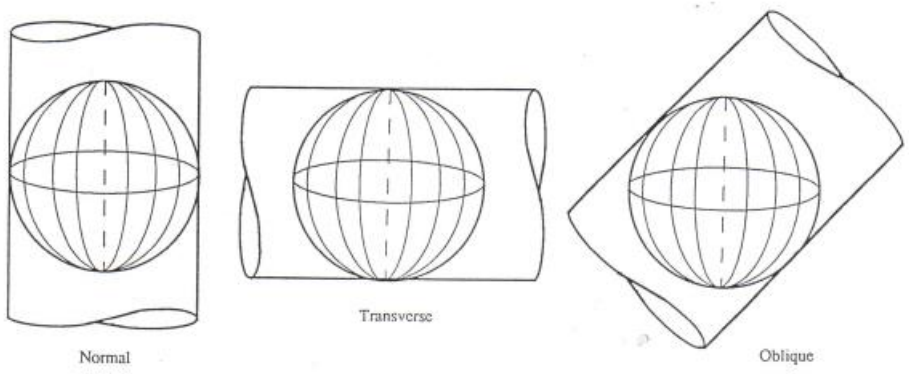

Figure 5-3 Attitude of Projection Surface (Moore, 1992).

Additionally, depending on the scale of the map to be projected and the accuracy needed, a spherical or ellipsoidal model of the Earth can be used.

The map projection allows transforming ellipsoid/spherical coordinates, usually expressed in terms of latitude and longitude, into cartesian coordinates (X, Y), directed as the magnetic North and East.

For the purpose of this research, the cylindrical tangential projection and the ellipsoid model have been considered, that are expressed by the followings equations to transform from geographical to cartesian (Eqs. 5.1) and vice-versa (Eqs. 5.2):

$$\begin{cases} X = a(\lambda - \lambda_0) \\ Y = a\, ln\left[tan\left(\frac{\pi}{4} + \frac{\phi}{2}\right)\left(\frac{1-e\, sin\, \phi}{1+e\, sin\, \phi}\right)^{e/2}\right] \end{cases} \quad (5.1)$$

$$\begin{cases} \lambda = \frac{X}{a} + \lambda_0 \\ \phi = \frac{\pi}{2} - 2\, tan^{-1}\left[e^{-Y/a}\left(\frac{1-e\, sin\, \phi}{1+e\, sin\, \phi}\right)^{e/2}\right] \end{cases} \quad (5.2)$$

Where:

- ϕ is the geodetic latitude
- λ is the geodetic longitude
- λ_0 is the longitude of an arbitrary central meridian (usually Greenwich)
- a is the sum of the equatorial radius of the ellipsoid and the altitude of the considered point above the surface.
- e eccentricity of the reference ellipsoid

In the inverse Eqs. (5.2), the computation of the geodetic latitude is not straightforward, but an iterative process is required until the difference between the previous and current values is lower than a predefined value (n):

Initial value: $\phi_0 = \frac{\pi}{2} - 2\tan^{-1} e^{-Y/a}$ (5.3)

accuracy: $(\phi_{k+1} - \phi_k) \leq n$ (5.4)

5.4. Flight Path Generator and Flight Path Modifier Algorithm

Description

As described in the previous chapters, aircraft routes are divided in different phases, each with its own requirements, predefined through a series of waypoints (Figure

5-4) and, as mentioned before, RAIM prediction is required if GPS is to be used to solely satisfy the RNAV requirements.

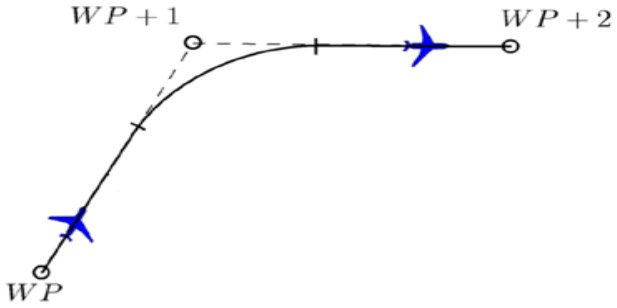

Figure 5-4 Trajectory in terms of waypoints.

In the pre-flight operations, the pilots prepare the expected route and related procedures to follow based on the constraints and the aircraft capabilities, this process can be performed using the avionics if the aircraft is equipped with the Flight Management System (FMS), that integrates the data coming from sensors, receivers, computers and the database, through the display of the FMS by selecting the waypoints along the desired flight path.

Waypoints are predefined geographical locations characterised by the coordinates (latitude and longitude), that can be a simple named point or located where a navaids is available to support the navigation. They are usually located in correspondence of a change, that can be in terms of direction, speed or altitude and they are mainly of two types:

- Fly-by WP: the aircraft can start the turn manoeuvre before reaching the WP
- Fly-over WP: the aircraft has to pass this type of WP before changing course.

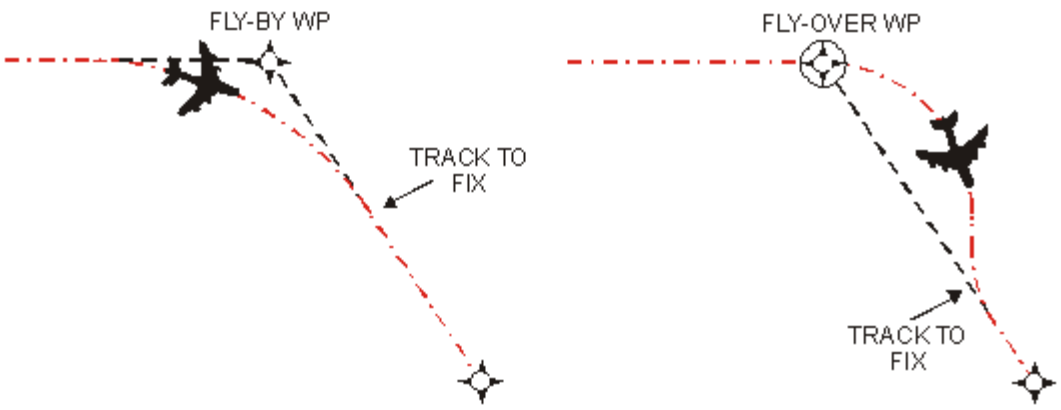

Figure 5-5 Difference Between Fly-By and Fly-Over Waypoints (FAA, 2006).

In RNAV procedures, Waypoints are then in turn connected by Legs that represent the desired path between WPs, the list in Appendix B summarises the different types (UASC, 2014).

In this chapter, a new algorithm is introduced that analyses the list of waypoints selected for the route, generates the expected trajectory, evaluates the integrity parameters along it using the APPATT ST tool and, in case of integrity outages, suggests a possible deviation from the current route in order to satisfy the requirements.

For the generation of the trajectory, the algorithm refers to the basic model provided in the Procedure Design Manual by ICAO (2009), in which ICAO described design criteria to aid states in the implementation of RNP operational procedures, for the determination of manoeuvres based on two parameters: speed and bank angle.

The new algorithm is divided in two main functions: the Flight Path Generator (FPG), that generates the trajectory, and the Flight Path Modifier (FPM), that generates a suggested modification of the trajectory.

5.4.1. FLIGHT PATH GENERATOR FUNCTION (FPG)

The Flight Path Generator function takes as input a text file containing the list of waypoints of the selected procedure. For each point are specified:

- Name
- Latitude, Longitude and Altitude
    - Type of WP (start of the procedure, check WP, turn WP, end of procedure WP)
- Turn type, if applicable (clockwise or counter-clockwise)
    - Preferred heading angles to next point (in some cases two consecutive WPs are not directly connected by a straight line but an intermediate turn manoeuvre is required, even though no intermediate turn WP is provided).

It has been assumed that aircrafts perform only a specific type of manoeuvre to change direction: fly-by turns.

The algorithm approximates the flight path to a series of adjoined lines and arcs in the 3D space using basic geometrical and kinematic equations.

As first step, the algorithm transforms the list of WPs from geographical to Cartesian coordinates using the equations for the Mercator Map Projections presented in the previous section (Eqs. 5.1 to Eqs. 5.4) and computes geometrically the heading angles between each two consecutive point in the list as the angle between the line adjoining the two WPs and the North direction.

$$m_{k+1,k} = \frac{(y_{k+1} - y_k)}{(x_{k+1} - x_k)} \tag{5.5}$$

$$\Psi_{k+1,k} = \begin{cases} 0 \quad if\ x_{k+1} = x_k\ and\ \ y_{k+1} > y_k \\ \pi \quad if\ x_{k+1} = x_k\ and\ \ y_{k+1} < y_k \\ \frac{\pi}{2} - \tan^{-1} m_{k+1,k} \quad if\ x_{k+1} > x_k \\ \frac{3}{2}\pi - \tan^{-1} m_{k+1,k} \quad if\ x_{k+1} < x_k \end{cases} \tag{5.6}$$

Where:

- k is the number of the waypoint
- x_k and y_k are the k-th cartesian coordinates of the waypoints
- m is the angular coefficient of the line that passes through the two waypoints
- $\Psi_{k+1,k}$ is the heading angle between two consecutive waypoints. The computation of the heading angles depends on the mutual position of the two WPs (since the same line can have two different heading angles) and on the direction of motion.

Before the FPG starts to compute the trajectory, it performs two main steps:

1) Evaluates if additional turn points are required by checking if any point in the list requires a preferred heading angle that does not allow the proceed directly to the following WP.

   Figure 5-6 shows an example in which WP_k and WP_{k+1} are two consecutive WPs, on the left side $\Psi_{k\text{-}k+1}$ is the direct angle between the two points and Ψ_f is the final heading angle (in this case WP_{k+1} is a turn point that leads to the next leg with a predefined heading angle), while on the right side the requirements is that the aircraft has to pass through WP_k with a specific heading angle (Ψ_p) and, in order to reach the following WP and the final direction angle, an intermediate waypoint (WP_{add}) is required, given by

the intersection of the two directions, computed by the tool using cartesian formulation.

Given the heading angles, it is possible to find the angular coefficients m of the two lines passing through WP_{k+1} and WP_k by inverting Eqs. (5.6).

Once the values are known, it is possible to determine the equations of the two lines as:

$$x - x_i = m_i(y - y_i) \tag{5.7}$$

Where i is k and k+1. The solution of the system of the two equations of Eqs. (5.7) gives as output the coordinates of the additional waypoint (WP_{add}).

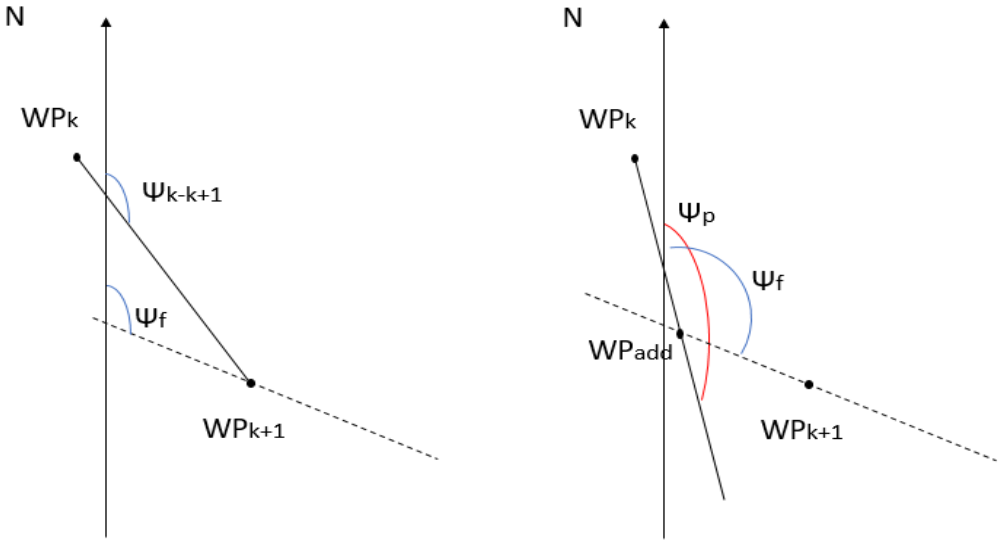

Figure 5-6 Difference between direct route between WPs (left) and a route with intermediate WP (right).

2) Then, for each turn point (WP_k = WP_{turn}) the algorithm determines an initial (WP_s) and end turn points (WP_e) that are located between the considered turn point and the previous (WP_{k-1}) and following (WP_{k+1})

waypoints, defined by the Distance of Turn Anticipation (DTA) used in the model described by ICAO (2009).

To compute the DTA, other two main inputs are required (defined by the user): the aircraft speed and the bank angle.

The aircraft avionics provides the Indicated Airspeed (IAS) that needs to be firstly converted in True Airspeed (TAS) using the following standard equation (SI units):

$$TAS = IAS * 171233 * \frac{\sqrt{(288+VAR-0.00198*H)}}{(288-0.006496*H)^{2.628}} \quad (5.8)$$

Where:

- VAR = variation from international standard atmosphere (ISA) (standard value +15) or local data for 95% high temperature, if available
- H = altitude (m)

However, a different speed (V) is required to compute the turn radius, given by:

$$V = TAS + TWD \quad (5.9)$$

Where TWD is the assumed tailwind (see Appendix 0).

Then, the rate of turn (R) in degrees/second can be computed as:

$$R = \frac{6355 \tan \alpha}{\pi V} \quad (5.10)$$

Where α is the bank angle.

Consequently, the turn radius is given by:

$$r = \frac{V}{20\pi R} \quad (5.11)$$

Knowing the radius of turn, it is possible to compute the minimum distance from the turn WP at which the aircraft needs to start the turn manoeuvre, known as Distance of Turn Anticipation (DTA, Figure 5-7), given by:

$$DTA = r \tan\frac{A}{2} \tag{5.12}$$

Where A is the turn angle, the change of angle between the initial and final heading ($\psi_{k\text{-}k+1}$ - ψ_f in Figure 5-6).

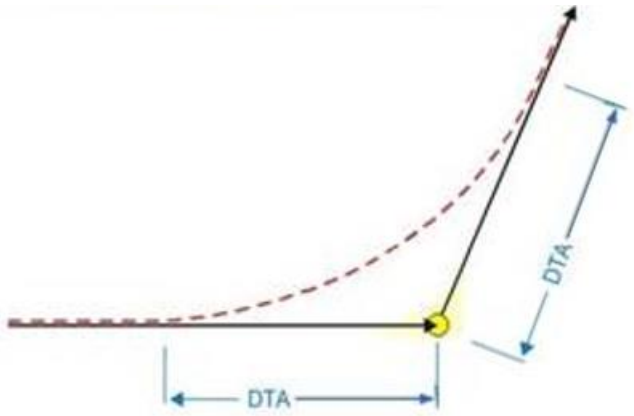

Figure 5-7 Graphical View of the Distance of Turn Anticipation (DTA) (FAA, 2007b).

From the DTA it is possible to geometrically find the coordinates of the starting and ending point of the turn manoeuvre using again cartesian formulas and the solutions obtained from two systems of two equations, the generic formula of a line given two points and the formula of the distance between two points:

$$\begin{cases} (y_{turn} - y_{s/e}) = m(x_{turn} - x_{s/e}) \\ (x_{turn} - x_{s/e})^2 + (y_{turn} - y_{s/e})^2 = DTA^2 \end{cases} \tag{5.13}$$

Where s/e indicates that in one system is used to compute the coordinates of the starting point, while the other for the ending point.

However, the systems of Eqs. (5.13) generate two solutions for each point (starting and ending turn point), so it is required a check on which solution satisfy the expected geometry. The tool checks that the distance between the starting and turn waypoint is smaller than the distance between the turn point (WP_k) and the previous waypoint (WP_{k-1}) (same for the turn ending point and the following waypoint WP_{k+1}). If none of the two solutions satisfies this condition, this means that the trajectory cannot be performed with the current parameters (e.g. bank angle and/or velocity) and that the aircraft is supposed to start the manoeuvre before reaching WP_{k-1}; in this case, the tool warns the user that there is an incompatibility in the trajectory that needs to be reviewed.

After the first two steps, the original list of WPs might have been modified with the addition of other turn points and the starting and ending points of each turn point (blue dots in Figure 5-8) and the tool automatically updates the list and converts all the cartesian coordinates in geodetical (see Eqs. (5.2).

Starting from the last WP (WP_{k+1}), the algorithm builds up the trajectory from the end to the beginning analysing two pairs of WPs at a time. For each pair, the tool evaluates what type of leg is required to connect them and the following two cases are the ones implemented in the tool:

a) Straight line (e.g. between two aligned checkpoints, a checkpoint and an initial turn point, an end turn point and a checkpoint). The tool generates the trajectory using basic cinematic equations of uniform motion ($v=v_0$) (at the current state of the algorithm only this simple case has been

implemented, but more complex dynamics could be easily included). The computation of the new WPs is performed in the Cartesian system and divided along the two different axes. First of all, the tool evaluates the distance between the two points and estimates the time required to travel it (to simplify the model, only a two-dimensional problem has been considered):

$$\begin{cases} s_{i,i+1} = \sqrt{(x_{i+1} - x_i)^2 + (y_{i+1} - y_i)^2} \\ t_{i,i+1} = {}^{s_{i,i+1}}/_{v_0} \end{cases} \quad (5.14)$$

Where:

- i is the i-th WP of the list
- $s_{i,i+1}$ is the distance between the two WPs under analysis
- $t_{i,i+1}$ is the time to travel from i to i+1 with constant velocity v_0.

From the time it is possible to compute the number of intermediate WPs between WP_k and WP_{k+1} using the update rate (t_{update}) defined by the user:

$$n_{WP} = {}^{t_{i,i+1}}/_{t_{update}} \quad (5.15)$$

in this research, an interval of one second has been considered between two subsequent points, equivalent to the GNSS update rate. The cartesian coordinates of these new points are given by:

$$\begin{cases} x_j = v_0 k \cos\alpha + x_0 \\ y_j = v_0 k \sin\alpha + y_0 \end{cases} \quad (5.16)$$

Where

- j is the index of the intermediate WPs
- k is an integer number that goes from 1 to $t_{i,i+1}$ (rounded down)

- α is the angle of the direction of the line connecting i and i+1 and the x-axis, given by the inverse of the tangent function of the angular coefficient (Eq. 5.5)

$$\alpha = \tan^{-1} m \tag{5.17}$$

b) Curved path. This situation is activated when the tool detects that the pair is composed by a turn point and an end turn point. In this case, the tool takes the full triad of points (start-turn-end) and it automatically starts from the start point. The curved path is approximated to an arc of a circle with the radius given by Eq. 5.11 generated considering the aircraft moving in a uniform circular motion. The tool computes the centre of the circle using cartesian formulations and solving the following system:

$$\begin{cases} x^2 + y^2 + ax + by + c = 0 \\ (x, y) = (x_s, y_s) \\ (x, y) = (x_e, y_e) \\ \sqrt{\left(\frac{a}{2}\right)^2 + \left(\frac{b}{2}\right)^2 - c} = r \end{cases} \tag{5.18}$$

- Where the first equation is the general equation of a circle in the bi-dimensional cartesian system.
- a, b and c are the coefficients that need to be found through the system to define the circle.

Once the coefficients are known, it is possible to find the centre of the circle as:

$$(x_c, y_c) = \left(-\frac{a}{2}, -\frac{b}{2}\right) \tag{5.19}$$

At this stage, to simplify the computation of the intermediate points, a new reference system is used (O_t) and the circle is translated and centred in it by using the following relations:

$$\begin{cases} (x_{c\_t}, y_{c\_t}) = (0,0) \\ (x_{s\_t}, y_{s\_t}) = (x_s - x_c, y_s - y_c) \\ (x_{e\_t}, y_{e\_t}) = (x_e - x_c, y_e - y_c) \end{cases} \quad (5.20)$$

Where the subscript represents the new coordinates in the translated reference system centred in the centre of the circle.

From the new coordinates of the start and end point of the turn, it is possible to evaluate the change of direction θ that the aircraft will perform along the trajectory as the difference of the heading angles:

$$\theta_{turn} = \psi_e - \psi_s \quad (5.21)$$

To fully define the intermediate points, it is then necessary to compute the time required to perform the turn, given by:

$$t_{turn} = \frac{\theta_{turn}}{R} \quad (5.22)$$

Based on the update rate set by the user, the tool will compute the number of new waypoints from which the trajectory will be generated:

$$n_{WP} = {}^{t_{turn}}/_{t_{update}} \quad (5.23)$$

Where n_{WP} is rounded down.

The coordinates of the new waypoints are given by:

$$\begin{cases} x_j = r\cos\theta_j + x_c \\ y_j = r\sin\theta_j + y_c \end{cases} \quad (5.24)$$

Where:

- j is the index that goes from 1 to n_{WP}
- x_c and y_c are the coordinates of the centre of the manoeuvre, that summed to the first element it translates the final coordinates x_j and y_j in the original reference frame (O).

- θ_j is the angular position of the j-th WP in the translated circle and it is given by:

$$\theta_j = \theta_s + j * R \tag{5.25}$$

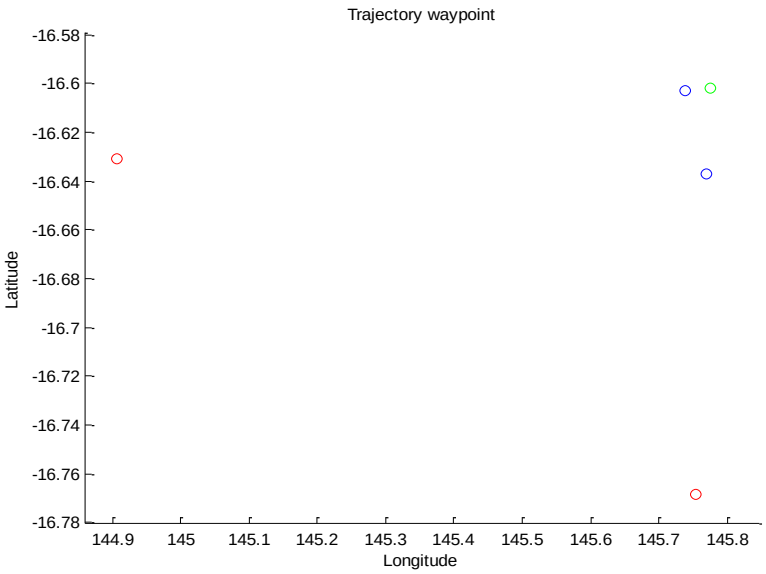

Figure 5-8 Example of initial and end turn points (blue dots) generated by the FPG tool for each turn point (green dots). The red dots are the precedent and following WPs (WP_{k-1} and WP_{k+1}). The DTA of each point is the same, even though in the picture seem different due to a different scale factor in the axis.

The generated path (an example in Figure 5-9) describes the aircraft trajectory in terms of position in the Cartesian reference frame (X,Y,Z) that is then transformed back in geographical (latitude, longitude and altitude) including attitude (roll, pitch and yaw angles) in time within a user-defined time step (e.g. 1s). In particular, the function monitors that the roll angle is always within the aircraft standard limits (commercial flights standard value is between 25-33°).

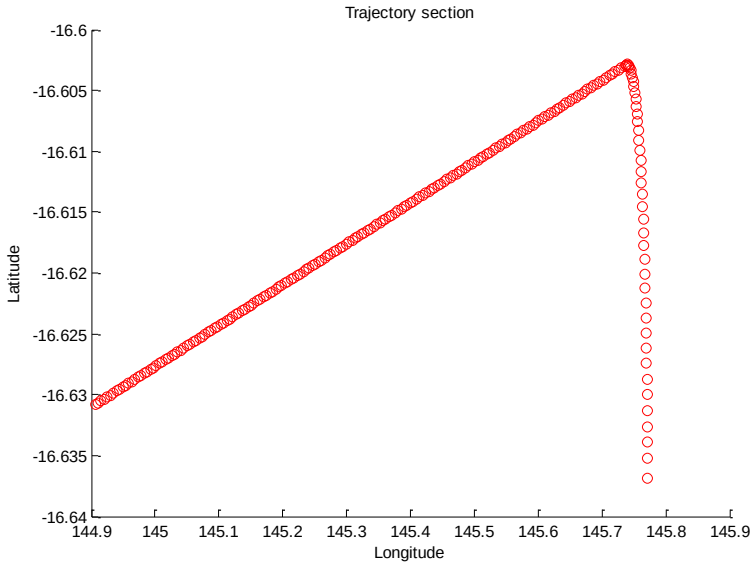

Figure 5-9 Example of a Section of the Flight Path generated by the FPG.

The trajectory is then analysed by APPATT ST with the objective of evaluating the integrity performance of the trajectory considering the attitude. if it doesn't satisfy the required navigation performance and it presents one or more integrity outages, the Flight Path Modifier (FPM) function is activated.

5.4.2. Flight Path Modifier Function (FPM)

In case of activation of the FPM function, the tool tries to modify the trajectory in order to remove the integrity outages and satisfy the required navigation performance. The algorithm behind the FPM function is quite simple and straightforward, it analyses the trajectory backwards from the final to the starting WP, examining which sections need to be modified. If the section presents an outage, the FPM performs the following steps:

- The function analyses the satellite lost due to the attitude shadowing effect; if more than one satellite is not in view, it selects the satellite with the highest elevation angle and forces the aircraft to perform the manoeuvre with a bank angle smaller than the elevation angle. In this way, the satellite is again in the GNSS receiver field of view.

- Forcing the bank angle to a defined value modifies the values of the turn radius (r), the rate of turn (R) and the distance of turn anticipation (DTA). The function checks that the rate of turn stays within the standard values (for commercial flights R ≈ 3 deg/sec) and generates the new trajectory arc using the new values.

- Checks that the new segment is compatible with the adjacent ones, otherwise the FPM attempts to modify the next section. An example of incompatibility is when there are two consecutive turns and the end turn point of one is located after the start point of the following turn, this means that the aircraft can't finish one turn that must start the next.

- Complete the analysis of the following sections and, if no compatibilities occur, the new trajectory is analysed again by APPATT. If the integrity outage is not removed and other satellites are still not in view, it selects the second highest elevation angle and repeats the previous steps.

If an incompatibility occurs, the tool warns the user that with the current configuration the trajectory can't be modified in order to meet the required navigation performance.

5.5. SCENARIOS AND RESULTS

The following results have been obtained analysing the RNAV STAR procedure Sunny Four Papa Arrival from KONDA of the International Airport of Cairns, Australia, in a single constellation configuration (GPS) (Figure 5-10).

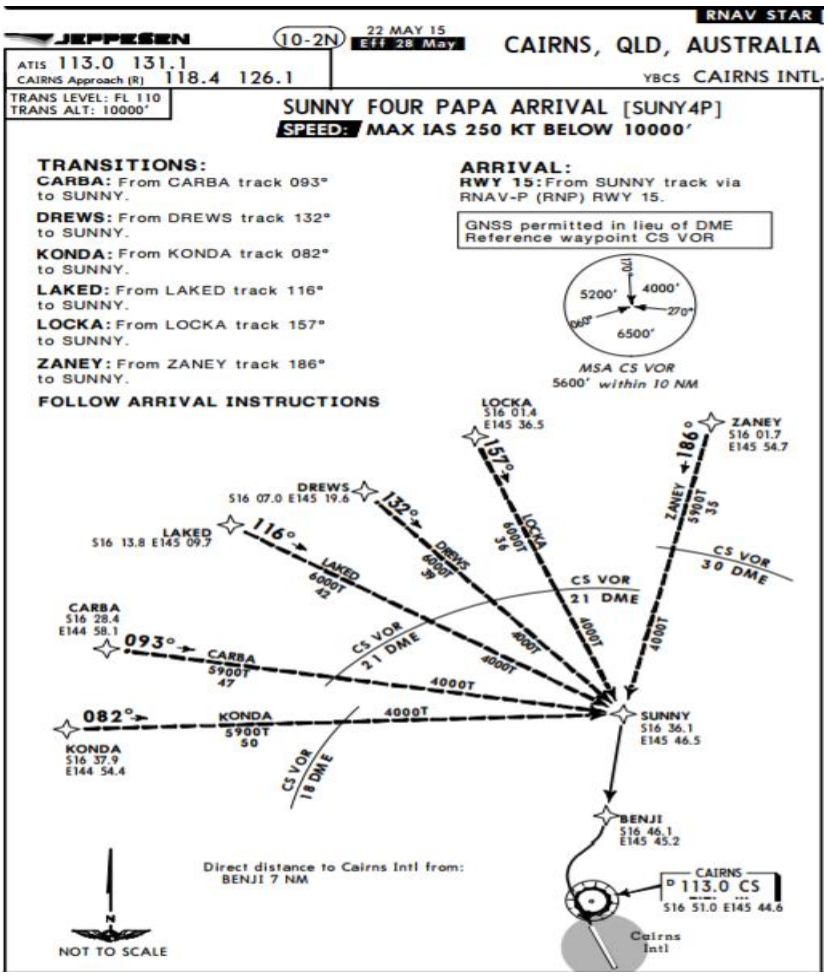

Figure 5-10 RNAV STAR procedure Sunny Three Arrival chart of the International Airport of Cairns, Australia.

Figure 5-11 shows the nominal trajectory generated by the FPG with a banking angle of 25° for each turn manoeuvre, while Figure 5-12 shows the aircraft attitude and Figure 5-13 to Figure 5-16 the ARAIM performance parameters along the trajectory computed through the APPATT ST tool.

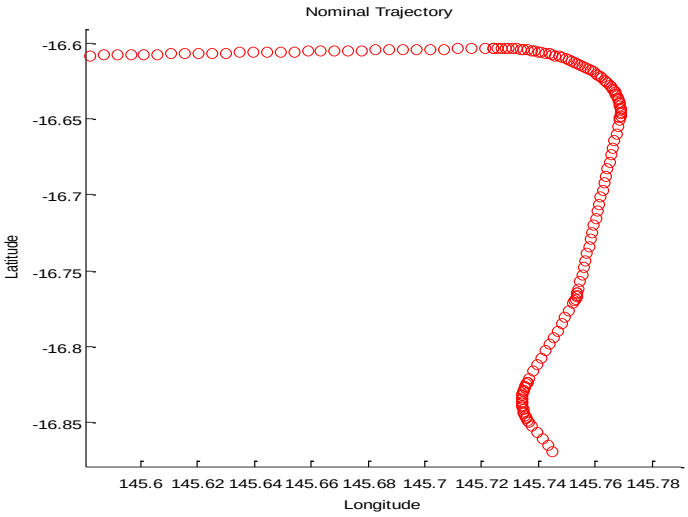

Figure 5-11 Nominal trajectory.

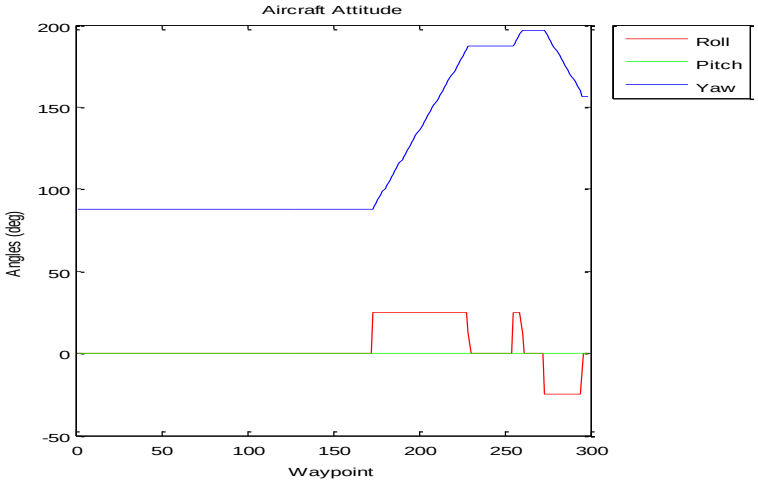

Figure 5-12 Aircraft Attitude Angles.

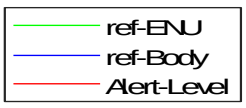

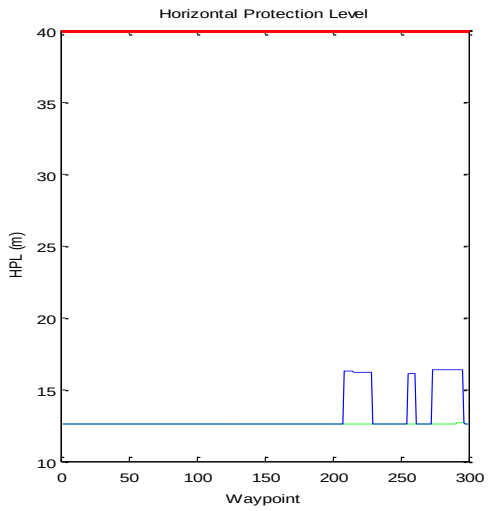

Figure 5-13 HPL in the ENU (green) and Body (blue) Reference Frames compared with the Alert Level (red).

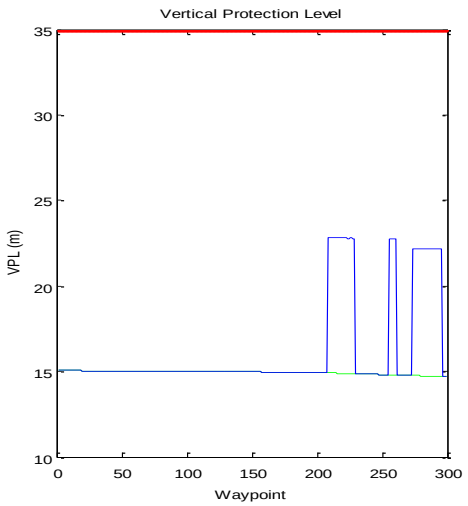

Figure 5-14 VPL in the ENU (green) and Body (blue) Reference Frames compared with the Alert Level (red).

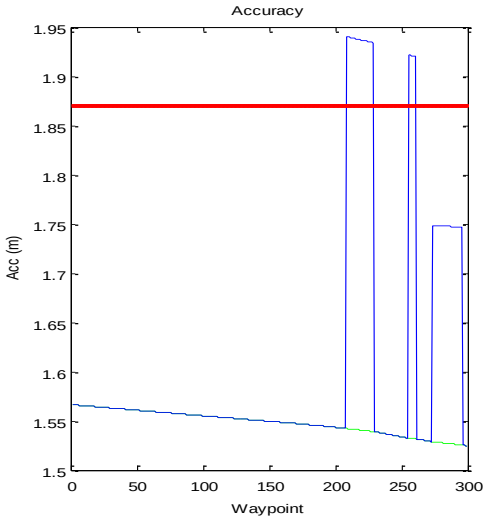

Figure 5-15 Accuracy in the ENU (green) and Body (blue) Reference Frames compared with the Alert Level (red).

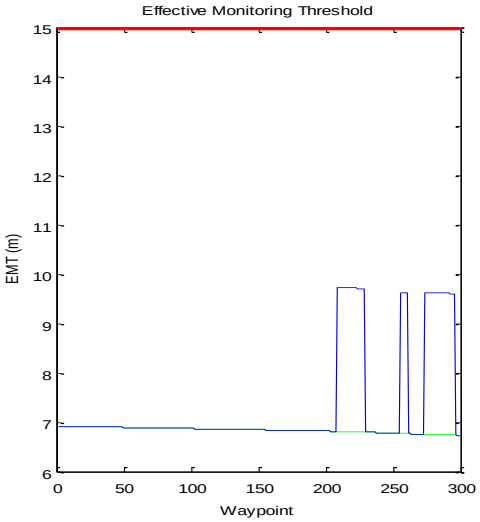

Figure 5-16 EMT in the ENU (green) and Body (blue) Reference Frames compared with the Alert Level (red).

It is clear that each turn generates a peak, due to the loss of one satellite, GPS Pseudorandom noise (PRN) 25 for the first turn, PRN 26 for the second and PRN 16 for the last turn. In this configuration, the accuracy only is severely affected in the first and second turn. Figure 5-18 shows the difference in satellites in view between the ENU and body reference frames.

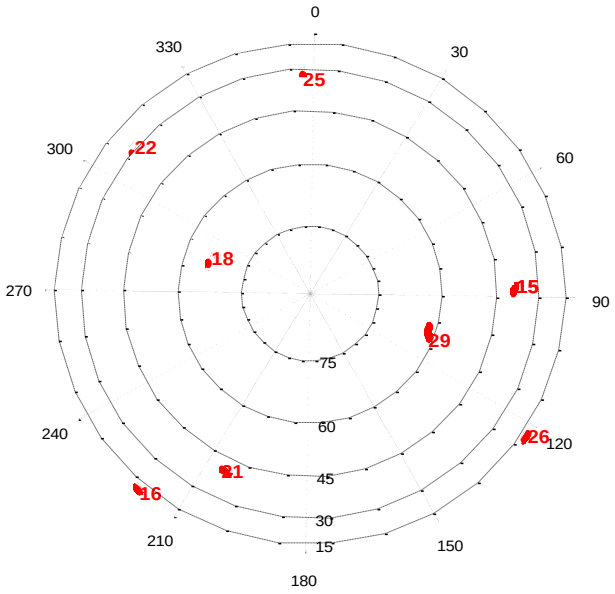

Figure 5-17 Skyplot of the constellation configuration.

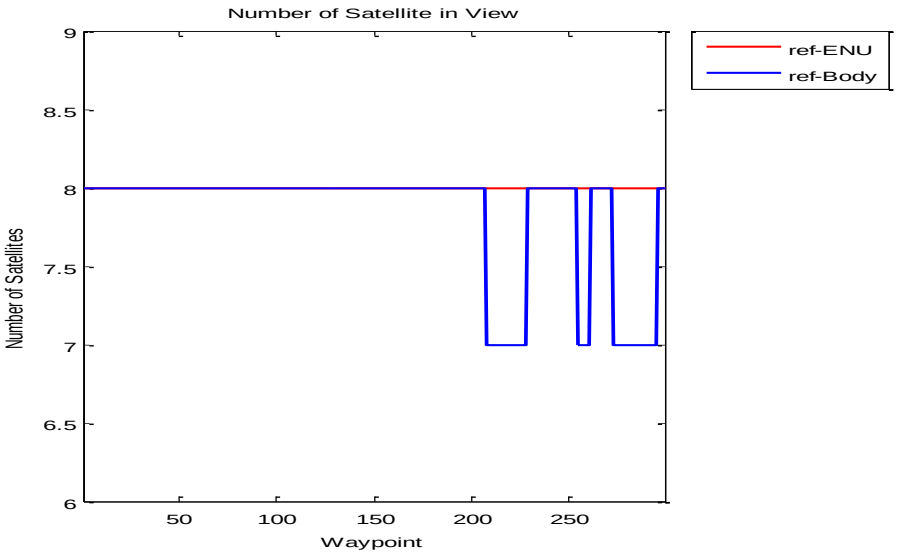

Figure 5-18 Satellite in view in the ENU (red) and body (blue) reference frames in the nominal trajectory.

At this point the FPM is activated and analyses the single sections of the trajectory and checks that no incompatibilities occur and tries to generate the new one.

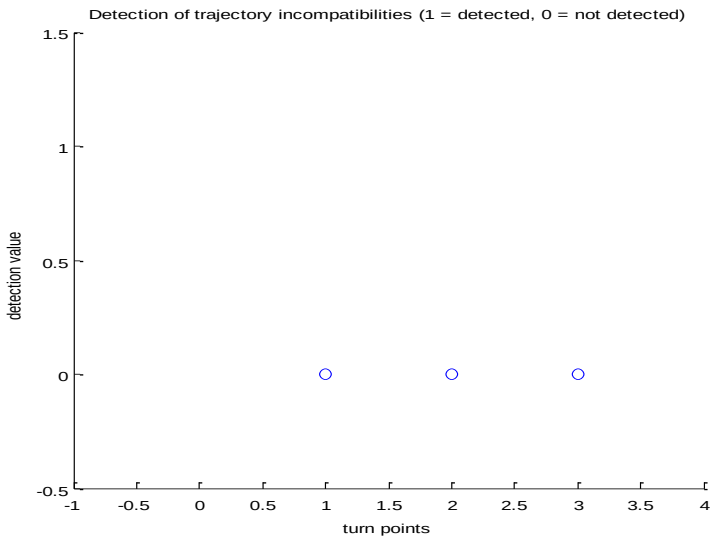

Figure 5-19 Trajectory incompatibility detection graph, 0 = no incompatibility, 1 = incompatibility detected.

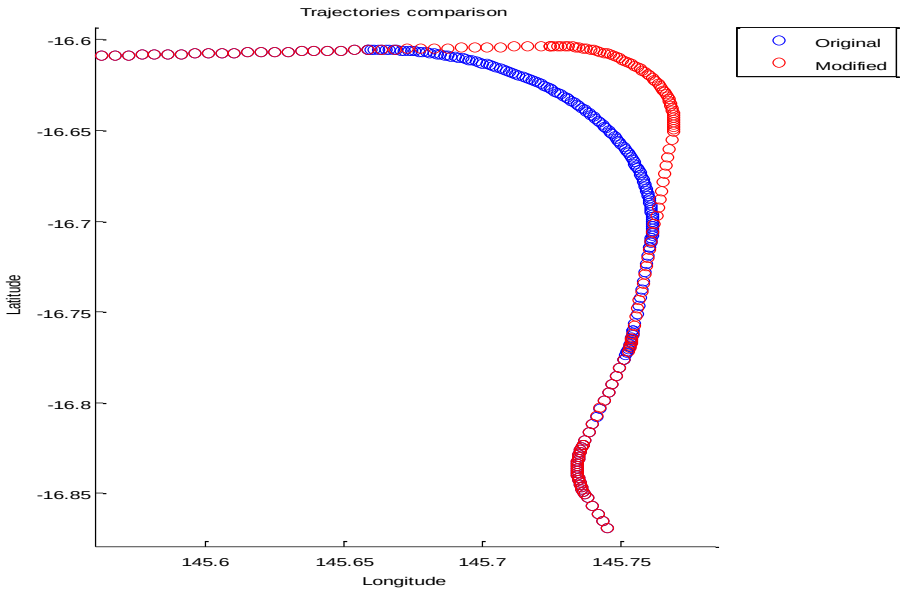

Figure 5-20 Nominal trajectory (red line) and modified trajectory (blue line).

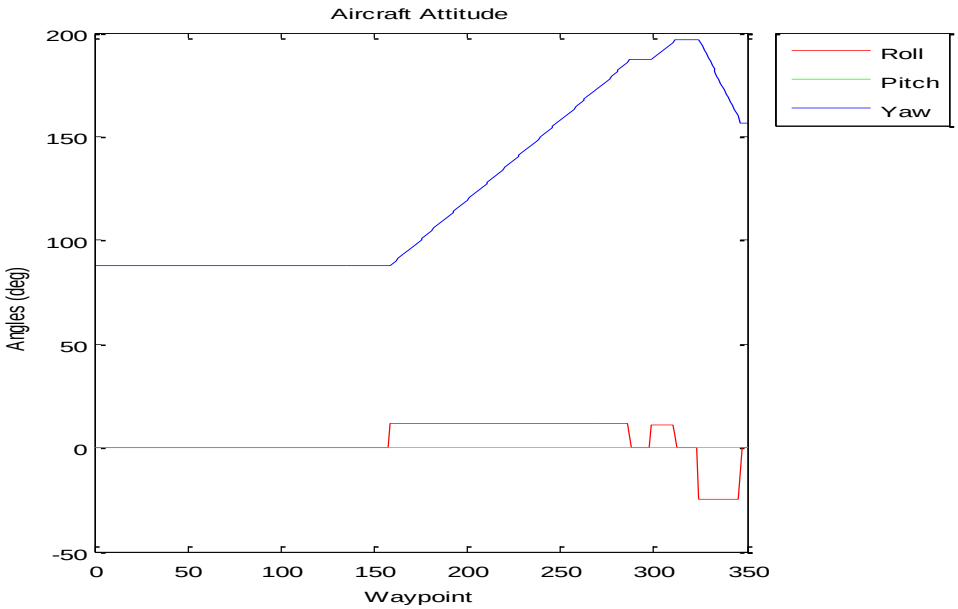

Figure 5-21 Aircraft attitude in the modified trajectory.

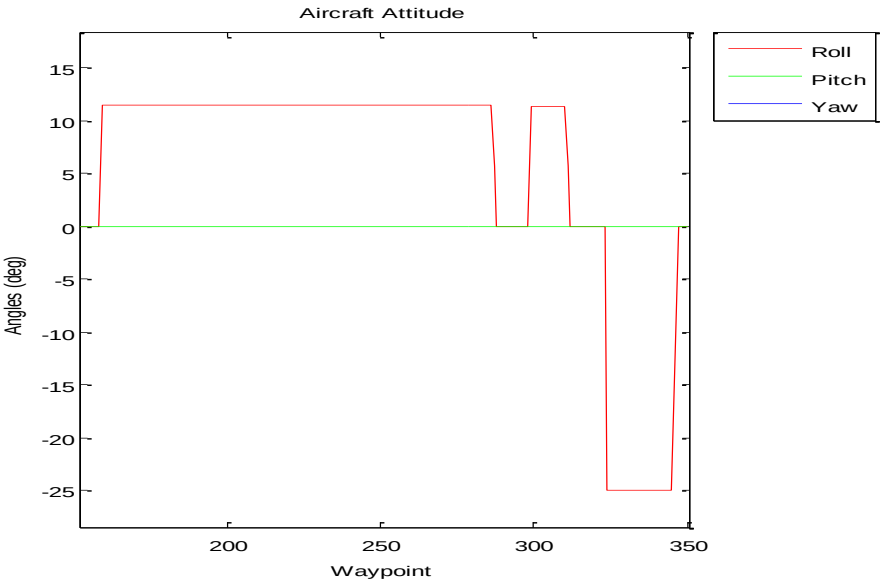

Figure 5-22 Focus on the modified roll angles.

Figure 5-20 shows that the tool successfully modified the first two turns using different values of bank angle (Figure 5-22) and the new trajectory does not present any incompatibility (Figure 5-19), while the third one is unchanged since the integrity parameters stay within the alert levels.

Figure 5-24 to Figure 5-27 show the number of satellites in view and the integrity parameters for the new trajectory.

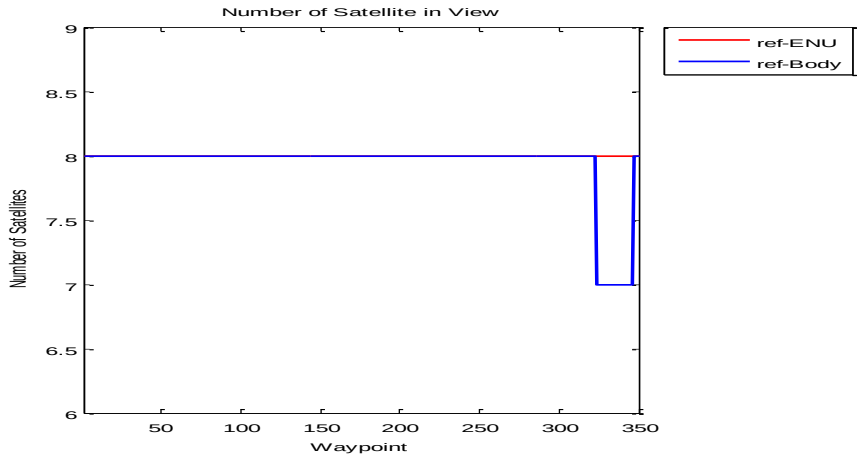

Figure 5-23 Satellites in view in the ENU (red) and body (blue) reference frames in the modified trajectory.

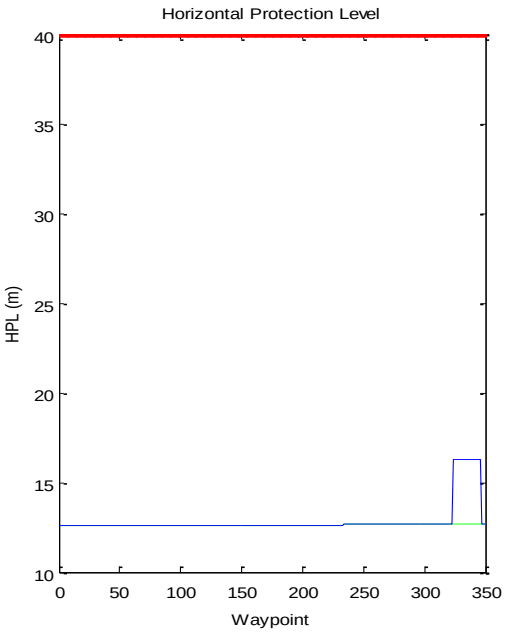

Figure 5-24 HPL in the ENU (green) and Body (blue) Reference Frames compared with the Alert Level (red).

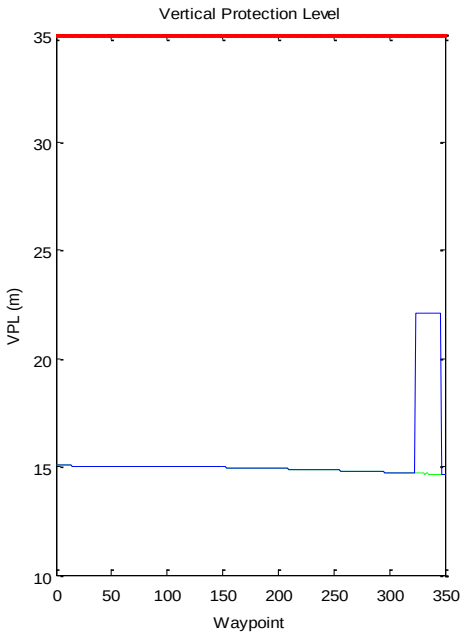

Figure 5-25 VPL in the ENU (green) and Body (blue) Reference Frames compared with the Alert Level (red).

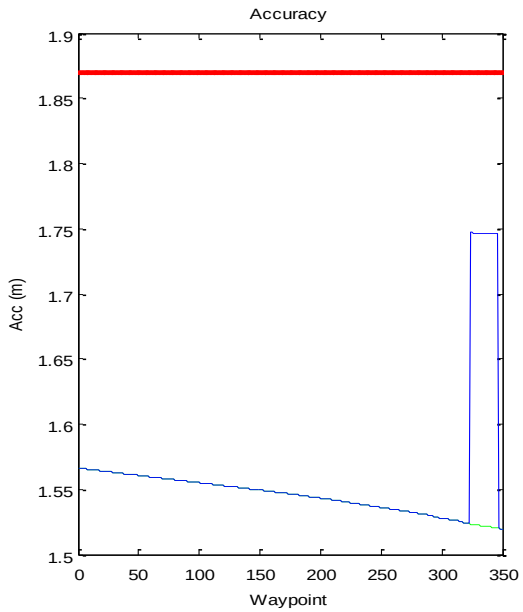

Figure 5-26 Accuracy in the ENU (green) and Body (blue) Reference Frames compared with the Alert Level (red).

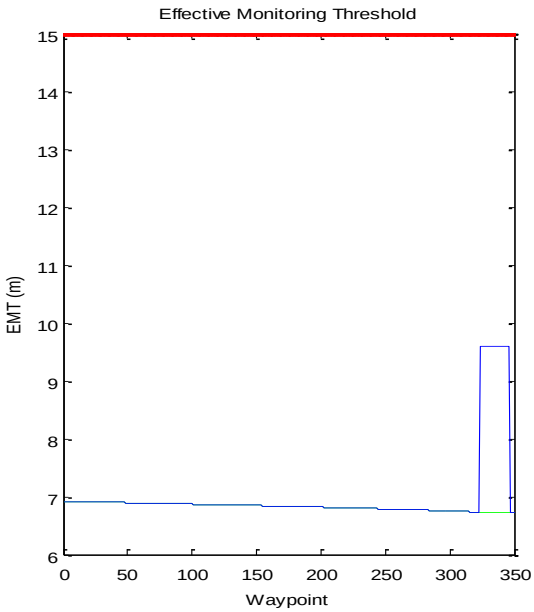

Figure 5-27 EMT in the ENU (green) and Body (blue) Reference Frames compared with the Alert Level (red).

The previous graphs show that the modified trajectory does not present integrity outages, making the expected flight path safe in GPS nominal conditions.

5.6. CONCLUSIONS

The results show that the algorithm allows the user to assess the benefits and limits of a selected procedure whether they are a procedure designer and tester or a pilot, while at the same time it gives the possibility of analysing alternative trajectories that are a slight modification of the nominal.

The analysis performed is far from the more complex concept of trajectory optimisation, since it doesn't include several determinants factors involved in the computation of the optimal trajectory, however it stresses out the importance of

including the integrity of GNSS into the process, due to the fact of the increasing involvement of GNSS as main navigation system in the future of civil aviation.

Another challenge of this concept is the reality: flown trajectories might differ from the ones predicted in simulations due to several factors, that can be within the simulation, such as the implemented models and assumptions, or related to events and situations of the real world, such as wind and pilot skills in following the expected route. The implemented path generator uses a very simple model that builds up flight paths as consecutive straight and curved segments, but aircraft trajectories can be far more complex. However, I believe that thanks to the technological advancement in computational capabilities and control systems, future systems will be capable of reducing deviations between the flown and the reference trajectory.

The proposed tool could be used as an additional tool during the transition phase between the current procedures and navigation technologies and the introduction of GNSS as primary navigation system once enhanced with further functions, such as no-fly zones and obstacle clearance controls, with the objective of providing a solution that oversees several problematic issues of an aircraft trajectory.

Increased awareness and better pre-flight planning could ultimately improve the safety of flights and contribute to the safe introduction of GNSS as a viable positioning method for instrument approach.

6. INTEGRATION OF ARAIM TECHNIQUE IN A PHYSICAL DEMONSTRATOR

This chapter presents and summarise the challenges of the integration of different technologies and explains the final objectives of the WP4 Physical Demonstrator, developed in collaboration with other two INNOVATE researchers, and its research contribution to the INNOVATE WP5.

The physical demonstrator integrates three technology/system demonstrators covering different areas of the operations related to the civil aviation field, such as:

- Integration of ARAIM as new avionics system that supports pilots in safety critical phase of flight by providing near real-time integrity performance prediction (the Near-Real-Time ARAIM Performance Prediction Tool or (NRT APPT)). Previous chapters demonstrated the integrity availability prediction capability of this new technique that could be integrated in support of functions and tasks such as the pilots in the pre-flight operations, designers in procedure development and testing and ATMs in the flight planning processes. The aim of the algorithm presented in this chapter is to make use of this prediction capability not only for off-line activities but also for real time operations in support of pilots to assess the flight status and possible or expected risks along the path.
- Optimisation of the ground movement operations before take-off and after landing that could reduce delays and related costs that could affect airports with high level of flight traffic

- Analysis of human performances and psychophysical status of subjects ((e.g. pilots and ATCs) using physiology parameters (e.g. temperature and hearth rate) to identify their level of tiredness and stress.

The final objective of the physical demonstrator would be to integrate and implement different new technologies and assess their impact on the tasks of the users. The physical demonstrator has been built and is at disposition of the University of Nottingham, ready to be tested on subjects. Due to the lack of time, these tests could not be performed in this research project time frame.

In this chapter, the sections dedicated to the other research projects have been provided by the other researchers, for additional information please refers to the PhD Theses of Marinescu (2017) and Stergianos (2017).

6.1. INTRODUCTION TO THE INNOVATE PHYSICAL DEMONSTRATOR PROJECT

A key objective of the Marie Curie Innovative Doctoral Program (IDP) is to develop an integrated air transport engineering vision and to train the next generation of research leaders to be well versed in the notion of integration.

The various individual research projects are clearly multidisciplinary in nature and therefore involve supervision teams to nurture the desired integrated systems approach.

At the core of the present IDP there are two concepts:

(i) Technology innovation across aircraft and operation systems

(ii) the integration of the new technologies to deliver a new air transport demonstrator and instil a new multidisciplinary approach to air transport

engineering. A series of key scientific challenges have been worked out to provide a holistic technological approach to improving the efficiency of air transport and reducing its impact on the surrounding environment.

Until now air transport has, at best, been considered along two separate strands, aircraft and air transportation systems and even in the case of aircraft engineering the integration of various technological components is not yet ideally executed: "[…] the entire aircraft should be viewed as a system, and systems architecting and engineering methods applied to its definition, design, production, operation and maintenance. This still tends to be the case more for military than commercial aircraft." In fact, this is still so much the case that "in some aircraft companies, the words 'systems engineering' is [only] applied to […] subsystems such as flight control, hydraulic, etc." (MIT, 2007). In our team of ESRs, we challenged that insular view and eventually propose the blueprint for an integrated system addressing key challenges and wishes identified and expressed by leading European industrialists and decisions makers (Airbus, 2013, UK.Gov, 2012, EC, 2011). This goes beyond leading existing programs such as the one at the MIT from which some of the previous quotes have been extracted.

We have therefore integrated our technological advances into physical demonstrators, thus formalising our apprenticeship of multi-disciplinary requirements. To do so we have:

- Drafted joint specification of requirements (SoR) as part of our joint session with the coordinator. These SoR has been reviewed and approved by members of the supervisory board, including industrial and training partners,

who have monitored progress on each project leading to the physical demonstrator.

- Proposed a preliminary system design to be reviewed by all the academics at Nottingham in a first instance, before being put out for consultation with the supervisory board and presented as part of a second review gate.
- Proposed and executed a complete system integration and physical demonstrators presented to the broader community (workshops, conferences, visits).

6.2. WORK PACKAGE 4 PHYSICAL DEMONSTRATOR DESCRIPTION

Work Package 4 Physical Demonstrator integrates the technologies developed by ESR 12 (myself) related to Advanced RAIM technique, ESR 13 (Adrian Marinescu) related to Human Performance Evaluation and ESR 10 (Christofas Stergianos), related to Ground Operations Optimization. The main aim is to integrate and test the Navigation and Ground Operations algorithms and techniques developed by ESR 12 and ESR 10 and to assess human performance using physiological measurements techniques outputted by ESR 13.

6.2.1. CHALLENGES

A. ESR 12 - ADVANCED RECEIVER AUTONOMOUS INTEGRITY MONITORING (ARAIM)

In the previous chapters, the proposed ARAIM-based algorithms have been used to analyse the integrity performances in advance respect to the execution phase of the planned flight with the main objective support the pre-flight operations, procedure development and testing and flight planning processes.

However, these configurations differ from another main application for ARAIM in Civil Aviation, that is intended to be used in real time for the analysis of the integrity parameters in nominal conditions and for the detection and exclusion of faulty measurements that could lead to a not reliable solution. The main drawback of this type of application is that the analysis is performed in parallel with the navigation solution computation and if a fault occurs, the system is supposed to warn the user within a defined time (Time-to-Alert). This means that the actual warning can be provided after that the solution has been “used”.

The aim and challenge of the algorithm proposed in this chapter is to partially compensate the lack of capability of the standard ARAIM concepts of providing timely warning to the user in case of integrity outages, partially because due to the unpredictable nature of the faults, only the problem of the degradation of the performance due to an adverse satellite configuration can be addressed.

B. ESR 13 – Human Performance Evaluation

The near future air transport challenges such as increased air traffic, the need for more efficient routes, free flight, and single pilot operations raise new issues from the human factors perspective. New technologies, including the ones developed by ESR 10 and ESR 12, will impact the performance by influencing the level of mental workload the pilots are subjected to, their situational awareness and the level of stress.

The output of ESR 13 will provide a way of assessing the impact that these technologies have on the pilot, in an objective way, by measuring their physiological parameters, such as heart rate data and facial thermography. The Flight Simulator will serve as a means of exploring the human physiological reaction during different flight scenarios in both normal classical instrument configuration and other configurations containing newly developed instruments.

C. ESR 10 – Ground Operation Optimization

With the constant increase in air traffic, airports are facing capacity problems. Optimisation methods for specific airport processes are starting to be increasingly utilised by many large airports. However, many processes happen in parallel and a more complex optimisation model is required, which can consider multiple processes simultaneously.

Having an accurate model for the pushback process is important for this and identifying all of the delays that may occur can lead to more accurate and realistic models that can be used in the decision-making process for ground movement operations. After testing a model with a more detailed pushback process we found

that a lot of the delays are not predicted if the process is not explicitly modelled. Having a more precise model with accurate movements of aircraft is highly important for an integrated model and will allow ground movement models to be used for more reliable integrated decision-making systems on airports. Minimising these delays can help airports increase their capacity and become more environmentally friendly.

6.2.2. PROPOSED SOLUTIONS

The three ESRs agreed that the physical demonstrator needed to validate the concepts should be a Flight Simulator Cockpit.

In order to mitigate and/or eliminate the challenges mentioned above, a number of solutions are being investigated:

A. ESR 12 – ARAIM NEAR REAL-TIME ON-BOARD PREDICTION SYSTEM

The results presented in the previous chapters show that a dedicated system that evaluates the effects of the attitude and the surrounding environment in real time, needs to be developed to support the pilots during the flight. The reason behind is that often the flown trajectory differs from the simulated, this also includes the timing of the trajectory, due to delays or other factors.

A different version of the ARAIM algorithm, named Near Real-Time APPT (NRT APPT) is integrated in the aircraft simulator as a new avionics system. The algorithm takes as input position and attitude of the aircraft, integrates in time the dynamics and estimates position, attitude and protection levels (PL), in order to evaluate if the current aircraft dynamics could lead to a safety critical configuration and provide

timely caution or warning flags to the users, depending on whether or not the critical condition can be avoided in time (the most critical flight phases requires a maximum Time-To-Alert of 6 seconds). The objective of this process is to develop a system that can be integrated into the Flight Management System or the Avionics of an aircraft/UAV and can provide timely warning to the user/pilot whenever the current aircraft configuration could lead to a dangerous situation.

B. ESR 13 – Physiological Monitoring

The flight simulator will have attached an infra-red and a visual field camera while the person flying the plane will be wearing a BioHarness monitoring his heart rate, breathing rate and posture. One of the main objectives is to use the data to compare the physiological reaction of the pilot while flying in different scenarios and using different technologies. The other major objective is to build an algorithm that will be capable of predicting a drop in the performance of the pilot so that measures could be taken before the situation could get worst.

C. ESR 10 – Modelling Ground Movements

The flight simulator will be an excellent opportunity to test how the pilot can use instruction from a screen for manoeuvring the aircraft rather than following the instructions from the tower. With the physical demonstrator, it will be possible to test the results of a more complex optimisation model and to see the results in the decision-making process.

6.2.3. PHYSICAL DEMONSTRATOR CURRENT STATE

The Flight Simulator is hocked to MATLAB allowing the extraction of the input data needed by the tool developed by:

A. ESR 12

The NRT APPT is integrated and it predicts the integrity, and so the reliability, of the navigation solution provided by the GNSS receiver in terms of Protection Levels. The protection levels are displayed on supplementary indicators generated by MATLAB in order to help the pilot to evaluate the availability and reliability of the GNSS navigation solution.

The algorithm has been successfully connected to a commercial flight simulator software, X Plane 10, through a tool, X-Plane Connect, developed by NASA (Teubert, 2008). The X-Plane Connect (XPC) Toolbox is an open-source research tool used to interact with the commercial flight simulator software X-Plane. XPC allows users to control aircraft and receive state information from aircraft simulated in X-Plane using functions written in C, C++, Java, MATLAB, or Python in real time over the network. This research tool has been used to visualize flight paths, test control algorithms, simulate an active airspace, or generate out-the-window visuals for in-house flight simulation software. Possible applications include active control of an X-Plane simulation, flight visualization, and recording states during a flight, or interacting with a mission over User Datagram Protocol (UDP).

For this project, the XPC tool extracts information related to the attitude, position and dynamics of the aircraft in real time that is used in the ARAIM tool to compute

the current state of the parameters. For each second, the tool integrates in time the dynamics of the airplane (Eqs. 6.1 to 6.7) for 6-10 seconds based on the inputs extracted from the flight simulator, in order to satisfy the Time-to-Alert (TTA) requirement, predicts the ARAIM parameters and displays them on dedicated instrument panels, as shown in Figure 6-1, following the layout of the graphs already presented in chapter 4.

Figure 6-1 Real-time ARAIM computation integrated in the X Plane software.

The tool uses a classical Three Degrees of Freedom (3-DOF) point-and-variable mass model. The assumptions are:

- The Earth shape is approximated as an ellipsoid using World Geodetic System 1984 (WGS-84) parameters.
- The atmosphere is considered at rest relative to the Earth.
- Temperature, pressure and density are modelled with the International Standard Atmosphere (ISA).

- The aircraft is considered as a rigid body with a vertical plane of symmetry.
- The mass reduction is due to fuel consumption only.
- Forces (Thrust, aerodynamic and weight) act on the aircraft Centre of Gravity (CoG).
- The flight is symmetric.

The 3-DOF scalar equations are:

$$m\frac{dV}{dt} = T\cos\alpha - D(V,h,L) - mg\sin\gamma \tag{6.1}$$

$$m\frac{d\gamma}{dt} = (T\sin\alpha + L)\cos\phi - mg\cos\gamma \tag{6.2}$$

$$m\frac{d\psi}{dt} = \frac{(T\sin\alpha + L)\sin\phi}{\cos\gamma} \tag{6.3}$$

$$\frac{dm}{dt} = c(V,h)T \tag{6.4}$$

$$\frac{d\theta}{dt} = \frac{V\cos\gamma\cos\psi}{r_M + h} \tag{6.5}$$

$$\frac{d\Lambda}{dt} = \frac{V\cos\gamma\cos\psi}{(r_M + h)\cos\Phi} \tag{6.6}$$

$$\frac{d\mathrm{h}}{dt} = V\sin\gamma \tag{6.7}$$

Where:

m = aircraft mass [kg]

V = longitudinal velocity [m/s]

T = thrust magnitude [N]

α = angle of attack [rad]

D = drag magnitude [N]

h = altitude [m]

L = lift magnitude [N]

g = gravity acceleration at sea level [m/s]

γ = flight path angle [rad]

ϕ = roll or bank angle [rad]

ψ = heading angle [rad]

c = specific fuel consumption [kg/s]

Φ = geodetic longitude [rad]

r_M = meridional radius of curvature [m]

Λ = geodetic latitude [rad]

r_T = transverse radius of curvature [m]

B. ESR 13

Test how different scenarios result in changes in human physiology in an attempt to predict the variations in performance by using objective physiological monitoring. The physiological monitoring will consist of gathering heart rate and face thermography data. We have acquired a FLIR A65 thermal camera (Figure 6-2) for WP4. ESR 13 is currently working on having the image processing algorithm run in real time and extract the temperatures from the tracked areas. A machine learning algorithm trained on previously collected data will be used as a starting point for classifying multiple levels of mental workload; as more data will be collected, the classifier will be updated to provide more accurate results.

Figure 6-2 FLIR Thermal Camera (Marinescu, 2017).

C. ESR 10

A software (Quickest path problem with Time Windows – QPPTW algorithm) will calculate the quickest path from gate to runway and vice versa and will take into consideration other aircraft that might be moving on the ground.

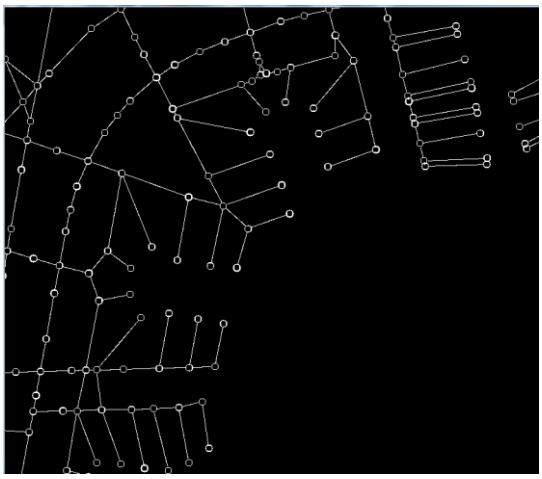

Figure 6-3 Virtual Representation of Airport (Stergianos, 2017).

Through this software, the user/pilot will be able to have a detailed plan to follow that will include instructions on how to manoeuvre in the ground and where to stop in order to avoid conflicts. This information will be displayed on a screen that will show.

This will make possible to also monitor the behaviour of a user/pilot when following instructions on the ground by a screen and that will help in identifying the feasibility and ease of this technology.

The model will use as input the position of the aircraft from the X-plane software with the help of a MATLAB tool.

6.3. RESULTS AND CONCLUSIONS

This tool proved to be a useful platform to test the ARAIM algorithm in a real-time configuration, used as an integrated avionics instrument, allowing to save time and avoiding the need of developing an aircraft dynamics simulator. Moreover, it could be used as test platform for a real-time trajectory optimizer. Due to a lack of time, a caution and warning system hasn't been implemented, at the current state the tool only shows the PLs and it is user's task to monitor them.

The tool can be further improved, implementing the above-mentioned caution and warning system, introducing user-defined parameters and settings, such as the selection of the YUMA almanacs, the number constellations to be included in the computation and the Integrity Support Message (ISM).

As final comment, we believe that the physical demonstrator could represent a possible configuration of how the future cockpit will look like, integrating new and innovative technology that will allow smoother and safer operations and flights:

- The ground operation tool will allow to reduce delays in congested airports and to directly guide pilots from the gate to the runway.
- The human physiology model will assess pilots' conditions and performances allowing to identify in advance high level of stress, workload and tiredness and ultimately improving the safety of flight.
- The ARAIM algorithm integrated as new avionics system for near real-time performance prediction will support pilots in identifying dangerous and hazardous situation from the navigation point of view.

Figure 6-4 and Figure 6-5 give an overview of the physical demonstrator output and an overview of its current configuration.

Figure 6-4 Overview of the Physical Demonstrator.

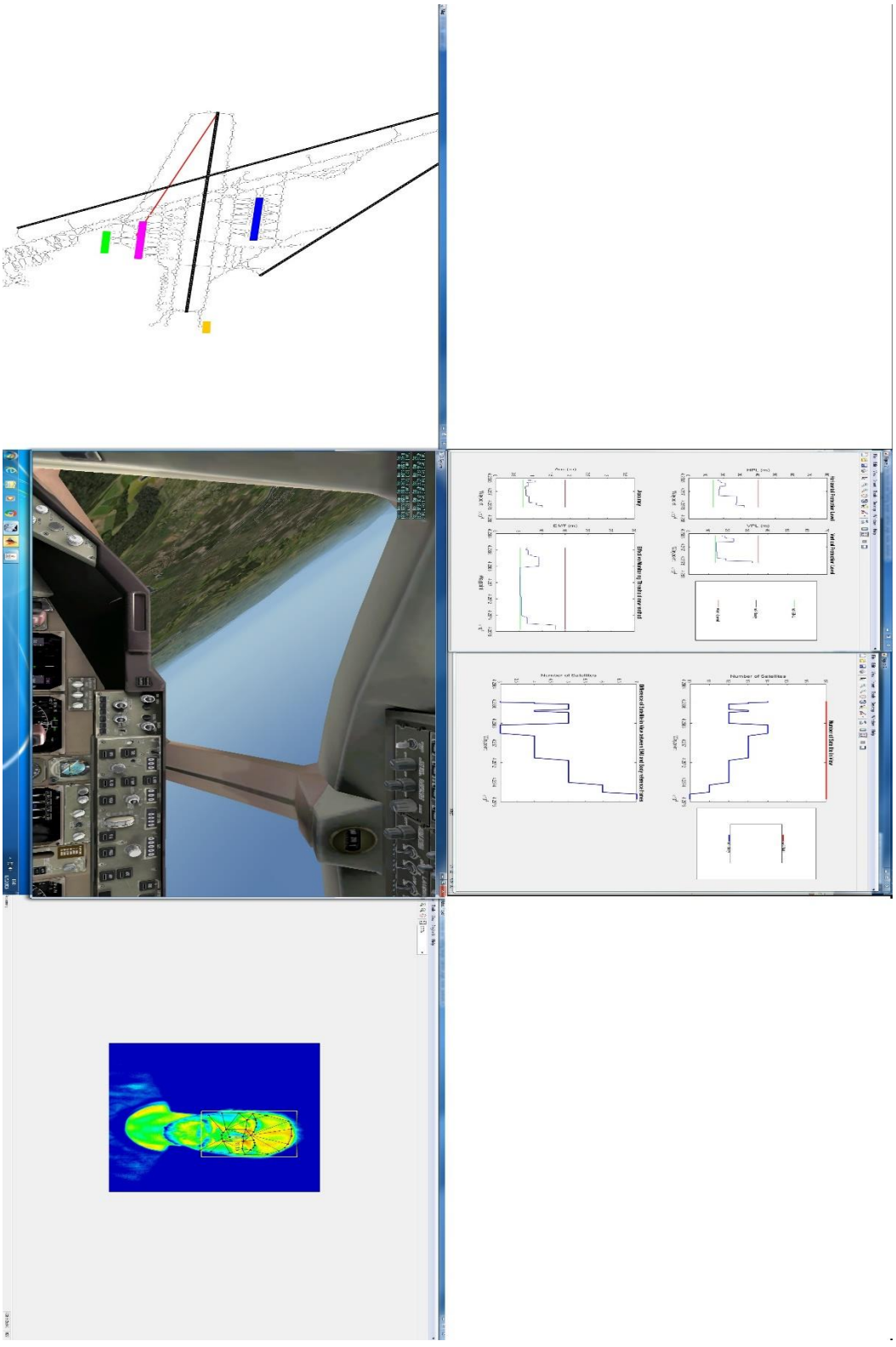

Figure 6-5 Screenshot (rotated 90° clockwise) of the three algorithms integrated in the flight simulator and working in parallel. Top screen: Ground Operation Optimiser. Middle Screen left: Flight Simulator view. Middle Screen right: near-Real Time Performance Prediction Tool. Bottom Screen: FLIR Thermal Camera analysing in real time pilot's performances.

7. CONCLUSIONS

7.1. SUMMARY AND RESULTS

This thesis consisted on an extensive analysis of ARAIM performances in operational configurations, considering the shadowing effect of the aircraft attitude and surrounding environments and the possible integration of new algorithms in civil aviation operation that use the ARAIM prediction capability to further improve the situation awareness. A review of the history of integrity monitoring has been provided together with an overview of the different techniques developed by the scientific community. In particular, a detailed presentation of the algorithm developed by Stanford University has been introduced, the MATLAB ARAIM Availability Simulation Tool (MAAST) that has been used as basis of the tools developed in this research. ARAIM is seen by the aviation community has the way forward for a safe introduction of GNSS as primary navigation system and for the reduction of ground support and costs. The four new algorithms cover aspects and support functions in the field of operations within the civil aviation world that have not been considered so far, showing interesting results on how ARAIM could be integrated in the daily routines, such us pre-flight operations and flight planning, but also as support in the design and assessment of flight procedures.

At the same time, one of the key word and factor of this research is “integration”, since it is part of a more complex project, INNOVATE, that involved other 12

researchers with the objective of integrating technologies from different areas of expertise to evaluate the overall improvement of aircraft performances.

A quick overview of the single chapters is now presented highlighting the principal aspects and outcome:

- Chapter 1 and Chapter 2 summarised the integrity monitoring problem and the different techniques developed and used until now.
- Chapter 3 presents the Stanford University ARAIM algorithm (MAAST) together with the modified version developed in this research, the APPATT, that includes the shadowing effect of the aircraft attitude and of the surrounding environment. The main difference between the tool is that the MAAST analyses static scenarios, providing global average values of the integrity performance parameters and highlighting the availability of a specific procedure. The APPATT focuses on the analysis of a specific operational scenario, highlighting if a determined route could be affected by one or more integrity outages due to unfavourable satellite configuration.
- Chapter 4 introduces two different versions of the APPATT algorithm, the Short-Term (ST) and Long-Term (LT). Both the tools analyse a determined trajectory using different combinations of the available satellite constellations (GPS, Galileo, GLONASS), however the ST version is intended to be used to support pilots in the pre-flight operations in assessing the integrity status of the expected route in nominal condition, while the LT version analyses a route within a defined time frame (that can be from few hours to several days) and it is intended to support the long-term planning of flights. The main objective

of both the tools is to make aware pilots, ATCs and planners of possible integrity outages in nominal condition (no faults in the satellite measurements) along the expected route and help them in finding alternative solution way in advance (e.g. using a different route or the support of another navigation system). The results of the two algorithms show that a dual-constellation GNSS receiver might not be sufficient for all the possible scenarios, supporting the need for an international collaboration for the development of multi-GNSS applications.

- Chapter 5 introduces a basic concept that could be integrated in the next algorithm for trajectory optimisation. Nowadays, flight paths are defined through a series of waypoints that the aircraft is supposed to follow. The algorithm presented is a combination of two functions, a path generator, that provides as output the expected trajectory based on the list of waypoints selected for the route, and a path modifier that analyses the integrity performance of the generated trajectory and, in case of an outage, suggests an alternative path that satisfies the required navigation performance of the procedure.
- Chapter 6 presents one of the main achievement of the INNOVATE project, the integration of different technologies in a physical demonstrator. A near-real-time performance prediction ARAIM algorithm has been implemented together with a ground operation optimiser and a human performance evaluator based on physiology parameters into a flight simulator cockpit. The physical demonstrator represents a possible example of technologies that will

be integrated in the next generation of aircraft to enhance the capabilities and improve the safety of the flights.

As final remark, the results show that a dedicated system, that evaluates the effects of the attitude and the surrounding environment in an operational configuration, needs to be developed and integrated into the flight management system if the ARAIM technique is to be used as an on-board system for integrity monitoring. The integration of such system could support the pilots, together with the ATM and procedure designers, in the pre-flight operations for the definition of the path to be followed to reach the arrival location.

The author of this thesis had contacted representatives of EUROCONTROL and ESA in order to get a feedback on the research and analysis performed.

Both the organizations confirmed that analyses of the performances considering the shadowing effect of the aircraft attitude and surrounding environment were never performed.

ESA is currently collaborating with the Working Group-C, and so the EU-US commission, by assessing the performances of the Galileo constellation, in order to evaluate the capabilities of the European system in supporting the implementation of ARAIM in the Civil Aviation systems. The ESA team expressed its concern to the commission regarding the fact that no simulations of operational scenarios were performed, but until now nothing has been done to address this concern yet.

The team in EUROCONTROL confirmed that at the current status the organization does not have any tool that analyses simulated aircraft trajectories. The main used software, named AUGUR, is a grid-based RAIM availability prediction tool with the

only feature of varying the masking angle between 0° and 5° (for further information the reader can refer to the EUROCONTROL (2018) website of the paper by Ober (1998)).

Additionally, no tool exists or is currently used that attempts to modify/optimise the trajectory using the integrity performance parameters as additional drivers in the computation.

The EUROCONTROL team has also stated that in the roadmap of ARAIM implementation, developed by GEAS (2016), and in the operational concepts presented by ICAO (2018) at the Navigation Panel it is considered the removal of the requirement of integrity availability prediction along the flight path, at least for the horizontal component while for the vertical component it might still be required, but it is currently under discussion pending on the analysis that will be performed in the following months.

Another point that the EUROCONTROL team has highlighted is what the industry is currently willing to implement. The approval of the use of a multi-frequency and multi-constellation systems that satisfy the ARAIM requirements is going to impact the design and development of the currently used hardware, representing a new and quite challenging task for the industries, that have expressed their concerns regarding the real need of this type of system.

This research is actually supporting both sides of the debate, since the results show that a multi-constellation system is required in order to have a safe and reliable integrity monitoring system, but at the same time it has highlighted that the computational workload required represents a challenging issue in the implementation of the concepts presented.

It is the author opinion that International organizations and industries should start to further and deeply analyse the performances of ARAIM in operational scenarios and to find a trade-off between safety and complexity.

Figure 7-1 summarises the research and integration effort made in this research, that involved different types of tools and information all implemented in different algorithms that have the main objective of supporting the introduction of GNSS as main navigation system in the civil aviation.

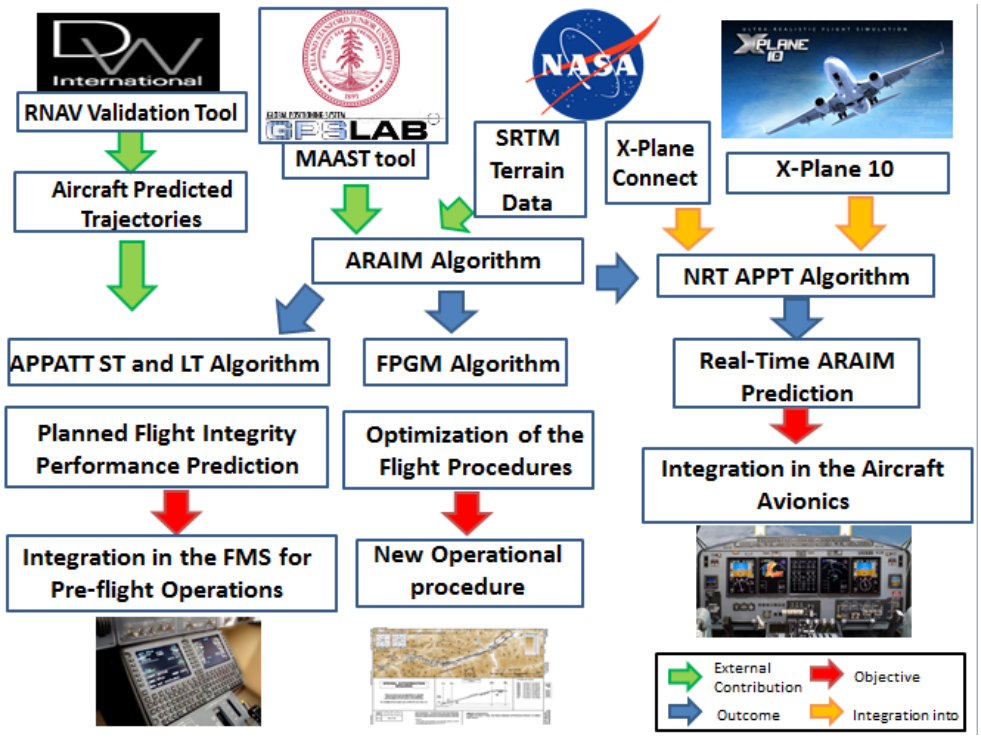

Figure 7-1 Summary Scheme of the Algorithms Developed and the Integration Effort.

7.2. OTHER REMARKS, RECOMMENDATIONS AND FUTURE WORK

All the algorithms developed in this research represent basic concepts that can be further developed due to the highly complex nature of the integrity monitoring problem.

Additionally, the analyses performed within this research project are all based and performed considering assumptions and using simplified models, which includes:

- Use of models for the simulations of trajectories, both for the satellite orbits and aircraft flight path and attitude.

  The tools integrate the satellite orbit propagation model based on the use of the almanac as main source of input for the orbital parameters. The main limit of this model is that the almanacs are not the most up to date product for the computation and analysis of the satellite orbits. An error or uncertainty not corrected quickly enough could lead at the wrong determination and propagation of the satellite positions that in sequence could lead to a wrong assessment of the loss of LoS in the body reference frame and the incorrect integrity performance prediction.

  Regarding the aircraft flight path and attitude simulation, the tools integrate very simple models to define the aircraft position and attitude angles. The main drawback of simple models, it is that the accuracy of the predicted trajectory might be very low and this could lead to an erroneous determination of the satellite in view in the body reference frame and so possible impact on the analysis of the integrity performances. In the FPG and FPM tools, this could also lead to the definition of a sub-optimal trajectory.

- Another approximation is given by the use of the environmental database, that has a spatial resolution of 100m. As mentioned in Chapter 5, this could lead to the misinterpretation of the scenario and declare a satellite not in view while in reality it is (or vice-versa)
- The developed tools are also based on other approximations, such as the use of parameters that are equal for all the constellations and satellites, like the a priori probabilities of satellite and constellation failure, biases and error distributions. The real implementation of the ARAIM technique is supposed to use the Integrity Support Message, that will carry the most updated information and estimate of these parameters that will allow a better estimate of the integrity performances.
- This research focused on looking at snapshots of data and locations, to analyse at a very coarse level the operational performances of ARAIM and the implications and consequences of its implementation in Civil Aviation. However, in order to have statistically useful results, further analysis needs to be performed that includes different geometries and error distributions.

The APPATT ST and LT algorithms require improvements from the computational point of you, the evaluation of the shadowing effect is not very efficient and it could be enhanced to reduce the time and computation power required to perform a complete simulation. The FPG&FPM could be used and integrated in more complex optimisation algorithm, adding a new constraint in the trajectory computation that takes into of the integrity requirements. For the Near-Real-Time APPATT, the

implementation of a more complex dynamic model could help to better represent the reality and have better predictions.

Currently, the international community is working towards the integration of ARAIM in Civil Aviation. In 2016, The Working Group-C published the third report that includes the proposed Implementation Roadmap for ARAIM Services, the consideration of institutional issues and their discussion, as well as the elaborated view of ARAIM complementing the services provided by SBAS systems (GEAS, 2016). At the same time, international organizations such as ICAO and EUROCONTROL are working on draft Standards and Recommended Practices (SARPS) and Dual-Frequency-Multi-Constellation GNSS Concept of operations (CONOPS) that includes ARAIM (ICAO, 2018). These drafts already include general guidelines for the standards to be included in the future GNSS systems, such as the use of the iono-free technique and the use of at least two constellations.

The author of this thesis believes that the obtained results and concepts developed within this research could be used by the international community and organizations in the assessment and definition of these standards that are going to impact the future of the Civil Aviation systems.

APPENDIX

A. SUMMARY OF THE THREATS

Table A-0-1 shows a summary of the threats that need to be considered when computing a position error bound. GEAS's report divides the threats in three different categories:

- First column (Nominal) includes all the errors that are always present and whose magnitude is not expected to change or only slowly. The faults in the first five rows are bounded by σ_{URA} and b_{nom} provided by the Integrity Support Message (ISM), while the other ones are modelled in the receiver.
- Second column (Narrow faults) includes the faults that can affect each satellite independently and cause the growth of the pseudorange error beyond its nominal behaviour. These faults are described by P_{sat} provided by the ISM.
- Third column (Wide faults) includes the faults that could cause a whole constellation to be faulted. These faults are described by P_{const} provided by the ISM.

Table A-0-1 Summary of the threat space.

	Nominal	Narrow Fault	Wide Fault
Clock and Ephemeris	Orbit/clock estimation and prediction and broadcast limits	Includes clock runoffs, bad ephemeris, unflagged manoeuvres	Erroneous EOPP, Inadequate manned ops, ground-inherent failures
Signal Deformation	Nominal differences in signals due to RF components, filters, and antennas waveform distortion	Failures in satellite payload signal generation components. Faulted signal model as described in ICAO	N/A
Code-Carrier Incoherence	e.g. incoherence observed in IIF L5 signal or GEO L1 signals	e.g. incoherence observed in IIF L5 signal or GEO L1 signals	N/A
Inter-Frequency Bias (IFB)	Delay differences in satellite payload signal paths	Delay differences in satellite payload signal paths TBC	N/A
Satellite Antenna Bias	Look-angle dependent biases caused at satellite antennas	Look-angle dependent biases caused at satellite antennas	N/A
Ionosphere	N/A	Scintillation	Multiple scintillations at solar storms
Troposphere	Nominal troposphere error (after applying SBAS MOPS model for tropo correction)	N/A	N/A
Receiver Noise and Multipath	Nominal noise and multipath terms in airborne model (TBC Galileo BOC(1,1) and L5/E5a))	e.g.: receiver tracking failure or multipath from onboard reflector. TBC	e.g.: receiver tracking multiple failures or multipath from onboard reflector. TBC

B. LEG TYPES

The following make up the twenty-two leg types that are currently in use:

Table B-1 Leg Types and related Codes.

Heading to Altitude	VA
Heading to a DME Distance	VD
Heading to a Next Leg Intercept	VI
Heading to a Manual Termination	VM
Heading to a Radial Termination	VR
Course to an Altitude	CA
Course to a DME Distance	CD
Course to a Next Leg Intercept	CI
Course to a Radial Termination	CR
Course to a Fix	CF
Tracking Between Two Fixes	TF
Direct to a Fix	DF
Course from a Fix to an Altitude	FA
Course from a Fix to an Along Track Distance	FC
Course form a Fix to a DME Distance	FD
Course from a Fix to a Manual Termination	FM
Constant DME Arc to a Fix	AF
Hold to a Fix	HF
Hold to an Altitude	HA
Hold to a Manual Termination	HM
Initial Fix	IF
Procedure Turn to Intercept	PI

C. TAILWIND VALUES

Table C-1 Tailwind values in function of Height Above the Aerodrome.

TWC (km/h) for turn calculations	
Turn Height Above Aerodrome (m)	Standard Tailwind Component (kph)
100	40
500	92
1000	100
1500	130
2000	157
2500	185
3000	220
3500	242

D. Single Constellation Configuration (GPS) with 0° Mask angle

- Single constellation GPS: Yuma almanac week 703 (TOA 319488s), reset time [0d 0h 0m 0s], mask angle 0°

As an extreme case, the receiver mask angle has been set to 0°, the equivalent of not setting a mask angle.

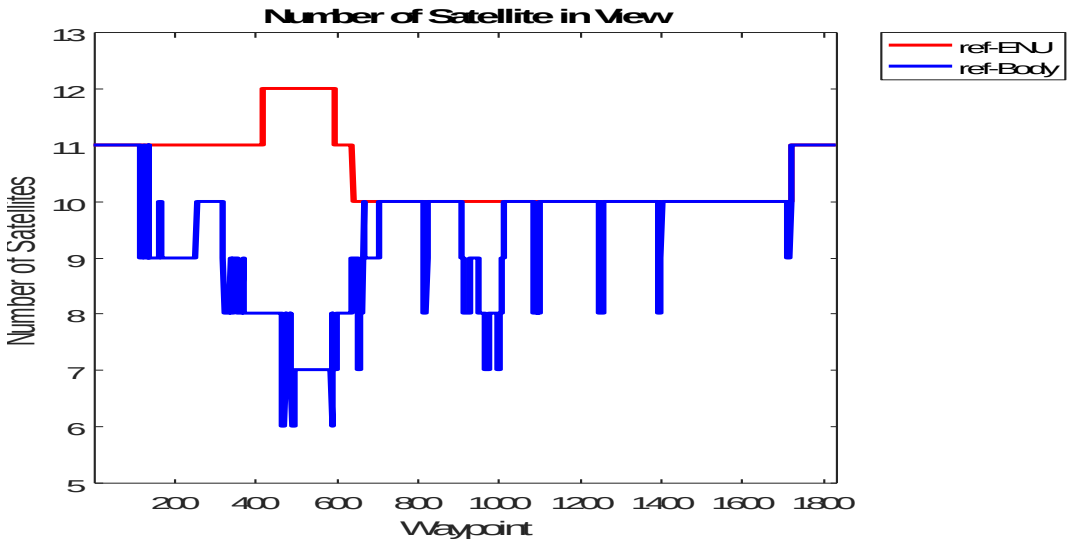

Figure D-0-1 Number of Satellites in view in the ENU (red) and Body (blue) Reference Frames along the Trajectory.

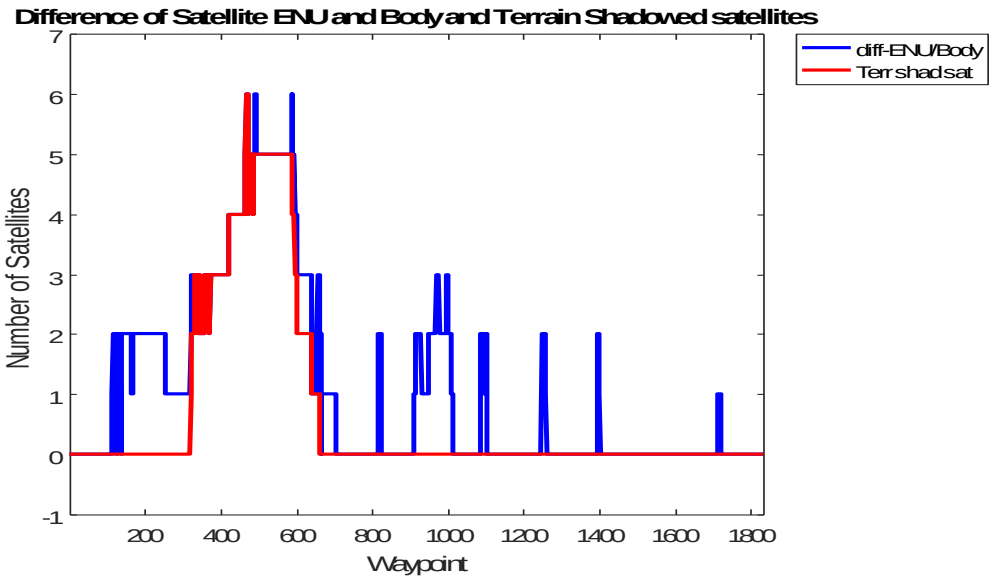

Figure D-0-2 Number of Shadowed Satellites by Aircraft Attitude (blue) and Terrain (red).

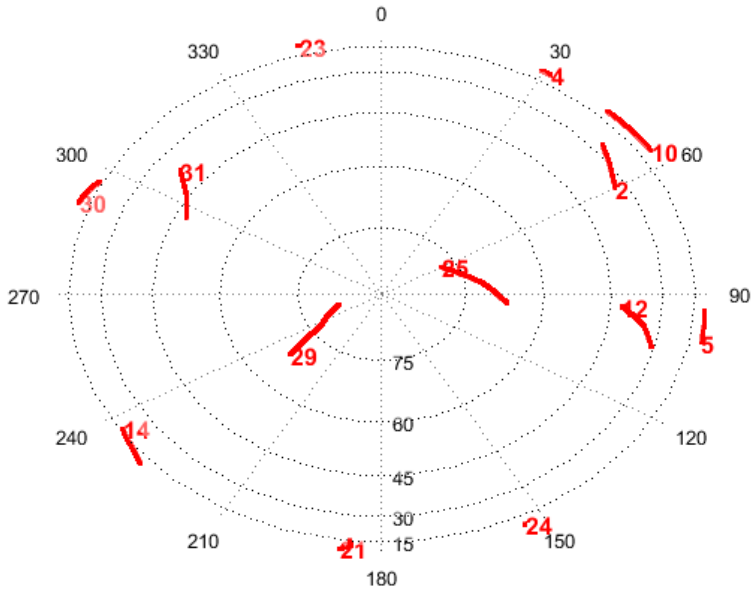

Figure D-0-3 Satellites in View Skyplot in the ENU reference frame.

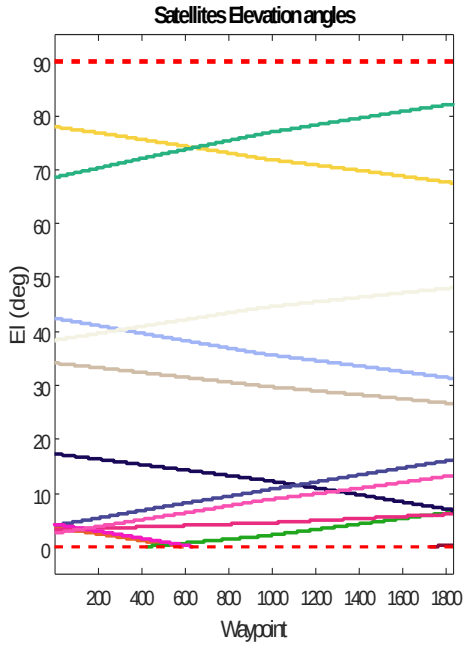

Figure D-0-4 Satellites Elevation.

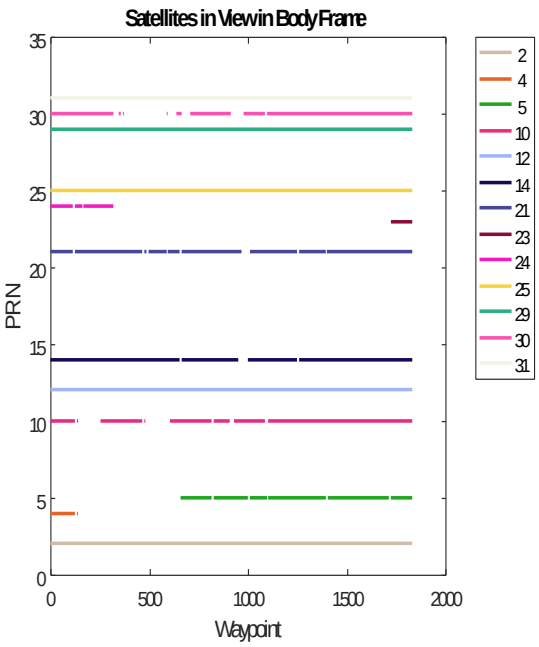

Figure D-0-5 Satellites visibility by PRN.

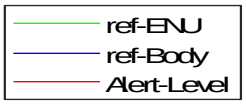

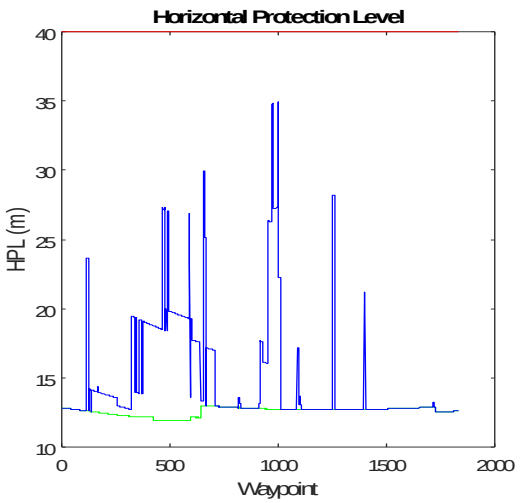

Figure D-0-6 HPL in the ENU (green) and Body (blue) Reference Frames compared with the Alert Level (red).

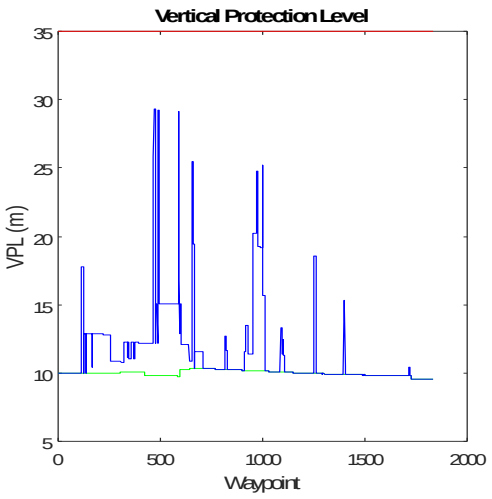

Figure D-0-7 VPL in the ENU (green) and Body (blue) Reference Frames compared with the Alert Level (red).

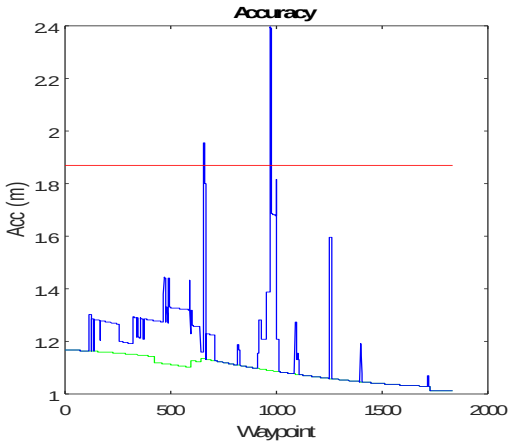

Figure D-0-8 Accuracy in the ENU (green) and Body (blue) Reference Frames compared with the Alert Level (red).

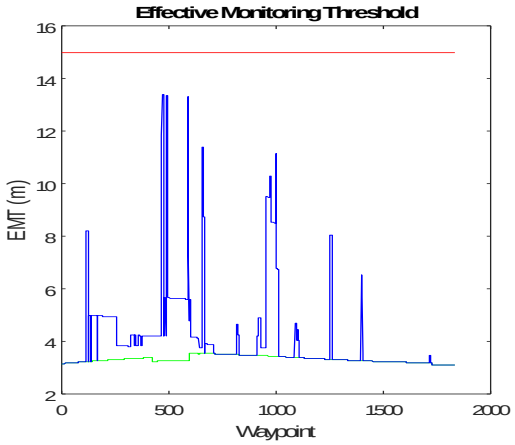

Figure D-0-9 EMT in the ENU (green) and Body (blue) Reference Frames compared with the Alert Level (red).

Table D-1 Values Comparison between ENU and Body Reference Frames.

Performance Parameter	Max_{ENU}	WP_{Max_ENU}	Max_{Body}	WP_{Max_Body}	ENU at WP_{Max_Body}	AL
HPL (m)	13.02	641	34.97	1001	12.73	40
VPL (m)	10.38	641	29.29	467	9.79	35
EMT (m)	3.56	641	13.37	467	3.25	15
Accuracy (m)	1.17	1	2.4	969	1.09	1.87

Table D-2 Percentage Differences between Max Values in Body Reference Frame, related ENU values and Alert Level.

Performance Parameter	Δ% between Body and ENU at WP_{Max_Body}	Δ% between Max_{Body} and AL
HPL (m)	174.63	-12.58
VPL (m)	199.11	-16.31
EMT (m)	311.29	-10.85
Accuracy (m)	119.73	28.08

REFERENCES

adcsforbeginners 2015. Perifocal reference frame [Online]. Available: https://adcsforbeginners.wordpress.com/tag/perifocal-frame/.

AIRBUS 2013. Future by Airbus [Online]. Available: http://com.airbus-fenice.customers.artful.net/innovation/future-by-airbus/.

AIRBUS 2015. PBN Implementation from the Industry Perspective [Online]. Available: https://www.icao.int/MID/Documents/2015/AFI-MID%20ASBU%20Impl.%20Workshop/2.1-3%20AIRBUS%20PBN%20Impl.%20from%20Industry%20perspective.pdf.

AIRDATA 2017. Coordinate System ECEF [Online]. Available: https://www.basicairdata.eu/knowledge-center/background-topics/coordinate-system/.

ATMRPP 2014. Sharing Trajectory Predictions in TBO. In: ICAO (ed.) Air Traffic Management Requirements And Performance Panel.

AUAWISE 2010. Aircraft axes [Online]. Available: https://www.decodedscience.org/how-airplanes-manipulate-air-achieve-flight/15993.

BLANCH, J., CHOI, M., WALTER, T., ENGE, P. & SUZUKI, K. 2010. Prototyping Advanced RAIM for Vertical Guidance. Proceedings of the 23rd International Technical Meeting of The Satellite Division of the Institute of Navigation, September 21-24 2010 Portland, OR. 285-291.

BLANCH, J., ENE, A., WALTER, T. & ENGE, P. 2007. An Optimised multiple hypothesis RAIM algorithm for vertical guidance. In: GNSS, P. O. I., ed. Institute of Navigation GNSS Conference, 2007 Fort Worth, TX.

BLANCH, J., WALTER, T. & ENGE, P. 2013a. Advanced RAIM System Architecture with a Long Latency Integrity Support Message. Proceedings of The ION GNSS 2013, September 16-20 2013 Nashville, TN.

BLANCH, J., WALTER, T. & ENGE, P. 2013b. Optimal Positioning for Advanced RAIM. Navigation: Journal of The Institute of Navigation, 60**,** pp. 279-289.

BLANCH, J., WALTER, T. & ENGE, P. 2013c. Results on the Optimal Detection Statistic for Integrity Monitoring,. International Technical Meeting of The Institute of Navigation, 2013 San Diego, California. pp. 262-273.

BLANCH, J., WALTER, T. & ENGE, P. 2014. Exclusion for Advanced RAIM: Requirements and a Baseline Algorithm. The Institute of Navigation International Technical Meeting. San Diego, CA.

BLANCH, J., WALTER, T., ENGE, P., LEE, Y., PERVAN, B. & SPLETTER, A. 2012. Advanced RAIM User Algorithm Description: Integrity Support Message Processing, Fault Detection, Exclusion, and Protection Level Calculation. Proceedings of ION GNSS 2012, September 17-21 2012 Nashville, TN. pp. 2828-2849.

BLANCH, J., WALTER, T., ENGE, P., WALLNER, S., FERNANDEZ, F., DELLAGO, R., IOANNIDES, R., PERVAN, B., HERNANDEZ, I., BELABBAS, B., SPLETTER, A. & RIPPL, M. 2013d. Critical Elements for Multi-Constellation Advanced RAIM. Navigation: Journal of The Institute of Navigation, 60(1)**,** pp. 53-69.

BLANCH, J., WALTER, T., ENGE, P., WALLNER, S., FERNANDEZ, F. A., DELLAGO, R., IOANNIDES, R., PERVAN, B., HERNANDEZ, I. F., BELABBAS, B., SPLETTER, A. & RIPPL, M. 2011. A Proposal for Multi-constellation Advanced RAIM for Vertical Guidance. Proceedings of the 24th International Technical Meeting of The Satellite Division of the Institute of Navigation, September 20-23 2011 Portland, OR. pp. 2665-2680.

BRENNER, M. 1990. Implementation of a RAIM Monitor in a GPS Receiver and Integrated GPS/IRS. Proceeding of the Technical Meeting of the Satellite Division of The Institute of Navigation, September 19-20 1990. pp 397-406.

BRENNER, M. 1995. Integrated GPS/Intertial Fault Detection and Availability. Proceedings of the 8th International Technical Meeting of The Institute of Navigation, September 12-15 1995 Palm Springs, California. pp. 1949-1958.

BRITS, L. 2008. Euler Angles [Online]. Available: https://www.revolvy.com/main/index.php?s=Euler%20angles.

BROWN, R. G. & CHIN, G. 1998. GPS RAIM: Calculation of Threshold and Protection Radius Using Chi-Square Methods - A Geometric Approach. The Institute of Navigation Monograph Series, Vol. V**,** pp. 155-178.

BROWN, R. G. & HWANG, P. Y. C. 1986. GPS Failure Detection by Autonomous Means Within the Cockpit. Proceedings of Annual Meeting of the Institute of Navigation, June 24-26, 1986, Seattle, WA. pp. 5-12.

BROWN, R. G. & MCBURNEY, P. W. 1987. Self-Contained GPS Integrity Check Using Maximum Solution Separation as the Test Statistic. Proceedings of the First Technical Meeting of The Institute of Navigation, 1987 Colorado Springs, CO. pp. 263-268.

CAA-PAPER 2003. GPS Integrity and Potential Impact on Aviation Safety. In: CAA (ed.) CAA Paper. United Kingdom: Civil Aviation Authority.

CEZON, A., CUETO, M. & FERNANDEZ, I. 2013. Analysis of Multi-GNSS Service Performance Assessment: ARAIM vs. IBPL Performances Comparison. Proceedings of the 26th International Technical Meeting of The Institute of Navigation Satellite Division (ION GNSS+ 2013), September 16-20 2013 Nashville, TN. pp. 2654-2663.

CHOI, M., BLANCH, J., AKOS, D., HENG, L., GAO, G., WALTER, T. & ENGE, P. 2011a. Demonstrations of Multi-constellation Advanced RAIM for Vertical Guidance Using GPS and GLONASS Signals. Proceedings of the 24th International Technical Meeting of The Satellite Division of the Institute of Navigation, September 20 - 23 2011 Portland, OR. pp. 3227 - 3234.

CHOI, M., BLANCH, J., WALTER, T., AKOS, D. & ENGE, P. 2012. Evaluation of Multi-constellation Advanced RAIM for Vertical Guidance Using GPS and GLONASS Signals with Multiple Faults. Proceedings of the 25th International Technical Meeting of The Satellite Division of the Institute of Navigation, September 17-21 2012 Nashville, TN. pp. 884-892.

CHOI, M., BLANCH, J., WALTER, T. & ENGE, P. 2011b. Advanced RAIM Demonstration Using Four Months of Ground Data. Proceedings of the 2011 International Technical Meeting of the Institute of Navigation, January 24-26 2011 Catamaran Resort Hotel, San Diego, CA. 279-284.

COLASURDO 2010. Lesson notes of the Spacecraft dynamics and control course, University La Sapienza of Rome.

CURTIS, H. D. 2013. Orbital Mechanics for Engineering Students, Elsevier Science.

DWINT 2013. RVT GUI [Online]. Available: http://www.dwint.com.

EC 2004. Single European Sky ATM Research (SESAR) [Online]. Available: https://ec.europa.eu/transport/modes/air/sesar_en.

EC 2011. Flight Path 2050 Europe's Vision for Aviation.

EGELAND, O. & GRAVDAHL, J. T. 2002. Modeling and Simulation for Automatic Control.

EL-MOWAFY, A. 2013. ARAIM for Vertical Guidance Using GPS and BeiDou Journal of Global Positioning Systems, 12(1), pp. 28-37.

ENE, A. 2007. Multiple Hypothesis RAIM with Real-Time FDE and Forecasted Availability for Combined Galileo-GPS Vertical Guidance. Proceedings of The European Navigation Conference - GNSS, May 28-31 2007 TimeNav, Geneva, Switzerland.

ENE, A. 2009. Utilization of Modernized Global Navigation Satellite Systems for Aircraft-Based Navigation Integrity. Doctor of Philosophy, Stanford University.

ENE, A., BLANCH, J., WALTER, T. & POWELL, J. D. 2008. Validation of Multiple Hypothesis RAIM Algorithm Using Dual-Frequency GNSS Signals. Proceedings of The European Navigation Conference - GNSS, April 22-25 2008 Toulouse Space Show, Toulouse, France.

EUROCONTROL 2008. EUROCONTROL Policy on GNSS for Navigation Applications in the Civil Aviation Domain In: EUROCONTROL (ed.).

EUROCONTROL 2018. AUGUR webpage on the EUROCONTROL website [Online]. Available: http://www.eurocontrol.int/augur

FAA 2006. Civil Utilization of Area Navigation (RNAV) Departure Procedures.

FAA 2007a. FAA AFS-400 Advisory Circular 90-100A - U.S Terminal and En Route Area Navigation (RNAV) Operations.

FAA 2007b. FAA AFS-400 Order 8260.58A. The United States Standard for Performance Based Navigation (PBN) Instrument Procedure Design.

FAA 2012. Next Generation Air Transportation System [Online]. Available: https://www.faa.gov/nextgen/.

FENG, S., OCHIENG, W. Y., WALSH, D. & IOANNIDES, R. 2006a. A highly accurate and computationally efficient method for predicting RAIM holes. Journal of Navigation, 59(1), 105-117.

FENG, S., OCHIENG, W. Y., WALSH, D. & IOANNIDES, R. 2006b. A dynamic sampling scheme for GPS integrity assessment. Aeronautical Journal, 110(1105), 129-143.

FENG, S & OCHIENG, W. 2005. An Efficient Worst User Location Algorithm for the Generation of the Galileo Integrity Flag. Proceedings of the 18th International Technical Meeting of the Satellite Division of The Institute of Navigation (ION GNSS 2005) September 13 - 16, 2005.

GEAS 2008. Phase I Panel Report of the GNSS Evolutionary Architecture Study. Federal Aviation Administration (FAA).

GEAS 2010. Phase II Report of the GNSS Evolutionary Architecture Study. Federal Aviation Administration (FAA).

GEAS 2016. Phase III Report of the GNSS Evolutionary Architecture Study. Federal Aviation Administration (FAA).

GPS.GOV 2017. Official U.S. government information about the Global Positioning System (GPS) and related topics [Online]. Available https://www.gps.gov/systems/gps/modernization/civilsignals/

GRAAS, F. V. & FARRELL, J. L. 1993. Baseline fault Detection and Exclusion Algorithm. Proceedings of the 49th Annual Meeting of the Institute of Navigation, June 21-23 1993. pp 413-420.

GROVES, P. D. 2013a. Principles of GNSS, Inertial, and Multisensor Integrated Navigation Systems, USA, Artech House.

GROVES, P. D. 2013b. Principles of GNSS, Inertial, and Multisensor Integrated Navigation Systems, Second Edition, Artech House.

GSC-EUROPA 2017. Orbital and Technical Parameters.

HOFMANN-WELLENHOF, B., LICHTENEGGER, H. & WASLE, E. 2008. GNSS – Global Navigation Satellite Systems: GPS, GLONASS, Galileo, and More, Springer.

HWANG, P. & BROWN, R. G. 2006. RAIM FDE Revisited: A New Breakthrough in Availability Performance with NIORAIM (Novel Integrity-Optimized RAIM). Navigation: Journal of The Institute of Navigation, 53(1), pp. 41-51.

HWANG, P. & BROWN, R. G. 2008. From RAIM to NIORAIM - A New Integrity Approach to Integrated Multi-GNSS Systems. InsideGNSS.

ICAO 1999. Manual on Required Navigation Performance. 2nd ed.: International Civil Aviation Organization.

ICAO 2000. Validated ICAO GNSS Standards and Recommended Practices (SARPS). International Civil Aviation Organization.

ICAO 2009. DOC 9905 AN/471 – Required Navigation Performance Authorization Required (RNP AR) Procedure Design Manual.

ICAO 2018. Report by the ICAO Navigation Systems Panel. Concept Of Operations (Conops) for Dual-Frequency Multi-Constellation (Dfmc) Global Navigation Satellite System (GNSS).

IERS 2010. Chapter 9 - Material and software associated with IERS Conventions (2010) [Online]. Available: ftp://maia.usno.navy.mil/conv2010/2010/2010_update/chapter9/icc9_until20130610.pdf

IMPARATO, D. 2016. GNSS-Based Receiver Autonomous Integrity

Monitoring For Aircraft Navigation, doctoral thesis, University of Delft, Delft.

INSIDEGNSS 2013. Integrity for Aviation [Online]. Available: http://www.insidegnss.com/node/3625.

INSIDEGNSS 2016. Satellite Selection [Online]. Available: http://www.insidegnss.com/node/5197.

IOANNIDES, R., WALSH, D., OCHIENG, W. & FENG, S. 2005. Towards A Complete FMEA Method to Assess the Performance of GPS system for GPS based applications, in Proceedings of ION GNSS, 13-16 September 2005 Long Beach Convention Center, Long Beach, California.

JIANG, Y. & WANG, J. 2011. A-RAIM vs. R-RAIM: A Comparative Study. International Global Navigation Satellite Systems Society (IGNSS Symposium 2011), November 15-17 2011 University of New South Wales, NSW, Australia.

JIANG, Y. & WANG, J. 2014. A New Approach to Calculate the Vertical Protection Level in A-RAIM. The Journal of Navigation, 67**,** pp. 711-725.

KALAFUS, R. M. 1987. Receiver Autonomous Integrity Monitoring of GPS. Cambridge, MA: U.S. DOT Transportation Systems Center.

KELLY, R. 1996a. Derivation of the RAIM Algorithm for the First Principles with Performance Comparison between Published Algorithm. Proceedings of the National Technical Meeting of The Institute of Navigation, January 22-24 1996. pp. 799-809.

KELLY, R. 1996b. Hypothesis testing as applied to GPS RAIM. Lecture Notes, January 22-24 1996, Ohio University Avionics Center, Athens, Ohio.

KELLY, R. 1997. The Linear Model, RNP, and the Near-Optimum Fault Detection and Exclusion Algorithm. Red Book of the Institute of Navigation, January 22-24 1997. pp. 227-259.

KELSO, T. S. 2015. CelesTrack [Online]. Available: https://celestrak.com/GPS/almanac/Yuma/.

KOVACH, K. 1998. Continuity: the hardest GNSS requirement of all. In: ION-GPS, ed. 11th International Technical Meeting of the Satellite Division of the Institute of Navigation, 15-18 September 1998 Nashville, Tennessee.

KROPP, V., MENDES, P. & EISSFELLER, B. 2011. Multi-Constellation Integrity Performance Expectations for Today's ARNS/RNSS Bands. Proceedings of the 24th International Technical Meeting of The Institute of Navigation Satellite Division, September 19-23 2011 Portland, OR. pp. 3192-3204.

LEE, Y. 2012. New Advanced ARAIM with Improved Availability for Detecting Constellatio-wide Faults, Using two Independent Constellations. Proceedings of the 2012 International Technical Meeting of The Institute of Navigation, January 30- 1 2012 Newport Beach, CA. pp. 1708-1723.

LEE, Y. C. 1986. Analysis of Range and Position Comparison Methods as a Means to Provide GPS Integrity in the User Receiver. Proceedings of the Annual Meeting of the Institute of Navigation, June 24-26, 1986, Seattle, WA. pp. 1-4.

LEE, Y. C. 2013. Performance of Advanced RAIM When an Earth Orientation Parameter Fault Affects the Satellites in View One at a Time. The Institute of Navigation ION GNSS 2013. Nashville, TN.

LEE, Y. C., BRAFF, R., FERNOW, J. P., HASHEMI, D., MCLAUGHLIN, M. P. & O'LAUGHLIN, D. 2005. GPS and Galileo with RAIM or WAAS for Vertically Guided Approaches. Proceedings of the 18th International Technical Meeting of the Satellite Division of The Institute of Navigation, September 13 - 16 2005 Long Beach, CA. pp. 1801-1825.

LÜKEN, T., GROLL, E., Antrack F. & KORN, B. 2008. Helicopter IFR Steep and Curved Approaches Using SBAS Guidance. 34th European Rotorcraft Forum. Liverpool, United Kingdom.

LUO, J., WANG, Z., CHENGWU, S., KUIJPER, A., WEN, Z. & LIU, S. 2016. Modelling and Implementation of Multi-Position Non-Continuous Rotation Gyroscope North Finder. Sensors 2016, September 20 2016, 16(9), 1513

MACABIAU, C., MILNER, C., TESSIER, Q., MABILLEAU, M., VUILLAME, J., SUARD, N. & RODRIGUEZ, C. 2014. Impact of Nominal Bias Bounding Techniques on Final ARAIM User Performance. Proceedings of the International Technical Meeting of The Institute of Navigation, January 27-29 2014 San Diego, CA. pp. 68-77.

MARINESCU, A. 2017. Facial thermography for assessment of workload in safety-critical environments, doctoral thesis, University of Nottingham, Nottingham.

MARTINI, I., RIPPL, M. & MEURER, M. 2013. Advanced RAIM Architecture Design and User Algorithm Performance in a Real GPS, GLONASS and Galileo Scenario. Proceedings of The ION GNSS 2013, September 16-20 2013a Nashville, TN.

MARTINI, I., RIPPL, M. & MEURER, M. 2013b. Integrity Support Message Architecture Design for Advanced Receiver Autonomous Integrity Monitoring. European Navigation Conference, April 23-25 2013b Vienna, Austria.

MILNER, C., MACABIAU, C., DULERY, C., MABILLEAU, M., SUARD, N., RODRIGUEZ, C. & PUJOL, S. 2013. An Analysis of ARAIM Performance Sensitivity to the Ground System Architecture Definition. Proceedings of The ION GNSS 2013, September 16-20 2013 Nashville, TN.

MILNER, C. & OCHIENG, W. 2010. ARAIM for LPV-200: The Ideal Protection Level. Proceedings of the 23rd International Technical Meeting of The Satellite Division of the Institute of Navigation, September 21-24 2010 Portland, OR. pp. 3191-3198.

MIT 2007. Aircraft Systems [Online]. Available: http://mit.edu/aeroastro/academics/grad/aircraftsystems.pdf.

MOORE, T. 1992. Map Projection Lecture Notes.

NASA 2000a. Perspective View, Mt. Etna, Italy [Online]. Available: https://www.jpl.nasa.gov/spaceimages/details.php?id=PIA03370.

NASA 2000b. Shuttle Radar Topography Mission (SRTM) [Online]. Available: http://www2.jpl.nasa.gov/srtm/.

NASA 2001a. Shuttle Radar Topography Mission Global Coverage [Online]. Available: http://www.fao.org/docrep/008/a0118e/a0118e06.htm.

NASA. 2001b. SRTD Downloader [Online]. Available: http://dwtkns.com/srtm/.

NASA 2007. Shuttle Radar Topography Mission [Online]. Available: https://directory.eoportal.org/web/eoportal/satellite-missions/s/srtm.

NAVCEN 1997. U.S. Department of Homeland Security, The Navigation Center of Excellence [Online]. Available: http://www.navcen.uscg.gov/?Do=gpsArchives&path=ALMANACS/YUMA&year=2015&exten=txt.

OBER, P. B., Harrisman, D. A. G. & Wilde, J. 1998. Algorithm Selection for AUGUR - EUROCONTROL's Predictive RAIM tool, GNSS 98 proceedings, Global Navigation Satellite Systems, 20-23 Oct 1998, Toulouse.

OBER, P. B. 2003. Integrity Prediction and Monitoring of Navigation Systems, Integricom.

PARKINSON, B. W. & AXELRAD, P. 1988. Autonomous GPS Integrity Monitoring Using the Pseudorange Residual. Navigation: Journal of The Institute of Navigation, 35(2), pp 255-274.

PARKINSON, B. W., Spilker J. J. JR., AXELRAD, P. & ENGE, P. 1996. Global Positioning System: Theory and Applications Volume II, American Institute of Aeronautics and Astronautics, Inc.

PATERNOSTRO, S. 2008. Effects of different models of tropospheric mapping functions on the performances of a software for GPS data compensation. Master of Space Engineering, La Sapienza University, Rome.

PEREPETCHAI, V. 2000. Global Positioning System Receiver Autonomous Integrity Monitoring. Master of Science in Computer Science, McGill University, Montréal.

PERVAN, B., PULLEN, S. & ENGE, P. 1998. A Multiple Hypothesis Approach to Satellite Navigation Integrity. Navigation: Journal of The Institute of Navigation, 45(1).

PHAM, K., MCHUGH, T. & LORGE, F. 2013. Demonstration of Viability of ARAIM for LPV and LPV-200 Service Using Flight Data. Proceedings of the 2013 International Technical Meeting of The Institute of Navigation, January 29-27 2013 San Diego, CA. pp 274-300.

PHELTS, R. E., BLANCH, J., WALTER, T. & ENGE, P. 2014. The effect of Nominal Signal Deformations on ARAIM Users. Proceedings of the International Technical Meeting of The Institute of Navigation, January 27-29 2014 San Diego, CA. pp. 56-67.

PULLEN, S., ENGE, P., SHAW, S., FREY, C., FRYE, J. & SOUDER, M. 2013. The impact of GPS Modernization on Standalone User Performance and Integrity with ARAIM. Proceedings of the 26th International Technical Meeting of The Institute of Navigation Satellite Division (ION GNSS+ 2013), September 16-20 2013 Nashville, TN. pp. 2637-2653.

RIPPL, M., MARTINI, I., BELABBAS, B. & MEURER, M. 2014. ARAIM Operational Performance Tested in Flight. ION International Technical Meeting 2014. San Diego, CA.

RTCA/DO-229D 2006. Minimum Operational Performance Standards for Global Positioning System/Wide Aerea Augmentation System Airborne Equipment. Radio Technical Commission for Aeronautics.

SEMPERE, J. 2009. Azimuth and elevation [Online]. Available: https://www.revolvy.com/main/index.php?s=Inertial_frame_of_reference.

SESAR 2014. Trajectory Based Operations [Online]. Available: http://www.sesarju.eu/newsroom/brochures-publications/trajectory-based-operations-concepts.

SESAR 2016. Addressing noise through enhanced arrival procedures [Online]. Available: http://www.sesarju.eu/newsroom/all-news/addressing-noise-through-enhanced-arrival-procedures.

SPEIDEL, J., TOSSAINT, M., WALLNER, S. & AVILA-RODRIGUEZ, J. A. 2013. Integrity for Aviation: Comparing Future Concepts [Online]. Glen Gibbons. Available: http://www.insidegnss.com/node/3625 [Accessed 07/07/2014 2014].

SPLETTER, A. & RIPPL, M. 2011. Novel Satellite Fault Isolation Method for Real-Time Advanced RAIM Algorithms. Proceedings of the 24th International Technical Meeting of The Satellite Division of the Institute of Navigation, September 20-23 2011 Portland, OR. pp. 3205-3216.

STANDFORD, U. 2014. MAAST download website [Online]. Available: http://waas.stanford.edu/staff/maast/maast.html.

STERGIANOS, C. 2017. Improving the Realism of Ground Movement Models, doctoral thesis, University of Nottingham, Nottingham.

STURZA, M. A. 1988. Navigation System Integrity Monitoring Using Redundant Measurements. Navigation: Journal of The Institute of Navigation, 35(4), pp. 483-501.

SU, H., ROSENTHAL, P. & NARBONNE, F. 2012. Integrity Performance of an ARAIM algorithm-PORIMA: Two-Year GPS SIS Monitoring Results. Proceedings of the 25th International Technical Meeting of The Institute of Navigation Satellite Division, September 17-21 2012 Nashville, TN. pp. 2808-2817.

TEUBERT, C. 2008. NASA X Plane Connect [Online]. Available: https://software.nasa.gov/software/ARC-17185-1.

UASC 2014. Procedural Leg Types: Sids, Stars, Approach Transitions, Missed Approaches [Online]. Available: http://www.uasc.com/docs/default-source/documents/service-bulletin/3039sv60x-70x.pdf?sfvrsn=2.

UK GOV 2012. Reach for the Skies: a Strategic Vision for UK Aerospace. In: Department For Business, I. S. (ed.).

UNKNOWN. 2015. RNP Approaches and their variations [Online]. Available: https://greatbustardsflight.blogspot.nl/2015/03/aproximaciones-RNP-rnp-apch-y-sus.html.

WALSH, D., OCHIENG, W.Y., IOANNIDES, R. & FENG, S. 2004. GPS failure modes and effects analysis, in Proceedings of NAV04, London, UK, Paper no.18.

WALTER, T., BLANCH, J. & ENGE, P. A 2012. Framework for Analysing Architectures that Support ARAIM. Proceedings of the 25th International Technical Meeting of The Satellite Division of The Institute of Navigation, September 17-21 2012 Nashville, TN.

WALTER, T., BLANCH, J. & ENGE, P. 2014. Reduced Subset Analysis for Multi-Constellation ARAIM. International Technical Meeting of the Institute of Navigation. San Diego, CA.

WALTER, T., ENGE, P., BLANCH, J. & PERVAN, B. 2008. Worldwide Vertical Guidance of Aircraft Based on Modernized GPS and New Integrity Augmentations. IEEE, December 2008.

WANG, Y., HUYNH, G. & WILLIAMSON, C. 2013. Integration of Google Maps/Earth with microscale meteorology models and data visualization. Computer & Geosciences 61, December 2013, pp. 23-31.

WG-C 2012. EU-U.S. Cooperation on Satellite Navigation - ARAIM Technical Subgroup - Interim Report.

YOUNG, R. S.-Y. & SURATHU, M. 2012. Advanced Fault Detection and Exclusion with Future GNSS Constellations. Proceedings of the 25th International Technical Meeting of The Satellite Division of The Institute of Navigation, September 17-21 2012 Nashville Convention Center, Nashville, TN. pp. 2758-2769.